Intraoperative Assessment of Breast Cancer Margins *ex vivo* using Aqueous Quantum Dot-Functionalized Molecular Probes

A Thesis

Submitted to the Faculty

of

Drexel University

by

Giang Hoang Thuy Au

in partial fulfillment of the

requirements for the degree

of

Doctor of Philosophy

September 2013

DEDICATIONS

Dedicated to :

My Mother – Ngo Thi Thuy Huong

My Husband – Hoang H. Ho

ACKNOWLEDGEMENT

First of all, I would like to express my sincere gratitude to my thesis advisors, Dr. Wan Y. Shih and Dr. Wei-Heng Shih, who has guided me on every phase of this entire journey. Beyond their invaluable scientific mentorship, I have benefited from their advice regarding all other aspects of my academic and professional career. Without their constant support and guidance, this dissertation would have never been completed and I would not be the scientist that I am now.

Secondly, I am grateful to my clinical collaborators - Dr. Ari B. Brooks, Dr. Linette Mejias, and Dr. Vanlila K. Swami. Their supports and suggestions were invaluable during my entire study.

I am grateful to my thesis committee – Dr. Andres Kriete, Dr. Ari B. Brooks and Dr. Lin Han who have provided me with valuable discussions and input throughout my time at Drexel University

I would like to extend my gratitude to my colleagues from Sensor and Functional Materials Group for their encouragement and friendships. Finally, I would like to thank Ms. Dolores Conover from Biomed for her long lasting support, allowing me to assess to various analytical equipments which were essential to with my experiments

Table of Contents

List of Tables

List of Figures

Abstract

Intraoperative Assessment of Breast Cancer Margins *ex vivo* using Aqueous Quantum Dot-Functionalized Molecular Probes

Giang H.T. Au
Wan Y. Shih, Ph.D.
Wei-Heng Shih, Ph.D.

Breast cancer is increasingly diagnosed at an early stage, allowing the diseased breast to be removed only partially or breast conserving surgery (BCS). Current BCS procedures have no rapid methods during surgery to assess if the surgical margin is clear of cancer, often resulting in re-excision. The current breast cancer re-excision rate is estimated to be 15% to as high as 60%. It would be desirable if there is a rapid and reliable breast cancer margin assessment tool in the operating room to help assess if the surgical margin is clean to minimize unnecessary re-excisions.

In this research, we seek to develop an intraoperative, molecular probe-based breast cancer surgical margin assessment tool using aqueous quantum dots (AQDs) coupled with cancer specific biomarkers. Quantum dots (QDs) are photoluminescent semiconductor nanoparticles that do not photobleach and are brighter than organic fluorescent dyes. Aqueous quantum dots (AQDs) such as CdSe and near infrared (NIR) CdPbS developed in Shih's lab emit light longer than 600 nm. We have examined conjugating AQDs with antibodies to cancer specific biomarkers such as Tn antigen, a cancer-associated glycan antigen for epithelial cancers. We showed that AQDs could achieve ~80% antibody conjugation efficiency, i.e., 100 times less antibodies than required by commercial, making such AQD molecular probe surgical margin evaluation economically feasible. By conjugating AQDs with anti-Tn-antigen antibody, the AQDs molecular probe exhibited 94% sensitivity and 92% specificity in identifying breast cancer against normal breast tissues as well as benign breast tumors in 480 tissue blocks from 126 patients. Furthermore, mice model and clinical human studies indicated that AQDs imaging did not interfere with the following pathological staining. More interestingly, we showed that it it possible to directly conjugate one antibody to multiple AQDs, further reduces the required amount of antibodies needed, a feat that could not be accomplished by commercial QDs. To date, using a home-built imaging system consisted of 4 LEDs and a NIR CCD camera we have successfully imaged several human breast surgical margins with high sensitivity in less than 30 min.

CHAPTER 1: MOTIVATION AND GOAL

Breast cancer is one of the most common form of cancer and second leading death in women in the United States and Western countries[1, 2]. An estimate of 226,870 cases of new invasive breast cancer and 63,300 new ductal carcinomas in situ (DCIS) cases will be diagnosed among women in 2012.[3] Improved breast cancer screening has resulted in smaller, nonpalpable lesions being detected earlier during the last 30 years[4]. Increased-5year survival rates have been attributed to increased awareness, earlier detection, improved treatment and management. Breast conservation therapy (BCT), which includes local excision – breast –conserving surgery (BCS or lumpectomy) and radiation treatment, has become the standard treatment for early invasive breast cancer (stages I and II) [5, 6]. Multiple large, randomized clinical trials have reported no significant difference in disease-free and overall survival between patients that undergo BCT and traditional mastectomy [7, 8]. BCT is considered to be associated with a diminished psychological burden compared with mastectomy, offers better cosmetic results, and reduces wound infection risk [9]. In addition, it was found that for every four local recurrences avoided in patients treated by BCT, one breast-cancer related death was averted.[10]

The most important disadvantage of BCT is the lifelong risk for local recurrence (LR) which is often associated with positive margin after lumpectomy and additional surgery[11]. The primary goal of lumpectomy is adequate surgical removal of breast tumors, in which an optimal balance between good cosmetic results and preservation of resection margins. However, the local recurrence (LR) rates are generally higher for BCT compared to mastectomy. Ipsilateral breast tumor recurrence (IBTR) is often thought as a marker for more aggressive disease, an increase risk of systematic recurrence, and poorer survival. Several studies have suggested that IBTR associated with BCT may be the cause of an increase in mortality on long-term follow-up[12-14]. In effort to avoid IBTR, the goal of BCS is to optimize local control while providing a satisfactory cosmetic outcome[8]. Obtaining tumor-free surgical margins decreases the incidence of LR of the primary tumor. LR rate is higher for positive or close margin (16%) than that for negative margin (6%)[15]. According to pathology, “close” margin is usually defined as the cancer cells being present within >0 and ≤ 2 mm of from the cut edge. Positive margin is defined as cancer cells being present at the surface of the cut edge. If the margin is found to contain cancer cells, re-excision is required often resulting in additional cost, time, and pain to the patients. Estimates of the re-excision rate vary from 12% to as high as 60% [5, 16-21]. Morbidity and recurrence rates were found to be much higher in patients who under-go re-excision due to positive or close margins [22]. Restricted visibility of the tumor and coexisting DCIS during surgery are the main factors of high positive margin rates[23]. Therefore, accurate evaluation of surgical margins is critical to the success of local treatment of breast cancer.

Current margin assessment is done as part of pathological examination. The margin status can only be obtained in the pathological report. On the other hand, if margin assessment can be done intra-operatively it can provide information about the margin status during the initial surgery, which can reduce the positive margin rate thereby the re-excision rate. Different approaches have been considered for the intraoperative evaluation of lumpectomy margins. Several techniques have been studied including gross examination, touch preparation cytology (TPC) [24, 25], frozen section analysis (FSA) [26, 27], radio-frequency spectroscopy (RFS) [28], tomography (TM) [29] and Raman spectroscopy (RS) [30, 31], each of which have various limitations with false negative diagnoses in 20-50% of the patients or prolong surgical time [19]. Although RFS, TM, and RS are more sensitive than TPC, they are limited by their dependence on tissue homogeneity. As a result, they are not as sensitive in heterogeneous tissues such as breast. FSA has been reported to have good sensitivity and specificity to cancer cells but has difficulties in performing frozen sections on adipose tissue results in increasing surgery time and cost due to additional pathology evaluation [26]. The most significant disadvantage of FSA is the inability to evaluate the entire surface area with sampling rate of 10-15% surface area. Other technologies such as wire-guided localization (WGL) can perform intra-operative tumor localization with positive margin ranges from 23% to 46%[32, 33] and does not provide a clear three-dimensional image of tumor edges [23]. Ultrasound guided resection is limited to ultrasound visible tumors while specimen radiography detects clips or calcifications in a tumor specimen, but both are limited in ability to establish clear margins reliably [34]. It would be desirable to have a method that is not affected by tissue heterogeneity.

On the other hand, molecular imaging has increasingly become more popular as a tool for fluorescence-guided surgery due to its sensitivity and specificity for cancer cells [35, 36]. It is a rapidly emerging biomedical field that provides the microscopic information about the visual representation, characterization and quantification of biological processes at the cellular and subcellular levels within living organisms. Fluorescence imaging has attracted great interest in the molecular imaging field. Fluorescent tagging techniques are widely used in microscopic and macroscopic imaging. Active fluorescent probes are fluorochromes attached to affinity ligands such as antibodies and peptide specific for tumors or molecular processes marking a disease [37]. Fluorescent probes typically consist of the active component, which interacts with the target specifically, and the reporting component, which is a fluorophore molecule. Engineered fluorescent probe can be use as an effective approach for molecular fluorescence-guided surgery. However, an effective fluorescent probe should consist of these features: (1) It should offer strong signal with minimal background interference, (2) It should bind tightly to the target cells, (3) It should not interfere with tissue morphology characterization, and (4) It should possess high photostability under constant light exposure. Antibody coupled with a fluorescent molecule probe is attractive for tumor types that express unique surface markers such as breast cancer.

The reporting component is crucial in designing the imaging probe for guided surgery. In the last 10 years new nanomaterials that exhibit unique photoluminescent properties such as quantum dots (QDs) have emerged as a promising fluorescent label for such applications. QDs are semiconductor nanoparticles that have unique photoluminescent capabilities. They exhibit a high fluorescence efficiency, are resistant to photobleaching[38] and have a size comparable to a green fluorescent protein (GFP)[39]. By changing the particle size of the same material, the emission wavelength can be tunable allowing the possibility of simultaneous imaging of different markers at the same pathological sites[40]. Bioimaging applications of QDs have been demonstrated in cell labeling and tracking[41, 42], cell proliferation[43], in vivo sentinel lymph node mapping in a pig[44], in vivo brain imaging in pig [45], molecular beacons for DNA detection[46-48] and *in* *vivo* tumor detection in mice[49, 50]. For specific imaging of a target antigen, QDs can be coupled with an antibody to detect the target antigen on the cell surface. QDs exhibit superior photostability compared to traditional organic dyes or auto-fluorescent flavin proteins, which allows the acquisition of many consecutive focal-plane images to be constructed into a high-resolution three-dimensional images. They have the potential to be a great fluorescent molecular probe when combined with specific receptors to image biomolecules of interest.

By combining the unique photoluminescent properties of QDs and the specific binding affinity of antibody, an engineered fluorescent probe can be designed to tailor to target molecular imaging of tumor cells. The overall goal of this research is to develop such fluorescent molecular imaging probe to target tumor cells specifically for breast cancer margins assessment in real-time using aqueous quantum dots.

CHAPTER 2: INTRODUCTION AND BACKGROUND

Breast conserving therapy (BCT), which includes breast-conserving surgery (BCS) or lumpectomy and radiotherapy, has become the standard of care for early-stage breast cancer. Many clinical trials have reported that survival rates after BCT are similar to those who undergo mastectomy[5, 6, 8, 51]. Several studies have shown that positive surgical margins where cancer cells are present at the surgical edges are associated with ipsilateral breast tumor recurrence IBTR in patients undergoing lumpectomy. Positive margin rates have been found ranging from 12% to 60%. While it is possible to reduce the positive margin rate by removing more tissue, the cosmesis is significantly impacted as the extent of the surgery is increased. The cosmesis suffers further when a second surgery is required due to a positive margin from the initial excision. Therefore, being able to accurately evaluate surgical margins intraoperatively is important for BCT[8]. Different approaches have been considered for intraoperative evaluations of surgical margins, depending on the size, histologic type of the tumor (in situ versus invasive), surgical techniques used for excision, and physical type of the tumor (palpable versus non-papable).

2.1 CURRENT INTRAOPERATIVE TUMOR LOCALIZATION AND MARGIN ASSESSMENT METHODOLOGIES

Several studies have reported that positive margin status in lumpectomy is an important risk factor for LR[23]. In addition, large tumor size, multifocality and lobular type are other factors that can result in positive margin status[8, 52]. The techniques that are used to visualize the tumor and assess margin status are important. Techniques that are currently used are summarized in the following.

2.1.1 Wire-Guided Localization

Wire-guided localization (WGL) is the standard technique for intraoperative tumor localization for more than 20 years. The wire is introduced in the tumor by ultrasound, X-ray mammorgraphy or MRI (Figure 2.1). After resection, the excised specimen is often imaged again by X-ray to confirm the removal of tumor and microcalcification.

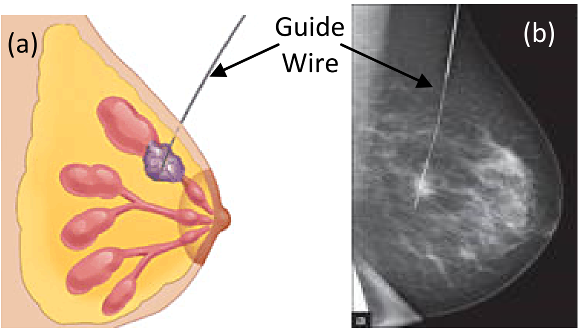

Figure 2.1: Wire Guided Localization. (a) Schematic of WGL; (b) Wire insert guided by X-ray mammography.

Multiple studies have reported high rate of positive to close margins ranging from 21.3-43% using WGL[4, 53, 54]. Burkholder et.al.[32] examined 511 patients guided by WGL and found that 21.3% of the patients had positive margins of which 26.7% needed re-excision. Because WGL does not provide a clear three-dimensional view on the tumor edges, it cannot effectively predict the surgical margins. Moreover, the guide wire is easily moved before and during surgery leading to inaccurate location of the tumor. The procedure is also time consuming and results in great discomfort to the patient that often leads to increased stress levels in the patients[23].

2.1.2 Intraoperative Ultrasound-Guided Resection

Intraoperative ultrasound (IOUS)-guided excision has become a new trend in BCT. Ultrasound (US) is performed before and during surgery to localize and improve tumor assessment. The margin status is also assessed by US after the excised tissue is removed. In case of positive or close margins, the patient's cavity margins are shaved to remove the residual cancer cells[23, 55]. Several studies reported that IOUS reduced the positive or close margin rate greatly compared to WGL (11% versus 45%). However, the disadvantage of IOUS is its inability to visualize nonpalpable breast tumors, which are the common characteristic of DCIS. In the study of Klimberg[56], only 50% of nonpalpable breast tumors could be seen by IOUS. In addition, DCIS lessons are not suitable for IOUS since microcalcifications cannot be detected by ultrasonography[57].

2.1.3 Frozen Section Analysis

For direct intraoperative margin assessment, frozen section analysis (FSA) is a common method that has been applied frequently during lumpectomy. The excised tissue is frozen, sliced, stained with hematoxylin and eosin (H&E), and analyzed microscopically by a pathologist. If cancer cells are detected, the wound can be reopened and additional surgical cavity shaving is performed, thus avoiding a re-excision at later time. FSA has a high specificity ranging from 98-100%[26, 58] but relatively lower sensitivity ranging 65-78%[27, 59]. Experience of the pathologists plays an important role in the sensitivity and specificity of FSA[23, 60]. Several studies showed that FSA resulted in

24-27% of the patients underwent additional tissue excision, whereas only 5-9% required a second re-excision after a definitive-pathological evaluation[26, 59]. FSA decreases significantly the re-excision rates compared with WGL or IOUS techniques. However, FSA is less reliable in evaluating small tumors with diameter less than 10 mm and the presence of DCIS[26, 59]. Another disadvantage of FSA is tissue loss during the evaluation, which can compromise the histological evaluation and tumor staging. FSA is a cost-effective and relatively safe procedure which can reduce the rates of re-excision. However, its reliability for negative margin is questionable due to the low sensitivity of the method[23].

2.1.4 Intraoperative Touch Preparation Cytology

Intraoperative touch preparation cytology (TPC) or “imprint cytology” is an alternative for FSA. The technique relies on the fact that malignant cells are adherent to glass surfaces, whereas benign mammary fat cells are not. The excised tissue is rolled on a glass slide. The cells that stick on the glass surface are fixed, stained and microscopically evaluated[23]. TPC has been reported to be both sensitive and specific[25, 61], which can significantly reduce LR rates compared with conventional methodsuch as maspectomy[62]. Although the overall outcome seems promising, TPC is not commonly used due to the likelihood of artifacts cause by draught and surface cautery[62]. In addition, TPC is less effective in identifying lobular carcinomas. Another shortcoming of TPC is that close margins are not detected by TPC because only superficial cancer cells can be detected.

2.2 UNDER RESEARCH MARGIN ASSESSMENT METHODOLOGIES

Most of the current margin assessment techniques are inadequate in predicting positive or close margins for all breast cancers. As a result, currently, there is no intraoperative margin evaluation. A new and innovative method for intraoperative margin assessment is needed to reduce the re-excision rate and hence the risk for LR[63].

2.2.1 Radiofrequency-based intraoperative margin assessment device

Recently, Dune Medical Devices Ltd. has developed a handheld device probe and a console system called MarginProbe. The device integrates radiofrequency spectroscopy to detect the difference in the dielectric properties between normal and malignant breast tissues[64]. Allweis et.al.[65] reported a reduction of 18% in the re-excision rate when the device was used in a study of a 300-patient cohort. The reduced re-excision rate, however, might have been due to the larger excised tissue volumes in the device group compared with the control group (107 cm^3 versus 95 cm^3)[60]. Also, the sensitivity and specificity of the device are only 71% and 68%[66], respectively due to the insensitivity of the device to detect tumors in heterogeneous tissues.

2.2.2 Molecular Imaging-based intraoperative margin assessment

Because most of the spectroscopy-based techniques use a physical property of a tissue to differentiate between normal and malignant breast tissues, their accuracy depends on the homogeneity of the tissue. However, breast tissue is heterogonous. As a result, spectroscopy-based methodologies are often inadequate to differentiate between normal and residue disease. A different approach has gained more attention in the past five years focusing on using fluorescent contrast agents coupled with a specific biomarker that could target tumor cells. Several animal and clinical studies have shown the potential of using fluorescence imaging to to guide surgery[23].

The most important component in fluorescent imaging lies in the design and use of fluorescence molecular probes (fluorochromes). Several groups have reported their own constructs on these fluoreochromes such as "targeted fluorochromes" that target specific biomarkers involved in breast cancer – vascular endothelial growth factor (VEGF) receptor, epidermal growth factor (EGF) receptor, or the HER2/neu receptor[67-70]. "Activatable probes" which exhibit no fluorescence activity in the native state due to self-quenching effect by arranging two fluorochromes in close proximity[71] are a popular approach for minimizing the background signal. However, the probe must be activated by a specific enzyme such as cathepsin B[72], cathepsin D[73], and matrixmetalloproteinases 2 (MMP2)[35, 74] to emit a fluorescent signal upon excitation (Figure 2.2).

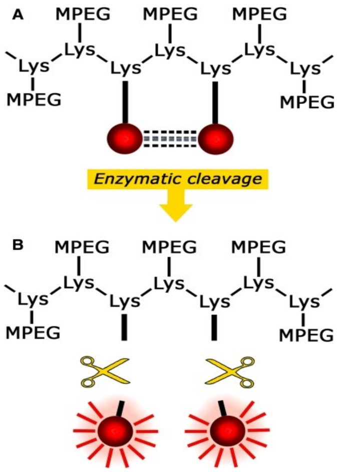

Figure 2.2: Schematic example of the mechanism of an activatable probe. (a) The probe is in native state with no fluorescence signal; (b) after cleavage by a specific enzyme, the probe emits bright fluorescent signal[23].

Nguyen et al.[35] engineered a Cy-5 labeled activatable cell-penetrating peptides (ACPPs) to improve the completeness of tumor removal during surgery. A breast tumor model was used with ACPPs injected into the mice 24 hours pre-operation. The tumors were visualized when excited and completely removed from the surgical bed. Animals whose tumors were resected with ACPPs guidance had better long-term tumor-free survival and overall survival than animals whose tumors were resected with traditional gross examination method[35]. Another study by Madajewski et.al. used NIR indocyanine green fluorophore and the enhanced permeability and retention effect of the tumor to image the surgical wounds after tumor resection to detect residual disease. A handheld optical spectrometer pen (Figure 2.3) was used as the optical imaging mechanism to detect fluorescence signal from the NIR probe. The result showed that the NIR examination of surgical cavity after resection can potentially enable a surgeon to locate and remove residue disease[75].

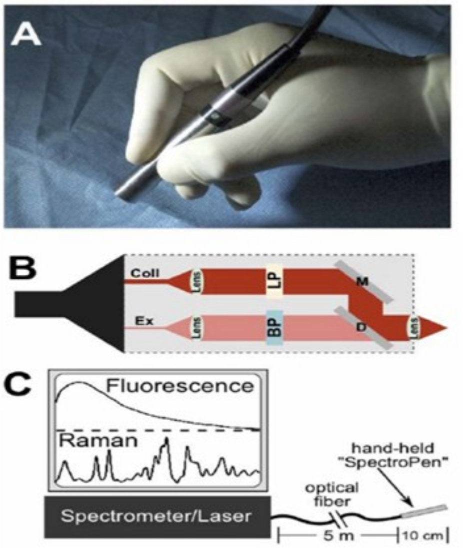

Figure 2.3: (a) Photograph showing the SpectroPen held in the operator's hand in a surgical setting. (b) Optical beam pathswith excitation at 785 nm. (c) Schematic diagram of the complete system for wavelength-resolved fluorescence and Raman measurement[76].

The use of optical imaging offers additional advantages: the technology is safe, simple to operate, fast, relatively inexpensive, makes use of nonionizing radiation, and target the molecular signature of the cells so that tissue heterogeneity is not a concern. This approach can potentially be used to assess the breast margin in lumpectomy surgery.

2.3 AQUEOUS QUANTUM DOTS AND THEIR SYNTHESIS ROUTES

Quantum dots (QDs) were introduced in the early 90's as one of the new nanomaterials with unique photoluminescent properties. Most QDs are traditionally synthesized using the organometallic method which involves the pryolysis of organometallic precursors in organic solvents such as tri-n-octylphosphin (TOP) and tri-n-octylphoshine oxide (TOPO) at high temperature (200-300°C)[77]. The most common and commercially available semiconductor QDs such as CdS, CdSe, CdTe, or CdSe/ZnS are carried out in organic solvents at high temperatures in the presence of surfactants to yield monodisperse and stable particles. This leads to the production of surfactant-coated particles. Here the polar surfactant head group is attached to the inorganic surface, the hydrophobic chain protruding into the organic solvent, mediating colloidal stability in organic solvents such as toluene or chloroform. Because of the hydrophobic surface coating such QDs are not soluble in aqueous media. To make the hydrophobic QDs into hydrophilic nanoparticles, the hydrophobic surfactant coatings are exchanged with ligand molecules that carry one end functional group reactive towards the QDs surface such as thiol (-SH) functionalities, and a hydrophilic group on the other end (such as carboxyl –COOH functionalities) to facilite water solubility (Figure 2.4).

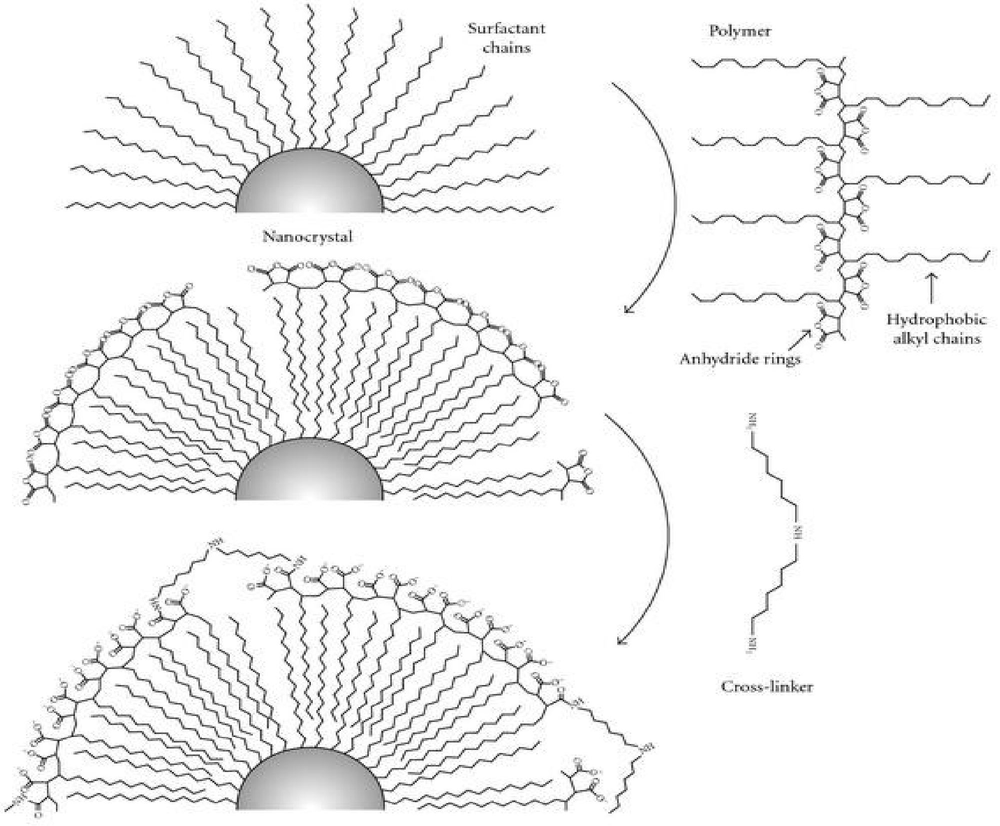

Figure 2.4: Scheme of polymer coating procedure to make the QDs hydrophilic. The hydrophobic alkyl chains of the polymer intercalate with the surfactant coating. The anhydride rings are located on the surface of the polymer coated nanocrystal. The amino end groups of the cross-linker molecule open the rings and link the individual polymer chains so that the surface becomes negatively charged and stable in water by electrostatic repulsion[78].

Mercaptohydrocarbonic acids are the most common source of these functional groups such as mercaptobenzoic acid, dihydrolopic acid, mercaptoundecanoic acid as well as synthetic peptides with multiple cysteines, and pyridine-functionalized polyethylene glycol (PEG) [78]. The ligand exchange can alter the chemical and physical state of the QD surface atoms and in most cases decreases the quantum yield of the QDs (about half or more of the original quantum yield)[79-81]. Because of the complicated synthesis and ligand exchange process, organic synthesized QDs are relatively high cost and difficult to conjugate with other bio-molecules.

A different route to produce QDs is through aqueous process which makes the QDs more compatible with other bio-molecules. Quantum dots that are produced directly in water are called aqueous QDs (AQDs). The preparation and synthetic methods of AQDs are generally safer, simpler, more environmental friendly, more cost-effective, easy to scale up and provide various functional groups by applying an appropriate capping molecule, which in turn may be further functionalized by electrostatic or covalent linking [82, 83]. The aqueous approach has yielded stable binary II-VI and IV-VI compounds. Vossmeyer et. al.[84] pioneered the examination of aqueous synthesis of CdS nanoclusters using cadmium perchlorate hexahydrous - $Cd(ClO_4).6H_2O$-, hydrogen sulfide H_2S, and 1-thioglycerol as precursors with mercaptoacetic acid (MAA) as stabilizing agent. The small CdS/MAA clusters were produced but dispersed individual QDs were difficult to obtain [85]. Later, a different approach was employed to synthesis CdTe nanocrystals via the reaction between Cd^{2+} and NaHTe precursor[86, 87]. The general synthetic procedure of thiol-capped QDs consists of 3 main steps as illustrated in Figure 2.5[82]: (1) formation of metal-thiol complexes at an appropriate pH, (2) injection of a chalcogen source into the metal/thiol solution results in the formation of a MeX precursor, and (3) nucleation and growth of the QDs by heating or microwave irradiation[83], usually upon reflux under open air conditions. The preparation of NaHTe precursor is complex, in which H_2Te is produced by reacting Al_2Te_3 with H_2SO_4, followed by titration into NaOH solution under nitrogen atmosphere. Several hours under reflux at 96°C is needed for the formation of the photoluminescence CdTe QDs.

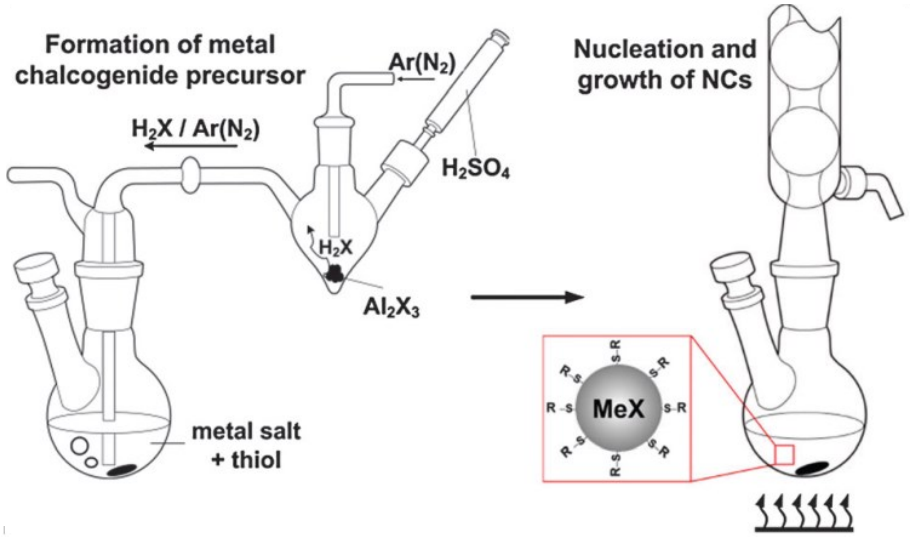

Figure 2.5: Schematic presentationof the synthesis of aqueous thiol-capped binary semiconductor QDs using aluminum chlcogenides as the chalcogen source [82].

Recently, a dramatically simplified aqueous procedure was introduced by stepwise addition of water, $CdCl_2$, thiol capping molecule, Na_2TeO_3, $NaBH_4$ and N_2H_4 to produce luminescent CdTe QDs in a conical flask at room temperature[88]. The particle sizes are controlled by the adjustment of the feed ratio. However, there are serious drawbacks of this protocol such as a large amount of highly toxic hydrazine and low concentrations of the monomers[82]. Li et. al. discovered another simplified approach to synthesize the AQDs. This method produces high quality AQDs with various compositions such as ZnS and CdS. The precursors' preparations are simple as the salts are dissolved completely in water at room temperature. A stepwise addition of water, a thiol-capping molecule, Cd^{2+} or Zn^{2+}, and S^{2-} are employed to produce the nanocrystals at high pH under room temperature. By manipulating the ratio between the capping molecule and cations, the photoluminescent (PL) intensity can be optimized[89-91]. The method produced stable, trap-state AQDs with broad emission wavelengths at 560 nm (CdS AQDs) and 400 nm (ZnS AQDs) with high quantum yield (around 35%). Although it is difficult to control the particle size using this method, band-gap tuning can be achieved by using different composition instead of changing the AQD size. These AQDs are ready to be applied in biological researches without ligand exchange procedure.

2.4 APPLICATION OF AQUEOUS QUANTUM DOTS FOR MOLECULAR IMAGING

Due to their unique optical and electronic properties, such as broad excitation spectrum, high PL intensity, long-term photostability and multiplex capabilities, QDs are considered to be superior candidates as luminescent probes and labels in biological applications, ranging from molecular histopathology, disease diagnosis, to biological imaging. To serve as fluorescent label probes, QDs need to be conjugated to other molecules, which can target specific cellular markers. This is the main challenges for traditional organic synthesized QDs since they are not water soluble. Although ligand exchanges can improve solubility and provide functional groups on the QD's surface, conjugation is still a big obstacle. AQDs, on the other hand, are ready to be conjugated. Recent studies have been focused on developing AQDs that emit longer wavelength ranging from 700-900 nm[92] to minimize the interference of tissue autofluorescence (emission between 400-600 nm)[93, 94].

Many studies have used AQD-labeled probe to imaging fixed cells such as MPA-capped CdS for Salmonella typhimurium cells labeling[91], or acid-capped CdSe/ZnS for HeLa breast cancer cells labeling[95]. Tracking of specific cells such as cancer cells becomes possible with the development of biomarkers. By conjugating QDs with biotinylated Annexin V, the complex can bind to phosphatidylserine (PS) moieties present on the membrane of apoptotic cells and not on healthy or necrotic cells[96]. The detection of apoptotic cells specifically is possible with AQDs as a tracker. Another application of QDs is in the tracking and diagnosis of cancer cells. Bagalkot et. al.[97] engineered a conjugate system involving QDs-aptamer (Apt)-doxorubicin (Dox) with the FRET principle to target, image, treat and detect prostate cancer cells that express the prostate-specific membrane antigen (PSMA) protein (Figure 2.6). Other examples including InP QDs conjugated with cancer antibodies and water-soluble-Silica-QDs micelles encapsulated with polymer chains to detect and track different cancer cells. Transfection is another major area that involves QDs. Many studies reported fluorescence imaging and nucleus targeting of living cells by transfection and RNA delivery. AQDs are often conjugated with cationic polymer such as polyethelenimine (PEI)[98, 99], nucleic translocate signal (NTS) peptides[100, 101] to achieve high transfection efficiency, which are promising for DNA gene delivery and cell labeling.

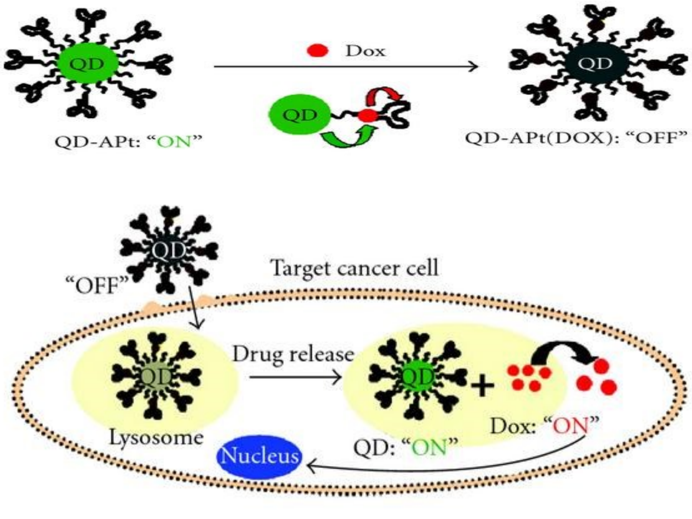

Figure 2.6: (a) Schematicillustration of QD-Apt(Dox) bi-FRET system. (b) Schematic illustration of specific uptake of QD-Apt(Dox) conjugates into target cancer cell through PSMA media endocytosis[97].

In addition to their usage as fluorescent probes and labels for *in vitro* imaging, QDs have been widely used for *in vivo* imaging. QDs can overcome the challenges in live animals fluorescence imaging such as intense autofluorescence of tissue chromophores or the poor transmission of visible light through living tissues because of their high PL, enhanced photostability under prolong laser illumination and longer wavelengths like NIR range[102]. Often, QDs are conjugated to cancer-specific antibody and injected into the blood stream to demonstrate *in vivo* localization of cancer antigens. Gao et. al.[103] administered QD coupled with anti-PMSA antibody to localize prostate tumor in mice transplanted with human prostate cancer. The detection results in a more accurate and sensitive imaging compared to GFP. Chen et.al.[104] examined the effectiveness of QD linked to alpha-fetoprotein (AFP) monoclonal antibody to target human hepatocellular carcinoma xenografted tumor in nude mice through intravenously injection. Papagiannaros et. al.[49] constructed a QD micelle (QD-Mic) structure and coupled it with 2C5 antibody for breast cancer. The 2C5-QD-Mic was able to localize the breast tumor as well as the pseudometastatic melanoma in the lung (Figure 2.7). The signal was strong enough to observe *in vivo* as well as *ex vivo* for confirmation of cancer presence. QD probe is important tool to image tumor and can potentially serve as tracking agent for fluorescent-guided surgery due to its optical properties surpass the traditional organic dyes.

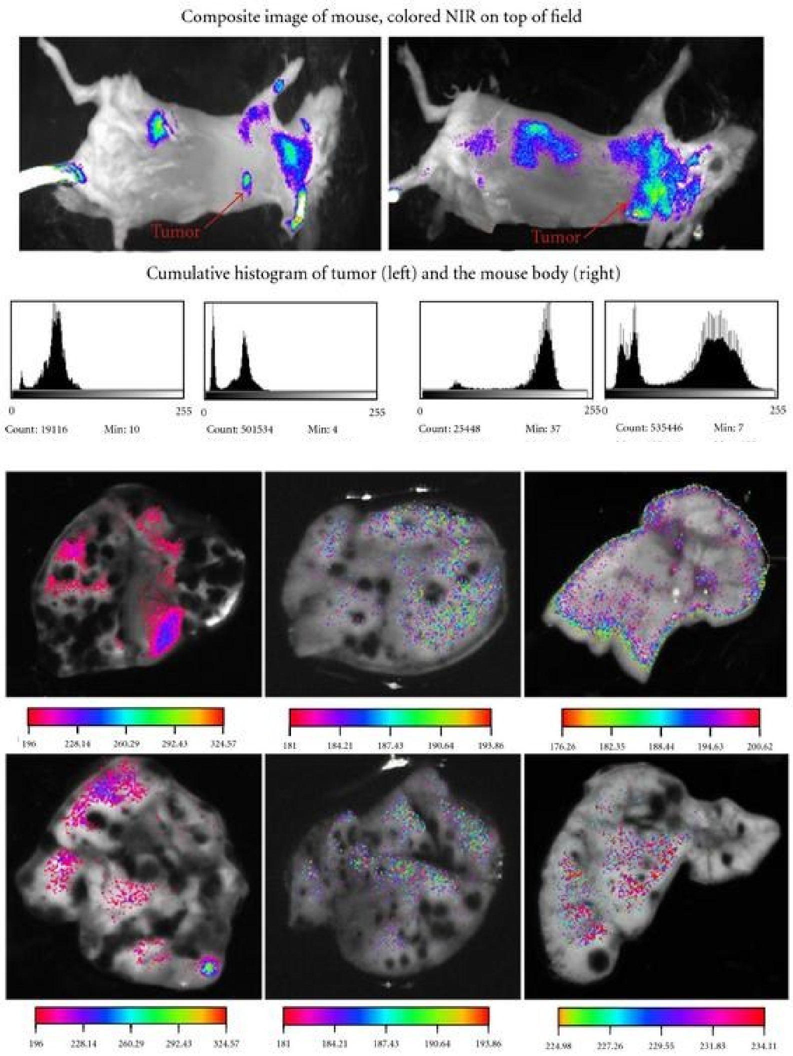

Figure 2.7: Targeting of lung melanoma tumor by injecting 2C5 QD-Mic in mice. (a) Tumor region within the body; (b) ex vivoimages of the lungs from mice bearing metastatic B16F-10 lung melanoma tumor [49].

2.5 TISSUE AUTOFLUORESCENCE

As optical imaging becomes more popular and important in fluorescent molecular imaging for *in vivo* and *ex vivo* systems, tissue autofluorescence is a big concern. The endogenous fluorophores include amino acids, structural proteins, enzymes and co-enzymes, vitamins, lipids and porphyrins. Their excitation maxima ranges from 250 nm to 450 nm, whereas the emission maxima ranges from 280 nm to 700 nm[105, 106] (Table 1). The absorption and scattering properties of the tissue will affect light at both excitation and emission wavelengths that fall in the range of these fluorophores. Therefore, the fluorophores contained within the tissue layers will emit light when excited with an appropriate light. Tissue scattering generally decreases monotonically with increasing wavelength over the ultraviolet, visible and NIR regions[105]. Hemoglobin absorbs the light over the same spectrum. The absorption in tissue generally decreases with increasing wavelength, whereas the penetration depth of light increases from few hundred microns (ultraviolet) to several centimeter (NIR)[107]. It has been reported that esophagus, stomach, breast and thyroid fluoresce in the range of 360 nm to 600 nm when excited at 330 nm[106]. Alfano et. al. reported the both normal and malignant breast tissues exhibit emission peaks at 515 nm, while normal tissue also had additional peaks at 556 nm and 592 nm when excited at 488 nm[108]. The fluorescence emission spectra of breast tissue at 340 to 380 nm excitation are associated primarily with connective tissue fibers in between lactiferous ducts and lobular complexes[109].

Table 1: Excitation and Emission Maxima of Endogenous Fluorophores[106]

Endogenous Fluorophores	**Excitation Maxima (nm)**	**Emission Maxima (nm)**	**Endogenous Fluorophores**	**Excitation Maxima (nm)**	**Emission Maxima (nm)**
Amino Acids			*Enzymes and co-enzymes*		
Tryptophan	280	350	FAD, Flavins	450	535
Tyrosin	275	300	NADH	290,351	440,460
Phenylalanine	260	280	NADPH	336	464
Structural Proteins			*Lipids*		
Collagen	325,360	400,405	Phospholipids	436	540,560
Elastin	290,325	340,400	Lipofucin	340-395	540, 430-460

NADH: reduced nicotinamide dinucleotide; NADPH: reduced nicotinamide dinucleotide phosphate

2.7 SUMMARY AND SPECIFIC AIMS

In summary, intraoperative evaluation of breast cancer margin is essential to reduce positive margin rate, improving the LR, preventing second surgical re-excision and achieving desired cosmesis. Fluorescent molecular imaging is a promising approach for margin assessment. A fluorochrome comprises of 2 components: a reporter and a detector. A detector is usually a cancer-specific antibody. A reporter can be an organic dyes, fluorophores or semiconductor quantum dots. The advantages of QDs over conventional dyes are photostability under prolong illumination, broad excitation spectra and high PL intensity. QDs can be tuned to have longer than 600 nm emission wavelength to minimize tissue autofluorescence.

The overall goal of this research project can be described with the following specific aims

1. Synthesis of water soluble QDs by a one-step reaction of inorganic chemicals to produce emission wavelength longer than 600 nm and into the NIR region. The AQDs are expected to be well-dispersed in water with a nano size, stable and ready to conjugate to other molecules. Various processing parameters and compositions are investigated to optimize the properties of AQDs.
2. Surface modification and conjugation of AQDs to various biomolecules for fluorescent molecular targeted imaging. The AQDs will be conjugated to antibodies or streptavidin as a protein model. The conjugates are expected to be stable in various buffer conditions. Various conjugation parameters are investigated to find the optimal conditions to achieve the desired complex with the least protein needed and high imaging capability.
3. Identification and validation of suitable breast cancer biomarkers for margin determination. The expression of these markers will be evaluated in one hundred twenty breast patient paraffin-embedded tissues using AQD probes and the conventional horse radish peroxide (HRP) immunohistochemistry staining for comparison.

Comparison between NIR CdPbS AQD and visible CdSe AQD probes for sensitivity and specificity that are due to autofluorescence will also be carried out.

4. Direct margin evaluation on animal tumor model and human excised breast tissues using AQD molecular probes. Various processing parameters are investigated to optimize the staining procedure and reduce the time to less than 30 minutes. Interference of AQD probes to the standard pathological examinations is studied. A standard small animal imaging system IVIS is used for *ex vivo* tissue imaging and is compared to a home-built AQD imaging system.

CHAPTER 3: SYNTHESIS AND CHARACTERIZATION OF AQUEOUS QUANTUM DOTS OF 600 NM EMISSION WAVELENGTH AND HIGHER FOR TISSUE IMAGING

Several studies have reported different routes to synthesis QDs directly in aqueous environment. Cadmium-based compositions are the most popular produced QDs. However, most of the AQDs synthesis methods require complex preparation of the precursors and presence of chalcogenide reaction. In addition, heating for several hours or microwave irradiation is necessary for particle formation. Recently, Li et al. has developed a one-step thiol capped ZnS[90] and CdS AQDs[91] synthesis process that is environmental friendly, simple and cost-effective. Both AQDs types have emission wavelength below 600 nm. In addition, this aqueous synthesis process is difficult to control and grow the size of the particle to achieve different emission wavelength. Different compositions have to be use to produce longer emission wavelengths.

Near-infrared (NIR) light within a spectral window of 700–1000 nm has a minimal overlap with the major absorption peaks of hemoglobin and water[110] . As a result, NIR light has the potential for deeper tissue penetration than visible light[111, 112]. For example, emission spectra centered at 840, 1110, 1320, and 1680 nm enable a detection depth of up to 5–10 cm[111, 113]. Recently, NIR QDs were demonstrated for direct infrared visual guidance throughout a sentinel-lymph-node mapping procedure in a pig, which had the potential to minimize incision and dissection inaccuracies as well as real-time confirmation of complete resection during surgery[44]. NIR QDs are also compatible with many infrared sensing and imaging technologies[114]. Moreover, NIR emission has minimal interference from tissue autofluorescence, which centers mostly around the green color (500–600 nm)[115]. Because of these benefits, much effort has been devoted to the development of NIR QDs[116]. InAs/InP/ZnSe and CuInSe/ZnSe (759 nm) NIR QDs with core/shell/shell or core/shell structures are examples of NIR QDs with the potential for deep-tissue imaging due to their longer wavelength and relatively low toxicity[117, 118]. The InAs(ZnCdS) NIR QDs have been conjugated with streptavidin for cellular imaging at a depth of up to 200 μm with multiple-photon microscopy[112]. However, these QDs were synthesized in an organic route that required multiple solvent- and ligand-exchange steps before they could be used for conjugation for imaging purposes solvent- and ligand-exchange steps before they could be used for conjugation for imaging purposes

In this research, we developed new compositions of AQDs using simple and cost-effective aqueous synthesis method to achieve longer emission wavelength. Cadmium-based compositions are explored. In addition, to extend the emission of AQDs to the NIR region, alloying of the AQDs with materials having narrower band gaps with similar lattice parameters. Several processing parameters are investigated for the AQDs formation, photoluminescence (PL) properties to synthesis CdSe with emission wavelength longer than 600 nm and alloyed CdPbS AQDs with emission in the NIR region.

3.1 MPA-CAPPED CdSe AQDs

In the synthesis of AQDs for this research, MPA ($HSCH_2CH_2COOH$) was used as direct capping molecule to control particle size as well as disperse the nanoparticles in water. The thiol group (HS^-) of the MPS was fully charge at pH > 5, which will chelate with the Cd cation on the particle surface. The carboxyl group (COO^-) required pH > 10 to fully charge and provide the negative charge on the AQD surface, resulting in dispersing the nanoparticles from each other through electrostatic repulsion.

3.1.1 Synthesis of MPA-capped CdSe AQDs

A cadmium precursor solution (0.08 M) was first prepared by dissolving 1.19 g of $Cd(NO_3)_2$ powder (Alfa Aesar, Ward Hill, USA) in 50 mL of deionizer (DI) water. The selenium precursor solution (0.08 M) was prepared by dissolving 0.315 g of a selenium powder (Sigma-Alrich, MA) and 8.2 g of sodium sulfite (Na_2SO_3) (Sigma-Alrich, MA) in 50 mL DI water at 80°C under constant stirring for 2 hours until the selenium was completely dissolved. These precursor solutions could be stored for later use. 0.16 mmol of MPA (Sigma-Aldrich, St Louis, MO, USA) was added to 40 mL of DI water and stirred for 10 minutes, followed by adjusting the pH to 11 using tetrapropylammonium hydroxide (TMAH) (Alfar Aesar, Ward Hill, USA). Next, 1 mL of the 0.08M $Cd(NO_3)_2$ precursor was added and stirred for 10 minutes. 1 ml of the selenium precursor was then added to the MPA-Cd mixture, followed by quickly adjusting the pH to 12 and stirring for 10 minutes to precipitate the CdSe AQDs. To further enhance the photoluminescence (PL) intensity, 2 mL of excess 0.08M $Cd(NO_3)_2$ precursor was added to the above CdSe AQDs suspensions followed again by a quick adjustment of the pH to 12. The thus-obtained CdSe AQD suspension was clear with a dark yellow tint. The final concentration of the CdSe AQDs was 1.6 mM in terms of the Se atom with a nominal molar ratio MPA:Cd:Se = 4:3:1. We have experimented with various MPA:Cd:Se ratios (see supplemental materials). It was found that CdSe AQDs with MPA:Cd:Se = 4:3:1 provided the best PL intensity. In what follows, all CdSe AQDs were prepared with a molar ratio of MPA:Cd:Se = 4:3:1. For storage, the suspension was kept at pH = 12 at 4°C.

3.1.2 Characterization of MPA-capped CdSe AQDs

The PL and the ultraviolet-visible (UV-Vis) absorption of the MPA-capped CdSe AQDs were measured using a QM4/2005 spectrofluorometer (Photon Technology International, Birmingham, MA, USA) and a USB2000 UV-vis spectrometer (Ocean Optics, NJ, USA) respectively. The X-ray diffraction (XRD) patterns of the AQDs were measured with a Siemens D500 X-Ray Diffractometer. The size, morphology and crystalline fringes of the AQDs were examined by transmission electron microscopy (TEM) (JEM-2100, JEOL, West Chester, PA). The quantum yield of the MPA-capped CdSe AQDs were determined by comparing the slope of the total emission intensity versus the total absorption intensity of the AQDs to that of Rhodamine 101 as described below. The size and zeta potential of the SA-AQD conjugates and those of the SA-OQD conjugates were measured using a ZetaSizer (Malvern).

The PL and UV-Vis absorption spectra of the MPA-capped CdSe AQDs and carboxylated CdSe/ZnS OQDs (Qdot 605 ITK, Invitrogen) are shown in Figure 9a for comparison. As can be seen, the emission of the AQDs peaked at 610 nm (which was close to the 605 nm emission peak of the OQDs) when excited at 460 nm. The luminescence of a MPA-capped AQDs suspension on a UV lamp appeared yellow-orange color as shown in the insert of Figure 3.1. This is due to the broad bandwidth of the emission peak compared to the narrow emission spectrum of OQDs, which resulted in red fluorescent color. The broad bandwidth of CdSe AQDs is due predominantly to defect-state emission[119] while the narrow emission of OQDs is due to band edge emission. The yellow-orange color of AQDs on a UV lamp is due to the broad emission bandwidth. If a cut-off filter of 600 nm is applied, the AQDs would appear red instead of yellow-orange.

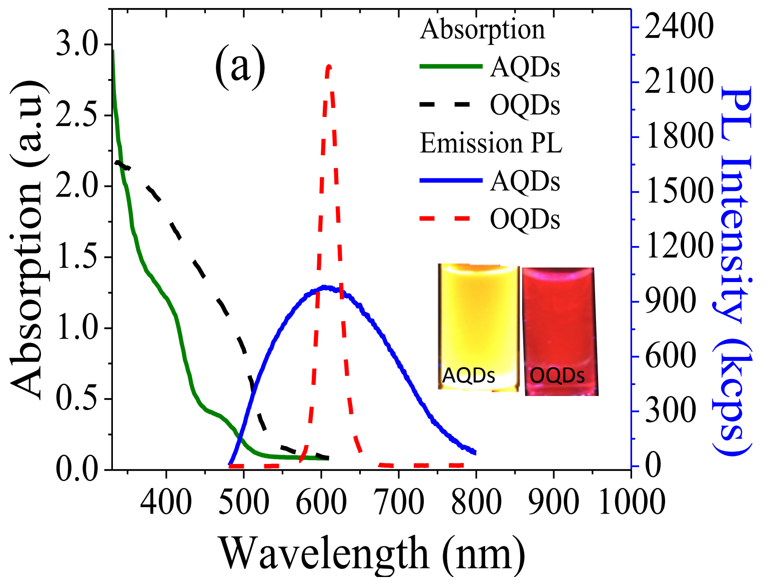

Figure 3.1: Photoluminescence (PL) spectrum (blue) excited at 460 nm and a UV-vis absorbance spectrum (green) of MPA capped CdSe AQDs measured at 80 nM and those (dashed lines) of CdSe/ZnS OQDs measured at the same concentration for comparison. The inserts in (a) show the luminescent color of an AQDs suspension and that of an OQDs suspension on a UV lamp.

In Figure 3.2, we showed the integrated PL intensity versus the absorption at 460 nm of the AQDs and OQDs together with that of Rhodamine 101 (Rd 101) as a reference. The quantum yield (QY) of the AQDs was determined using the following equation [120]

$$\phi_{QD} = \phi_{Rd}\left(\frac{Grad_{QD}}{Grad_{Rd}}\right)\left(\frac{\eta_{QD}^2}{\eta_{Rd}^2}\right) \quad (1)$$

The AQDs and that of the Rd 101, $Grad_{QD}$ and $Grad_{Rd}$ denote the slope of the integrated emission intensity (i.e., the total area under the emission peak instead of peak height) versus absorbance of the AQDs and that of the Rd 101 in Figure 3.2, respectively, and ϕ_{QD} and ϕ_{Rd} are the refractive index of the medium of the AQDs suspension which was water (hence η_{QD}= 1.33)[120] and that of the solvent of the Rd 101 solution, which was ethanol (hence, η_{Rd}= 1.36)[120], respectively. The QY of the AQDs as determined from Figure 8b was 70±2.5% with the QY of Rd 101 being 96±2.1% [121], comparable to that of the commercial CdSe/ZnS OQDs which was 81.6±2.5%.

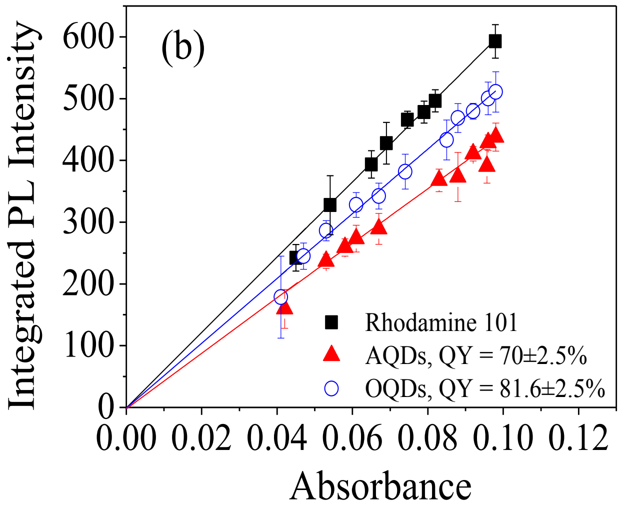

Figure 3.2: Integrated PL intensity versus absorbance of MPA-capped CdSe AQDs (circles) and CdSe/ZnSe OQDs (triangles). The quantum yield (QY) as deduced from the slopes were 70±2.5% for AQDs and 81.6±2.5% OQDs with the QY of Rhodamine 101 (squares) being 96±2.1%; Note that the slopes were determined by forcing the fitted line through the origin.

The reason that the current AQDs had such a high quantum yield was associated with the optimal MPA:Cd:Se molecular ratio in the present study. Note that even though Figure 8 shows that the emission peak height of the OQDs was about six times that of the

AQDs, the emission peak width of the AQDs was about three times that of the OQDs. After integrating the area under the emission peak, the integrated PL intensity of the

AQDs were roughly half that of the OQDs at the same concentration, which was similar to the ratio of the absorbance between the AQDs and OQDs at 460 nm (see the absorption spectra in Figure 3.1). As a result, the quantum yield of the AQDs and that of the OQDs are similar.

The crystalline structure of the AQDs was zinc-blende structure as evidenced by the X-ray diffraction (XRD) pattern shown in Figure 3.3a. From the size distribution and TEM micrograph of the AQDs shown in Figure 3.3b, one can see that the AQDs had a size of about 3 nm.

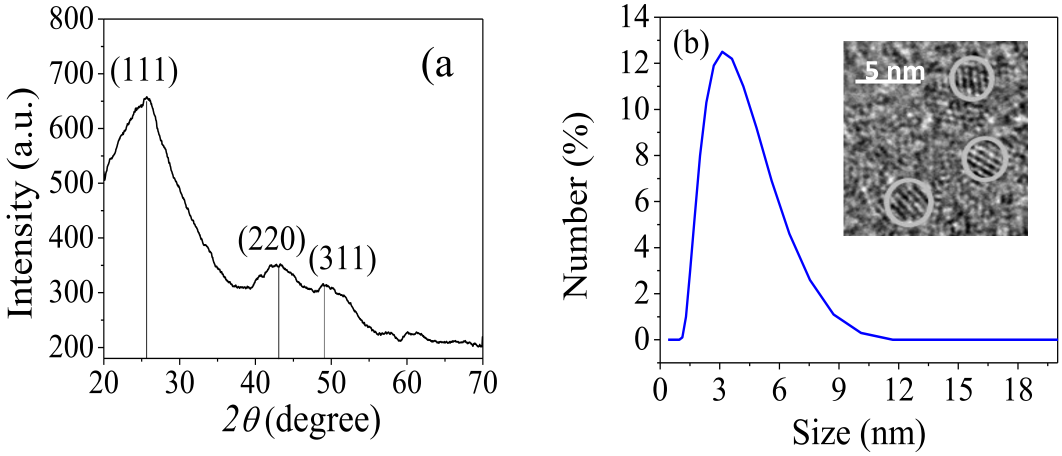

Figure 3.3: (a) an X-ray diffraction (XRD) pattern shows that the AQDs had a cubic zinc blend structure; and (b) AQDs size distribution that showed an average AQDs size of about 3 nm as measured by a Nanosizer. The insert is a TEM image of AQDs that also showed the size of AQDs to be about 3 nm.

Note that if the QDs were to exhibit edge-state emissions, 3-nm QD would emit green light of 540 nm[77, 122] rather than yellow/orange light of broad bandwidth around 600 nm in Figure 3.1. This is because the present AQDs exhibited defect-state emission involving energy difference from the bottom of the conduction band to the defect states inside the band gap, which is smaller than the band gap (the energy difference involved in edge-state emissions).

3.1.3 Effect of capping molecule to cation ratio

MPA is served as a capping molecule to stabilize and provide charge to the AQDs in the aqueous. With the same CdSe concentration of 1.6 mM, different MPA: Cd molar ratios were examined. The stepwise additional of excess Cd^{2+} is extremely important to improve PL intensity and stability of the AQDs. As shown in Figure 11a, with Cd:Se maintained at 1:1, the ratio of MPA:Cd = x(2:1), where x = 1,2,3…, was optimal which exhibited the highest PL intensity (Figure 3.4a).

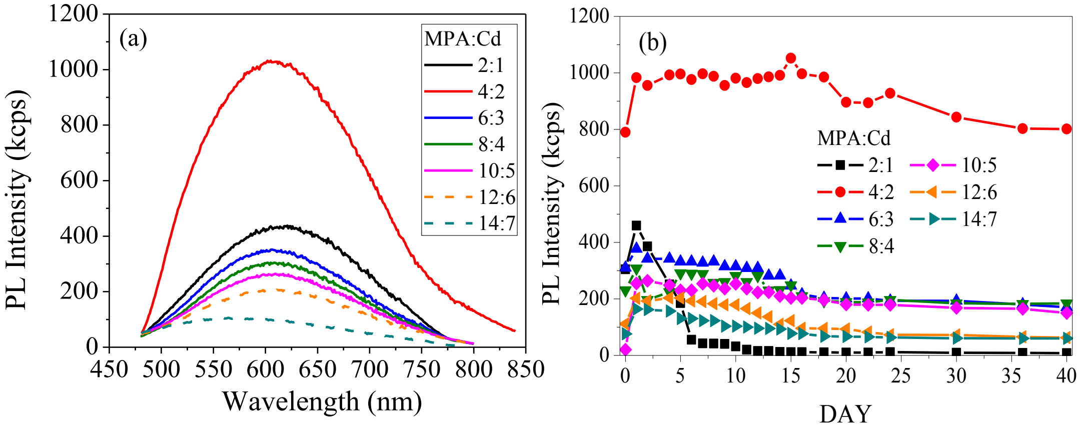

Figure 3.4: (a) PL emission spectra of CdSe AQDs synthesized with different x(2:1) MPA:Cd: ratios; (b) PL intensity versus time with different MPA:Cd ratios

Each Cd precursor was chelated to two MPAs. When these extra Cd precursors were added to the suspension with more than twice as many MPAs, each excess Cd will be chelated with 2 MPAs and these MPA-chelated Cd would mostly likely sit on top of

Se sites, forming a MPA-chelated Cd shell on the AQDs surface. Given that the emission of the AQDs was due to surface trap states the notion that the AQDs had a MPA-chelated Cd "shell" was consistent with the fact that the emission of the AQDs increased with an increasing amount of extra Cd and MPA (with a 1:2 molar ratio) Note packing an extra amount of MPA on the AQD surface through the chelation of extra MPA to extra Cd precursor was only possible in an aqueous environment.

From previous studies, the ratio of MPA:Cd = 2:1 is the optimal ratio, in which highest PL intensity can be achieved. However, with different x, the PL varies. For CdSe, $x = 2$ or MPA:Cd = 4:2 was the optimal condition to produce the highest PL intensity. At MPA:Cd = 2:1 or MPA:Cd:Se = 2:2:1, there were probably not enough MPA-Cd complexes to cover the surface defect of CdSe AQDs. On the other hand, as $x > 2$, too many MPA-Cd complexes resulted in lower PL intensity, which could due to formation of AQD clusters. CdSe AQDs were very stable in the absence of light. As shown in Figure 3.4b, most of the ratios could maintain its PL intensity to more than 45 day.

3.2 MPA-CAPPED CdPbS AQDs

Near-infrared (NIR) light within a spectral window of 700–1000 nm has a minimal overlap with the major absorption peaks of hemoglobin and water[110]. As a result, NIR light has the potential for deeper tissue penetration than visible light[111, 112]. For example, emission spectra centered at 840, 1110, 1320, and 1680 nm enable a detection depth of up to 5–10 cm[111, 113]. Recently, NIR QDs were demonstrated for direct infrared visual guidance throughout a sentinel-lymph-node mapping procedure in a pig, which had the potential to minimize incision and dissection inaccuracies as well as real-time confirmation of complete resection during surgery[44]. NIR QDs are also compatible with many infrared sensing and imaging technologies[114]. Moreover, NIR emission has minimal interference from tissue autofluorescence, which centers mostly around the green color (500–600 nm) [123]. Because of these benefits, much effort has been devoted to the development of NIR QDs [116]. InAs/InP/ZnSe and CuInSe/ZnSe (759 nm) NIR QDs with core/shell/shell or core/shell structures are examples of NIR QDs with the potential for deep-tissue imaging due to their longer wavelength and relatively low toxicity [117, 118]. The InAs(ZnCdS) NIR QDs have been conjugated with streptavidin for cellular imaging at a depth of up to 200 μm with multiple-photon microscopy [112]. However, these QDs were synthesized in an organic route that required multiple solvent- and ligand-exchange steps before they could be used for conjugation for imaging purposes. For aqueous synthesis route, CdHgTe nanoparticles have been developed. The approach is to incorporate Hg^{2+} ions into already prepared 2-mercaptoehanol (ME)-capped CdTe nanoparticles. In order to shift the emission wavelength to the NIR and IR regions, the procedure requires layer-by layer addition of HgTe layers[124]. This procedure is tedious and the alloyed QDs are mainly applied for the fabrication of field-effect thin film instead of bioapplications[82]. Here we report a new NIR QD system, CdPbS, obtained using an aqueous synthesis route and its demonstration in bioimaging applications.

3.2.1 Synthesis of MPA-capped CdPbS AQDs

0.08 M Cd precursor solution and 0.08 M Pb precursor solution were prepared by dissolving 1.19 g of cadmium nitrate tetrahydrate Cd(NO3)2 (Alfa Aesar, MA) and 1.32 g of lead nitrate Pb(NO3)2 (Alfa Aesar, MA) in 50 ml of de-ionized (DI) water, respectively. The precursor solutions were stirred for 15 min at room temperature. The precursors which were then stored in the dark could be stable for several weeks. Note that all AQD synthesis and processes were carried out at room temperature.

CdPbS AQDs with an initial nominal molar fraction of Pb, x_i ranging from 0.1 to 0.9, were prepared as follows, where $x_i = [Pb]_i/([Cd]_i + [Pb]_i)$ with $[Pb]_i$ and $[Cd]_i$ being the initial nominal concentrations of Pb and Cd, respectively. First, 21 µl of MPA (molecular weight=106 Da; density =218 g cm^{-3}, Alfa Aesar, MA) was dissolved in 40 ml of de-ionized (DI) water and stirred for 10 min, followed by the addition of $(1-x_i)$ ml of the 0.08 M Cd precursor solution and x_i ml of the 0.08 M Pb precursor solution. The solution was stirred for 10 min. The pH was then adjusted to 10.5 with tetramethylammonium hydroxide (TMAH), followed by the addition of 375 µl of 0.08 M Na2S precursor (Sigma-Aldrich, MA). This would make the initial nominal MPA:$(Cd_{1-x-i}Pb_{xi})$:S molar ratio 8:2.6:1. The solution was stirred for 10 min. Following the precipitation of CdPbS AQDs, 2.4 mol excess Cd^{2+} was added relative to each S^{2-} and the pH was adjusted to 12 with TMAH to improve the PL intensity. The final nominal QDs concentration was 0.6 mM, based on the concentration of S. After the synthesis, the CdPbS QD suspension was kept at 4°C overnight.

3.2.2 Characterization of MPA-capped CdPbS AQDs

Bulk CdS and bulk PbS have band gaps of 2.4 eV and 0.37 eV, corresponding to wavelengths of 517 nm and 3351 nm, respectively. This suggests that a NIR QD system is possible if Cd and Pb can both be incorporated in the AQDs to form a solid solution. Here we show that indeed, under basic conditions (preferably at pH > 11), both Cd and Pb could be incorporated in the AQDs and that the emission wavelength of the AQDs changed with the Cd/Pb molar ratio. In the following, we use the ‘initial’ molar fraction of Pb, xi, to denote CdPbS QDs of different Cd/Pb ratio. By varying xi, we have examined the formation of CdPbS QDs and the resultant PL to identify the optimal x_i for NIR emission in the 700–1000 nm window. The formation of the CdPbS AQDs and their resultant PL can be enhanced by the amount of MPA included in the initial precursor solutions and the amount of excess Cd^{2+} added after the initial precipitation of the AQDs. A typical synthesis condition is characterized by the MPA:cations:S molar ratio among the MPA, the cations, namely Cd^{2+} and Pb^{2+}, and the sulfur in the solution. It was found that the optimal synthesis condition consists of having an initial MPA:cation:S molar ratio of 8:2.6:1 followed by adding 2.4 of excess Cd^{2+} to result in a final MPA:cation:S molar ratio of 8:5:1. In other words, there were 8 moles of MPA and 5 moles of cations for every mole of sulfur. Note that a similar PL enhancement by the addition of excess cations after the initial AQD precipitation was also observed in ZnS and CdS systems[89, 125].

The final 'nominal' molar fraction of Pb, x_f, was related to the initial nominal molar fraction of Pb, x_i, as $x_f = (2.6/5)x_i = 0{:}52x_i$. The PL spectra of the CdPbS QDs of various x_i were shown in Figure 3.5a. As can be seen, the PL emission spectra of the AQDs with $x_i = 0.1$ and 0.2 peaked at around 500 nm, similar to that of CdS QDs[46]. In contrast, for $x_i \geq 0.3$, the PL emission peak shifted to the NIR range above 800 nm. The photoluminescence excitation (PLE) and the PL wavelengths of the CdPbS AQDs versus xi are shown in Figures 3.5b and 3.5c. There was an abrupt shift of the PL peak wavelength from around 500 nm for $x_i \leq 0.2$ to above 800 nm for $x_i \geq 0.3$. There was also a similar abrupt shift of the PLE wavelength above $x_i = 0.2$, although the up-shift of the PLE wavelength at $x_i = 0.2$ was not as drastic as that of the PL wavelength (Figure 3.5b).

These results indicate that at xi ≤ 0.2, the PL of the CdPbS QDs behaved like that of CdS, while at xi ≥ 0.3, a PbS-like behavior emerged (Figure 3.5c). The x-ray diffraction (XRD) patterns of CdPbS AQDs for xi = 0.1– 0.9 were shown in Figure 3.5d. The XRD results for xi ≤ 0.2 exhibited the 110 and 220 peaks of a zinc blende structure, which is the structure of CdS[91].

For AQDs with $x_i \geq 0.3$, the rock salt structure, which is the structure of PbS[126], began to appear and coexist with the zinc blende structure. Roughly in the range of $0.3 \leq x_i \leq 0.6$, both the zinc blende and the rock salt structure coexisted. To further clarify if the CdPbS QDs were solid solutions in the range of $x_i \leq 0{:}2$ and $x_i > 0{:}6$, we plot the position of the 220 peaks for both zinc blende and rock salt structures versus xi in Figure 3.5e. According to Vegard's law[44], the lattice constant should vary linearly with the composition of the solid solution. In the range of $x_i \leq 0.2$, the solid solution behavior was evident by the shift of the 220 peak to a small angle due to the increase of the lattice constant by the increasing amount of Pb in the zinc blende structure. A similar decrease of the 220 peak position was also evident for $x_i > 0{:}6$, indicating a solid solution of the rock salt structure for $x_i > 0.6$. These XRD results indicate that the CdPbS AQDs were crystalline solid solutions with a zinc blende structure at $x_i \leq 0.2$ and a rock salt structure at xi > 0.6. For $0.3 \leq x_i \leq 0.6$, the AQDs were a mixture of the zinc blende and rock salt structures. The abrupt transition in the PL behavior shown in Figures 3.5a–c was well correlated with the structural change from the zinc blende structure of the CdS to the rock salt structure of PbS. The behavior of PLE shown in Figure 3.5b indicates that, for 0.3 ≤ xi ≤ 0.6, the excitation wavelength is a linear combination of the zinc blende and the rock salt phase, consistent with the XRD results shown in Figures 3.5d and 3.5e, only that the

PL in the 0.3 ≤ xi ≤ 0.6 range seemed to be more dominated by the rock salt phase with an emission wavelength >800 nm. Further close spectroscopic examinations showed that all suspensions with $x_i \geq 0.3$ lacked emissions at around 500 nm, supporting the notion that the rock salt phase dominated the PL behavior. Note that the highest NIR emission intensity occurred at $x_i = 0.7$.

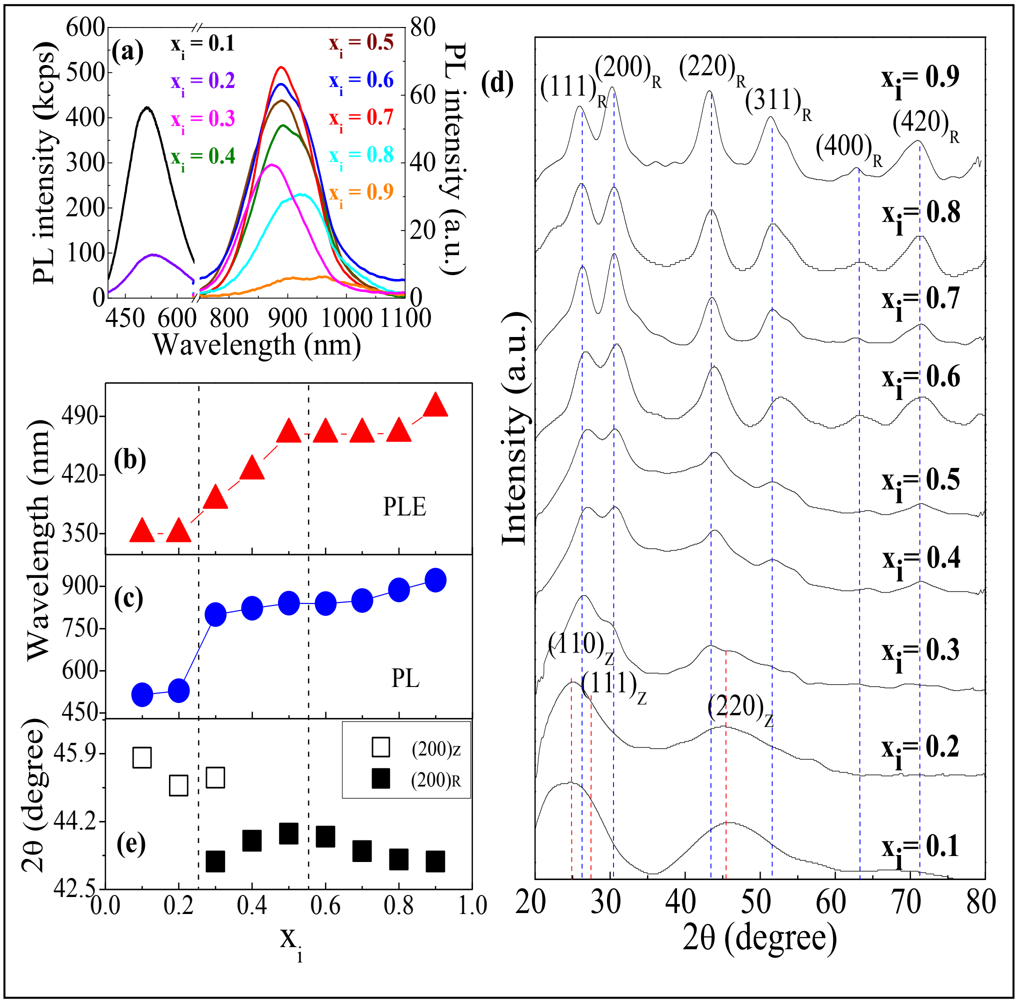

Figure 3.5: (a) Photoluminescence intensity of the QDs, emission peak changed from 500 nm to 850 nm when $x_i \geq 0.3$ (b) PLE versus x_i; (c) PL versus x_i; (d) CdPbS obeys Vegard's law with respect to the $(220)_R$ peak; (e) XRD patterns evolve from zinc blend (Z) to rock salt (R) structure as the content of Pb, x_i, in CdPbS increases; blue-dashed lines indicate rock-salt peaks at $x_i = 0.7$, red dash-dotted lines indicate zinc blend peaks at $x_i = 0.2$.

To determine the actual composition between Cd and Pb in the AQDs we carried out atomic absorption (AA) spectroscopy studies. Before the AA measurement, the free Cd^{2+} and Pb^{2+} ions in the AQDs suspensions were removed by three repeated microcentrifugations with a 10 kDa filter, as described above. After each microcentrifugation, distilled water was added to bring the volume of the AQDs suspension back to its initial value. The measured AA intensities for Pb and Cd were converted to concentrations according to the calibration curves. The result is shown in Figure 3.6a, where we plot the measured Cd and Pb concentrations versus the nominal concentrations of Cd and Pb.

We denote the measured final molar fraction of Pb, x_m, where $x_m = [Pb]_m /([Pb]_m + [Cd]_m)$. The measured x_m (full squares) together with the nominal x_f (open circles) were plotted versus x_i in Figure 3.6b. As can be seen, the concentrations of the Cd and Pb incorporated in the AQDs were lower than the initial nominal Cd and Pb concentrations, indicating that not all the Cd^{2+} and Pb^{2+} ions in the synthesis solution were incorporated into QDs. However, as shown in Figure 3.6b, the measured x_m final molar fraction of Pb incorporated in the QDs were quite similar to the nominal x_f for x_i up to 0.7. For $x_i \geq 0.8$, it was found that x_m was much larger than x_f, suggesting the Cd was harder to incorporate in the rock salt structure once the x_i exceeded 0.8. As a result, QDs with $xi \geq 0.8$ exhibited a higher Pb molar fraction than the nominal value. It was known that excess Cd can improve the PL of the precipitated AQDs[89]. We speculate that the PL intensity peak at $x_i = 0.7$ was related to the difficulty of incorporating Cd at $x_i \geq 0.8$.

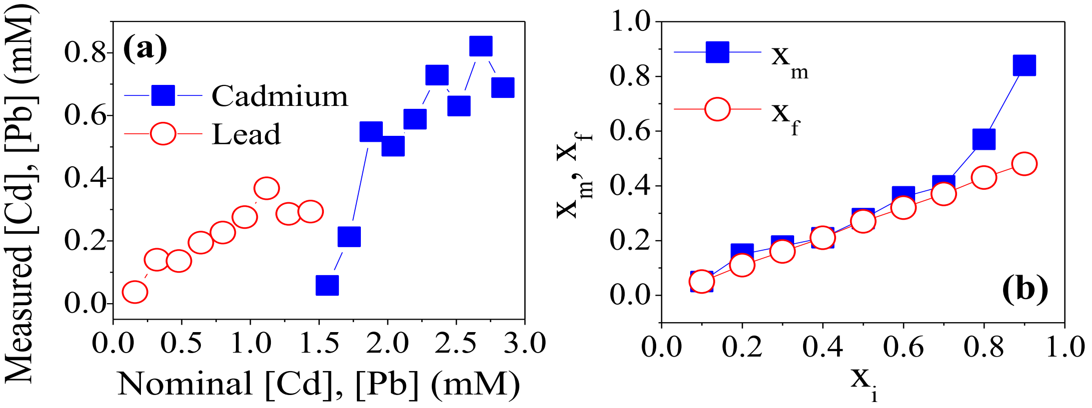

Figure 3.6: (a) Cadmium and lead concentrations measured by AA versus nominal cadmium (full squares) and lead concentration (open circles); (b) x_m and x_f versus x_i where x_m, x_f, and x_i are as defined in the text

Since the highest PL intensity was at $x_i = 0.7$, we focused the remainder of the study, i.e., QDs stability and bioimaging on the QDs with $x_i = 0.7$. The stability of the CdPbS QDs over time was evaluated by monitoring the QY of the AQDs over time. To measure the QY of the QDs, Rhodamine 101 (RD) (Fisher Scientific, Fairlawn, NJ) was used as the standard. Diluted RD solutions and QD suspensions were prepared. The absorption spectra of the diluted RD solutions and QDs suspensions were measured with the USB4000. The emission spectra were measured with the PTI with a common excitation wavelength of 460 nm. The integrated emission intensity and integrated absorption of each RD solution and each QD suspension were obtained by integrating the area under the emission peak and that under the absorption curve, respectively. The obtained integrated emission intensity was then plotted versus the integrated absorption for both the RD and QDs. As an example, we show the integrated emission versus integrated absorption of the RD and the QDs of the first day in the inset of Figure 3.7a. With the QY of RD being 100% [121], the QY of the QDs could be obtained by dividing the slope of the integrated emission versus integrated absorption of the QDs by that of the RD as equation 1. The QY of the CdPbS AQDs versus time is shown in Figure 3.7a. As can be seen, the QDs had an initial QY of about 12% and retained a QY of about 8% even after 21 days of storing at 4°C in the dark, indicating that the CdPbS AQDs had a high QY and were stable over a long period of time. A TEM micrograph of the CdPbS AQDs is shown in Figure 3.7b, which shows the QDs to be about 4 nm and unagglomerated.

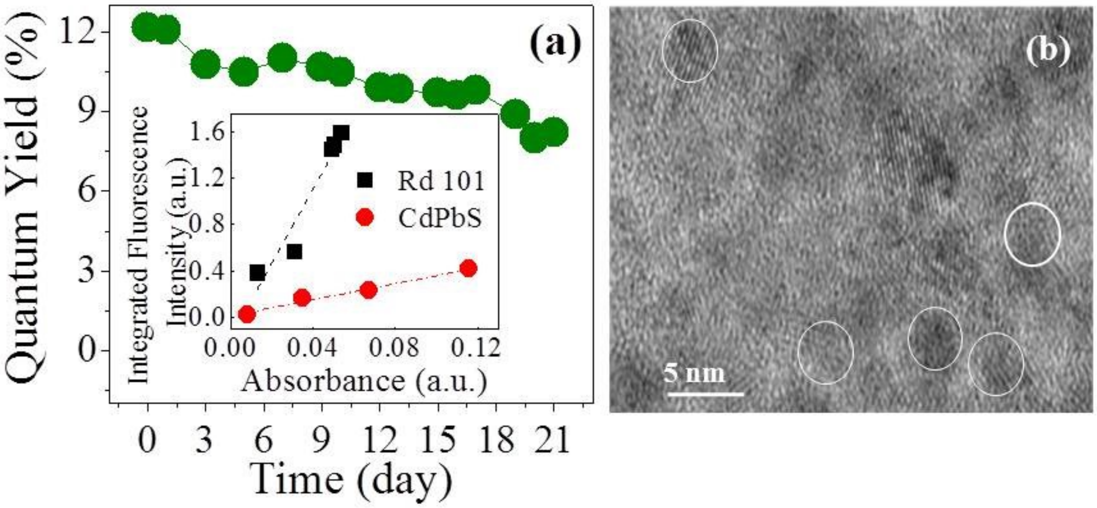

Figure 3.7: (a) Quantum yield (QY) versus time; and (b) a TEM image of the CdPbS QDs with an $x_i = 0.7$. The insert is the integrated fluorescence intensity versus integrated absorption of the CdPbS QDs at $x_i = 0.7$ right after synthesis. The circles in (b) are to denote the QDs whose size was around 4 nm.

3.2.3 Imaging application of CdPbS AQDs

To demonstrate the fluorescence molecular imaging capability of the newly synthesized CdPbS NIR AQDs, the AQDs were tested in intracellular delivery and tracking as well as membrane staining experiment by coupling the AQDs with different molecules.

a. Intracellular delivery of AQDs

NIH 3T3 mouse fibroblasts (ATCC, Manassas, VA) were cultured with complete DMEM medium. The cell culture media contained 10% fetal bovine serum (FBS) and 1% penicillin–streptomycin. Cells were incubated at 37°C with 5% CO2 and split every 2–3 days. Polyethylenimine (PEI) (MW = 25 kDa, branched, Sigma- Aldrich, MA) was first diluted in a phosphate-buffered saline (PBS) solution at 1.43 mM. Various amounts of the PEI solution ranging from 10 to 1000 µl were added to 1 ml of a 0.6 mM MPS-replaced CdPbS QDs suspension to achieve a PEI=AQD number ratio of 1, 10, 20, 30, 50, 80, 100, 300, and 500 based on the AQD particle concentration. The QD particle concentrations were estimated based on a QD size of 4 nm, as evident in the TEM and a lattice constant of 0.593 nm, which was calculated according to XRD pattern obtained in this study. Assuming the AQDs to be cubes, an AQD concentration of 0.6 mM based on S was equivalent to 0.733 µM based on AQD particle concentration. For example, mixing 102 µl of a 1.43 mM PEI solution with 1 ml of a 0.6 mM AQDs suspension (0.733 µM based on particle concentration) would yield a PEI/AQD number ratio of 200. To maintain the same AQD concentration at 0:366 µM by particle concentration for all PEI–AQD mixtures, an appropriate amount of de-ionized water was added to bring the final volume to 2 ml. The pH of all PEI–AQD mixtures was adjusted to 7 before transfection.

NIH 3T3 cells were transferred onto chamber slides and incubated in complete DMEM medium. After one day, the medium was replaced by a fresh medium. PEI–AQD mixtures (20 µl) were added to the cell culture and incubated at 37°C with 5% CO2 for 24 h. Cells were then washed with PBS three times and fixed with 4% paraformaldehyde

(EMS, Hatfield, PA) for 15 min, followed by washing again with PBS. 4', 6-diamidino-2-phenylindole (DAPI) was added at the end to stain the nuclei.

To test the utility of the CdPbS AQDs at $x_i = 0.7$ in bioimaging, we show two examples. The first example is the transfection of CdPbS AQDs in the cytoplasm of mouse fibroblast cells NIH 3T3 (using PEI as a carrier. For transfection, we first examined the size and charge of the PEI–AQD complex at various PEI/AQD number ratios 1, 10, 20, 30, 50, 80, 100, 200, 300, 500, 800–1000. We started all PEI–AQD mixtures at an AQD particle concentration of 0.366 μM, a volume of 2 ml, and an initial pH of 12. The mixtures were incubated at room temperature for 10 min. The suspension pH was then adjusted to 7 using nitric acid. PEI was positively charged in water due to the amine groups in the PEI. On the other hand, AQDs were negatively charged. When the PEI/AQD ratio increased, heterogeneous aggregation occurred due to the opposite charges carried by the PEI and the AQDs[127]. The size and the zeta potential of the PEI–AQD complex, as measured by the ZetaSizer (Malvern), versus the PEI/AQD ratio are shown in Figures 3.8a and 3.8b, respectively. The PL intensity of the PEI–AQD complex versus PEI–AQD number ratio, as measured by the Tecan plate reader (Infinite 2000, Tecan, MA), was plotted in Figure 3.8c. At zero PEI concentration, the size of the QDs as measured by the ZetaSizer was around 3–5 nm (Figure 3.8a), consistent with the 4 nm size obtained by TEM, and the zeta potential of the AQDs was -25 mV (Figure 3.8b). As we can see from Figure 3.8a, the size of the PEI–AQD complex increased rapidly, exhibited a maximum of about 600 nm at a PEI/AQD number ratio of around 10, decreased with further increase of the PEI/AQD number ratio, and saturated at a size of about 30 nm at PEI/AQD number ratios > 200. At the same time, the zeta potential of the complex increased sharply from negative to neutral at the PEI/AQD number ratio where the PEI–AQD complexes exhibit a maximal size. The size distribution of PEI/AQD = 300 is narrow compared to the PEI/AQD = 10 where the PEI formed big aggregate with the AQDs. It indicates the complex was more stable at higher PEI/AQD ratios, so that they were able to repel each other, whereas PEI/AQD of lower ratios were not stable and formed aggregates of random pattern, resulting in large distribution in size. A further increase of PEI/AQD ratio increased the positive charge of the complex, resulting in the breakup of the PEI–AQD complex reducing its size. This kind of behavior is typical of systems where hetero-aggregation occurs[128, 129] and was also observed in the previous studies of CdS QDs with PEI [98].

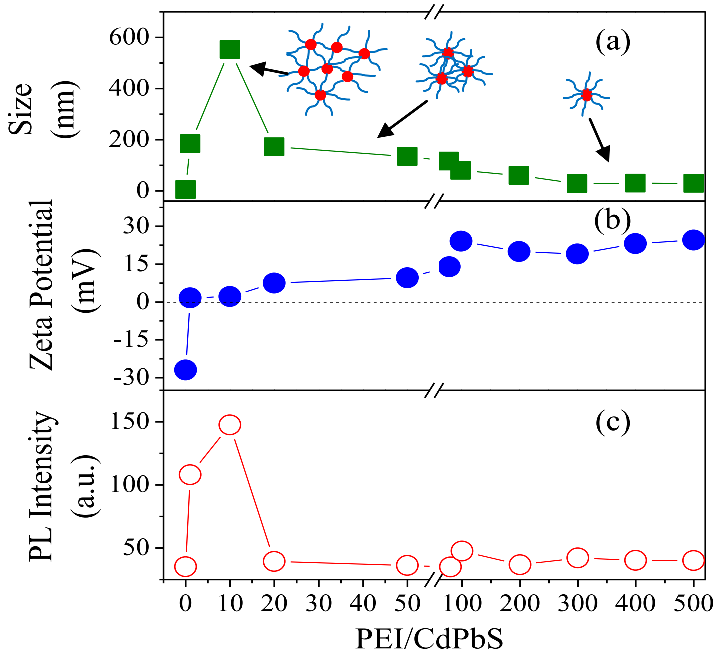

Figure 3.8: (a) Particle size of QDs as a function of PEI/CdPbS molar ratio. The maximum size was 550 nm at PEI/CdPbS = 10. The size decreased as PEI/CdPbS ratio increased. The size reached the saturated point as PEI/CdPbS > 200. The PL intensity of all the complexes >50 was very similar to the non-conjugated QDs suggesting a single QD with many PEI molecules on the surface. (b) Zeta potential of CdPbS QDs as a function of PEI/CdPbS molar ratio. The zeta potential changed to positive as the PEI/CdPbS ratio increased. The potential reached +25 mV as PEI/CdPbS > 200. This indicates the complex was stable as PEI/CdPbS > 200. (c) Photoluminescence intensity as a function of PEI/CdPbS molar ratio.

A schematic of such heterogeneous aggregates is depicted near the peak of the PEI–AQD size in Figure 3.8a. At large PEI/QD ratio > 200, the zeta potential of the PEI–AQD complex was above +25 mV and its size was about 30 nm, suggesting that PEI–AQD complexes may be thought of as sunflowers, with the AQDs as the 'sunflower head' and the PEI as the 'petals' around the sunflower head, as schematically shown in Figure 3.8a. A schematic of such a 'sunflower-like' PEI–AQD complex is depicted near the plateau above PEI/AQD number ratio > 200. Note the size of an individual PEI was about 8 nm (data not shown) and that of the AQD was about 4–5 nm. That the overall size of a complex was about 30 nm suggests that the adsorbed PEI on the AQD surface was stretched outwardly due to the high PEI/AQD ratios.

Figure 3.8c shows the PL behavior of the PEI–AQD complex. One can see that as the PEI/AQD ratio increased to 10, where the size of the PEI–AQD complex exhibited a maximum, the PL intensity of the PEI–AQD complex also exhibited a maximum. As the PEI/AQD ratio increased to above 50, the PL intensity of the PEI–AQD complex decreased and saturated at a value that was similar to that of QDs alone. Figure 3.8 shows that a larger PEI–AQD complex has a higher PL intensity. The reason why a larger PEI–AQD complex is brighter is unknown, and will be addressed in future study. That, at higher PEI/AQD ratios, the PL intensity of the PEI–AQD complex was similar to that of AQDs alone was consistent with the notion that, under these conditions, AQDs were well separated due to the PEI layer surrounding each AQD.

We tested the transfection performance of PEI–AQD complexes of various ratios. PEI–AQD complexes with a PEI/AQD ratio of 300 showed the best transfection results, as judged by the intensity of the PL and the uniformity of the distribution of the PL inside the cells after transfection. As an example, we show a bright-field image, a DAPI image, a AQDs image, and the overlap of all three of the same cells in Figures 3.9a–d, respectively. These four images together indicate that the PEI–AQD complex was able to enter the cytoplasm and remain fairly uniformly distributed inside the cytoplasm. Although the present study could not provide the distribution of the AQDs in the thickness direction to unambiguously indicate that the AQDs were inside the cells, there was no fluorescence signal overlapping with the outlines of the cells. This indicates that the AQDs were likely inside the cells rather than on the membrane surface. For the present study, we did not perform cytotoxicity test on the transfected cells, as our focus was more on the imaging of the NIR AQDs. However, in our previous transfection study of CdS AQDs to PC12 cells, we found that the toxicity of the PEI–AQD complex was lower than that of PEI alone and cells were viable after transfection[98]. It is likely the present CdPbS AQDs will behave similarly. More detailed CdPbS AQDs transfection studies will be carried out in a future study.

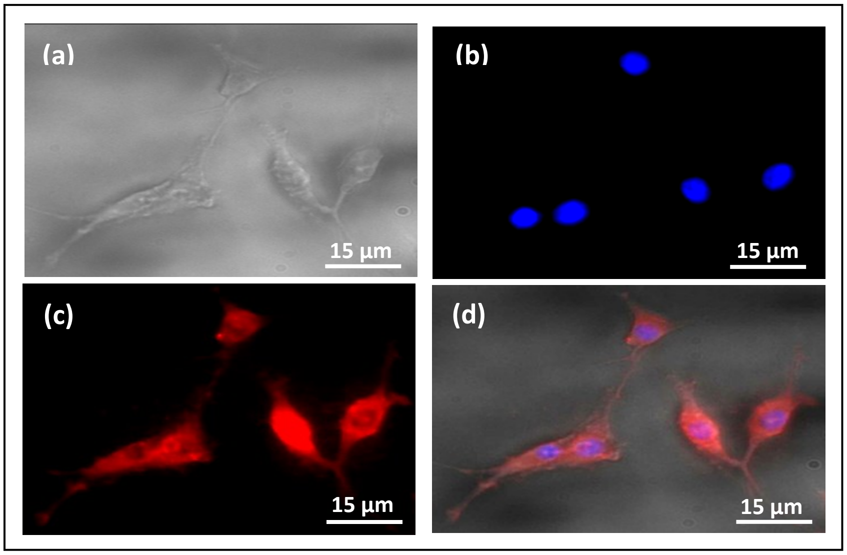

Figure 3.9: Fluorescent Images of NIH 3T3 cells with transfected PEI-CdPbS AQDs. (a) Bright Field, (b) DAPI - nuclei, (c) PEI-CdPbS AQDs, (d) overlay of bright field and fluorescent fields. The AQDs were co-localized with the cytoplasm indicating AQDs entered the cells through transfection.

b. Cell Membrane Imaging

The second bioimaging example was cellular membrane imaging using 1,2-distearoyl-sn-glycero-3-phosphoethanolamine- polyethylene glycol-maleimide (DPSE-PEG-Mal) conjugated AQDs (Figure 3.10a). The conjugated AQDs were tested on both cells and paraffin-embedded breast tissue slides. The best ratio for DSPE-PEG-Mal/AQD ratio was 50, as judged by the intensity of the PL and the uniformity of the distribution of the QDs on the cells. As an example, we show a bright-field image, a DAPI image, a QD fluorescence image, and the overlay of all three of the same cells treated with the DSPE-PEG-Mal–AQD mixture at a DSPE-PEG-Mal/AQD ratio of 50 in Figures 3.10b–e, respectively. As can be seen from Figure 3.10d, all cell membranes were uniformly stained by the AQDs. In particular, the overlay in Figure 3.10e clearly showed that the PL images of the QDs were contained well by the bright-field contour of the cells, indicating that the DSPE-PEG-Mal conjugated AQDs were indeed capable of imaging cell membranes.

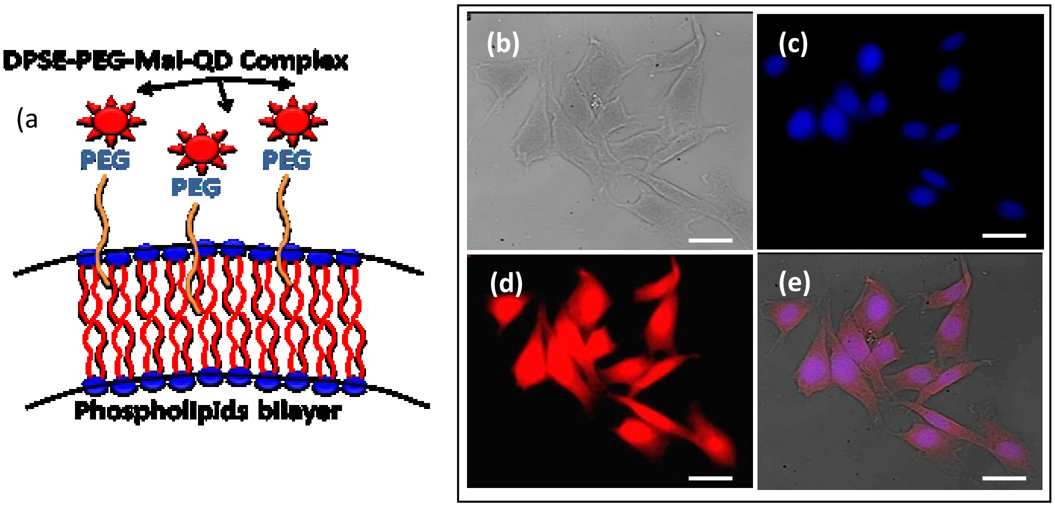

Figure 3.10: Mouse Fibroblast NIH 3T3 membrane imaging using DSPE-PEG-Mal-CdPbS. (a) Schematic representation of DPSE-PEF-Mal-AQD membrane penetration mechanism; (b) Bright field; (c) DAPI – nuclei; (d) CdPbS AQDs - cells membrane; (e) Bright field, DAPI and CdPbS QDs overlay. Signal was distributed evenly throughout the entire cells. Scale bar 20 μM.

We speculate that the DSPE part of the PEG mimics the tail of the phospholipids in the bi-layer of the cell membrane, with the maleimide reacting with the thiol of the MPS on the QD surface to covalently link to the QD. Confocal microscopy was used to determine whether the signal came from the QDs on the cell membrane or the internalized QDs in the cytoplasm. A z-stack of the cells was obtained. A 3D surface plot was constructed at different depth (Figure 3.11a), z. At the depth of the cell nuclei, there was no QDs emission. Emission was seen only at the bottom of the nucleus where the cell membrane was located. Furthermore, when moving away from the plane of nuclei, only the membrane of the cell was visible, and not the nuclei (Figure 3.11b and 3.11c). This indicates that the designed DSPE-PEG-Mal conjugated AQDs stayed on the cell membrane and not inside the cytoplasm.

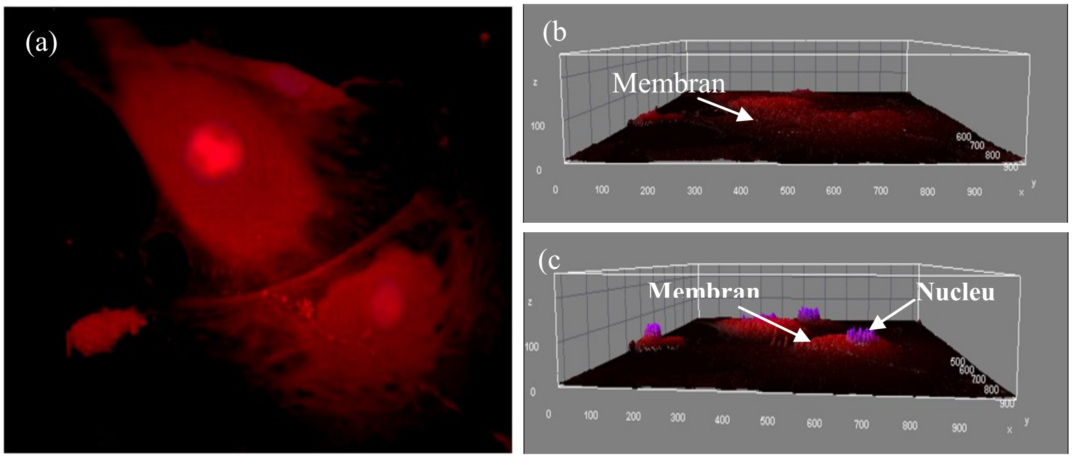

Figure 3.11: 3D reconstruction of 3T3 NIH fibroblast cells which showed that the QD stained only the membrane of the cells. (a) re-construction of the z-stack consists of 79 images at different depth by confocal; (b) 3D surface plot at highest point z=13.86 nm away from the nucleus showed the membrane of the cells (c) 3D surface plot at nucleus plane at z = 13.56 nm, no staining was observed in the cytoplasm at the same nucleus position.

CdPbS AQDs, fluorescence images of transfected cells were taken beneath layers of chicken muscle tissue of various thicknesses. The excitation intensity of the lamp was 13 mW/mm^2 , with an image acquisition time of 270 μs. We show the fluorescence image of the same transfected cells alone, underneath 0.1 mm, 0.4 mm, and 0.7 mm thick chicken tissue in Figures 3.12a–d, respectively. As can be seen, the image of the transfected cells could be seen underneath a chicken muscle layer of up to 0.5 mm thick. The depth capability of the QDs was further analyzed using digitized images with ImageJ. The background fluorescence signal from the chicken tissues, although minimal, was subtracted from the QDs fluorescent signals from the fibroblast cells. We found that the QD-to-background contrast decreased with an increasing thickness of the chicken tissue with a maximal detection depth of about 0.7 mm due to microscope limitations. It is worth noting that the depth capability of the QDs shown above was achieved without the aid of multiple-photon microscopy.

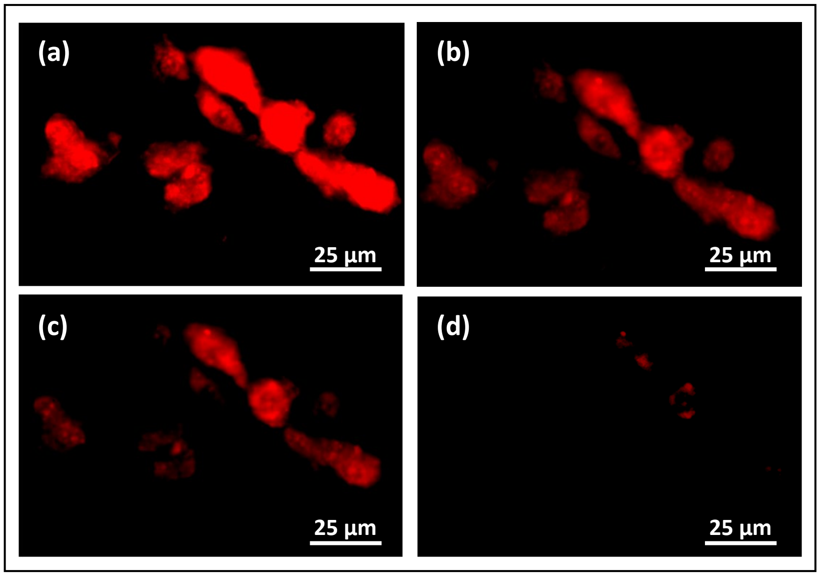

Figure 3.12: Tissue depth penetration capability of CdPbS AQDs. Muscle laps were placed on top of transfected NIH 3T3 mouse fibroblasts. The maximum detection depth is around 0.7 mm. Penetration depths: (a) 0 mm, (b) 0.1 mm, (c) 0.4 mm, (d) 0.7 mm.

It is of interest to note that because the emission wavelength of the CdPbS QDs was well in the NIR range, imaging cells using the CdPbS QDs essentially removed the auto-fluorescent signal of cells. As a result, in a fluorescent microscopy session, the CdPbS QDs stained slides would appear pitch dark to the human eye and only when the NIR CCD camera was switched on did a clear fluorescent image of the QDs appear on the computer screen. As an example, Figure 3.13 showed that NIR QDs cannot be seen by naked eyes under UV-lamp excitation whereas CdS QDs exhibited torquoise color under both UV-lamp and fluorescent microscope. On the other hand, CdPbS QDs can be observed under NIR CCD camera but not UV-lamp. This indicates that the fluorescent image that we observed in CdPbS QD system was due to the NIR emission of the CdPbS and the CCD camera could capture the NIR emission. This also indicates that imaging using the NIR CdPbS QDs can enhance the signal to noise ratio of the images as cellular and tissue auto-fluorescence were minimal in the NIR range.

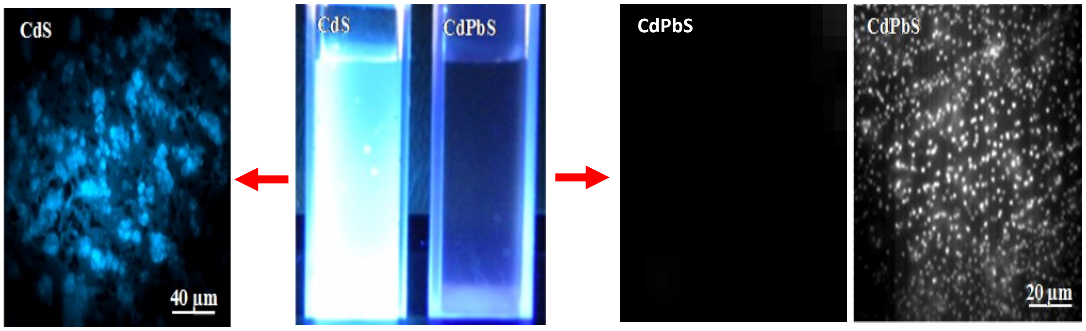

Under Fluorescent Microscope
CdS QDs show blue color to

Under UV lamp
CdS QDs show blue color
while CdPbS QDs cannot be seen with

Under Fluorescent Microscope
CdPbS QDs cannot be seen

Under Fluorescent Microscope
CdPbS QDs can be seen using NIR

Figure 3.13: Under UV-lamp, CdS AQDs showed blue luminescent color whereas CdPbS AQDs did not show any color due to the NIR range. A drop of AQD suspension was placed on glass slide surface and observed under fluorescent microscope. When observed in the microscope, blue CdS AQD dots were seen but not CdPbS AQDs. However, when the NIR CCD camera was turned on, bright dots were observed.

3.3 SUMMARY

In summary, we have successfully synthesized MPA-capped CdSe AQDs that emited at 610 nm and had QY = 70±2.5%, which was comparable to commercial available organic CdSe/ZnS OQDs. Multiple MPA:Cd:Se ratios were investigated to find the optimal ratio. With the addition of excess Cd, a chelated complex of 2 MPAs and 1 Cd was formed to improve the PL intensity of the AQDs. The best ratio is MPA:Cd:Se 4:3:1 with stability of more than 6 months.

MPA-capped CdPbS QDs using an aqueous synthesis route under basic conditions with initial Pb molar fraction (x_i) in the synthesis solution followed by the addition of excess Cd^{2+}. It was shown that the measured final Pb mole fractions were similar to the nominal final mole fraction for $x_i \geq 0.7$. At $x_i \geq 0.3$, CdPbS QDs exhibited NIR emissions with the optimal emission intensity occurring at $x_i = 0.7$ and a peak emission wavelength of 850 nm. These NIR CdPbS QDs were synthesized completely in aqueous route which was different from the currently reported NIR system. The quantum yield at $x_i = 0.7$ was 12% and the XRD analysis showed that it was a solid solution in a rock salt structure. The imaging capability of CdPbS NIR QDs was demonstrated with membrane staining and transfection experiments. We also demonstrated that the fluorescence of stained cells could still be observed under a slab of chicken tissue 0.7 mm thick without a confocal microscope. We believe that the current work will have a significant impact in the synthesis of new NIR materials as well as offering a new tool in tissue imaging.

Acknowledgements

We would like to thank the support of Grants W81XWH-09-1-0701 from DoD and from Coulter Translational Research Partnership. S-Ja Tseng thanks the support of the National Science Council, Taiwan (NSC97-2917-I-007-102).

CHAPTER 4: SURFACE MODIFICATION and CONJUGATION OF AQDS TO VARIOUS BIOMOLECULES FOR TARGET MOLECULAR IMAGING

MPA-capped AQDs have been successfully developed to achieve longer emission wavelength (> 600 nm). Both MPA-capped CdSe and CdPbS AQDs are stable for several days under 4°C storage condition. It has been observed the life-time of MPA-capped CdPbS AQDs is significantly shorter than MPA-capped CdSe AQDs. In previous studies, surface modification with (3-mercaptopropyl) trimethoxysilane (MPS) can significantly improve the stability of the MPA-capped AQDs, since SiO_2 network can be form encapsulating the core of the AQDs to stabilize and protect the AQDs from photo-degradation. In addition, the MPS network can provide sulfhydryl functional groups to couple with other biomolecules.

4.1 SURFACE MODIFICATION – MPS REPLACEMENT

After the synthesis of MPA-capped AQDs as describe in chapter III, AQDs suspension was stored at 4°C overnight. Before replacement, the suspension was filtered using 10-KD filters (Amicon ultracel, Millipore, CA) three times to remove excess MPA and precursors[130]. The fitrate containing free MPA and access ions were discarded. The volume of the retentate was brought back to 50 mL after each filtering cycle and the pH was adjusted back to 12. After filtering, 14 μL of MPS (Sigma-Alrich) was added with its pH adjusted to 12 to the retentate. The suspension was stirred continuously for 30 minutes at room temperature. The molar ratio of MPS:cations:S was 1:5:1 for CdSe and 1:3:1 for CdPbS AQDs. The MPS-replaced AQDs suspension was filtered again to remove potentially unreacted MPS. After filtering , the suspension was stored at 4°C.

For CdSe AQDs, the MPS replacement was straight forward and similar to that for other AQDs systems as developed by Li et.al.[130] The MPS-replaced CdSe AQDs were stable with high PL intensity and ready for bio-conjugation. For NIR CdPbS AQDs, the MPS-replacement was more difficult due to stronger binding of the MPA to Pb^{2+} ions. We found that conjugation was difficult to achieve with the above MPS replacement protocol after one day of MPA-capped AQDs synthesis. The surface condition of the CdPbS AQDs after 1 day, 2 days and 3 days of the MPA synthesis was then examined using Fourier Transform Infrared (FTIR) spectroscopy. For each sample, 10 mg AQDs powder was mixed with 290 mg of potassium bromide (KBr) powder, ground and pressed into a pellet with a diameter of 13 mm. A control sample of 300 mg KBr powder was used to measure the background signal. The pyroelectric detector deuterated triglycine sulfate (DTGS) was used during the experiment. The sensitivity and resolution were set at 2 cm^{-1} and 4 cm^{-1}, respectively. The chamber was purged with dry air for 10 minutes right after the sample was loaded to eliminate the water vapor. Each sample was scanned 32 times to obtain an average spectrum.

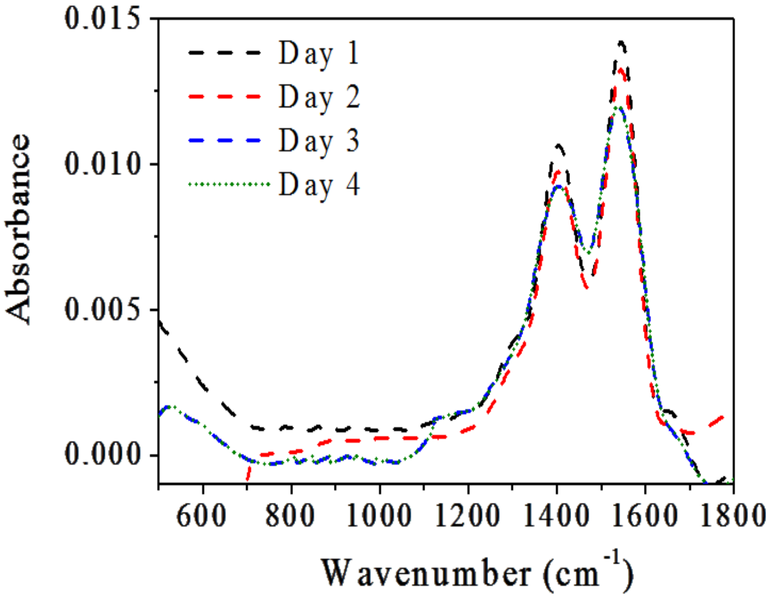

Figure 4.1: FTIRspectra of MPA-capped CdPbS QDs at different time points and MPS capped CdPbS QDs.

The resultant FTIR spectra of aged MPA-capped CdPbS AQDs is shown in Figure 4.1. Since all the free MPA and free ions in the solvent were removed, the observed signature peaks of MPA can only be attributed to the MPA on AQD surface. As can be seen, the MPA-capped AQDs exhibited strong absorbance peaks at around 1400 cm^{-1} and 1570 cm^{-1}, which resulted from the starching vibration of C=O and C-OH bonds in the carboxyl group of MPA[131]. These peaks' intensities decreased as the AQDs aged and reached a saturation point at day 3 after synthesis when the peaks' intensities dropped to 80% of those of the freshly made CdPbS AQDs. The result indicates that MPA was degraded slowly. Due to the strong binding of MPA and Pb, MPS replacement at 24 hours after synthesis was not an optimal condition. However, waiting too long would cause all the MPAs to degrade and no longer be able to stabilize the AQDs. An optimal time point was needed. Day 3 seems to be a good starting point for MPS replacement due to the weakening of the MPA binding but not completely degraded yet. MPS replacement was performed 3 days after synthesis according to the protocol described above with MPS:(Cd+Pb):S = 1:5:1. FTIR signals showed significant decreased in more than 50% of the MPA peaks intensity (Figure 4.2a) and also the emergence of the MPS peaks (around 980 cm^{-1}), which resulted by the Si-OH bond. The MPS peaks signal stayed relatively stable for more than 7 days after the replacement indicating that MPS had been successfully replaced the MPA (partially) and stabilized the AQDs.

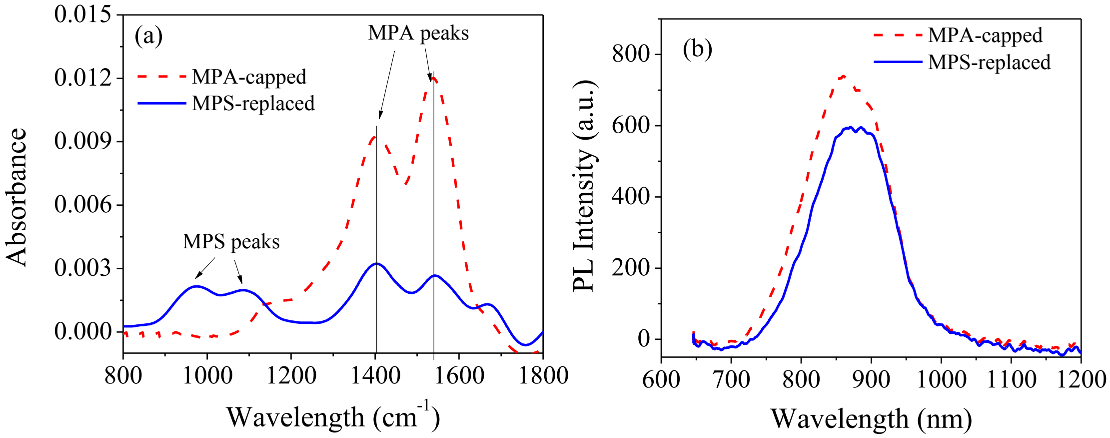

Figure 4.2: (a) FTIR spectrum of MPS-replaced CdPbS AQDs (solid line), along with that of the MPA-capped CdPbS AQDs (dash line) after 3 days of synthesis. The vertical lines indicate the position of the MPA signature peaks; (b) PL spectra of the MPS-replaced CdPbS AQDs with MPS:(Cd+Pb):S =1:5:1 and MPA=capped CdPbS AQDs with MPA:(Cd+Pb):S = 1:5:1.

After centrifugation and filtering, the concentration of free MPA was reduced significantly, allowing MPS to attach on the surface once the MPA dissociate. The fact that no MPS could attach on the surface of the AQDs after 24h and 48h post synthesis indicated that the binding of MPA was still strong under 4°C storage condition. By day 3, the MPA started to dissociate more from the surface due to the possible disulfide reaction[132]. With MPS, the silane groups can form silanol bonding network due to the hydroxylation condensation reactions which trap the MPS to the AQDs surface.

Figure 4.2b shows the PL spectra of MPA-capped and MPS-replaced CdPbS AQDs at day 3 after synthesis. The optimal ratios were chosen for the PL measurement with MPA-capped AQDs ratio of 8:5:1 and MPS-capped AQDs ratio of 1:5:1. The ratios exhibited the maximum emission intensity. The MPA-capped AQDs had the peak wavelength at 865 nm whereas MPS-replaced AQDs had a peak at 885 nm. There was a red shift in the emission wavelength. The emission of MPS-replace AQDs was also slightly lower than the emission of MPA-capped AQDs.

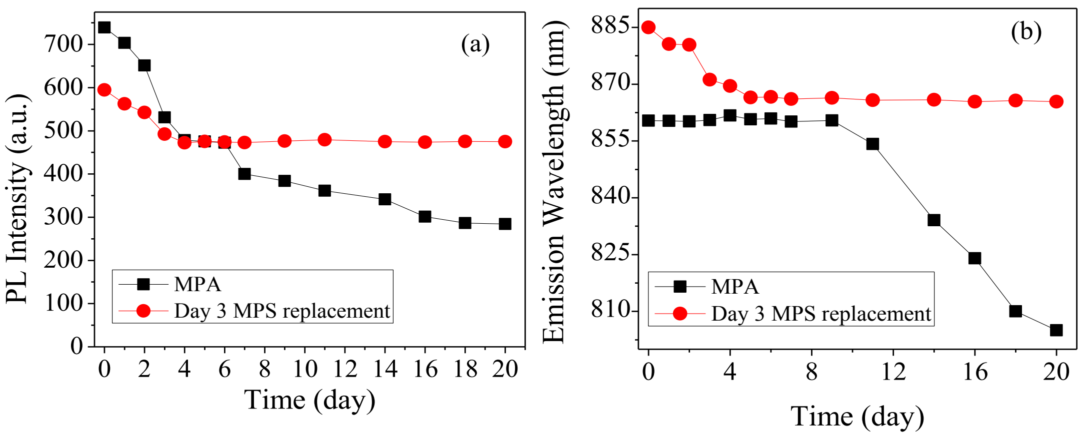

Figure 4.3: Stability of MPS replaced CdPbS QDs at day 3 post MPA synthesis compares to MPA capped QDs. (a) PL intensity versus time; (b) Emission wavelength versus time.

Stability of MPS-replaced CdPbS AQDs was also examined. As shown in Figure 4.3a, the PL intensity of both MPA-capped and MPS-replaced AQDs continued to drop until day 4, MPS-capped AQDs PL became stable as well as the blue shift in emission peak whereas the MPA-capped AQDs PL intensity and emission peak continued to drop. The emission wavelength of MPS-capped AQDs increased to 885 nm from the initial 850 nm (MPA-capped AQDs). However, the emission wavelength gradually shifted back close to the initial wavelength. There could be a loss of Cd ions during the initial MPA replacement process causing the emission wavelength to be close to lead-reached wavelength. However, as the MPS start to stabilize the particles, the original wavelength of the solid solution was recovered which resulted in the blue shift (Figure 4.3b). Also the initial 4 days were needed for MPA be dissociated from the surface of the AQDs making room for MPS to attach. It took longer for MPS to stabilize the CdPbS AQDs compared to other AQDs system.

With MPS on the surface, CdPbS AQDs contained thiol functional groups, were stable and were ready for bio-conjugation.

4.2 PROTEIN CONJUGATION

The QDs can be conjugated to antibody to directly image the target molecule or conjugated to streptavidin (SA) to indirectly image the target molecule where the SA-linked QDs bind to biotinylated secondary antibodies that are bound to the primary antibodies captured by the target molecules. Since MPA provides abundant –COO- groups on the surface of AQDs, 1- 3-[3-dimethylaminopropyl] carbodiimide (EDC) and N-hydroxysulfosuccinimide (sulfo-NHS) are used as cross-linkers between AQDs and protein of interest. EDC is a zero-length cross linker used to couple carboxyl groups to primary amines (-NH_2) through two-step reaction (Figure 4.4). Firstly, EDC reacts with a carboxyl group on the surface of AQD, forming an amine-reactive O-acylisourea intermediate. Failure to react with an amine without sulfo-NHS will result in hydrolysis of the intermediate and regenerate of the carboxyl. Therefore, this intermediate is converted to an amine-reactive sulfo-NHS ester by the addition of sulfo-NHS, which stabilizes the short-live amine-reactive intermediate. Sulfo-NHS is used to increase the coupling efficiency of EDC-mediated reactionThe amine-reactive sulfo-NHS ester intermediate reacts with an amine on protein molecule such as SA. The charged sulfonate group due to sulfo-NHS helps to preserve or increase water solubility of the modified carboxylated QDs[133, 134].

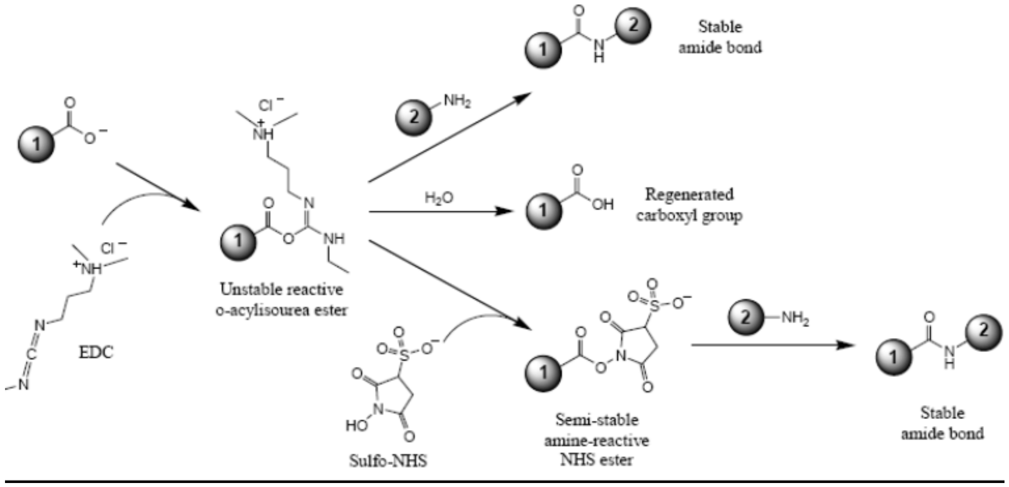

Figure 4.4: Schematic representation of the reaction between MPA-capped AQD (1) and the primary amine containing protein (2) with EDC and sulfo-NHS as cross-linkers[135].

In this study, we used the indirect imaging protocol involving SA-biotin binding for conjugation efficiency comparison. The model target biomolecule was Tn-antigen, a truncated glycan carcinoma biomarker of epithelial cancers such as breast [136], gastric [137], ovarian [138], colorectal [139], and pancreatic cancers [140]. The model cell line was HT29 colon cancer cells. The nominal SA-to-AQD and SA-to-OQD ratios were varied to identify the optimal ratio for the AQDs and that of the OQDs, respectively. Gel electrophoresis was used to quantify the numbers of SA bound to each QD and to evaluate the conjugation efficiency of the QD. In addition, we measured the zeta potentials and sizes of the AQDs and OQDs before and after conjugation in phosphate buffer saline (PBS) solution and cell culture media over time to assess their colloidal stability.

4.2.1 Streptavidin/AQD Ratio > 1 and Comparison to OQD System

a. Conjugation of SA to AQDs and OQDs

The freshly made AQDs suspension was first stored in a refrigerator (4°C) overnight followed by removal of free MPA's in the suspension by centrifugation with a 10 kDa filter (Millipore Co., Beillerica, MA) at 3000 rpm for 10 minutes three times. The commercial OQDs, carboxylated CdSe/ZnS (Qdot605-ITK), were purchased from Invitrogen (Grand Island, NY, USA). The OQDs have a core-shell structure, which is made in triocytlphonine oxide (TOPO) solvent at 300°C. They are further coated with a polymer layer containing $-COO^-$ surface groups. The polymer layer allows facile dispersion of the OQDs in an aqueous suspension (borate buffer pH =9). Commercial carboxylated CdSe/ZnS OQDs were used for comparison to the MPA-capped CdSe AQDs. The conjugation procedure of SA to the MPA-capped CdSe AQDs and that to the carboxylated CdSe/ZnS OQDs were similar to that published in the literature [141] and is described below. First, N-ethyl-N'-dimethylaminopropyl-carbodiimide (EDC) (Thermo Scientific, Rockford, IL, USA) and N-hydroxysuccinimide (NHS) (Thermo Scientific, Rockford, IL, USA) were used to facilitate the peptide bond formation between a primary amine of the SA and a carboxyl on the AQD or OQD surface. First, 4 mg of EDC and 6 mg of NHS were dissolved in 1 ml of 0.1 M 2-(*N*-morpholino)ethanesulfonic acid (MES) buffer (TEKNOVA, Hollister, CA) at pH = 6.5. 2 mM of EDC and 5 mM of NHS were added to the suspension of the OQDs (1 μM particle concentration) or that of the AQDs (1.07 μM particle concentration) at pH =7 in borate buffer. The reaction was incubated for 15 min at room temperature followed by the addition of 2-mercaptoethanol (20 mM) to quench the EDC. The suspension was then run through a desalting column (Zeba Spin

7 KW, Pierce, Rockford, IL) to remove unbound reagents and electrolytes in the suspension. The suspension was then mixed with an SA solution at room temperature and pH = 7.0 for 2 hr. To achieve optimal SA/AQD and SA/OQD conjugation, we experimented with SA/AQD molar ratio of 1, 2, 3, 4, 6, and 10, and SA/OQD ratios of 2, 4, 10, 40, 60, and 80. Note that for all the molar ratios, the concentrations of AQDs and OQDs were kept at 1 μM. Note for OQDs, the vendor suggested SA/OQD was 40. The unused NHS esters bound on the QD surface were then quenched by hydroxylamine hydrochloride (10 mM) (Sigma-Aldrich, St. Louis, MO, USA). Unconjugated QDs and SAs were then removed by microcentrifugation at 12,000 rpm using 100 kDa filters for 5 minutes five times. After each microcentrifugation, the volume of the suspension was restored with a 50 mM borate buffer solution of pH 8.3. After five consecutive microcentrifugations, the suspension was filtered through a syringe with a 0.2 μm filter (Fisher Scientific, Newark, DE) to remove large aggregates if any. The conjugated AQDs and OQDs suspensions were then stored at 4°C.

b. ***Custom Polyacrylamine/Agarose Gel System***

To characterize the SA-AQD and SA-OQD conjugates, a custom gel system consisting of a revolving gel with 2% polyacrylamide and 0.5% agarose and a stacking gel with 1% polyacrylamide and 0.5% agarose was made following the procedures of Liu et al.[142] All the reagents for the custom gel system were purchased from Fisher BioReagents (Allentown, PA, USA). The revolving gel was made by mixing a 1% agarose solution in distilled water with an equal volume of 4% of a 37.5/1 molar ratio acrylamide/bis acrylamide solution in a 2X tris/boric acid/EDTA (TBE) buffer solution at 60°C and by adding 0.05% (by weight) ammonium persulfate and 0.04% (by volume) of etramethylethylenediamine (TEMED) right before pouring. The stacking gel which consisted of 1% polyacrylamide with 0.5% agarose was prepared in a similar fashion as the revolving gel and was poured after the revolving gel had solidified completely (0.5 – 1 hour). After purification, 15 μL each SA-QD complex was loaded into the wells of the gel at 1 μM in terms of QDs concentration.

c. ***Characterization of SA-QD complexes***

We examined the conjugation of SA to AQDs and that of SA to OQDs under the conditions where there were more SAs than AQDs or OQDs. To characterize the SA-AQD and SA-OQD conjugates, after the final filtration with a 100 kD filter, we ran the retentate and the filtrate of each SA-AQD and SA-OQD conjugate through the custom-made gel. Figure 4.5a shows the fluorescence of the QDs in the SA-AQD and SA-OQD conjugates from the retentate taken with FluorChem E (Protein Simple, San Jose, CA). Coomassie blue (Brilliant R250, Across Organic, NJ, USA) was used to visualize the SA. Figure 25b shows the image of SA in the SA-AQD and SA-OQD conjugates from the retentate. A protein ladder was included in lane 15 of the bright field image in Figure 4.5b. Lane 1 in Figure 4.5b contained free SA which showed as a dark band at about 55 kDa in the bright field image but not in the fluorescent image of Lane 1 in Figure 4.5a. Lane 2 contained free AQDs, which were present in the fluorescent image in Figure 4.5a but not in the bright field image in Figure 4.5b since no protein was present. Lane 3 to 7 contained SA-AQD conjugates with SA/AQD number ratios 3, 4, 6 and 10 respectively. Lane 8-13 contained SA-OQD conjugates with SA/OQD number ratios 2, 4, 10, 40, 60 and 80 respectively. As can be seen from the bright field images in Figure 4.5b, both SA-AQD conjugates with SA/AQD =3, 4, and 6 and SA-OQDs conjugates with SA/OQD =

40, 60, and 80 exhibited a thick band in the range of 130-250 kD, which was much larger than the SA (55 kD) and QD (<55 kD). Furthermore, the bands in the 130-250 kD range were fluorescent as evident in Figure 4.5a, indicating that SA and QDs are co-localized in these bands forming SA-QD conjugates.

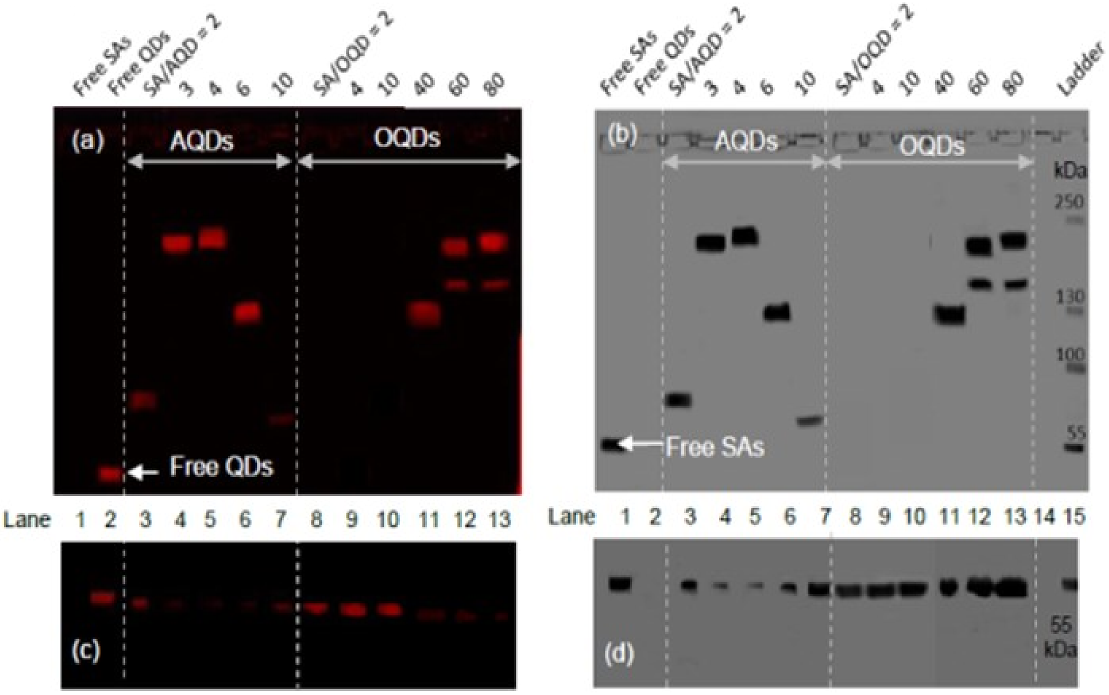

Figure 4.5: Gel electrophoresis images of SA-AQD and SA-OQD conjugates: (a) fluorescent image and (b) bright-field images of the gel with the retentates, (c) fluorescent and (d) bright-field images of gel with the filtrates: lane 1 contained free SA; lane 2: free QDs; lanes 3-7, SA-AQD conjugates with nominal SA/AQD = 2, 3, 4, 6,and 10, respectively; lane 8-13, SA-OQD conjugates with nominal SA/OQD = 2,4,10,40, 60, and 80; lane 15: the protein ladder. Note red color in the fluorescent images was due to the AQDs and OQDs and the dark color in the bright field images was due to Coomassie Blue Staining of the SA. The fluorescent bands of the SA-AQD and SA-OQD conjugates in (a) co-localized with the SA bands in (b) at the same positions indicated SA and QDs were indeed covalently bound in the retentates whereas the positions of the SAs and the QDs were not in the same position indicating that they were indeed not chemically linked.

Furthermore, SA-AQD conjugates with a SA/AQD = 2 and 10 exhibited a band at a smaller molecular weight range indicating even smaller SA-QD conjugates which were larger than the SA or the AQDs. When SA/AQD > 4 ratios were used, large aggregates were observed during the conjugation process, which could be due to the cross-linking between multiple complexes. The aggregates were removed at the last step with a 0.2 µm filter. Therefore, the remaining retentate contained only conjugates of smaller sizes resulting in a lower band than those SA/AQD= 3 and 4.There were no visible bands in both the fluorescent and bright field images for the SA-OQD conjugates with a SA/OQD<40 indicating that no SA-OQD conjugation occurred at SA/OQD<40. Note that the SA-OQD conjugates with SA/OQD ratio of 60 and 80 exhibited two bands above 130 kD within the same lane with the primary band at around 200 kD and the additional band at around 150 kD, a sign of multiple SAs bound to a QD, which was also observed in other studies [142, 143].

To account for the unbound SA and unbound QDs in each SA-AQD and SA-OQD conjugation procedures, in Figures 4.5c and 4.5d we show the fluorescent and bright field image of the filtrates of the various SA-AQD conjugates (lanes 3-7) and SA-OQD conjugates (lanes 8-13). As can be seen, there were many SA and OQDs left in the filtrates of the SA-OQD conjugates especially for the SA/OQD ratios < 40. Meanwhile, there were very little SA and almost no visible AQDs left in the filtrates of SA-AQD conjugates especially with SA/AQD =3, 4, and 6.

To determine the number of bound SA per AQD or OQD, we followed the method of Pathak et.al. [144]. Gel pictograph allows visual validation of the conjugation if the signal of the SA and that of and QDs were co-localized in the gel channels. With carefully analysis of both the SA and QDs in the same gel systems, it is reliable to quantify the amount of the SA and QDs for the complexes in the gel channels, which in fact is no different from the procedures needed to do when using a UV-vis or fluorescent spectrometer for quantification. To generate the standard curves for SA and QDs, we loaded each channel with 15μL of a SA solution or of a QD suspension of different concentrations. We first measured the Coomassie blue intensities of SA solutions of various concentrations and the fluorescent intensities of AQDs and OQDs of various concentrations using AlphaView software (Protein Simple, San Jose, CA).

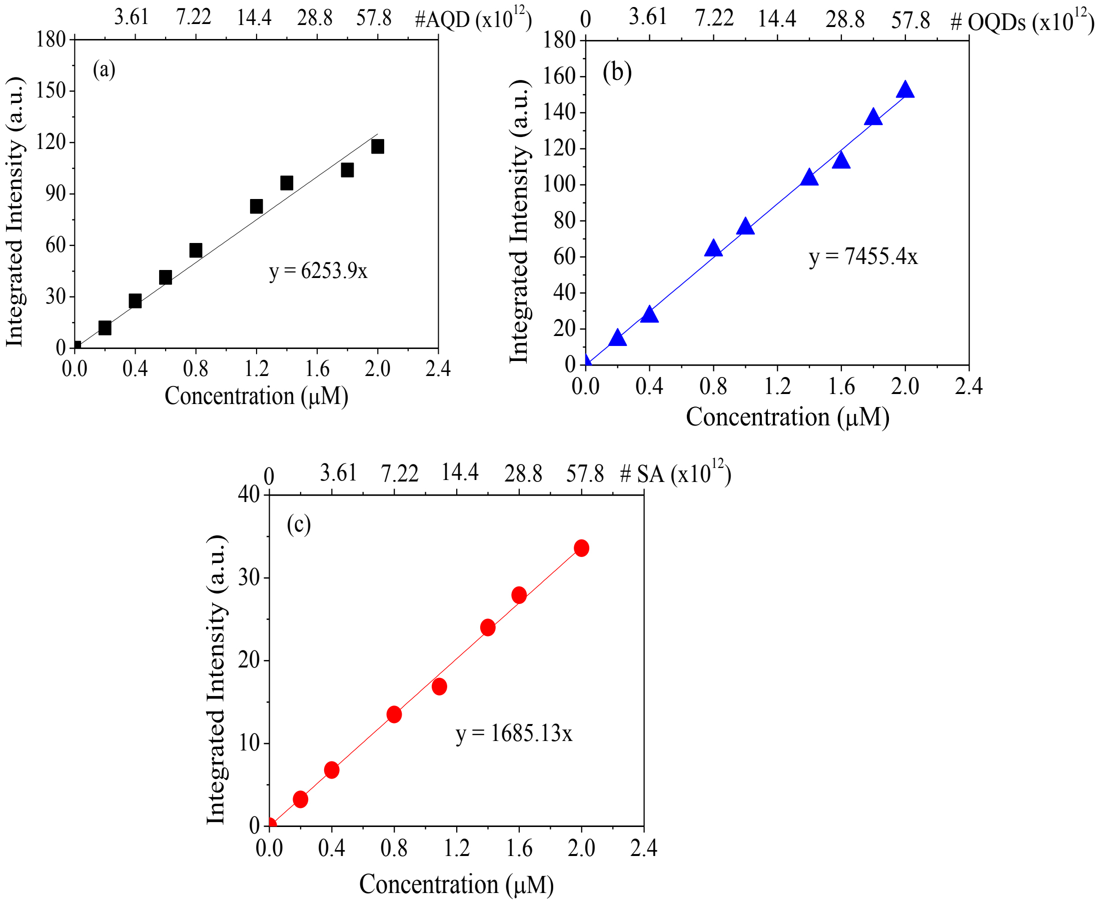

Figure 4.6: Standard curve of integrated intensity vs. concentration of (a) AQDs, (b) OQDs, (c) SA. The number of AQDs, OQDs, and SA deduced in the 15ml of each concentration was labeled on the top x-axis of (a), (b), and (c), respectively.

The total intensity of each band was obtained by integrating over the entire area of the band for each SA or QD concentration. The concentration range was 0.2-2 μM for both SA and QDs. Each molar concentration was converted to the number of SA or QD by multiplying the molar concentration by the volume. Standard curves were plotted based on the integrated band intensity versus number of AQDs, OQDs, and SA are shown in Figures 4.6a, 4.6b, and 4.6c, respectively. Also shown on the top x-axis are the corresponding total numbers of AQDs, OQDs, and SA in a volume of 15 μl.

For each SA/AQD or SA/OQD ratio, the total Coomassie blue and the total fluorescence intensity in each band were obtained by integrating the intensity per unit area over the entire area of each band and were converted to the total SA number or the total AQDs or OQDs numbers based on the standard curves. The number of bound SA per AQD (or per OQD) was then obtained by dividing the total number of SA by the total number of AQDs (or OQDs). The number of bound SA per AQD versus nominal SA/AQD number ratio and that of bound SA per OQD versus the nominal SA/OQD number ratio were plotted in Figure 4.7a. Note that for the SA-OQD conjugates with nominal SA/OQD = 60 and 80, there were two bands in the gel. As a result, there were two numbers of bound SA per OQD for nominal SA/OQD = 60 and 80. For example, for nominal SA/OQD=80, one was 2.7 ± 0.4 for the upper band (green) and the other was 1.8 ± 0.2 for lower band (blue). Meanwhile, for SA/OQD below 40 there was no observable SA-OQD conjugation. In comparison, the largest number of bound SA per AQD was 3 ± 0.3 at a nominal SA/AQD number ratio of 4 as illustrated in Figure 4.7b. To give a quantitative analysis, we define the conjugation efficiency (E) by dividing the experimental SA/QD ratio by the nominal SA/QD ratio (equation 2).

$$E = \frac{experimental\,SA/QD\ ratio}{nominal\,SA/QD\ ratio} \quad (2)$$

Using the results in Figure 4.7a, we obtained a E = 75 ± 7.5% for the SA-AQD conjugates at the optimal SA/AQD=4. Similarly, using the results in Fig.3a for OQD calucalted E =3.4 ± 0.5% for the SA-OQD conjugates at their optimal SA/OQD=80. Clearly, more than 20 times more SA was needed for OQDs than for AQDs to achieve the same coordination number of about 3 bound SA per QD.

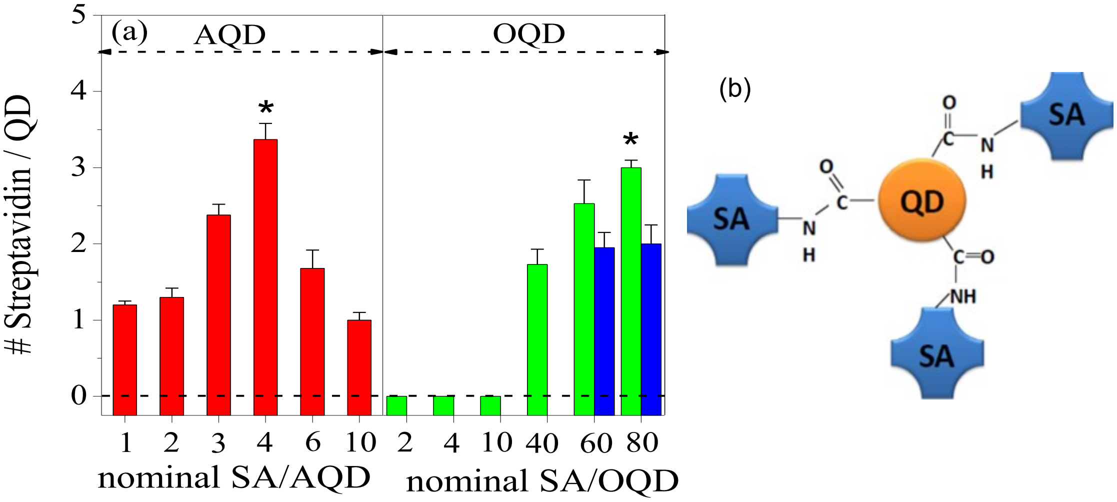

Figure 4.7: (a) Bound SA/QD versus nominal SA/AQD and nominal SA/OQD: red for AQDs and green for OQDs' primary band at around 200 kD and blue for the additional band at around 150 kD at the nominal SA/OQD = 60 and 80, and (b) a schematic illustrating the optimal SA-AQD and SA-OQD conjugate obtained at nominal SA/AQD=4 and nominal SA/OQD=80 where each AQD and each OQD was bound by three SAs--Note 20 times more SAs were needed for OQDs than AQDs to achieve the same optimal conjugate configuration. * Optimal SA/QD ratios.

How effectively the conjugation of SA to QD can be examined using the data of the filtrate in Fig. 2d as well. For example, we calculate the fraction of bound SA (F_{SA}) by dividing the number of bound SA (as determined from Figure 4.5b) by the sum of the number of the bound SA found in Figure 4.5b from the retentate and the number of unbound SA found in the same lane in Figure 4.5d from the filtrate (equation 3).

$$F_{SA} = \frac{\#\, bound\ SA\ from\ retentate}{\#SA\ from\ filtrate + \#SA\ from\ retentate} \quad (3)$$

Figure 4.8 showed the fraction of bound SA versus SA/AQD and SA/OQD ratios. The largest F_{SA} for AQDs was 83±1.3% which was consistent with the conjugation efficiency of 75±7.5% for the SA-AQD conjugates at the optimal SA/AQD = 4. Also, Figure 4.8 showed that the largest δ_{SA} forOQDs was 6.5±1.2% which was close to the conjugation efficiency of 3.4±0.5% for the SA-OQD conjugates at their optimal SA/OQD = 80. Considering the small numbers of the experimental uncertainty in gel filtration, the number agreed with each other.

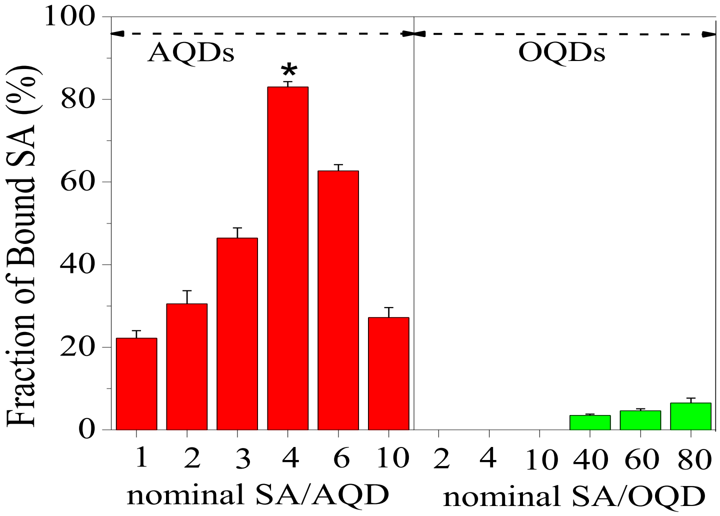

Figure 4.8: Fraction of bound SA versus nominal SA/AQD and nominal SA/OQD ratios: Red for AQDs and green for OQDs. AQDs could achieve >80% maximal SA conjugation efficiency at nominal SA/AQD=4 while the maximal SA conjugation efficiency was only 6% at nominal SA/OQD=80. *Optimal SA/QD ratios.

d. Immunofluorescent Staining (IF) of SA-QD complexes

HT29 human colon cancer cells (ATCC) which expressed Tn antigen were grown on cover glasses overnight and then fixed with 4% paraformaldehyde for 15 minutes followed by washing with Tris buffer saline containing 0.1% Tween (TBS). Biotin/Streptavidin kit (Vector Laboratories, Burlingame, CA) was used to block endogenous biotin in cells. Cells were then washed with TBS three times and blocked with 10% normal goat serum (Jackson ImmunoResearch, West Grove, PA) for 1 hour at room temperature. Mouse anti-Tn antigen antibody (1:20 dilution, Genetex, CA) was added and incubated for 1 hour at room temperature to bond to the Tn antigen on the cell surface followed by washing with TBS three times to remove unbound anti-Tn antibody. Biotinylated goat anti-mouse antibody (1:50 dilution, Invitrogen, Grand Island, NY) was then added to the cells for 30 minutes at room temperature to bond to the mouse anti-Tn antibody. Unbound biotinylated goat anti-mouse antibody was then removed by washing with TBS three times. SA-AQD (or SA-OQD) conjugates were then added to the cells for 30 minutes to bond to the biotinylated goat anti-mouse antibody. Finally, cells were washed with TBS three times to remove the unbound SA-AQDs (or SA-OQDs) and counter-mounted with mounting medium containing DAPI (Vector Laboratories, Burlingame, CA).

Figure 4.9a shows the fluorescent images of fixed HT29 cells stained by SA-AQD conjugates with an SA/AQD = 4, 6, and 10 and by SA-OQDs conjugates with an SA/OQD = 40, 60 and 80 obtained in a BX51 Olympus fluorescent microscope. Using images similar to those shown in Figure 29a, the fluorescent intensity per cell was further analyzed using ImageJ and averaged over 100 cells for each SA-AQD and SA-OQD conjugates.

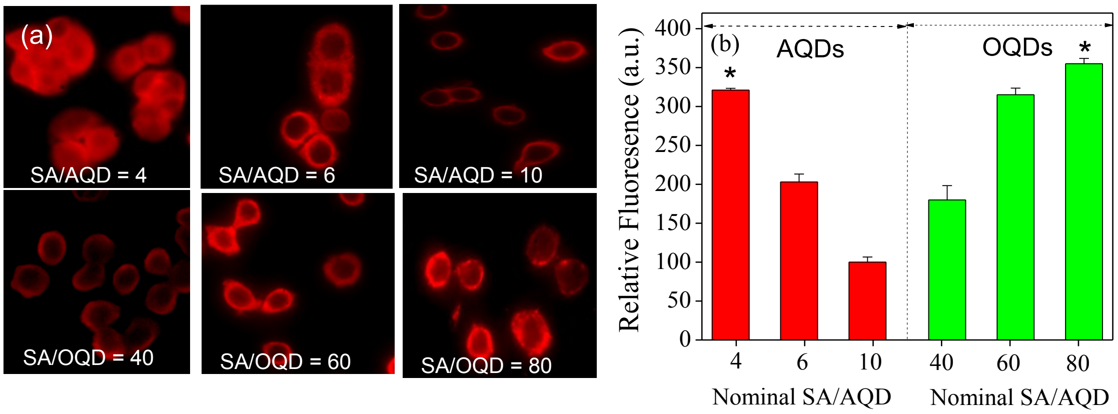

Figure 4.9: Immunofluorescent staining of HT29 colon cancer cells by SA-QD conjugates.(a) HT29 cells stained by SA-QD conjugates to image Tn antigen on the cell surface with various nominal SA/AQD and SA/OQD ratios. Conjugates with nominal SA/AQD =4 gave the brightest images; (b) Relative fluorescent intensity per cell versus nominal SA/AQD and nominal SA/OQD. * Optimal SA/QD ratio

In Figure 4.9b, we plot the average fluorescent intensity per cell versus the nominal SA/AQD for AQDs and that versus the nominal SA/OQD ratio for OQDs. As can be seen, the fluorescent intensity per cell could reach 320 with SA-AQD conjugates with nominal SA/AQD = 4 in which there were 3±0.3 bound SAs per AQD (see Figure 4.7a). In contrast, the fluorescent intensity per cell could only reach 350 by SA-OQD conjugates with a nominal SA/OQD = 80, i.e.,. Although the final number of SA per QD is similar for the optimal condition of both AQD and OQD systems, the OQDs staining signal is slightly higher than the AQDs due to the OQD have higher QY than the AQDs. Clearly, OQDs need 20 times more SA to achieve similar result as AQDs. Therefore, high protein conjugation efficiency was an advantage of the AQDs over OQDs.

e. $-COO^-$ *functional groups quantification for AQDs and OQDs*

We hypothesize that the easier conjugation of SA to AQDs than to OQDs was a result of more carboxyl groups on the AQDs than on the OQDs due to the *in situ* incorporation of the MPAs as the capping molecules in the AQDs synthesis process. In contrast, carboxyl groups on the OQDs needed to be incorporated after synthesis by ligand exchange. To compare the amount of the bound carboxyl groups on the AQDs to that on the OQDs, we carried out Fourier transform infrared (FTIR) spectroscopy on AQDs and OQDs suspensions of the same concentration. Both the AQDs and OQDs suspensions were filtered to remove unbound MPA if any. The resultant FTIR spectra of AQDs (black line) and that of OQDs (red line) are shown in Figure 4.10. Since all free capping molecules and ions were removed and the water background was subtracted, the peaks in the remaining spectra could only be attributed to the QDs. The experiment was performed with the same volume and concentration for both OQDs and AQDs. The carboxylic acid O-H stretch appeared as a very broad band in the region of 3300-2500 cm^{-1}. The carbonyl stretch C=O stretch appeared from 1760-1690 cm^{-1} [145] in both AQDs and OQDs with AQDs exhibited stronger peaks. As can be seen, the AQDs exhibit much stronger O-H bend and C-O stretch peaks at around 1440-1395 cm^{-1} and 1320-1210 cm^{-1} regions, a C=O peak at around 1750 cm^{-1} [145]. The O-H bend and C-O stretch peaks were the results of MPA which was 4 times stronger than the carboxylated surface on OQDs when the intensities of these peaks were integrated, indicating that indeed AQDs had more carboxylated groups on the surface. Furthermore, we also measured the zeta potential of the AQDs and that of the OQDs in PBS at pH 7. The zeta potential of the AQDs in PBS was found to be -30 mV and that of the OQDs to be -22 mV. AQDs were more negatively charged than OQDs which was consistent with the above FTIR results and further supported the hypothesis that more MPA were on the AQDs than on the OQDs.

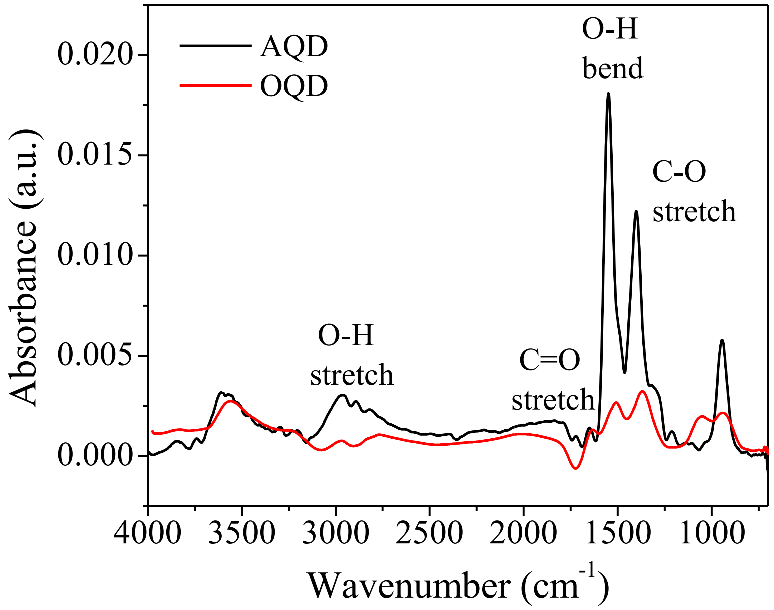

Figure 4.10: FTIR spectrum of AQDs (black) and that of OQDs (red) with a focus on the capping carboxyl group. The carboxylic acid O-H stretch appears as a very broad band in the region of 3300-2500 cm^{-1}. The carbonyl stretch C=O stretch appears at from 1760-1690 cm^{-1}. The C-O stretch is in the region 1320-1210cm^{-1} and the O-H bend is in the region of 1440-1395 cm^{-1} indicates the presence of the surface carboxyl group on the AQDs and OQDs surfaces. Integrated peak intensities indicated that ADQs had 4 times more COOH groups on the surface compared to OQDs

f. ***<u>Stability of the SA-QD complexes</u>***

For biological application of the functionalized AQDs, the conjugated AQDs complexes must be stable under biological condition. To study the stability of SA-conjugated AQDs (SA-AQD) and SA-conjugated OQDs, we used SA-AQD complexes with SA/AQD = 4 and the SA-OQD complexes with SA/OQD = 80 as model complexes because at these ratios AQDs and OQDs exhibited comparable fluorescent intensity per cell in imaging

Tn-antigen on HT29 cells as we will show below. The SA-AQD and SA-OQD complexes were added into the cell culture media with 10% fetal bovine serum (FBS) and incubated at 37°C for 24h, 48h, and 72h. It has been known that OQDs form large aggregates in cell media due to the binding of OQDs with the proteins.[146] In this study, the size of the SA-AQD complexes and that of the SA-OQD complexes as a function of time as well as the zeta potential of the SA-AQD complexes and that of the SA-OQD complexes were examined using NanoSizer (Malvern, MA).

In order for SA-AQD and SA-OQD conjugates to be used as molecular probes to image living systems, they must be stable under physiological conditions[147]. There have been very few studies addressing this aspect. We measured the size of the SA-AQD conjugates with SA/AQD = 4 and that of the SA-OQDs conjugates with a SA/OQD = 80 in a cell culture medium with 10% FBS at 37°C and in PBS every 24 hr over a 72 hr period for comparison. The results are shown in Figure 4.11. As can be seen the size of the SA-AQD conjugates remained at around 32 nm in both the cell culture medium and in PBS throughout the 72 hr period indicating that there was no observable aggregation of the SA-AQD conjugates in the cell medium (full squares) or in the PBS (open squares). In contrast, the size of the SA-OQD conjugates increased with time in both PBS and in cell medium indicating that the SA-OQDs conjugates were less stable. By 72 hours, the size of the SA-OQD was increased to about 80 nm and 160 nm in PBS and in cell medium, respectively, which is consistent with literature that OQDs were shown to bind to albumin non-specifically in cell media resulting in large aggregates and reduced PL intensity and stability[148]. The stability of the SA-AQD conjugates was further supported by the zeta potential measurement of the SA-AQD conjugates with a SA/AQD=4 showing -15 mV whereas that of the SA-OQD conjugates with a SA/OQD=80 showing -3 mV, consistent with the observed aggregation of the SA-OQD conjugates over time shown in Figure 4.11.

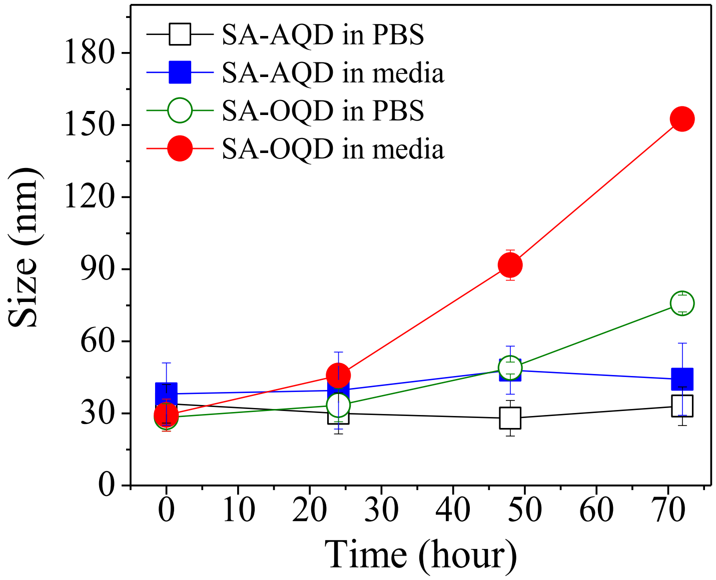

Figure 4.11: Stability of SA-AQD and SA-OQD conjugates in PBS and in cell media for up to 72 hours after conjugation. SA-AQD conjugates were stable in both PBS and cell media with little change in size whereas SA-OQD conjugates were only stable for 24 hr and started to show signs of aggregation after 48 hr in PBS and 24 hr in cell media.

We also examined the binding capability of cell culture medium-aged SA-conjugated AQDs to stain live cells in a flow that mimicked physiological conditions. Live HT29 colon cancer cells grown on a cover glass were pre-treated with the mouse anti-Tn antibody and biotinylated goat anti-mouse antibody and placed in a flow chamber at 37° in an incubator (MCO-20AIC, Sanyo, Japan). A schematic of the flow system is shown in Figure 4.12. Note all cell slides were blocked with 1% bovine serum albumin

(BSA), and biotin/streptavidin kit before exposure to the treatment of antibodies and SA-AQD conjugates as described in the experimental section. The SA-AQD conjugates of SA/AQD=4 were aged in a cell culture medium at room temperature for 24, 48, and 72 hr before they were introduced in the sample holder of the flow system to stain HT29 cells in the flow chamber in a flow driven by a peristaltic pump (7712062, Cole-Parmer, Chicago, IL) at a flow rate of 1 ml/min for 30 min.

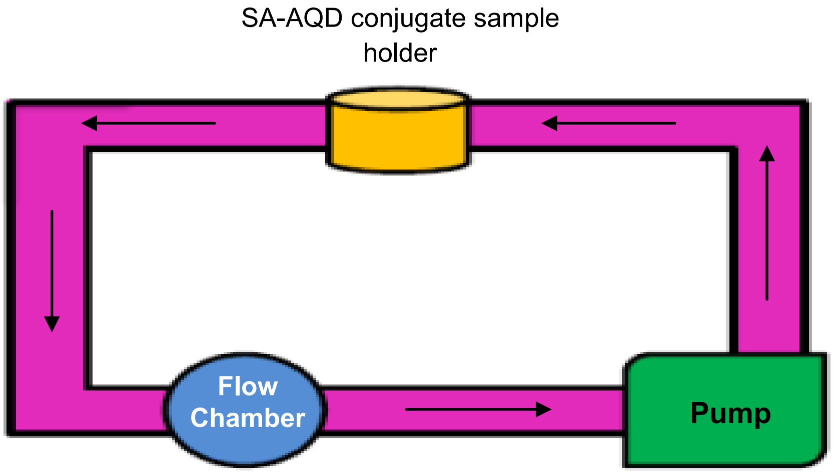

Figure 4.12: A schematic of flow system consisting of a peristaltic pump, a SA-AQD conjugate sample holder, and a flow chamber containing live HT29 cells on a cover-slit. SA-AQD conjugates were added in the sample holder and circulated in the flow driven by a peristaltic pump to reach the cells in the flow chamber.

Figures 4.13a, 4.13b and 4.13c show the fluorescent micrographs of the HT29 cells stained by the SA-AQD conjugates aged in a cell culture medium for 24, 48, and 72 hr, respectively. A negative control is shown in Figure 4.13d where HT29 cells untreated by mouse anti-Tn antigen antibody were stained by un-aged SA-AQD conjugates. Figs. 9e and 9f show the micrographs of HT29 cells stained without flow at room temperature by SA-AQD conjugates aged in PBS and in cell culture medium for 2 hr, respectively. Note the blue color in these figures was due to the DAPI staining of the nuclei and the red color was due to the fluorescence of the AQDs. As can be seen, all the micrographs in Figures 4.13a-4.13f were similar, indicating that the SA-AQD conjugates were stable in cell media with serum for the whole 72 hr period and the SA-AQD conjugates were able to specifically stain the Tn-antigen on the cell surface under such flow conditions, another evidence of the stability of the SA-AQDs complex in the cell culture media.

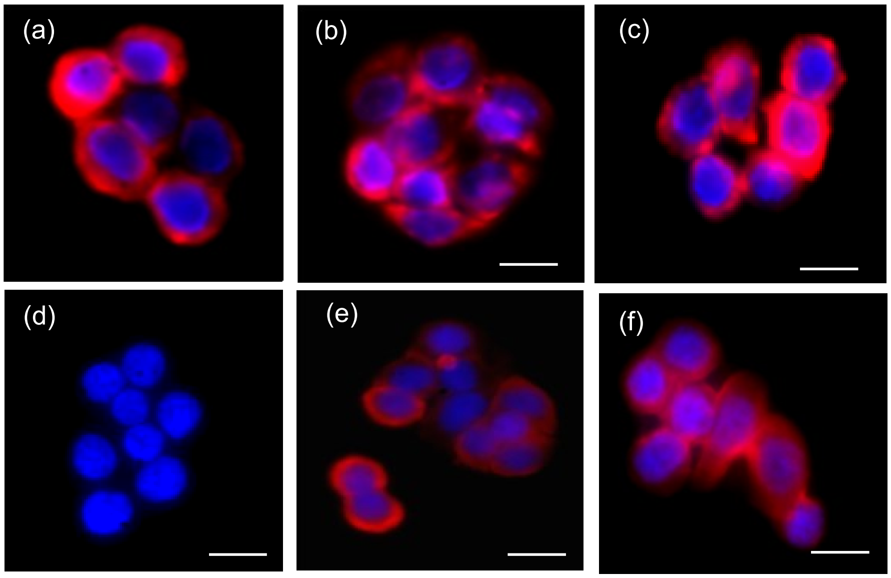

Figure 4.13: Immunofluorescent staining of Tn antigen on HT29 colon cancer cell surface in a flow system. SA-AQD conjugates were incubated in cell-culture for (a) 24 hours, (b) 48 hours, and (c) 72 hours before circulating and exposure to cells. (d) Negative control: no primary antibody to allow for specific binding. Positive controls without circulation: (e) SA-AQD conjugates were incubated in PBS for 24 hours prior to exposing to the cells. (f) SA-AQD conjugates were incubated in cell culture for 24 hours prior to exposing to cells. . Blue: DAPI for nucleus, Red: SA-AQD for Tn-antigen expression. Scale bar = 80 μm

g. ***Summary***

The conjugation and imaging efficacy of MPA-capped CdSe AQDs have been examined and compared them to those of CdSe/ZnS OQDs. The optimal nominal SA/AQD ratio occurred at 4 that yielded one AQD bound with 3±0.3 SAs with

75±7.5%SA conjugation efficiency. The optimal nominal SA/OQD ratio occurred at 80 that yielded one OQD bound with 2.7±0.4 SAs with 3.4±0.5% SA conjugation. The ease of conjugation of the AQDs--i.e., 10 folds fewer SA were needed for AQDs than for OQDs--was attributed to the fact that AQDs had more MPA capping molecules on the surface than OQDs, a result of the direct aqueous synthesis of the AQDs, as evidenced in FTIR study as well as zeta potential measurements. The SA-AQD conjugates were shown to be stable in PBS as well as in cell media at room temperature for 72 hr contrasting the SA-OQD conjugates whose size grew with time in both PBS and cell culture media. We have also shown that the SA-AQD conjugates were also stable with no diminishing imaging efficacy in flowing cell culture media at 37°C, pH = 7 for 72 hr.

4.2.2 AQD/Streptavidn ≥ 1

Traditionally, multivalent conjugation refers to a system where one QD can be conjugated to multiple protein molecules since the QDs are larger in size and surface area compared to the single reactive site organic dyes[142]. Multivalent conjugation, where one protein/antibody can be linked to multiple QDs has not been achieved. It is of a great interest because multivalent antibody could improve quantification especially when the QD concentration is relatively high and target concentration is relatively low[142]. No amplification is needed for detection. In addition, multiple QDs per antibody is desirable to study biological processes that are sensitive to protein clustering, such as cross-linking cell surface receptors by multiple ligands could activate unwanted cell signaling pathways[149-151]. In this study, we examined the effects of multiple AQDs per SA in term of conjugation and imaging capability.

As describe in section 4.2.1, AQDs were conjugated to SA using EDC and sulfo-NHS as cross-linkers. The SA/AQD ratios were 0.1, 0.14, 0.2, 0.3 and 1. In contrast, conjugation of OQDs could only be carried out under conditions with more SA than OQDs due to aggregation tendency of the OQDs at higher concentrations. In addition, the used of protein was minimal in this conjugation strategy, which was not possible to link to OQDs even under a 1:1 ratio.

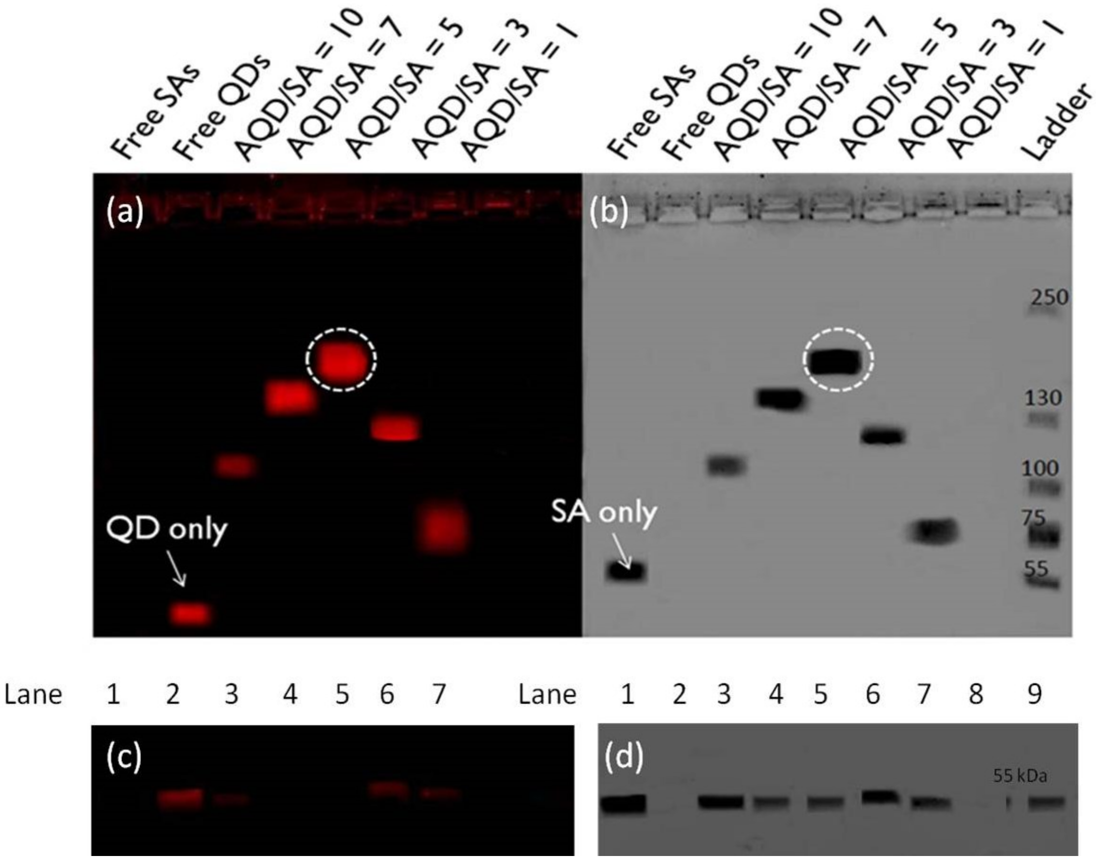

Figure 4.14: Gel electrophoresis images of SA-AQD conjugates: (a) fluorescent image and (b) bright-field images of the gel with the retentates(c) fluorescent and (d) bright-field images of gel with the filtrates. Lane 1 contained free SA; lane 2: free QDs; lanes 3-7, SA-AQD conjugates with nominal AQD/SA = 10, 7, 5, 3,and 1, respectively; lane 9: the protein ladder. Note red color in the fluorescent images was due to the AQDs and OQDs and the dark color in the bright field images was due to Coomassie Blue Staining of the SA. The fluorescent bands of the SA-AQD and SA-OQD conjugates in (a) co-localized with the SA bands in (b) at the same positions indicated SA and QDs were indeed covalently bound in the retentates whereas the positions of the SAs and the QDs were not in the same position indicating that they were indeed not chemically linked.

Figure 4.14a shows the fluorescence of the AQDs in the SA-AQD conjugates from the retentate taken with FluorChem E (Protein Simple, San Jose, CA). Coomassie blue (Brilliant R250, Across Organic, NJ, USA) was used to visualize the SA. Figure 4.14b shows the image of SA in the SA-AQD conjugates from the retentate. A protein ladder was included in lane 9 of the bright field image in Figure 4.14b. Lane 1 in Figure 4.14b contained free SA which showed as a dark band at about 55 kDa in the bright field image but not in the fluorescent image of Lane 1 in Figure 4.14a. Lane 2 contained free AQDs, which were present in the fluorescent image in Figure 4.14a but not in the bright field image in Figure 4.14b since no protein was present. Lane 3 to 7 contained AQD-SA conjugates with AQD/SA number ratios 10, 7, 5, 3, and 1 respectively. As can be seen from the bright field images in Figure 4.14b, both SA-AQD conjugates with AQD/SA =5 exhibited a thick band in the range of 130-250 kD, which was much larger than the SA (55 kD) and AQD (<55 kD). Furthermore, the bands in the 130-250 kD range were fluorescent as evident in Figure 4.14a, indicating that SA and QDs are co-localized in these bands forming AQD-SA conjugates. The biggest conjugates occurred at AQD/SA = 5. Furthermore, AQD-SA conjugates with a AQD/SA = 10, 3 and 1 exhibited a band at a smaller molecular weight range but larger than free SA and AQD indicating even smaller AQD-SA conjugates.

To account for the unbound SA and unbound AQDs in each AQD-SA conjugation procedures, in Figure 4.14c and 4.14d, we show the fluorescent and bright field image of the filtrates of the various AQD-SA conjugates (lanes 3-7). Meanwhile, there were very little SA and almost no visible AQDs left in the filtrates of AQD-SA conjugates especially with AQD/SA = 5 and 7. To determine the number of bound SA per AQD or

OQD, we followed the method of Pathak et.al. [144] as described in section 4.2.1. Gel pictograph allows visual validation of the conjugation if the signal of the SA and that of and QDs were co-localized in the gel channels. The number of bound AQD per SA versus nominal SA/AQD number ratio was plotted in Figure 4.15a. The largest number of bound AQD per SA was 2.9 ± 0.2 at a nominal AQD/SA number ratio of 5 as illustrated in Figure 4.15b. Using the results in Figure 4.15a, we obtained a conjugation efficiency (E) of 60 ± 5.3% for the SA-AQD conjugates at the optimal AQD/SA=5.

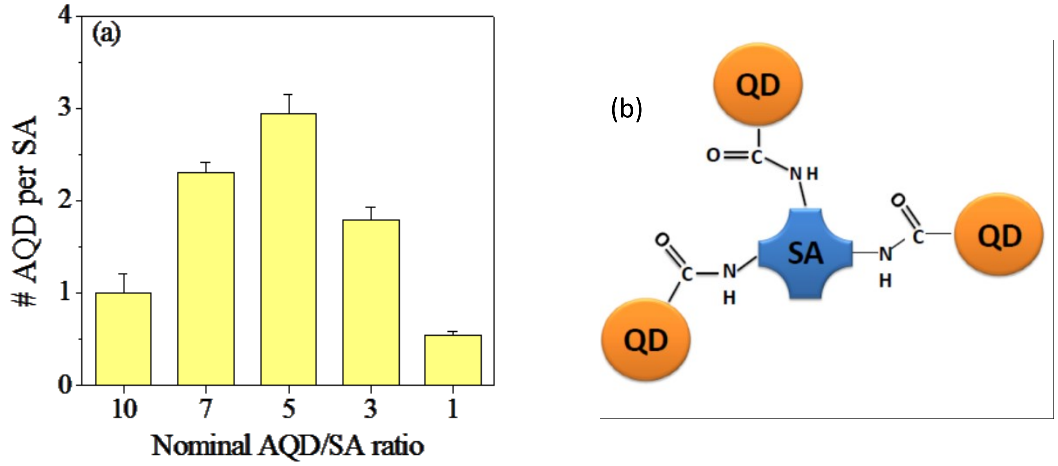

Figure 4.15: (a) Bound AQD per SA versus nominal AQD/SA (b) a schematic illustrating the optimal AQD-SA conjugate obtained at nominal AQD/SA=5 where each SA was bound by three AQDs, which cannot be achieved by OQDs.

How effectively the conjugation of AQD to SA can be examined using the data of the filtrate in Figure 4.14c as well. For example, we calculate the fraction of bound SA (F_{SA}) by dividing the number of bound AQD (as determined from Figure 4.15a) by the sum of the number of the bound AQD found in Figure 4.15a from the retentate and the number of unbound AQD found in the same lane in Figure 4.14c from the filtrate (equation 3).

Figure 4.16 showed the fraction of bound AQD versus SA/AQD. The largest F_{SA} for AQDs was 71.2±1.4% which was consistent with E= 60±5.3% for the SA-AQD conjugates at the optimal SA/AQD = 0.2. Considering the small numbers of the experimental uncertainty in gel filtration, the number agreed with each other. Multiple AQDs can be linked to a single protein. although there was only one chance of binding, one target binding signal was amplified 3 times because of 3AQD per SA resulting in similar result as more SA molecules per AQD. This conjugation strategy plays important role in signal detection and signal amplification in system with low concentration of target receptor.

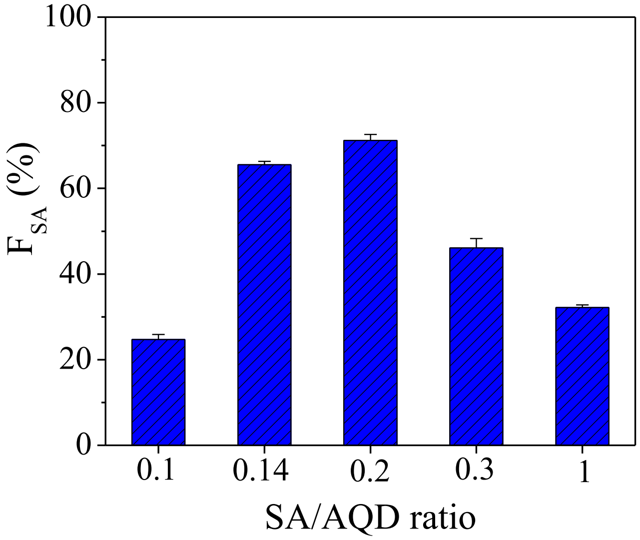

Figure 4.16: Fraction of bound SA versus nominal AQD/SA. AQDs could achieve >70% maximal SA conjugation efficiency at nominal SA/AQD=5 while OQD could not success under this conjugation strategy.

To test the imaging capability of the new conjugation strategy, HT29 human colon cancer cells, which expressed Tn antigen, were used. The IF staining procedure was described in section 4.2.1. Figure 4.17a shows the fluorescent images of fixed HT29 cells stained by SA-AQD conjugates with an SA/AQD = 10, 5, and 1 obtained in a BX51 Olympus fluorescent microscope. Using images similar to those shown in Figure 4.17a, the fluorescent intensity per cell was further analyzed using ImageJ and averaged over 100 cells for each SA-AQD and SA-OQD conjugates.

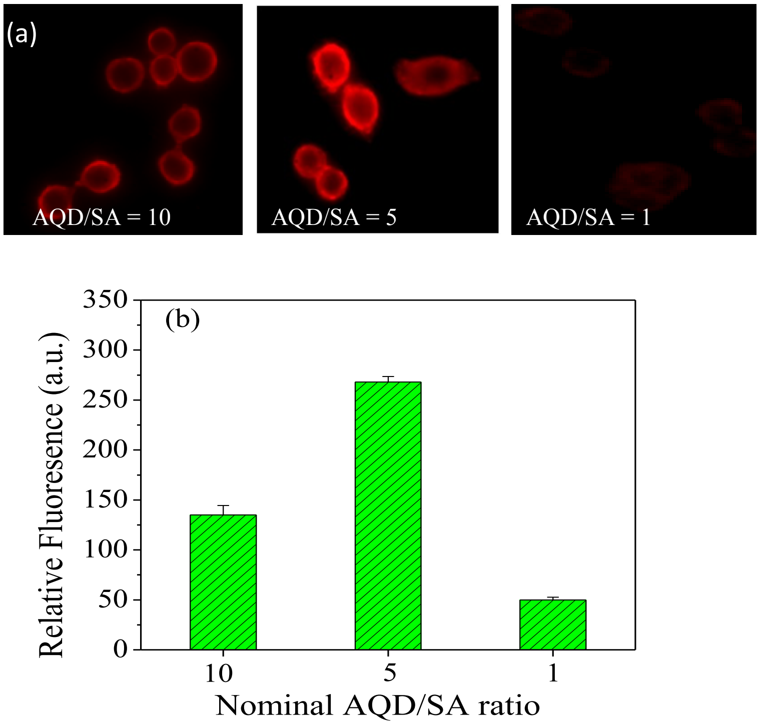

Figure 4.17: (a) Immunofluorescent staining of AQD-SA conjugates to image Tn antigen on the cell surface with various nominal AQD/SA ≥ 1 ratios. Conjugates with nominal AQD/SA =5 gave the brightest images; (b) Relative fluorescent intensity per cell versus nominal AQD/SA ratio.

In Figure 4.17b, we plot the average fluorescent intensity per cell versus the nominal SA/AQD. As can be seen, the fluorescent intensity per cell could reach around 270 with SA-AQD conjugates with nominal AQD/SA = 5 in which there were 2.9±0.2 bound AQDs per SA (see Figure 4.17a). Similarly, the fluorescent intensity per cell could only reach 320 by SA/AQD = 4 . Although the fluorescent intensity of AQD/SA = 5 was smaller than SA/AQD=4, the cell surface did probably not saturate with the probes due less amount of SA. However, the signal was close with each other. Depend on the application purposes, AQDs give the flexibility to apply different conjugation strategies, in which the OQDs cannot be achieved.

4.3 ANTIBODY CONJUGATION

Molecular imaging technologies based on functional nanoprobes have become great interest[152]. In recent years, nanoparticles such as QDs, magnetic, gold/silver nanoparticles have been coupled with antibody of specific target for immunofluorescence assays, micro-PET, MRI and CT in small animal tumor imaging[153-156]. Antibody is one of the most specific protein recognition ligands. Monoclonal antibody (mAb) can detect the cell-surface receptor (antigen) associated with an activated cellular oncogene and shows higher specificity than other small molecules[157, 158]. In recent years, cancer-specific antibody, coupled with QDs, has become the one of the most popular agents for tumor targeted imaging. As immunofluorescent probes, QDs are required to have high sensitivity and high specificity for cancer cells[78]. QDs are often covalently linked to antibody directly or to an adapter protein such as Streptavidin that bridges the inorganic fluorophores and biotinylated antibody[159].

Either QDs are covalently bound directly to antibody or through streptavidin linkage, QDs mutivalency is a grave concern, as cross-linking of surface proteins can activate signaling pathways and dramatically reduce receptor mobility[151]. Many approaches have been developed to produce monovalent particles. For examples, nickel affinity was use to separate the monovalent and multivalent with little success due to the overlapping between the two types[160]. DNA strands were attached on the surface of the nanoparticles to separate according to the number of DNA strands[161]. However, this approach often lead larger particle sizes and promotes nonspecific binding to cells[151]. Another approach is to engineer the monovalent streptavidin with only a single biotin binding site and separate the monovalent QDs using gel electrophoresis. This approach again increases the size of the particles and decrease conjugation efficiency with antibody[151]. It is very difficult to control the valency using OQDs.

Several kinds of conjugation methods can be used to covalently bind antibody to QDs. The most popular conjugation method involves the use of EDC/NHS for the formation of amide bond between carboxyl groups and primary antibody. There is a possibility that the antigen binding sites are blocked by the non-selective formation of amide bonds near the F_{ab} region of the antibody[162, 163]. In addition, EDC is not an effective cross-linker due to the fast hydrolysis reaction, which can covert back the carboxyl groups. To avoid these problems, sulfosuccibimidyl-4-(N-maleimidomethyl)cyclohexane-1-carboxylate (sulfo-SMCC) is used for selective conjugation of partial reduced antibodies to QDs. The sulfhydryl groups at the F_c are exposed to bind to the maleimide groups on the SMCC activated QDs[164]. However, this method often required a large amount of antibody for conjugation since the reduction can deactivate the antibody (separation of light and heavy chain)[165].

The AQDs that were developed in our lab have shown the capability to attach multiple AQDs to one SA or multiple SAs to one AQD, depending on the SA/AQD ratio.

Using the same strategy, we examined the conjugation efficiency of AQDs to monoclonal Tn antigen antibody (mAb) without antibody cleavage. We used MPS-replaced CdSe AQDs as a model system due to their visual emission wavelength for characterization.

4.3.1 The effect of mAb/AQD ratio

The synthesis of MPS-replaced CdSe AQDs is described in section 4.1. The MPS can form a network through the cross-linking of silane groups, which protect the AQDs surface and provide the stability at lower pH close to the physiological environments. MPS also provides sulfhydryl functional groups for bioconjugation since the cross-link between sulfhydryl and amines is more efficient due to better stability of the cross-linkers. NHS-polyethylene glycol-Maleimide ($SM(PEG)_n$) is a heterobiofunctional cross-links that differ in length from 17.6 to 95.2 A° as a result of PEG spacer arms containing n equals 2 to 24 ethylene glycol units. $SM(PEG)_n$ activated molecules can link primary amines (NH_2) to sulfhydryl (SH) groups similar to sulfosuccibimidyl-4-(N-maleimidomethyl)cyclohexane-1-carboxylate (sulfo-SMCC). The NHS ester reacts with primary amines at pH 7-9 to form stable amine bonds (Figure 4.18). On the other side, stable thioether bonds are formed by the reaction between the maleimides and sulfhydryl groups at pH 6.5-7.5. The maleimides are stable up to pH = 7.5 due to hydrolysis. Conjugation experiments involving molecules with these two heterobiofunctional groups are usually performed at pH 7.2-7.5 with the NHS-ester reaction being accomplished before or simultaneous with the maleimide reaction[166].

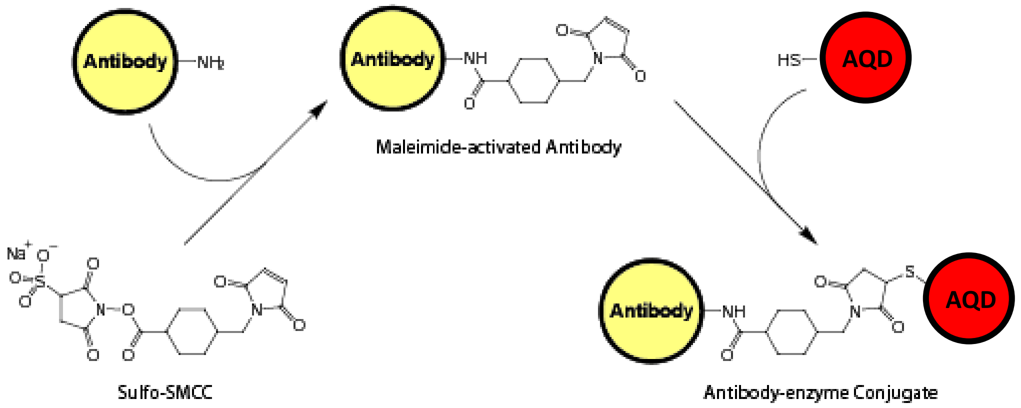

Figure 4.18: Reaction scheme of amine-containing antibody and the sulfhydryl-containing AQDs with sulfo-SMCC as the cross-link[167].

In this experiment, we prepared the MPS-replaced CdSe AQDs as described in section 4.1 and, followed by filtering the suspensions with 10 kDa filtered to removed free MPS three times. Each time, the retentate volume was brought back to the original volume by 10 mM borate buffer at pH =7.5. As the first step of the conjugation, $SM(PEG)_{12}$ at 160 µM was added into the AQDs suspension at pH = 7.5. The reaction was incubated 30 minutes at room temperature. The suspension was then run through a desalting column (Zeba Spin 7 KW, Pierce, Rockford, IL) to remove unbound reagents and electrolytes in the suspension. The suspension was then mixed with an Tn antigen mAb (Tn218, Abcam, NJ) at room temperature for 1 hours. To achieve optimal Ab/AQD conjugation, we experience with AQD/mAb = 7, 5, 3, 1, 0.5, and 0.25. Note that for AQD/mAb ratio ≥ 1, mAb concentration was kept at 80 nM , for Ab/AQD > 1, AQD concentration was kept at 80 nM. Unreacted maleimide groups of $SM(PEG)_{12}$ was quenched by 10 µL of mercaptoethanol (10 mM aqueous solution). The suspension was filtered through a syringe with a 0.2 µm filter (Fisher Scientific, Newark, DE) to remove large aggregates if any Unconjugated AQDs and Abs were then removed by microcentrifugation at 12,000 rpm using 300 kDa filters for 5 minutes three times. After each microcentrifugation, the volume of the suspension was restored with a 10 mM borate buffer solution of pH 7.5.. The conjugated AQDs suspensions were then stored at 4°C

The same custom polyacrylamine/agarose gel system as describe in section 4.2.1b was used to characterize the mAb-AQD conjugates. To characterize the mAb-AQD conjugates, after the final filtration with a 300 kD filter, we ran the retentate and the filtrate of each mAb-AQD through the custom-made gel. Figure 4.19a shows the fluorescence of the AQDs in the mAb-AQD conjugates from the retentate taken with FluorChem E (Protein Simple, San Jose, CA). Coomassie blue (Brilliant R250, Across Organic, NJ, USA) was used to visualize the mAb (Figure 4.19b). A protein ladder was included in lane 1 of the bright field image in Figure 4.19b. Lane 2 in Figure 4.19b contained free mAb which showed as a dark band at about 120 kDa in the bright field image but not in the fluorescent image of Lane 2 in Figure 4.19a. Lane 3 contained free AQDs, which were present in the fluorescent image in Figure 4.19a but not in the bright field image in Figure 4.19b since no antibody was present. Lane 4 to 9 contained mAb-AQD conjugates with AQD/mAb = 7, 5, 3, 1, 0.5, and 0.25 respectively. Figure 4.19c and 4.19d are the filtrate portions of unbound antibodies and unbound AQDs for the mAb-AQD conjugates. As can be seen from the bright field images in Figure 4.19b, both mAb-AQD conjugates with AQD/mAb =7, 5, and 0.25 exhibited a thick band in the range of 130-250 kD, which was larger than the free mAb (120 kD) and AQD (<75 kD). Furthermore, the bands in the 130-250 kD range were fluorescent as evident in Figure

4.19a, indicating that mAb and AQDs are co-localized in these bands forming mAb-AQD conjugates.

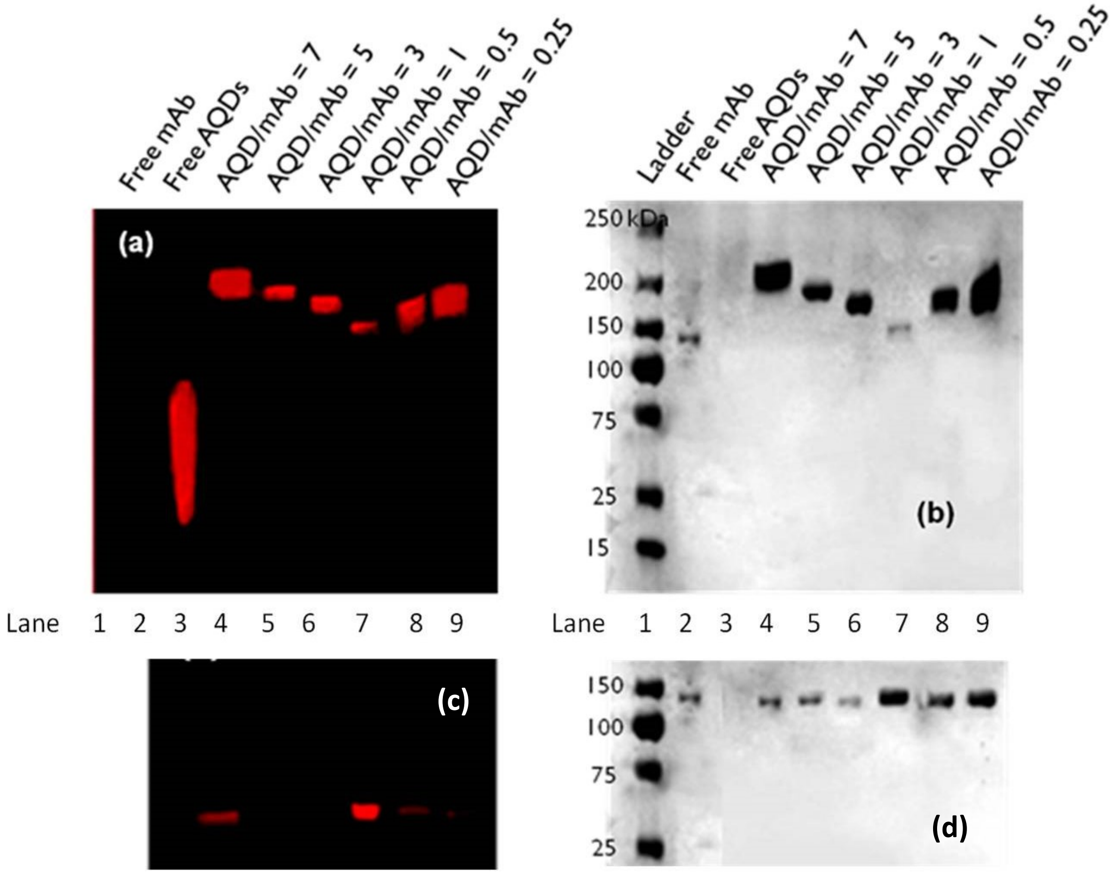

Figure 4.19: Gel electrophoresis images of Ab-AQD conjugates: (a) fluorescent images and (b) bright-field images of the gel with the retentates; (c) fluorescent and (d) bright-field images of gel with the filtrates. Lane 1: ladder; lane 2: free antibody; lanes 3: free AQD; lane 4-9, mAb-AQD conjugates with nominal AQD/mAb = 7, 5, 3, 1, 0.5 and 0.25, respectively;Note red color in the fluorescent images was due to the AQDs and the dark color in the bright field images was due to Coomassie Blue Staining of the mAb. The fluorescent bands of the mAb-AQD (a) co-localized with the mAb bands in (b) at the same positions indicated mAb and AQDs were indeed covalently bound in the retentates whereas the positions of the Abs and the AQDs were not in the same position indicating that they were indeed not chemically linked.

To determine the number of bound mAb per AQD, we followed the method of Pathak et al. [144] as described in section 4.2.1c. We established standard curves for mAb and AQDs. The concentration range was 0.2-2 μM for both mAb and AQDs. Each molar concentration was converted to the number of mAb or A QD by multiplying the molar concentration by the volume. For each AQD/mAb ratio, the total Coomassie blue and the total fluorescence intensity in each band were obtained by integrating the intensity per unit area over the entire area of each band and were converted to the total mAb number or the total AQDs numbers based on the standard curves.

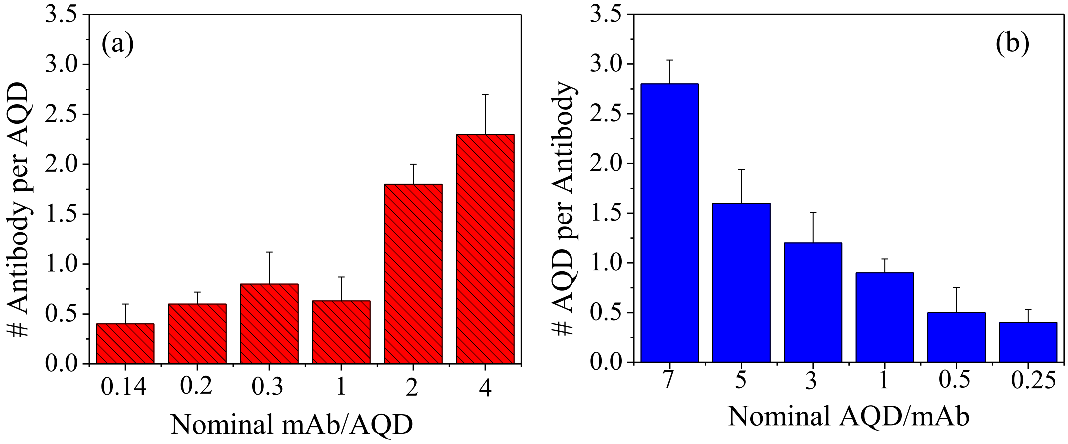

Figure 4.20: Quantification of AB-AQD complexes; (a) number of antibody per QDs ; (b) reversal ratios , number of QD per antibody.

The number of bound AQDs per mAb (or mAbs per AQD) was then obtained by dividing the total number of mAb by the total number of AQDs. The number of bound mAb per AQD versus nominal AQD/mAb number was plotted in Figure 4.20a. As shown, when AQD/mAb > 1, there was less than one antibody per AQD, indicating that more AQDs attached on the surface of a single mAb since the total number of bound AQDs was greater than the total number of bound mAb. To be more precise, we inverted the ratio to AQD/mAb instead of mAb/AQD. As shown in Figure 4.20b, as the nominal ratio of more AQD to mAb resulted in more AQDs bound to a single mAb. The maximal amount of AQD bound to one single mAb was around 3 AQDs per mAb at mAb/AQD = 0.14 or AQD/mAb = 7. It is possible to achieve more AQDs per mAb for aqueous QDs, which is an advantage for bioimaging application. The conjugation efficiency is lower than the SA-AQD conjugation system due to the shape of antibody compared to globular protein, which is easier to assess.

4.3.2 Impact of linker length on antigen binding of mAb-AQD conjugates

The choice of linker that couples the AQDs to the mAb is a critical factor in determining the sensitivity and specificity of conjugated antibody. The linker should be stable to allow the antibody to bind to surface antigen on the cell of interest as well as minimizing non-specific binding. The site of conjugation is also another factor. Ideally, the site for conjugation must not interference with the binding affinity. Heterobifunctional linkers are the most common choice in coupling nanoparticles to antibody. These linkers consist of a spacer with chemically distinct reactive groups on either end that can conjugate to various functional groups on the antibody and nanoparticles. One advantage of using the AQDs is the ability to utilize amine conjugation on the antibody which increases the nanoparticles load on the antibody[165]. In this study, we examined the affect different linker lengths on the sensitivity and specificity of mAb-AQD probes.

Sulfo-SMCC (8.3A°), SM(PEG)$_{12}$ (53.8 A°), and SM(PEG)$_{24}$ (89.2 A°) were chosen as cross-linkers for coupling AQDs to mAb. The ratio of AQD/mAb = 7 was used since it was the optimal ratio as shown in section 4.3.1. The conjugation procedure was described in section 4.3.1. The binding of mAb molecules to AQDs was confirmed by the measurement of the hydrodynamic size of AQDs. The hydrodynamic diameters were determined to be 4±0.3 nm for AQDs, 12±1.5 nm for sulfo-SMCC mAb-AQD, 23±2.4

nm for SM(PEG)$_{12}$ mAb-AQD, and 35±1.5 nm for SM(PEG)$_{24}$ mAb-AQD. After the conjugates were purified, they were used to IF staining study of HT29 human colon cancer cells. The cells were grown on cover glasses overnight and then fixed with 4% paraformaldehyde for 15 minutes followed by washing with Tris buffer saline containing 0.1% Tween (TBS). Cells were and blocked with 10% normal goat serum (Jackson ImmunoResearch, West Grove, PA) for 1 hour at room temperature. mAb-AQD conjugates (10 nM) were added and incubated for 1 hour at room temperature to bind to the Tn antigen on the cell surface followed by washing with TBS three times to remove unbound conjugates. Finally, cells were counter-stained with mounting medium containing DAPI (Vector Laboratories, Burlingame, CA).

Figure 4.21a, 4.21b, and 4.21c shows the fluorescent images of fixed HT29 cells stained by mAb-AQD conjugates with sulfo-SMCC, SM(PEG)$_{12}$ and SM(PEG)$_{24}$ as cross-linker respectively. The images were obtained in a BX51 Olympus fluorescent microscope. Using images similar to those shown in Figure 4.21, the fluorescent intensity per cell was further analyzed using ImageJ and averaged over 100 cells for each cross-linker. In Figure 4.21d, we plot the average fluorescent intensity per cell versus the linker. As can be seen, the fluorescent intensity per cell could reach 320 with SM(PEG)$_{12}$ whereas sulfo-SMCC had the lowest intensity around 100. The spacer aim of SM(PEG)$_{12}$ was the same size as the AQDs providing flexibility for the antibody to bind to the antigen even if the formation of the amine bonds near the F$_{ab}$ regions. Meanwhile, sulfo-SMCC has been commonly use in antibody conjugation showed the worst binding signal due to steric hindrance or blockage of the antigen binding sites. However, the spacer aim too long would cause less mobility for the conjugates to move around. Because of the negative charges on the surface of AQDs and large particle size, repulsive force could occur between to conjugates, preventing the maximum coverage of the cell surface.

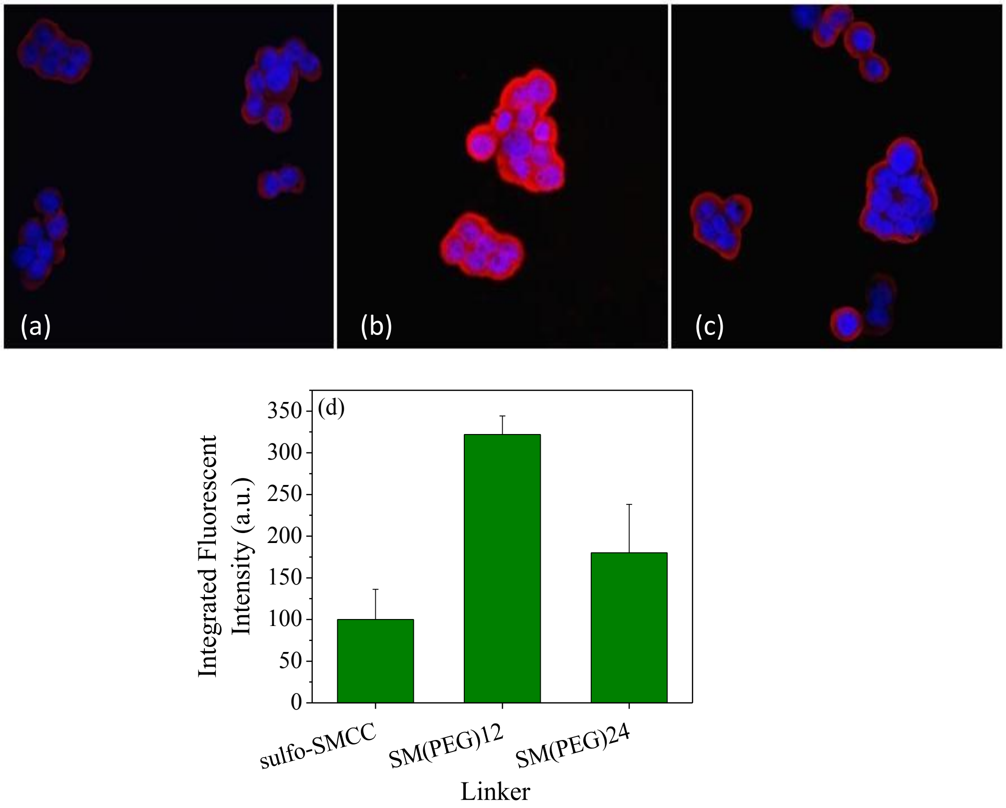

Figure 4.21: Immunofluorescent staining of HT29 colon cancer cells by AQD-mAb (AQD/mAb = 7) with different cross-libkers.(a) sulfo-SMCC; (b) SM(PEG)$_{12}$; (c) SM(PEG)$_{24}$; (d) Relative fluorescent intensity per cell versus linker

Direct primary antibody conjugation with multiple AQDs per mAb can only be achieved using AQDs system. The conjugation strategy showed high fluorescent intensity and sensitivity without signal amplification – indirect staining or SA-biotin system. With this strategy, the amount of antibody required for conjugation is significant less than any other conjugation approach method, which provides an economical and time-saving route to utilize QDs as fluorescent probes for immunofluorescent assays.

4.3.3 Comparison with Commercial QDs for direct antibody conjugation

Carboxylated CdSe/ZnS OQDs were purchased from Invitrogen with a concentration of 8 μM. Conjugation between antibody (Ab) and OQDs was studied by varying the concentration of antibody according to the following ratios OQD:Ab = 5:1, 3:1, 1:1, 1:5, 1:80, and 1:100 with 1 = 80 nM. EDC (5 mM) and NHS (4 mM) were added into the OQDs solution at pH = 7.3 in borate buffer and incubated for 30 minutes at room temperature. Then, 1.4 μL of 2-mercaptoethanol was added into the solution to quench the reaction of EDC. Next, appropriate amount of antibody was added into the solution according to the ratios. The solution was incubated for 2 hours at room temperature. After reaction is completed, the solution is centrifuged using 300 kDa ultrafiltration unit for 3 times and quenched with hydroxylamine .

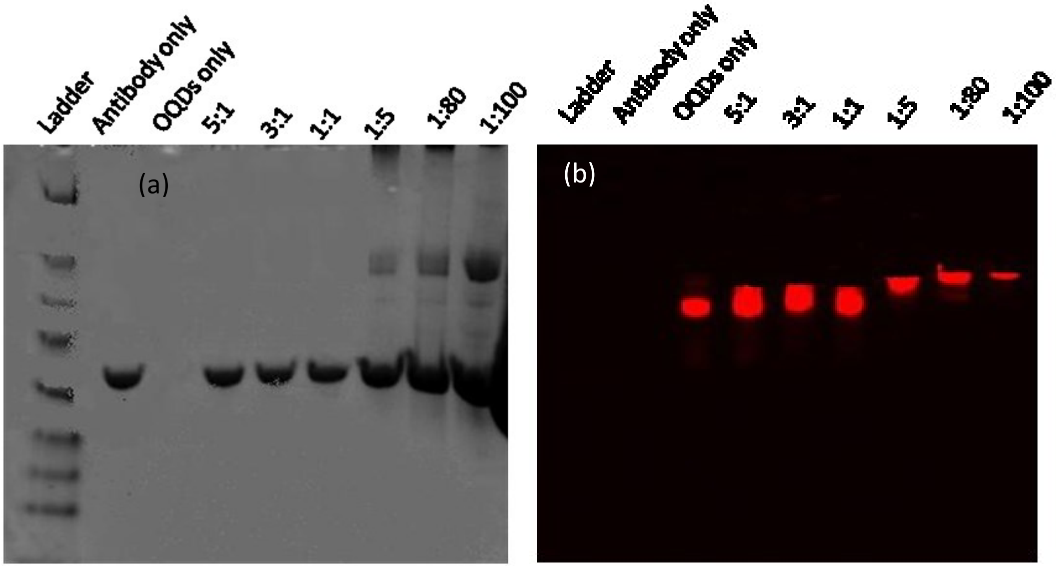

Figure 4.22: Gel electrophoresis quantification of OQD-Ab complexes with EDC-NHS as a linker. (a) Coomassie blue stained image; (b) Fluorescent image.

Because of SDS in acryamide as well as 2-mercaptoethanol in the loading buffer, antibody could be reduced into half as evidence in the 75 kDa band (Figure 4.22a). The bands for conjugated complexes showed different positions indicated that different they have different number of OQDs per antibody or number of antibodies per OQDs. The ratios of more OQDs to Ab did not show any conjugated complex. On figure 4.22a, all the Ab bands were at the exact same position as free Ab as well as OQDs bands as the same of free OQDs. For OQD/Ab = 1/5, 1/80 and 1/100, there were bands around 120-150 kDa on both coomassie blue stained and fluorescent images that colocalized with each other. For the other region where OQD/Ab <1, OQD/Ab = 1/100 showed the highest molecular weight indicates that the complex has the most antibody number. To verify the imaging capacity of the conjugates, IF staining was performed on HT29 cells with all the ratios.

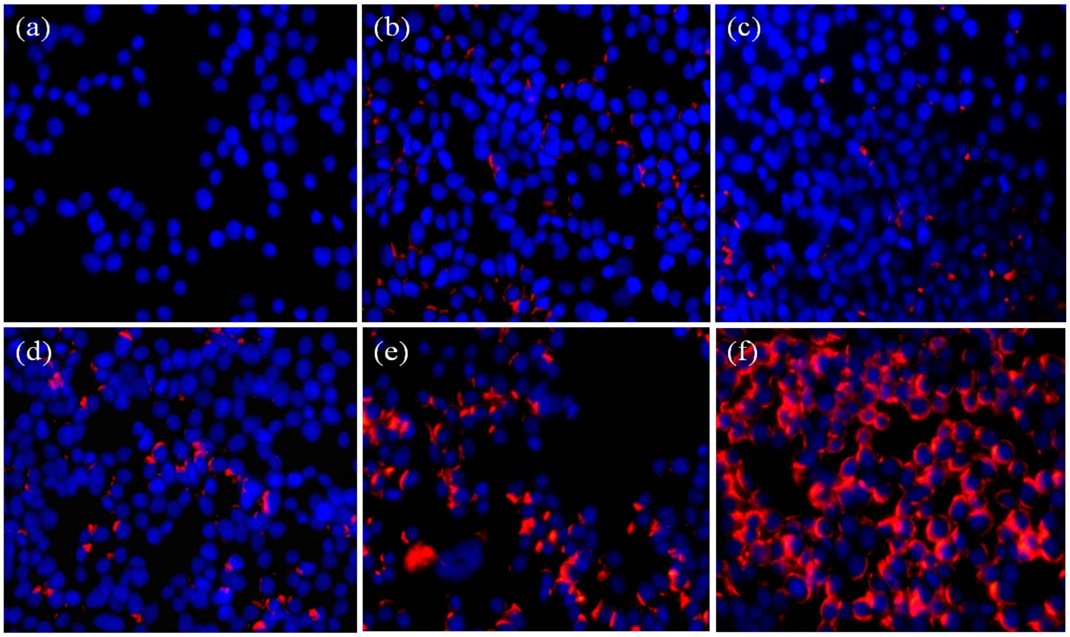

Figure 4.23: IF staining of HT29 cells using OQD-Ab conjugates at different ratios using EDC-NHS as linkers. (a) OQD:Ab = 5:1; (b) OQD:Ab = 3:1; (c) OQD:Ab = 1:1; (d) OQD:Ab = 1:5; (e) OQD:Ab = 1:80; OQD:Ab = 1:100. Blue: DAPI, Red : OQDs

As shown in Figure 4.23, IF staining images of fixed HT29 cells stained by different OQD:mAb ratios. The best ratio was OQD:mAb = 1:100 which stained HT29 cells membrane nicely (Figure 4.23f). All other ratios show non to little staining indicates that the conjugates were not effective. This could due to the reduced of antibody due to 2-mercaptoethanol during the conjugation process which cleaved the antibody into light and heavy chains. This resulted in inactivating antibody. Therefore, although the fraction of antibody bound to OQDs, the conjugates couldn't detect marker on the cell membrane. The conjugation of OQDs to antibody showed difficult to achieve and require high concentration of antibody.

An alternative conjugation scheme for OQD to antibody is to use amine groups on the surface of OQDs and thiols on antibody. First, 8 μM of SM(PEG) was added to OQDs solution at pH = 7.3 in borate buffer. The mixture was stirred slowly for 1 hour at room temperature. The reducing of antibody was started when there were 30 minutes remaining of the OQD activation reaction. DTT solution (6.1 μL of 1M) was added to the antibody solution and mixed briefly. The solution was incubated for 30 minutes at room temperature. The top and bottom caps of desalting columns were removed (1 columns for antibody and 1 column for OQDs). When the liquid in each column was approaching the top of the column gel bed, each column gel bed was equilibrated with 10 ml exchange buffer. While there was still exchange buffer visible above the gel bed on each column, cap the bottom of each column and set aside until the antibody reduction was completed. 500 μL of water was added to a centrifugation tube and marked the outside tube at the meniscus. Another 500 μL of water was added and a second mark was made on the outside of the tube corresponding to the new level. Then, the water was discarded. When the antibody reduction was completed, 20 μL of dye labeled marker was added to the reduced antibody. The antibody desalting column was uncapped and allowed remaining exchange buffer to enter gel bed and as soon as it had done, the reduced antibody mixed was immediately added to the top of the gel bed. After the antibody mixture entered the gel completely, 1 ml of exchange buffer was added to the top of the gel bed to elute the antibody. The antibody was collected into a centrifugation tube when the first colored drop eluted. Collect no more than 500 μL (to the lower marked line from the earlier step). The OQD desalting column was uncapped and allowed remaining exchange buffer to enter gel bed. Activated OQDs was added to the column immediately to the top of the gel bed. After the OQDs mixture entered the gel completely, 1 ml of exchange buffer was added to the top of the gel bed to elude the OQDs. The OQDs were collected into the antibody contained centrifugation tube when the first drop eluted. Collect no more than 500 μL to the higher marked line from the earlier step). Mix both antibody and OQDs briefly. The reaction was allowed to react for 1 hour at room temperature. 10 μL of 2-mercaptoethol (10 mM) was added to the mixture to quench to reaction and incubated for 30 minutes at room temperature. Unbound SA and QDs were filtered out by micro-centrifugation 3 times with 300 kDa filters. Each time, the solution volume was brought back to its initial by borate buffer. Finally, the pH of QD conjugated antibody was adjusted to 7.5 to maintain the stability of the complex.

This conjugation strategy required cleavage of antibody to expose thiol groups[164]. However, because of the cleavage, there was a large percentage of inactive antibody (separation of light and heavy chain) which caused low conjugation efficiency. Sulfo-SMCC was used as a linker before but proved insufficient for tissue imaging. This might have occurred due to steric hindrance of antibody. When QDs are too close to the binding site, they could prevent antigen-antibody reaction resulting in less binding in which reduces fluorescent signal. SM(PEG)$_{12}$ was used to replace SMCC since the spacer arm is 5.9 nm. It could potentially avoid this steric hindrance. AQDs had been successful conjugated to antibody using SM(PEG)$_{12}$ as linker. Therefore, this linker was used for OQDs comparison in term of conjugation efficiency.

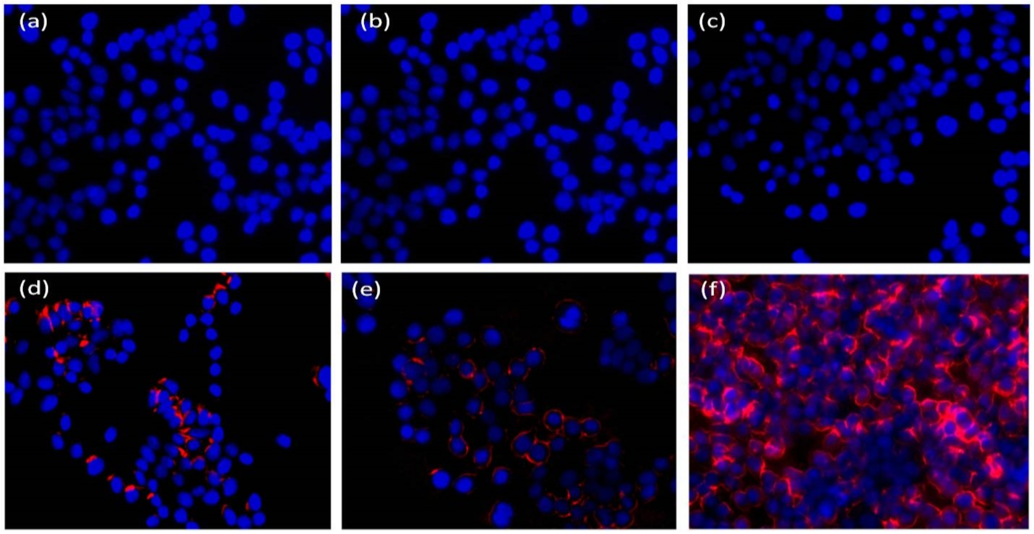

Figure 4.24: IF staining of HT29 cells using OQD-Ab conjugates at different ratios using SM(PEG)$_{12}$ as linkers. (a) OQD:Ab = 5:1; (b) OQD:Ab = 3:1; (c) OQD:Ab = 1:1; (d) OQD:Ab = 1:80; (e) OQD:Ab = 1:100; OQD:Ab = 1:120. Blue: DAPI, Red : OQDs

Figure 45 showed different ratios of OQD:Ab. The best ratio was OQD:Ab = 1:120 which stained HT29 cells membrane nicely (figure 4.24f). All other ratios show no to slight staining indicates that the conjugates were not effective. This could be due to the reduction of the antibody due to DTT during antibody reduction process which could separate the antibody into light and heavy chains. This resulted in inactivated antibody. Therefore, although some part of an antibody is bound to an OQD, the conjugate couldn’t detect the marker on the cell membrane because the part bound to the OQD dos not have the binding site. The conjugation of OQDs to antibody was difficult to achieve and required an even higher concentration of antibody than the amine conjugated antibody scheme. This result again showed that AQDs are superior in term of conjugation with biomolecules.

CHAPTER 5: INDENTIFICATION AND VALIDATION OF SUITABLE BREAST CANCER MARKERS FOR BREAST MARGIN ASSESSMENT

5.1 Tn ANTIGEN (CD175)

The Tn antigen was first discovered in 1959 as a carbohydrate antigen on the surface of red blood cells with a very rare Tn-syndrome or Tn polyaggulutinability[168]. The Tn antigen is designated CD175 and its sialylated form (sTn) CD175s. In 1975, the structure of Tn antigen was defined with Ser/Thr-linked GalNac in tryptic glucopeptides of erythorocytes from Tn syndrome patients[169]. However, not until the 1990's, Tn antigen was discovered to express in a variety of malignant cancers opening a new interest for this moiety as a cancer associate marker[170]. Tn antigen is one of the tumor-associated carbohydrate antigens (TACAs). Their structures are derived during neoplastic transformation changes within the glycosylation pathways. It has been known that the TACAs contribute to the malignant phenotype of cancer cells [171]. Tn antigen is formed due to the incomplete elongation of O-glycan saccharide chains due to lack of activities of ß1-3 Dgalactosytransferase and a2-6 sialyltransferase enzymes [172]. This results in shorter carbohydrate structures in multiple glycoprotein and in mucins. It has been used as a prognostic indicator in primary breast cancer tissues [173]. Tn antigen expression is strictly in cancer cells and absent in a broad range of normal adult tissues including normal breast tissues [174-177] (Figure 5.1). Between 60-80% cancer cells express Tn antigen in DCIS and 20-50% in lobular carcinoma in situ. For IDC, the expression also varied according the tissue differentiation, stage I : 70% cancer cells, stage II: 90-100%, and stage III: 40-60% [136]. Although Tn antigen is present in some benign breast lesions such as atypical ductal hyperplasia (ADH), ADH is generally considered a cancer precursor [175, 178].

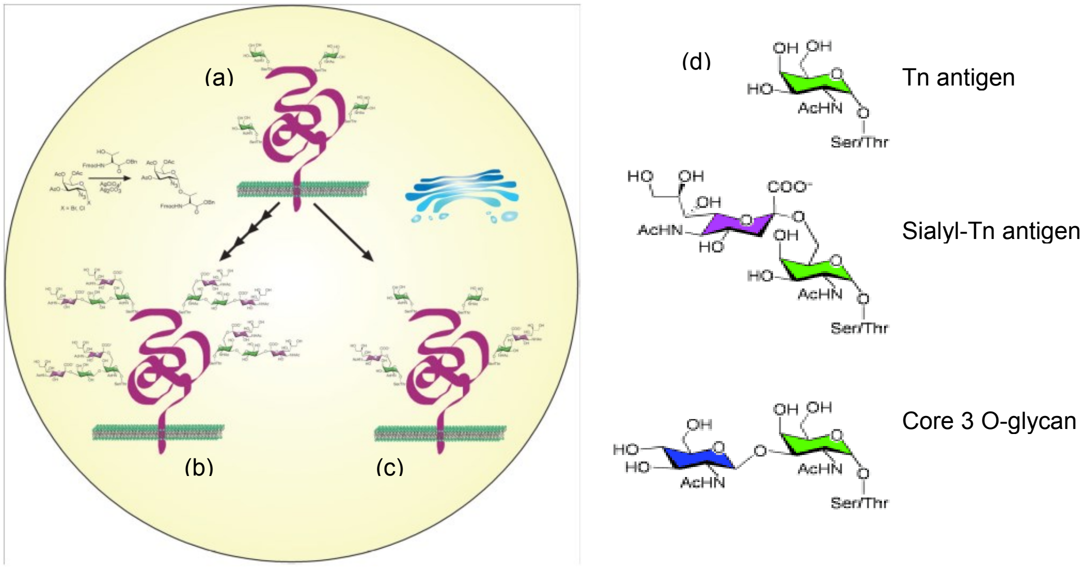

Figure 5.1: (a) Tn antigen on the back-bone of membrane-bound mucin; (b) additional sugar is added to Tn antigen in normalcell; (c) truncated form of of a glycosylation exposing Tn antigen in cancer cells; (d) Strucutes of Tn antigen and O-glycan derivatives of the Tn antigen [179].

Detection of Tn antigen can be divided into three categories: chemical, lectin-based and antibody-based. For direct chemical approach, N-acetylgalactosaminitol is associated with modified Ser or Thr amino acids, which is evidence for the presence of Tn antigen on glycopeptides or glycoprotein. In the presence of $NaBH_4$, glycopeptides are degraded and generate N-acetylgalactosaminitol. The method is difficult to perform on the small amount present in cells or tissue. The dominant strategies to detecting Tn antigen are lectin and antibody-based methods. Several lectins derived from plant such as *Dolichos biforus* agglutinin (DBA)[180], *Marrubium candidissimum* agglutinin[181], *Maclura pomifera* lectin (MPL)[182], *Salvia horminum* agglutinin (SHA)[183], *Salvia sclarea* agglutinin (SSA)[184], *Salvia bogotensis* lectin[185], *Bauhinia purpurea* agglutinin (BPA)[169, 186], the B4 isolectin of *Vicia villosa* agglutinin (VVA-B4)[136, 187], and the snail-derived *Helix pomatia* agglutinin (HPA)[188]. The two most common lectins that are used for detecting Tn antigen are VVA-B4 and HPA. However, the use of lectins to identify Tn antigen can be problematic due to cross-react with nonreducing and terminal GalNAc residues[179, 189]. The most specific approach to detecting Tn antigen is based on anti-Tn antibodies. However, the specificity of the antibodies to the Tn antigen can be varies and cause problematic for researcher due to the cross-react with other GalNAc-containing glycans, such as blood group A antigen[179].

5.2 VASCULAR ENDOTHELIAL GROWTH FACTOR (VEGF)

Vascular endothelial growth factor (VEGF) plays major role in angiogenesis which has been investigated intensively over the past decade. Recent studies have shown that VEGF-signaling representing the rate-limiting step in physiological angiogenesis[190]. The level of VEGF is negligible in normal cells but can be elevated during wound healing process. There are evidences suggest that VEGF is a mediator of tumor angiogenesis due to the highly level of secretion of this diffusible molecule from many tumor cell lines *in vitro* [190, 191]. The VEGF mRNA level is highest in hypoxic tumor cells adjacent to the necrotic areas. Tumor size cannot exceed 1-2 mm in diameter without angiogenesis. During the in situ stage of breast cancer, as the tumor grows, hypoxia occurs which triggers the expression of VEGF (Figure 5.2). In response to chemotatic stimuli, stromal cells are recruited into the tumor and produce VEGF in addition to the tumor cells [192] (Figure . In breast cancer, although the expression of VEGF varies through stages, its presence is usually observed. The distribution of VEGF positive cells are not the uniform in one nest. The strong expression ones concentrated mainly in tumor invasive edges. This is a major advantage for margin detection. VEGF expression is correlated to the tissue differentiation degree. For invasive ductal carcinomas (IDC), VEGF positive rate is 40% of cancer cells at stage I, 75.6% at stage II and 77.8% at stage III [193]. As the tissue differentiates higher, the expression is also higher. For the non-invasive type of breast cancer, ductal carcinomas in situ (DCIS), positive expression of VEGF is between 93-100% [194, 195]. This makes VEGF a good candidate for the specific margin assessment.

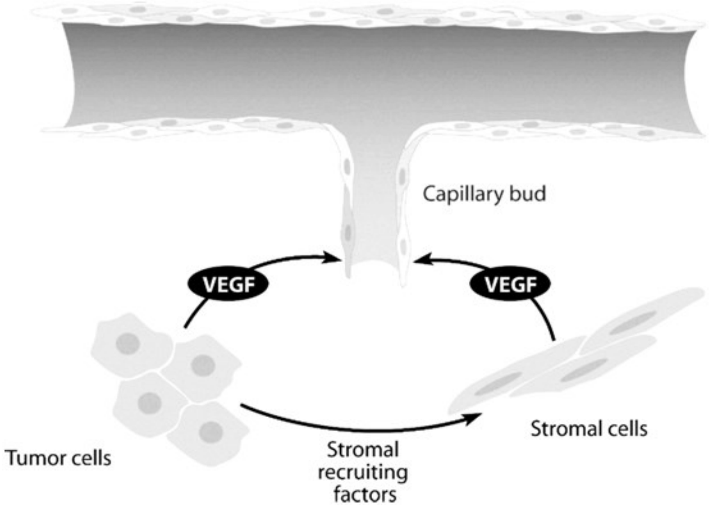

Figure 5.2: Both tumor and stromal VEGF contribute to tumor angiogenesis. In response to chemotatic stimuli, stromal cells are recuited into the tumor and produce VEGF and other angiogenic factors.

5.3 TISSUE MICRO-ARRAYS CONSTRUCT and SA-AQD PROBE CONJUGATION

Each patient had multiple paraffin-embedded tissue blocks which were made from their original surgical excised tissues. Each tissue block was reviewed by a pathologist to identify appropriate areas to be included in the TMAs. When an appropriate area was identified, a 2-mm diameter punch was made and the tissue was randomly placed in a

TMA block as a core. For each malignant case, we included 3 punches from the malignant region and a punch from the normal breast region. For each benign case, we included three punches from the benign tumor region. A TMA contained 50-60 cores that were from at least 15 patients and were randomly distributed within the TMA to eliminate potential correlation from core to core. There were a total of 115 patients--58 breast cancer patients with various breast cancer types and 57 patients with benign breast pathology--and 395 cores--395 out of a total of 403 punches were successfully made into cores.

The synthesis of MPA-capped CdSe AQDs is described in Chapter III. The freshly made AQDs suspension was first stored in a refrigerator (4°C) overnight followed by removal of free MPA's in the suspension by centrifugation with a 10 kDa filter (Millipore Co., Beillerica, MA) at 3000 rpm for 10 minutes three times. N-ethyl-N'-dimethylaminopropyl-carbodiimide (EDC) (Thermo Scientific, Rockfold, IL, USA) and N-hydroxysuccinimide (NHS) (Thermo Scientific, Rockfold, IL, USA) were used to facilitate the peptide bond formation between a primary amine of the SA and a carboxyl on the AQD. First, 4 mg of EDC and 6 mg of NHS were dissolved in 1 ml of 0.1 M 2-(*N*-morpholino)ethanesulfonic acid (MES) buffer (TEKNOVA, Hollister, CA) at pH = 6.5. 2 mM of EDC and 5 mM of NHS were added to the suspension of the AQDs (1.07 μM particle concentration) at pH =7 in borate buffer. The reaction was incubated for 15 min at room temperature followed by the addition of 2-mercaptoethanol (20 mM) to quench the EDC. The suspension was then run through a desalting column (Zeba Spin 7 KW, Pierce, Rockford, IL) to remove unbound reagents and electrolytes in the suspension. The suspension was then mixed with an SA solution at room temperature and pH = 7.0 for 2 hr. The unused NHS esters bound on the AQD surface were then quenched by hydroxylamine hydrochloride (10 mM) (Sigma-Aldrich, St. Louis, MO, USA). Unconjugated AQDs and SAs were then removed by microcentrifugation at 12,000 rpm using 100 kDa filters for 5 minutes five times. After each microcentrifugation, the volume of the suspension was restored with a 50 mM borate buffer solution of pH 8.3. After five consecutive microcentrifugations, the suspension was filtered through a syringe with a 0.2 μm filter (Fisherbrand, Newark, DE) to remove large aggregates if any. The conjugated SA-AQD probes were then stored at 4°C before use.

5.4 IMMUNOFLUORESCENT STAINING OF BREAST CANCER CELL LINE TO VALIDATE THE AQD-SA PROBES

The MDA-MB-231 human breast cancer cell line was obtained from the American Type Culture Collection (ATCC) as it is expressed Tn antigen abundantly. MDA-MB-231 cells were maintained in DMEM high glucose medium supplemented with 10% fetal bovine serum (Bioexpress, Kaysville, UT), 1% penicillin and streptomycin (Mediatech Inc., Manassas, VA) and cultured at 37°C in a 5% CO_2 incubator. To test the staining capability of the SA-AQD probes, MDA-MB-231 cells were grown on cover glass overnight and then fixed with 4% paraformaldehyl for 15 minutes. Cells were washed with PBS three times. Cells were blocked with 10% normal goat serum for non-specific binding for 1 hour at room temperature. Slides were then washed with 0.1% Tween/Tris buffer saline (TBS) for 3 times. The slides were then incubated with mouse anti-Tn antigen antibody (1:50 dilution, Tn218 Genetex, CA) or VEGF (1:100 dilution, Invitrogen) for 1 hour at room temperature. Next, they were washed with TBS 3 times for 5 minutes each and incubated with biotinylated goat anti-mouse IgG/IgM (1:50 dilution, Invitrogen, OR) for 30 minutes at room temperature, followed by TBS washes prior to incubation with SA- AQD probes for additional 30 minutes at room temperature. Slides were washed with TBS for 3 times and mounted with DAPI (Mounting medium with fluorescence, Vector Laboratories, CA, USA) for nucleus staining. Samples were stored in the dark at 4°C. A negative control was the sample without primary antibody. The slides were observed under an Olympus BX51 fluorescent microscope.

MDA-MB-231 is a breast cancer cell line that exhibits Tn antigen on the cell surface. As an example, the AQD-stained MDA-MB-231 cancer cells using the method described above are shown in Figure 5.3a. The presence of Tn antigen on MDA-MB-231 cells was detected by the SA-AQD IF staining method as can be seen from Figure 5.3a. For comparison, MDA-MB-231 cancer cells stained by Cy3-labeled SA are shown in Figure 5.3b. As can be seen, both SA-AQD and SA-Cy3 showed fluorescent signals on the cancercells while the negative control (Figure 5.3c)--which underwent all the AQD staining steps except the primary antibody step--showed no sign of fluorescence. This indicates the specificity of the AQD staining method. Furthermore, as can be seen, AQD-stained cells exhibited stronger fluorescent signals than Cy3 using the same concentrations of the antibodies, indicating that AQDs provided a better signal-to-noise ratio than Cy3. One possible explanation was that AQDs were nanoparticles which theoretically should be brighter than cy3 which was only a molecule. In addition, the separation of the excitation wavelength and the emission wavelength of the AQDs was more than 100 nm, which was advantageous when compared to the conventional dyes such as Cy3 whose excitation and emission wavelength separation was less than 20 nm with likely interference between excitation and emission.[196] A wider separation between the excitation and the emission can minimize the noise in the emission generated by the overlap from the excitation. Furthermore, the 600 nm long-pass filter allowed only the red and the near infrared (NIR) part of the AQD emission spectrum for imaging, which was the wavelength range where autofluorescence of the paraffin-embedded tissues fell off sharply.[197] This permitted the AQDs to have very low background noise levels in imaging paraffin-embedded tissues[198].

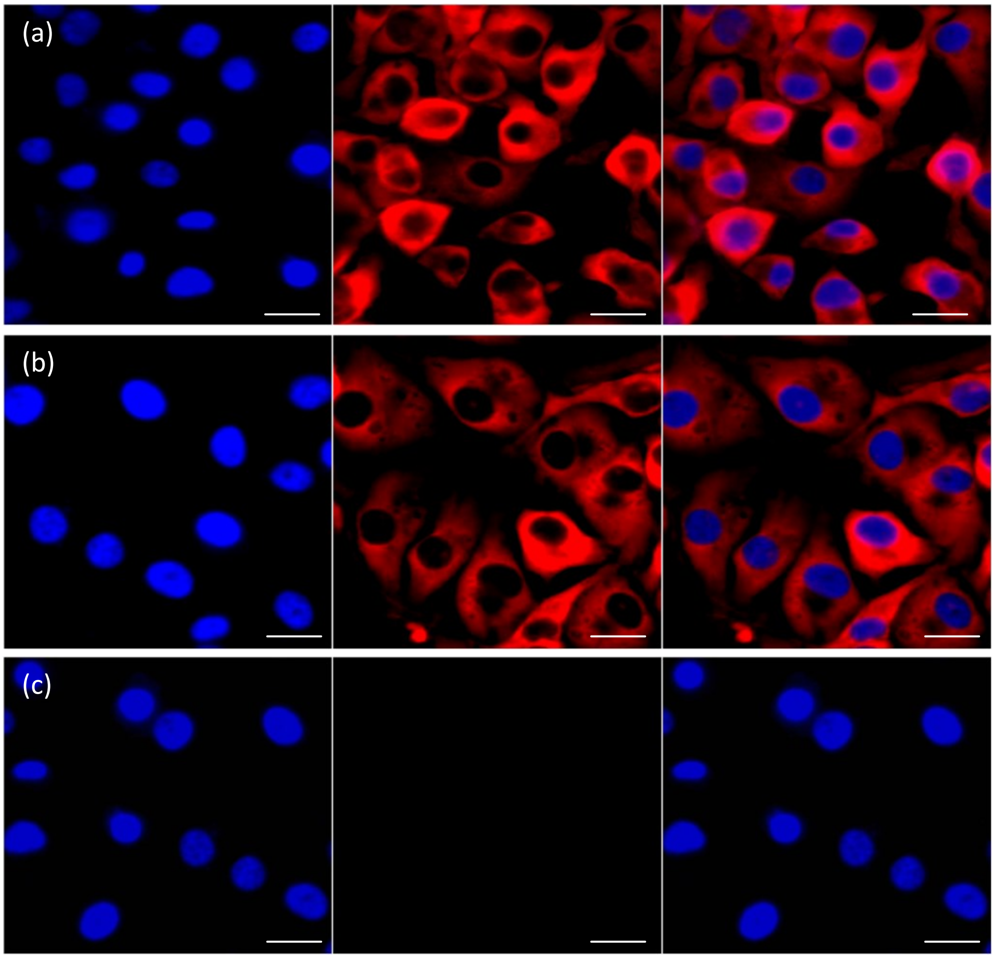

Figure 5.3: Immunofluroscent staining of MDA-MB-231 cells for Tn antigen expression. (a) MDA-MB-231 cells stained with AQD-SA complexes; (b) HT29 cells stained with Cy3-SA (c) negative control, without primary antibody. Blue: Nuclei – right columns, Red: Tn antigen expression – middle columns. Overlay images – left columns. Tn antigen expression was mostly on the membrane and in cytoplasm. Scale bar: 30 µm

5.6 IMMUNOFLUORESCENT STAINING (IF) AND IMMUNOHISTOCHEMICAL STAINING (IHC) FOR FIXED TISSUES AND IMAGING ANALYSIS

For the AQD-based IF and Horse Radish Perioxide (HRP) IHC imaging, we used MPA-capped CdSe AQDs each conjugated to 3.3 SA[199] as the fluorescent label and HRP labeled SA for a three-step indirect staining strategy consisting of (1) binding the primary antibody on the cancer cells, (2) binding the biotinylated goat anti-mouse antibody to the primary antibody, and (3) binding of the HRP-labeled SA to the biotinylated goat anti-mouse antibody.

TMAs were cut into 5 µm sections, mounted on glass slides, and stained for Tn antigen and VEGF as follows. Following paraffin removal, hydration and antigen retrieval in sodium citrate (pH = 6, Thermo Scientific, NJ) at 95°C for 20 min, the sections were blocked for 1 hour with 10% normal goat serum (Vector Laboratories, Burlingame, CA, USA) in 0.1% Tween Tris buffer saline (TBS); washed in TBS for 3 times, 5 minutes each and then blocked with Streptavidin (Streptavidin/Biotin Blocking Kit, Vector Laboratories) for 15 min; followed by a TBS wash; prior to block for 15 min in biotin (Streptavidin/Biotin Blocking Kit, Vector Laboratories). The slides were then incubated with mouse anti-Tn antigen antibody (1:25 dilution, Genetex, CA) for 1 hour at room temperature. Next, they were washed with TBS 3 times for 5 minutes each and incubated with biotinylated goat anti-mouse IgG/IgM (1:50 dilution, Invitrogen, OR) for 30 minutes at room temperature, followed by TBS washes prior to incubation with SA-AQD probes for additional 30 minutes. Finally, the slides were washed again with TBS. Sections were counterstained and mounted with DAPI mounting medium (Vector Laboratories, Burlingame, CA, USA)

For IHC staining, the slides were stained using the same steps as described in the QD-stained slides except an additional blocking of 0.3% hydrogen peroxide (Fisher, Allentown, PA) for 15 min before incubating with mouse anti-Tn antigen antibody (IgM, 1:25 dilution) or mouse anti-VEGF antibody (IgG, 1:50 dilution) for 1 hour at room temperature. Biotinylated goat anti-mouse IgG/IgM (1:50 dilution, Invitrogen, OR) for 30 minutes at room temperature, followed by TBS washes prior to incubation with SA-HRP probes for additional 30 minutes. . The slides were washed with TBS, followed by incubated in 3,3'-diamiobenzidine (DAB) for 5 min, and then washed with TBS. The slides were counterstained with hematoxyline.

The AQD-stained IF slides and the standard HRP-stained IHC slides were examined using a BX51microscope (Olympus) in the fluorescent mode and in the bright field, respectively. A MicroVista charge-coupled device (CCD) camera (Intevac, Carisbad, CA) was mounted on the microscope to take the images. For CdSe AQD imaging, we chose an excitation filter with a wavelength window of 460 nm ±20 nm (Chroma, Bellows Falls, VT) and a 600-nm long-pass emission filter to allow any emission with a wavelength longer than 600 nm. For Cy3-labeled SA, a 550-nm excitation filter and a 570-nm emission filer were used.

NIH ImageJ was used to analyze the images of the AQD-stained slides. For each core, six images each from a different area of the core were taken. Therefore, for each malignant case there would be a total of 18 images from the tumor cores and 6 images from the normal-tissue cores. For each case of benign tumors, there would be 18 images from the tumor cores. In each tissue array, there was a placebo (unstained) heart tissue core. For any fluorescent image analysis, the placebo was first examined to determine the baseline background auto-fluorescent intensity. This baseline background fluorescent intensity was then subtracted from all the images to minimize the interference by autofluorescence. After the background subtraction, the fluorescent intensity per unit area (FPA) of each cell was then determined within the area of that cell using ImageJ, which we defined as the cellular fluorescent intensity per unit area (CFPA). CFPA was then recorded for each cell. A histogram of CFPA was then constructed for each core, from which the average CFPA of that core was then computed. The average CFPA of each core was then recorded as the quantitative CFPA of that core. After the AQD staining results were reported to the pathologist (LM), the disease status of each core of the TMAs was then unblinded and the reported CFPA of each core was then compared to the disease status of the core. With this comparison, the numbers of true positives, true negatives, false positives, and false negatives were then computed to obtain the sensitivity and specificity of the AQD imaging both by the core and by the case. A receiver operating characteristic (ROC)--sensitivity versus (1-specificity)--curve was also constructed. The area under the ROC curve represents the diagnostic accuracy [200]. Student t-test was used for statistical analysis of normal versus malignant and normal versus benign at 95% confident level. ANOVA test was used to analyze the different in Tn antigen expression according to cancer stage and grade.

5.5 QUANTITATIVE FLUORESCENT STAINING OF TISSUE MICROARRAY FOR EXPRESSION LEVEL OF TN ANTIGEN AND VEGF USING SA-AQD PROBES

Generally, both AQD IF and HRP IHC staining showed strong Tn antigen signal in the cytoplasm and the cell membrane in all malignant lesions including IDC, ILC, and DCIS, but minimal Tn antigen staining on the normal tissues of the malignant cases, as well as the benign breast conditions. Examples of the AQD IF staining of a Stage II IDC, a Stage III IDC, and a benign breast condition of ductal hyperplasia without atypia are shown in Figures 5.4a, respectively and the HRP IHC staining of the same tissues are shown in Figures 5.4b as well as H&E images, which showed histological texture of the tumors (Figure 5.4c). As can be seen from Figures 5.4a and 5.4b, both the AQD staining and the HRP staining showed intense signal of Tn antigen in the cytoplasm and the cell membrane of the IDC cores. There were 42 cases of benign breast tissues with pathological changes. Most of these benign changes exhibited no Tn antigen staining as well. However, there were a few cases of benign changes that were positive with Tn antigen staining in either AQD or HRP staining which is discussed below. In addition, there were 3 cases that AQD-IF staining showed negative expression of Tn antigen whereas HRP. AQD-IF and HRP-IHC staining for VEGF showed similar results as Tn antigen(data not shown). IHCshowed a positive level indicating AQD IF method has higher specificity. It suffices to say that by and large, both the AQD staining and the HRP staining could differentiate malignant breast tumors from normal breast tissues and benign breast lesions. There were 15 cases of benign breast tissues with no pathological changes. These cases were considered as normal tissues. There was no positive signal in AQD IF staining for these cases. HRP-IHC staining, however, resulted in 2 cases with positive signal.

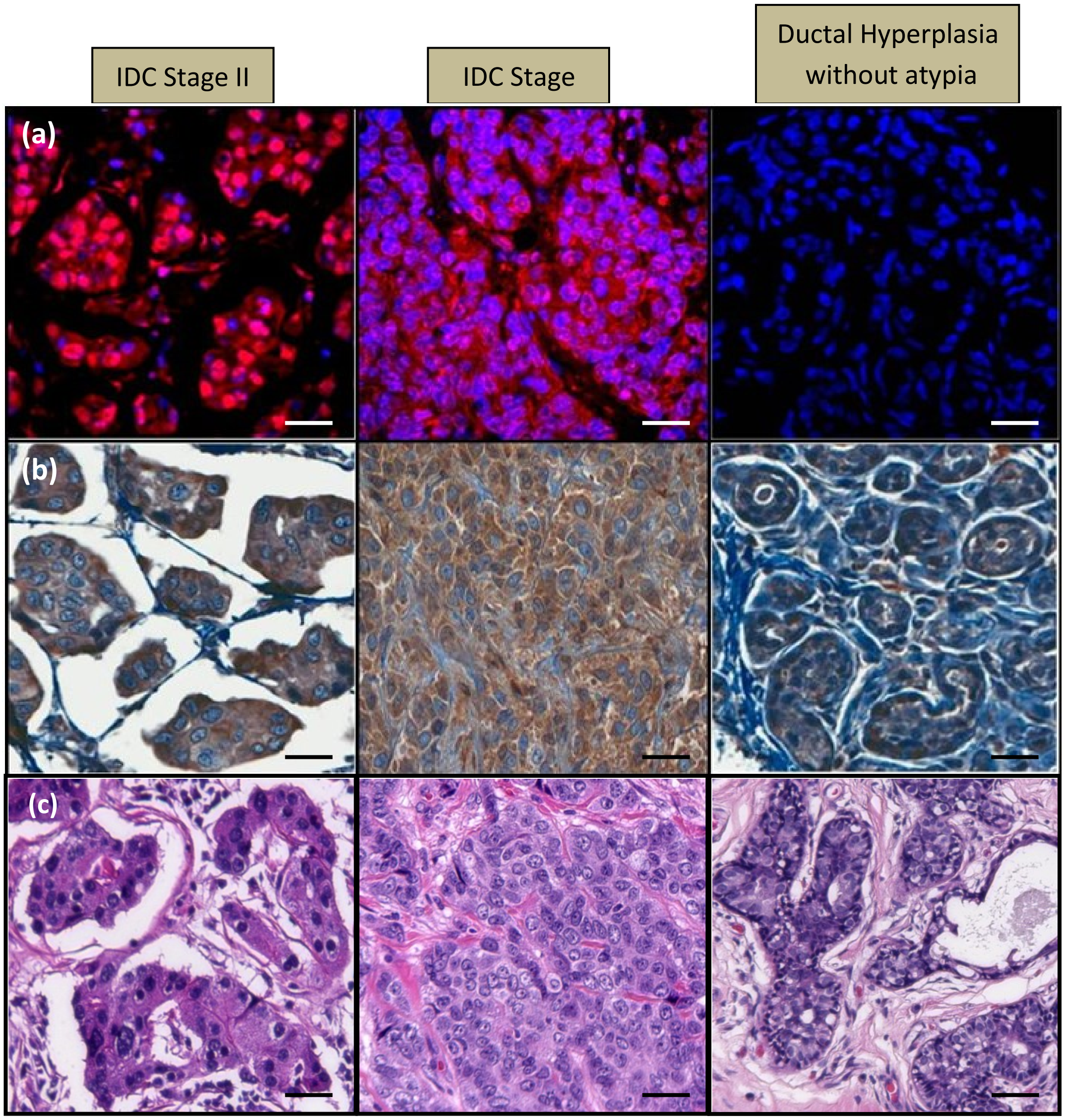

Figure 5.4: Tn antigen expression in invasive ductal carcinomas and benign changes. (a) AQD-IF staining:. Strong staining of all cells were for both IDC Stage II and IDC Stage III. No staining was observed in AQD-stained section for Ductal hyperplasia without atypia. (b) Corresponding HRP IHC staining for the same section: Strong staining of all cells for both IDC Stage II and IDC Stage III as well as Ductal hyperplasia without atypia. (c) H&E images of the same case. AQD IF staining is more specific than HRP IHC staining method. AQD-IF stained sections, blue: nuclei, red: Tn antigen. Scale bars: 200 μm.

Figure 5.5 summarizes the average fluorescent intensity per unit area (CFPA) of the tumor region for each of the 115 cases (full symbols for various malignant tumors and stars for benign conditions) and those of the normal regions (open circles) of the malignant cases. Each dot represents one case. As can be seen in Figure 5.5a and 5.5b, the CFPA for the normal tissues of the malignant cases (including all breast cancer types: DCIS, IDC and ILC) were mostly below 20 whereas the CFPA of the malignant tumors were mostly above 20. The CFPAs of most of the benign lesions were also below 20, which are similar to those of the normal tissues of the malignant cases. This supports the conclusion that AQD staining of Tn antigen was quite sensitive and specific for breast cancer detection.

Based on the results shown in Figures 5.5a and 5.5b, we obtained histograms of the CFPA of malignant tumors, benign tumors and the normal tissues (open circles in Figure 5.5c and 5.5b). After fitting the histograms with a lognormal distribution (for benign and malignant) and generalized extreme value distribution for normal using MATLAB (Gaussian fit), the fitted distribution of the CFPA of the malignant tumors (red), that for the normal tissues (blue), and that for the benign lesions (green) based on AQD staining are shown in Figure 5.5c and 5.5d. As can be seen, the CFPA distribution for the malignant tumors overlaps with those of the normal tissues and the benign lesions near a CFPA= 20. Indeed, a threshold CFPA of 20 could separate malignant tumors from normal tissues with p value of 0.0036 for Tn antigen and p=0.03 for VEGF. A prediction regarding the malignancy of the tissue was then made using this threshold. Similarly, using this threshold to compare the benign tumor to normal tissue, a p value of 0.065 for Tn antigen was computed indicating that there were no different in Tn expression between normal tissue and benign tumors. After un-blinding, these predictions were then compared with the known status of the tissues to determine true positives, true negatives, false positives, and false negatives, from which the sensitivity and specificity were computed.

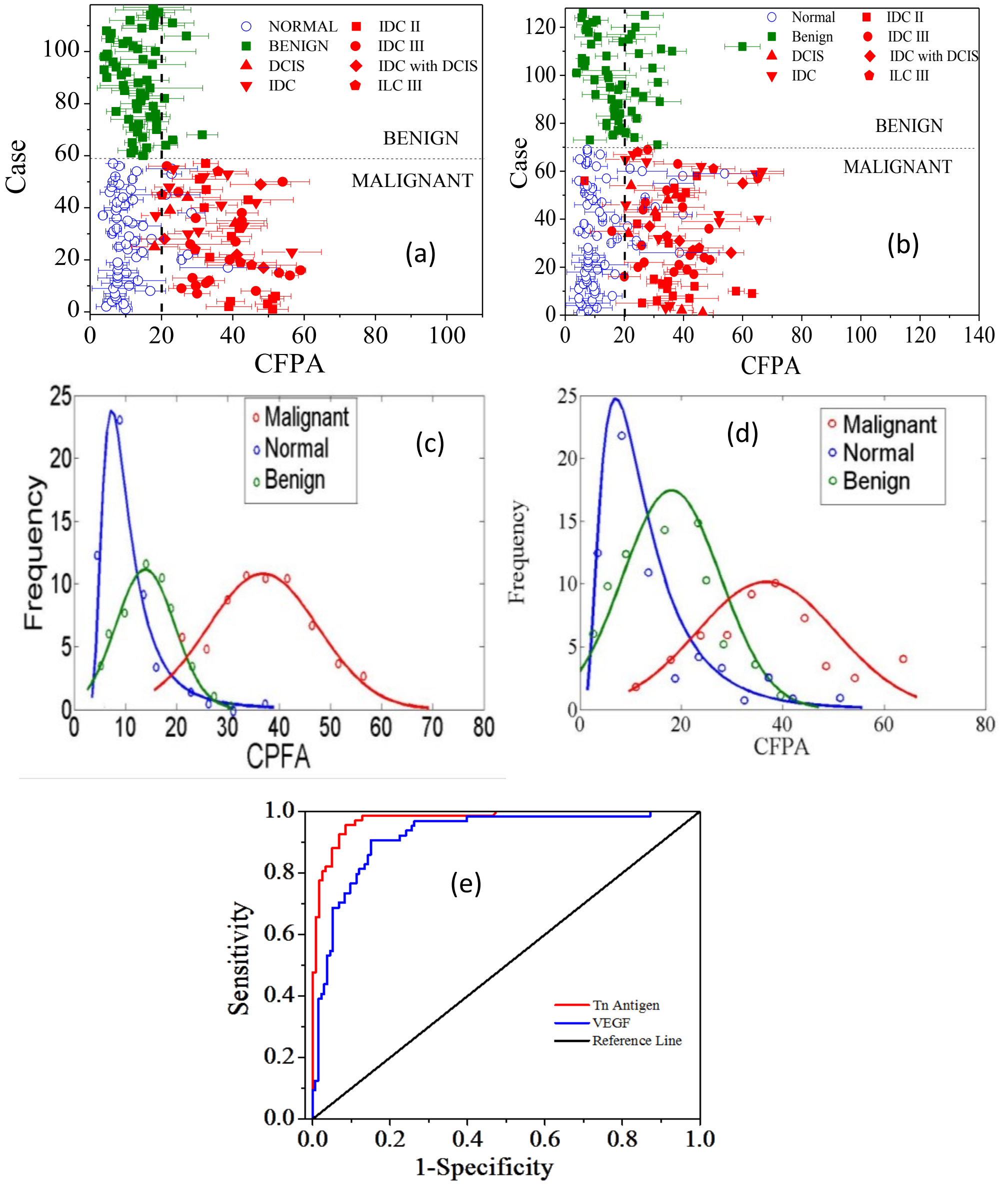

Figure 5.5: (a) Fluorescent Intensity of AQD-stained sections of 115 cases for Tn antigen expression; (b) Fluorescent Intensity of AQD-stained sections of 115 cases for VEGF expression; (c) Tn antigen frequency distribution; (d) VEGF frequency distribution. Open circles are distribution histograms with solid lines as fitted curves; (e) ROC curve of cancer detection using Tn antigen as marker. Area under ROC curve is 0.976 (95% CI 0.956 – 0.995) for Tn anigen and 0.92 for VEGF (95% CI 0.878-0.966).

The sensitivity and specificity of the HRP-stained slides were analyzed similarly except that the malignant prediction of each core was based on the pathologist's judgment of the staining instead of the quantitative analysis for the AQD-based staining shown above. A sensitivity-versus-(1-specificity) receiver operating characteristic (ROC) curve is shown in Figure 5.5f. The area under ROC curve represents the accuracy of the malignancy decision using the AQD staining. An area of 1 represents a perfect prediction. In this study, the area under the ROC curves of AQD staining was 0.97 and VEGF was 0.92. This indicates that the AQD-based Tn antigen staining is a good tool for breast cancer detection and better than the well-know VEGF.

The sensitivity and specificity of AQD Tn antigen staining and those of HRP-based Tn antigen staining for breast cancer are summarized in Table 2. As can be seen, AQD-based staining resulted in 95% sensitivity and 90% specificity whereas HRP-based staining resulted in 90% sensitivity 80% specificity, indicating that AQD-based staining provided better sensitivity and specificity than HRP-based staining using the same Tn antigen as the marker to detect breast cancer. In addition, the 95% sensitivity obtained by the AQD staining was also better than the 90% sensitivity and 77% specificity obtained by Springer earlier[201].

Table 2 : Comparison of the sensitivity and specificity of (a) AQD staining and (b) HRP staining of Tn antigen and VEGF for detecting breast cancer.

	Tn Antigen		VEGF	
(a)	Pathologic Malignant	Pathologic Benign	Pathologic Malignant	Pathologic Benign
AQD-IF positive	55	6	52	12
AQD-IF negative	3	51	6	45
Total Cases	58	57	58	57
Sensitivity	**95%**		**90%**	
Specificity	**90%**		**78%**	

	Tn Antigen		VEGF	
(b)	Pathologic Malignant	Pathologic Benign	Pathologic Malignant	Pathologic Benign
HRP IHC positive	52	11	50	17
HRP IHC negative	6	46	8	40
Total Cases	58	57	58	57
Sensitivity	**90%**		**86%**	
Specificity	**80%**		**71%**	

Since Tn antigen expression showed a higher sensitivity and specificity than VEGF, Tn antigen is studied more closely. In Table 3, we summarize the CFPA and percentage of cells stained by the AQD-Tn antigen staining in various types of breast cancers including DCIS, IDC and ILC, in normal breast tissues including normal breast tissues from the cancer cases and benign breast conditions without pathological changes, and benign breast conditions with pathological changes. As can be seen, regardless of the tumor type and stage, all malignant breast tumors showed a high CFPA (>20) and a high percentage (>90%) of cells stained by Tn antigen, indicating that Tn antigen was indeed a very good marker for all breast cancer.

Table 3: CFPA and percentage of cells stained by AQD-anti-Tn in various types of breast cancer tissues (including DCIS, IDC, and ILC), normal breast tissues (including both the normal tissues of malignant cases and benign conditions with no pathological changes), and benign breast conditions with pathological changes.

	Cancer Type	# cases	CFPA	% of cells stained by AQD-Tn antibody
DCIS	Ductal	4	18 - 41	95 ± 5%
IDC	IDC with DCIS Stage I Stage II Stage III	4 11 14 19	21 - 48 28 - 57 31 - 52 22 - 59	92 ± 2% 98 ± 3% 91± 6% 90 ± 3%
ILC	Stage II Stage III	1 4	31 20-45	95 ± 2% 91 ± 3%
Normal		74	6 - 18	3 ± 5%
Benign changes	Stromal Fibrosis	11	7 -18	5 ± 3%
	Fibroadenoma	7	13 - 23	20 ± 10%
	Hyperplasia without atypia	10	7 - 23	10 ± 12%
	Apocrine metaplasia	5	13 - 17	3 ± 4%
	Adenomyepithelioma	1	13	4 ± 3%
	Papiloma intraductal	2	16 - 18	6 ± 2%
	Ductal ectasia	4	4 - 13	5 ± 4%
	Acute inflammation	1	7	0
	Sclerosing adenosis	1	18	7 ± 2%

We want to look further into the Tn expression pattern according to breast cancer characteristics such as cancer type, stage and grade. Figure 5.6 shows examples of different cancer stages stained by AQD-IF method and their corresponding HRP IHC staining H&E images. For DCIS, cytoplasmic staining could be observed in most of the cases although the staining intensity varied greatly between the cases. Granular aggregations were observed in some of the cases. There was one case of high grade DCIS. Although the fluorescent intensity signal was slightly lower, the expression was fairly uniform and mostly on the membrane of the cells. We also included one case of malignant myoepithelioma, which is a rare case of breast cancer. Strong fluorescent intensity (>40) could be observed with AQD-IF staining (Figure 5.6), which was consistent with the results from HRP-IHC staining

For IDC, AQD-stained intensity varied widely depending on the stage of tumor development. Stage I and II (Figure 5.4a) showed strong homogenous intensity within the same case with more than 90% of the cells expressed Tn antigen. Also, the majority of the cells showed intense fluorescent signal was not uniform within the same tumor. Similar staining pattern was observed for ILC although the fluorescent intensity level was similar for both stage II and III (Figure 5.6a). The fluorescent signal was uniformly distributed throughout the tumor areas. Each cancer case had one adjacent normal tissue. The majority of these normal tissues showed no positive reaction. However, weak signals could be observed in some of the cases, indicating the rapid across-tissue penetration of cancer cells[202]. Tn antigen expression was not depended on cancer type or stage.

From previous studies, the expression of Tn antigen was shown to vary with cancer stages. The percentage of cancer cells expressing Tn antigen is the lowest for DCIS/LCIS (20-50%) and for IDC stage III (40-60%). However, using AQD probes, we found that Tn antigen was expressed in most of the cancer cells (>90%) and was independent to the cancer stages. This could be understood as follows. Most of the previous studies used the conventional IHC method to detect the expression of Tn antigen. IHC “posistive” and “negative” are depended on the skill of the interpreter, which could vary from reader to reader. In contrast, the AQD method was quantitative and had little interference from tissue autofluorescence. As a result, the AQD method could detect Tn antigen expression more sensitively and specifically, thus leading to more accurate assessment of the percentage of cancer cells expressing Tn.

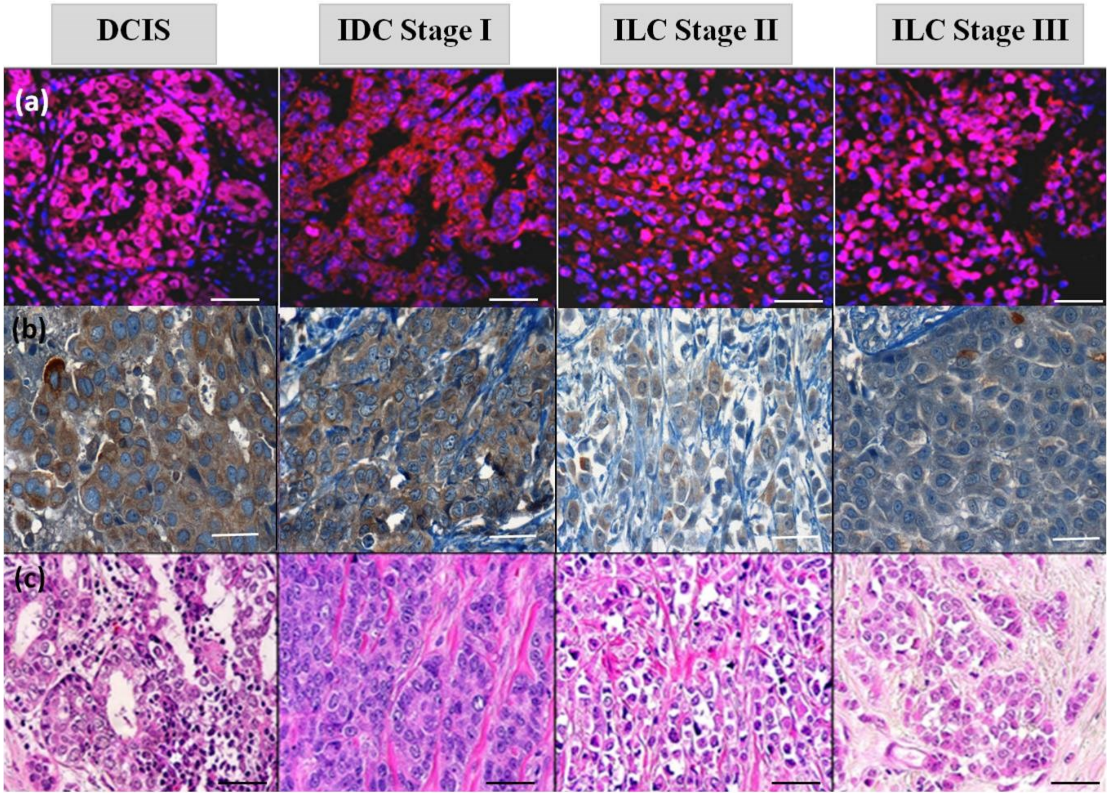

Figure 5.6. (a) AQD-IF staining of Tn antigen according to cancer stage, (b) HRP IHC staining of Tn antigen according to cancer stage; (c) H&E staining of the same sections. Tn antigen expression level does not depend on cancer stage. Scale bars: 200 μm

Figure 5.7 shows the Tn expression in various grades of breast cancer and their corresponding H&E images). Since grade information was not always identified on pathology report for older cases, we were only able to gather 10 cases that had grade information out of 58 malignant cases. Tn antigen expression was at the lowest level for grade I and the expression increased as the cancer grade increased to grade 2 and 3. These results indicate that Tn antigen expression could be correlated with the aggressiveness of the tumor, which was in agreement with the finding of Springer et al[170]. Although the number of cases was small, this result showed promising information about Tn antigen expression and cancer grade. Correlation of quantitative expression of Tn antigen to the aggressiveness of the cancer, may be useful for therapeutic treatment for breast cancer patient. In fact, since the AQD-IF method can examine the expression of Tn antigen or any other markers quantitatively; it can be a useful clinical tool to aid the treatment strategy of breast cancer.

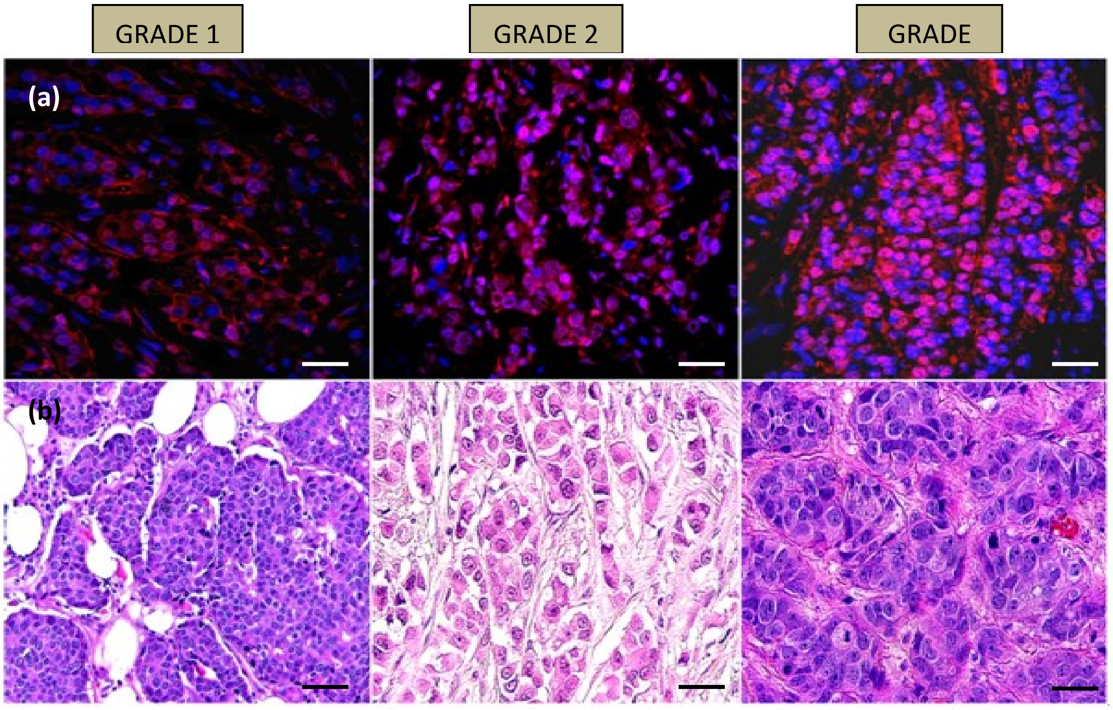

Figure 5.7. (a) AQD-IF staining of Tn antigen according to cancer grade; (b) H&E staining of the same sections. Tn antigen expression level does not depend on cancer stage. Scale bars: 200 µm

Figure 5.8a showed the summary of CFPA for Tn expression signal according to cancer stages for all 58 malignant cases. ANOVA test was computed with a p-value of 0.76 confirming that Tn antigen expression was independent to cancer stages. Similar data was analyzed for cancer grades even though only 10 cases were analyzed (Figure 5.8b). A p-value of 0.04 indicates that Tn antigen had some correlation to the cancer grade. More data is needed to confirm this point.

As can be seen from the CFPA and the percentage of cells expressing Tn antigen, there are very few cells exhibiting Tn antigen expressions in the normal tissues from cancer patients and the 15 benign conditions without pathological changes. Among the 42 cases of benign tissues with pathological changes, most did not show Tn antigen staining. However, 2 out of 7 fibroadenoma and 1 sclerosing adenosis showed high CFPA throughout the cytoplasm in >80% of the cells by both AQD and HRP-IHC staining. In contrast to an earlier study [202], AQD staining did not show significant fluorescent signal above background level for the majority of benign cases.

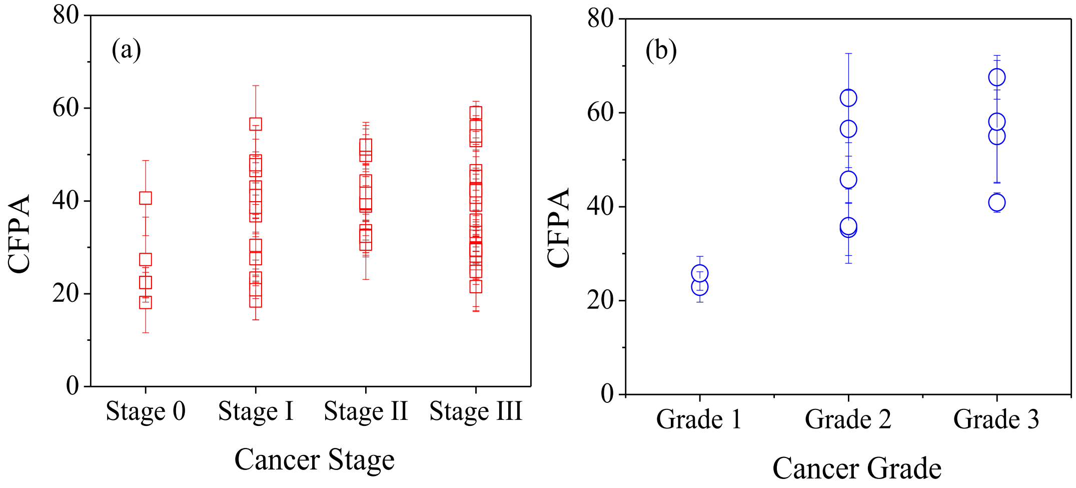

Figure 5.8. (a) CFPA of AQD-stained sections of 58 cases for Tn antigen expression according to cancer stages, p value = 0.76 ; (b) Tn antigen expression according to cancer grades, p value = 0.04. A total of 10 cases with different cancer stages were included.

Although there wasn't enough data to have a definite conclusion on the role of Tn antigen and cancer grades, we had conducted a small study on various breast cancer cell lines with known aggressiveness for Tn antigen expression. BT474, MCF-7, SK-BR-3, and MDA-MB-231 were chosen to test for Tn antigen expression with the aggressiveness increasing accordingly to the order. Figure 5.9 showed the Tn antigen expression of these breast cancer cell lines. MDA-10A is a normal breast cell line. Neutrophill like cells were used as negative control and extracted Tn antigen was used as positive control. As the figure showed, normal breast cell line didn't express Tn antigen whereas all the breast cancer cell lines showed positive signal. However, the expression level of Tn antigen was correlated to the aggressiveness of the cells. As the result, MDA-MB-231 expressed Tn antigen strongest since it's the most aggressive cell line. The MDA-MB-231 cell line express epidermal growth factor (EGF) and transforming growth factor alpha (TGF-α). Due to its aggressiveness, MDA-MB-231 is a popular cell line for xenografting by forming solid tumor in relatively short period of time (2-3 weeks)[203, 204]. In addition, with all the other breast cancer cell lines expressed Tn antigen, it's an important feature to study treatment for triple negative cases using Tn antigen as a biomarker.

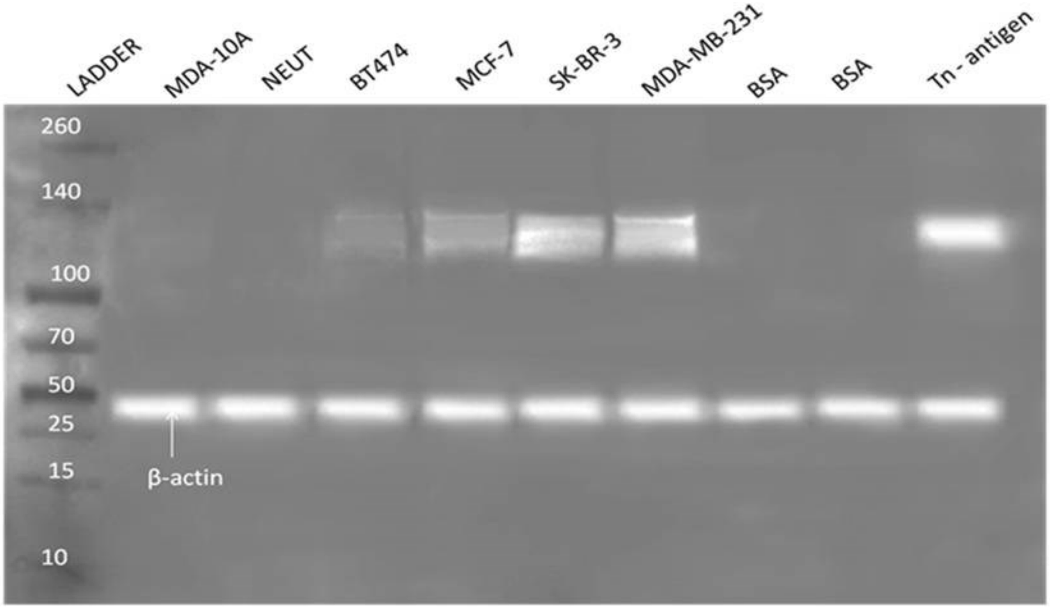

Figure 5.9: Tn antigen expression in multiple human breast cancer cell lines using Western Blot

It is of interest to note that on a macroscopic scale, the fluorescent image of the AQD staining could also be easily seen by unaided human eyes. As an example, the fluorescent image of a slide containing an entire AQD-stained array when placed under a UV lamp that could be easily seen by naked eyes and captured by a consumer camera is shown in Figure 5.10a where each core was 2 mm in size. An H&E stained slide of the same tissue array is shown in Figure 5.10b. As can be seen in Figure 5.10a, only the malignant cores were visible in the fluorescent image. The yellow circles indicate the normal cores that were invisible in the fluorescent image. There were some missing cores (white circles) which were lost during the sectioning of the block. The fact that malignant cores were easy to observe without any magnification and that there was no observable loss of signal during a continuous light exposure indicate that AQDs were an excellent fluorescent label and that Tn antigen was a specific and sensitive marker to distinguish breast cancer from normal breast tissues.

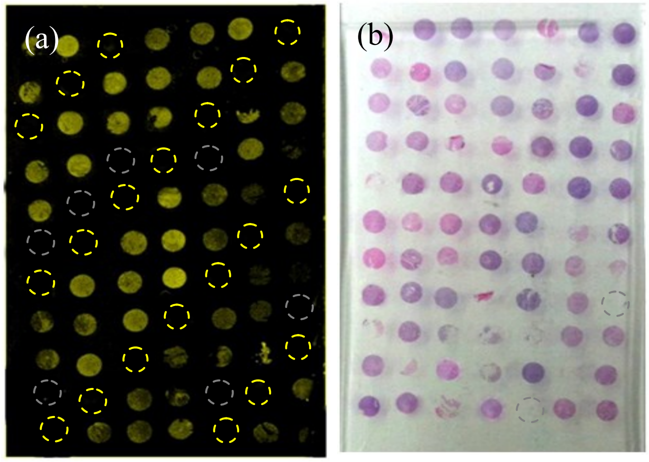

Figure 5.10. Entire TMA consists of cores from 19 cancer cases. (a) TMA under UV light; (b) H&E stained section. Cancer cores showed fluorescent signal that could be detected with naked eyes while benign cores didn’t show visible signal. Yellow-dotted circles are benign cores. Gray circles are missing core due to cutting of the section.

Immunostaining is an integral part of pathological analysis for diagnostic and therapeutic decisions and monitoring [205, 206]. Immunostaining is used to visualize cellular or tissue constituents (antigens) based on antigen-antibody interactions. Two main staining methods in immunostaining are immunohistochemical (IHC) staining which uses an enzyme such as horse radish peroxidase (HRP) to react with its "substrate" to produce a colored substance to show the molecules of interest and immunofluorescence (IF) which uses fluorescent molecules to "light up" the molecules of interest. HRP-labeled antibodies are widely used in pathological examination due to the stability and durability of the staining over a long period of time. However, the extent of the expression of the bio-markers often requires semi-quantitative evaluation. Many factors can affect the assessment including different scoring systems, amount of chemicals, etc. Determination of whether a tissue is "positive" or "negative" often depends on the experience and skill of the interpreter, possibly leading to inaccurate results. Since the late 1980s, computerized image analysis systems have been introduced and shown to be a more accurate means to quantify the image. However, the non-linear relationship that occurs at higher levels between the amount of the antigen and the absorption intensity of diaminobenzidine (DAB) which is used as a chromogen in HRP-IHC[205, 207] can result in inaccurate interpretations. It remains a challenge to quantify HRP-IHC accurately. Recent approaches have explored the use of IF-based methods and fluorescent microscopy to better quantify protein expression in tissues[208, 209]. Conventional organic fluorescent dyes have several limitations such as small Stokes shifts resulting in reduced detection sensitivity and difficulty in distinguishing the positive signal from the autofluorescence in formalin-fixed-and-paraffin-embedded tissues[210]. Moreover, photoinstability is a major drawback for conventional dyes since the signal can photobleach which makes it impossible to view the same region repeatedly[211].

Compared to the quantitative analysis of the AQD-staining as discussed above, the analyses of HRP-IHC-stained sections relies on visual scoring[205] of "high", "moderate" or "weak" staining. It was often difficult to distinguish the true signal from the background signal. Although there have been many scoring systems introduced such as the Allred score,[212] IHC interpretation still depends on the experience and skill of the interpreter. A study in Germany involved 172 pathologists assessed estrogen receptor staining resulted in 24% false-negative assessment [213]. The analysis of AQD-stained sections was quantitative and did not require visual scoring by a highly trained pathologist.

Various factors have been reported to be associated with an increased risk of local recurrence after breast conserving surgery (BCS); however, the most important factor is a positive margin. The entire surgical margin of the lumpectomy specimen needs to be examined intra-operatively if re-excision is to be avoided. Some of the techniques employed for this evaluation have included frozen section analysis, imprint cytology and gross examination combined with radiologic evaluation. None of these approaches are ideal, either being technically difficult or difficult in differentiation of neoplastic from benign tissue in addition to being time consuming. In most hospitals, surgical margins are processed after marking with ink, sectioning, and overnight processing similar to other tissues. To properly examine the margins, all surgical margins need to be sectioned and submitted in entirety for histopathological examination. Sometimes, these results in more than 100 sections from the surgical margins of one lumpectomy specimen and slides are available for the microscopic examination next day. In this scenario, if the surgical margin is positive, the patient will need repeat surgery for re-excision.

As demonstrated by the results above, the AQD staining method is sensitive and specific. For the future, we foresee that the AQD-based imaging can play significant role in pathology. For BCS, if the lumpectomy specimen can be evaluated by AQD technique for detection of tumor at the surgical margin the surgeon can immediately excise additional tissue if the margin is positive and prevent repeat surgery for the patient. If the margin is negative, the Pathology department may elect to take a few random samples from the surgical margin or none may be needed after gaining some experience and confidence with this new technique utilizing intraoperative margin assessment with AQD method. This will result in tremendous reduction in expense and the time required for microscopic examination of surgical margins as well as decreasing the rate of reexcision in cases of BCS. Besides the potential use associated with BCS, the AQD staining method may be useful in other types of specimens to help identify areas to concentrate on for sectioning margins, speed up detection of cancer in frozen section type biopsies, and facilitate the screening of large amounts of tissue.

In conclusion, the use of CdSe AQDs each conjugated to three streptavidin as a fluorescent label to image Tn antigen expression in various breast tissues via a sandwich staining procedure, where the primary monoclonal anti-Tn antibody was bound to the Tn antigen on the tissue, a biotin-labeled secondary antibody was bound to the primary anti-Tn antibody, and finally the streptavidin conjugated AQDs were bound to the biotin on the secondary antibody, was examined. We have evaluated the AQD staining of Tn antigen on tissue microarrays of a total of 395 cores from 115 cases including various breast cancer cores, normal tissues cores from breast cancer patients and benign breast tumor cores and compared to HRP-based staining of the same tissues. We showed that AQD-Tn antigen staining stained >90% of breast cancer cells but not cells in the normal breast tissues and benign breast tumors. The AQD-Tn antigen staining exhibited 95% sensitivity and 90% specificity which were better than the 90% sensitivity and 80% specificity exhibited by the HRP-based staining using the same antibodies on the same tissues as well as other fluorescent imaging of Tn antigen of breast cancer reported in the literature. We also showed that CFPA of Tn antigen could be correlated with tumor grade (consistent with the previous report that Tn antigen was associated with tumor aggressiveness, invasion, and spreading) but definitely independent of tumor stage and type. In addition to better sensitivity and specificity, AQD-based imaging is also quantitative with a well-defined cutoff as compared to the qualitative visual determination of the conventional IHC staining method.

5.7 PHOTOSTABILITY OF SA-AQD PROBES

Immunofluorescent staining is a well-studied technique and widely used in the biomedical research field. However, currently available organic fluorescent dyes such as Alexa Fluor dyes and cyanine dyes will photobleach rapidly and irreversibly under high-intensity illumination, rendering them unsuitable for many clinical applications. QD-based immunostaining method is resistant to photobleaching with much longer life time than conventional organic dyes. In this study, we also examined the durability of the AQD-stained slides. All slides were stored in the refrigerator (4°C) and wrapped in an aluminum foil. The slides were periodically examined for the average CFPA. As an example, the fluorescent images of a slide right after staining, 6 months and 10 months later are shown in Figures 5.11a-5.11c, respectively. As can be seen, even after 10 months, the fluorescent image was still almost as good as that obtained right after staining. In Figure 8d, we have plotted the average CPFA versus storage time of 7 slides that had been stored for the longest time. As can be seen, even after 10 months of storage and periodic examinations under strong light, the average CFPA still retained >90% of CFPA after 6 months and no further change up to 10 months. Such durability indicates the potential of AQD-based staining for molecular pathological applications. Furthermore, unlike organic dyes, protection from light was not necessary during laboratory processes, further making it an ideal tool for biomarker study during pathological examination.

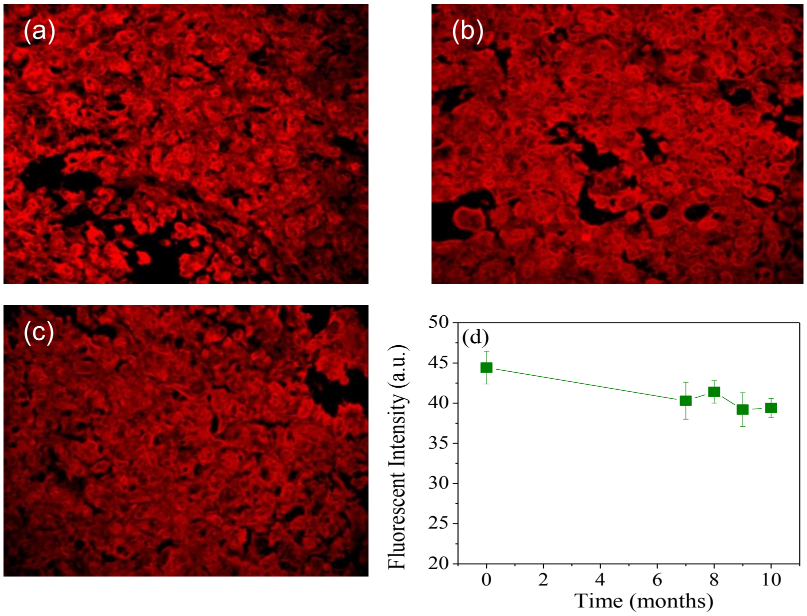

Figure 5.11. Stability of AQD-probe for imaging Tn antigen expression in breast cancer tissue. (a) Image was taken right after staining procedure; (b) image was taken after 6-month storage (4ºC); (c) image was taken after 10-month storage (4ºC); (d) quantitative fluorescent intensity signal over different periods of time.

5.8 CdPbS AQD CONJUGATED ANTI-Tn ANTIGEN ON TMAS

CdSe AQD-SA probes have shown to be a good quantitative method to detecting Tn antigen and VEGF expression in tissues. However, this approach requires long staining period with multiple steps. The probes cannot be used directly for breast cancer margin assessment. WE have shown that AQDs are capable to be conjugated to antibody directly with multiple AQDs per mAb so that the signal is amplified without the amplification steps such as streptavidin-biotin binding. In this study, we used NIR CdPbS AQDs as the labeling probes and conjugated directly to anti-Tn antibody. We also performed AQD-IF staining on the same TMAs as in CdSe AQDs and compared the sensitivity and specificity of the AQD-mAb probe with the AQD-SA probe.

The TMAs slides were prepared as described in section 5.6 before exposing to the NIR AQD-mAb probes. Following paraffin removal, hydration and antigen retrieval in sodium citrate (pH = 6, Thermo Scientific, NJ) at 95°C for 20 min, the sections were blocked for 1 hour with 10% normal goat serum (Vector Laboratories, Burlingame, CA, USA) in 0.1% Tween Tris buffer saline (TBS); washed in TBS for 3 times, 5 minutes each. The slides were then incubated with NIR AQD-mAb probes for 1 hour at room temperature. Next, they were washed with TBS 3 times for 5 minutes each and counterstained and mounted with DAPI mounting medium (Vector Laboratories, Burlingame, CA, USA).

Examples of the AQD-IF staining of a ductal carcinomas Stage 0-3 are shown in Figure 5.12. As can be seen, NIR AQD-mAb IF staining and showed intense signal of Tn antigen in the cytoplasm and the cell membrane of all the stages. There were 42 cases of benign breast tissues with pathological changes. Most of these benign changes exhibited no Tn antigen staining as well using the NIR AQD-mAb probes. There were 15 cases of benign breast tissues with no pathological changes. These cases were considered as normal tissues. There was no positive signal in AQD IF staining for these cases.

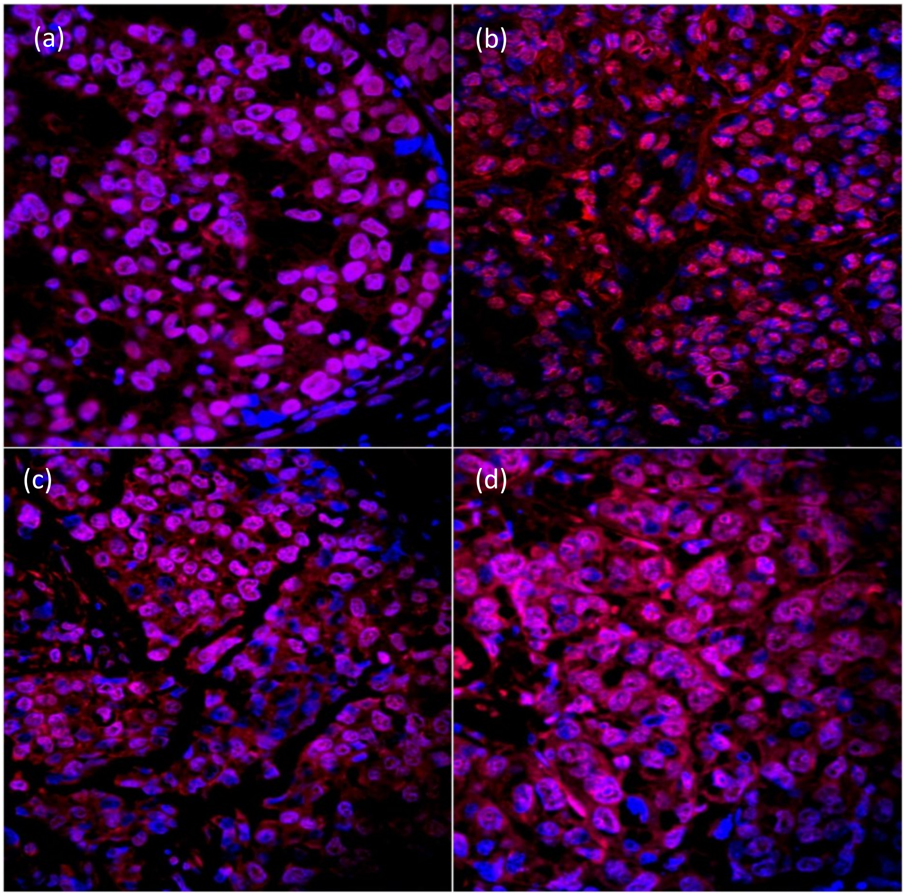

Figure 5.12: NIR AQD-IF staining of Tn antigen expression in ductal carcinomas (a) DCIS; (b) IDC Stage I; (c) IDC Stage II; (d) IDC Stage III. All the stages showed intense fluorescent signal for Tn antigen expression

Figure 5.13 summarizes the average fluorescent intensity per unit area (CFPA) of the tumor region for each of the 115 cases (full symbols for various malignant tumors and stars for benign conditions) and those of the normal regions (open circles) of the malignant cases. Each dot represents one case. As can be seen in Figure 5.13a, the CFPA for the normal tissues of the malignant cases (including all breast cancer types: DCIS, IDC and ILC) were mostly below 20 whereas the CFPA of the malignant tumors were mostly above 20. The CFPAs of most of the benign lesions were also below 20, which are similar to those of the normal tissues of the malignant cases. This supports the conclusion that NIR AQD-mAb is as sensitive and specific as the AQD-SA probes.

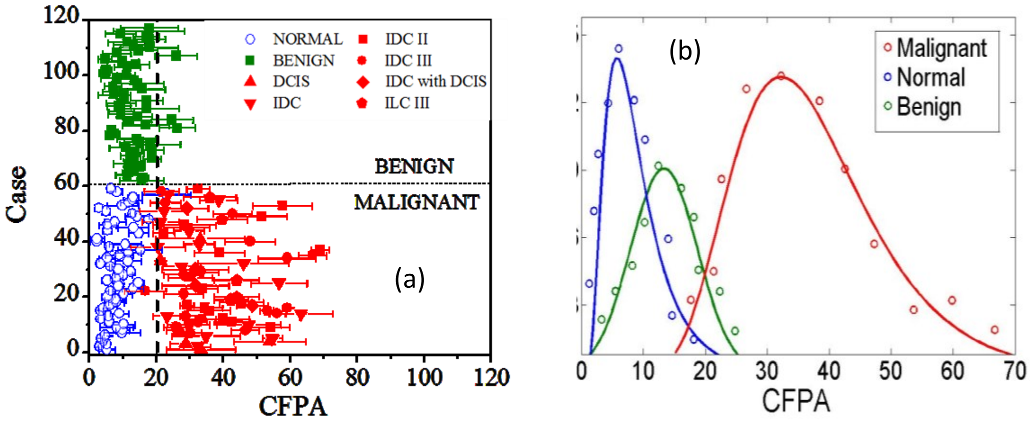

Figure 5.13: Quantification of Tn-antigen in IF staining for 115 cases. (a)Tn-antigen average fluorescent signals; (b)Frequency distribution of Tn antigen. From the distribution, the overlap between normal and cancer is around 20. Open circles are distribution histograms with fitted curves as solid lines.

Based on the results shown in Figures 5.13a, we obtained histograms of the CFPA of malignant tumors, benign tumors and the normal tissues. After fitting the histograms with a lognormal distribution using MATLAB, the fitted distribution of the CFPA of the malignant tumors (red), that for the normal tissues (blue), and that for the benign lesions (green) based on AQD staining are shown in Figure 5.13b. As can be seen, the CFPA distribution for the malignant tumors overlaps with those of the normal tissues and the benign lesions near a CFPA= 20. Indeed, a threshold CFPA of 20 could separate malignant tumors from normal tissues . A prediction regarding the malignancy of the tissue was then made using this threshold. Similarly, using this threshold to compare the benign tumor to normal tissues. The sensitivity and specificity were 95% and 96%, respectively which even better than the CdSe AQD-SA probes. In addition, a clear separation between the malignant and normal tissues could be observed in the case of the NIR AQDs. The result indicates that the direct NIR AQD-mAb probe can be a promising probe to use in real time margin detection since there is no difference in the signal strength compared to the indirect immunofluorescent staining method with signal amplification.

CHAPTER 6: DIRECT BREAST CANCER MARGIN EVALUATION USING ANIMAL TUMOR MODEL and HUMAN EXCISED BREAST SPECIMENS

The recent development of nanomaterials has provided considerable improvement in specificity and sensitivity for tumor imaging by using targeted contrasting agents [103, 214]. Quantum dots (QDs) are semiconductor nanoparticles that have unique photoluminescent capabilities. They exhibit a high fluorescence efficiency, are resistant to photobleaching[38] and comparable to green fluorescent protein (GFP) in size [39]. By changing particle's size, the emission spectra can be tunable which allows simultaneously imaging of different markers at the same pathological sites [40]. Bioimaging applications of QDs include cell labeling and tracking [41, 42, 99], cell proliferation [43], sentinel lymph node mapping [44], brain imaging [45], molecular beacons for DNA detection [46-48] and *in vivo* tumor detection [49, 50]. For specific target imaging, QDs can be coupled with antibody to detect biomarker on cell's surface. QDs can be used as labeling agents in immunofluroescence-based assay.

From previous chapters, AQDs had been successfully conjugated to streptatividin and monoclonal anibodies. The CdSe AQD-SA and CdPbS-mAb probes were used to quantify the expression of Tn antigen in human breast cancer tissues in chapter 5. The sensitivity and specificity of Tn antigen in cancer cells were 95% and 90%, respectively.

The purpose of this aim is to demonstrate the use of a molecular probe consisting of a monoclonal antibody of Tn antigen coupled with CdSe AQDs or CdPbS AQDs to image margin status of human cancers grown in nude mice and human excised specimens. This approach is molecularly specific, rapid, and not affected by tissue heterogeneity, which sets it apart from all other technologies that are available or being developed.

6.1 ANIMAL TUMOR MODEL

It is well known that incomplete removal of a tumor is a major factor that compromises the long term survival rate of cancer patients. This study presents the first demonstration of molecular imaging for intraoperative ex vivo tumor margin assessment. By providing a quantitative threshold level, AQD-Tn mAb probe provides surgeons the ability to evaluate margin status in real-time, potentially reducing the number of positive margins found postoperatively, and thus reducing the need for the second operation and risk of local recurrence. AQD-Tn mAb effectively identified cancer areas that could be missed by the current gross visual examination. Furthermore, AQD-Tn mAb bound specifically to the cancer cells and not adipocytes and stromal cells as verified by histopathology.

6.1.1 Development of Tumor Model in Nude Mice

In this study, we used HT29 colon cancer cell as our tumor model instead of a breast cancer cell line. HT29 cells expressed Tn antigen strongly without any need of transfection to express the protein, as verified by Western blot. Because this was a proof of concept study, we wanted to ensure that our tumors express the marker strongly so that we could control over the methodology development. The HT29 cells were obtained from the American Type Culture Collection as it is the best characterized Tn antigen expression in solid tumor that is easily available and reproducible. The HT29 cell line is a colorectal adenocarcinoma which secretes carcinoembryonic antigen (CEA), transforming growth factor beta binding protein and mucin with high level of Tn anigen. Under standard growth conditions, the cells form a multilayer of non-polarized cells that display an undifferentiated phenotype [215]. Therefore, the HT-29 cells are aggressive. They form solid tumor in a short amount of time (2-3 weeks). HT29 cells were maintained in McCoy's 5A medium supplemented with 10% fetal bovine serum (Bioexpress, Kaysville, UT) and 1% penicillin and streptomycin (Mediatech Inc., Manassas, VA) and cultured at 37°C in a 5% CO_2 incubator.

The cells were harvested by trypsinizing a confluent T-150 cell culture flask. Viability was verified to be greater than 95% using trypan blue (Amresco, Solon, OH). The cells were resuspended at 10^6 cells per 10 μL of PBS, mixed 1:1 with Matrigel (BD Biosciences, San Jose, CA). The 10 μL of prepared mixtures were injected subcutaneously in eight-week-old female nude mice having an average weight of 20 g. The tumors were allowed to grow for three weeks to reach the suitable size for study.

A total of 12 nude mice were used in the experiments. One mouse was used as a negative control without any cancer cell injection. Three weeks after injections, the mice were euthanized. Sharp dissection was used to excise the tumors with a small amount of the surrounding muscles still attached to the tumors. The tumors were round and regular in shape with unifocal characteristics on macroscopic appearance. The fresh tumors were immediately processed *ex vivo* with the staining procedure as described below, imaged and analyzed with IVIS imaging system (Lumina XR, Caliper, CA). First, the entire tumor's surface was washed with TBS then emerged in 1% bovine serum albumin solution (BSA) for non-specific blocking for 10 minutes. Next, the tumor was removed from BSA solution and washed with TBS to remove BSA residue. The tumor was then immersed in AQD-Tn mAb solution for Tn-antigen staining of cancer cells . The prepareation of AQD- Tn mAb probes was describe in chapter 4.3.1 Finally, the tumor was washed again with TBS. The tumor was placed inside of IVIS for acquiring images. Each image acquisition would take about 30 seconds to complete.

6.1.2 Minimizing Tissue Autofluorescence

Autofluorescence has always been a challenge for fluorescent imaging especially in tissue with high adipose content such as breast and liver. Normal tissues are known to emit autofluorescent signal that ranges from 380 nm to 550 nm under UV light excitation (350 – 400 nm) [30, 106]. Here, we tried to establish a clear cut-off threshold to separate the background autofluorescence signal and the positive signal. Livers, muscles and kidneys were used as normal tissue (negative controls) to evaluate the background threshold (Figure 6.2). At emission wavelength 509 nm, autofluorescent signal could be observed in liver (Figure 6.2b). Although other tissues did not show positive signal in the images, there were still background signals when the analysis was performed. With the emission at 610 nm, the background signals were reduced in all of the tissues especially livers (30% reduction) compared to emission at 509 nm (Figure 6.2d). A fluorescent intensity threshold of 400×10^6 could be used as the cut-off to separate normal mouse tissues since all the tissues autofluorescence background was below this level.

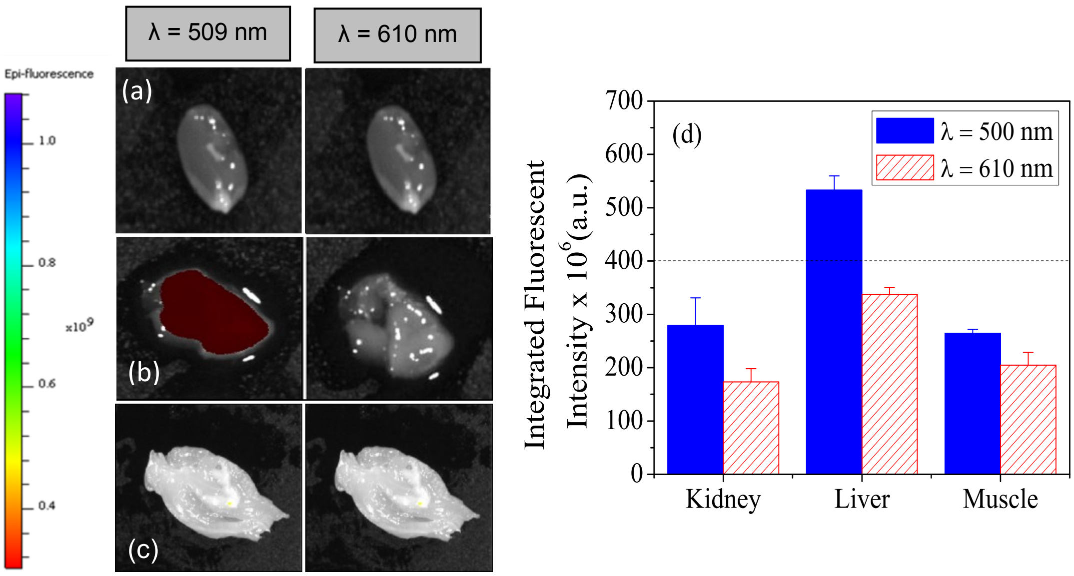

Figure 6.1.Background signal from normal tissues when excited at 460 nm. There were 2 emission cut-off wavelengths:509 nm and 610 nm. (a) Kidney; (b) liver; (c) muscle; (d) integrated fluorescent intensity depended on the emission cut-off wavelength. Dash-line indicates background signal.

Tissue autofluorescence is a serious background noise issue in any fluorescent imaging and can lead to false positives. Many biomolecules exhibits endogenous fluorescence including amino acids, structural proteins and lipids. Their emission maxima range between 280 nm to 550 nm [106]. For epithelial tissues such as breast, the concentration of endogenous fluorophores can be substantial between the surface epithelium and the underlying stroma to result in strong autofluorescence in adipose tissue and the stroma. In this study, the CdSe AQDs were imaged with a 610 nm emission filter due to the constraint of the imaging system. However, the CdSe AQDs probe can be viewed with a 700 nm long-pass emission filter, which will allow the signal of the AQDs further separated from tissue autofluorescence, with a higher signal to noise ratio and make the AQD-Tn mAb probe even more sensitive and specific in the future. Meanwhile, unlike fluorophores, AQDs can undergo constant light exposure with minimal photobleach, which often leads to loss of signal. AQDs allow convenience in handling the probe without the need of a dark room.

6.1.3 Protocol Development

The total staining process of AQD-Tn mAb probe to evaluating excised tumor margin is summarized in Figure 6.3. First, lumpectomy specimen is removed from patient and oriented with sutures. The tumor is washed with TBS and then blocked with 1% BSA solution. Next, the tumor is removed from BSA solution, washed with TBS and immersed in AQD-Tn mAb probe suspensions for staining. Finally, the tumor is washed again with TBS and imaged on each side with correct orientation.

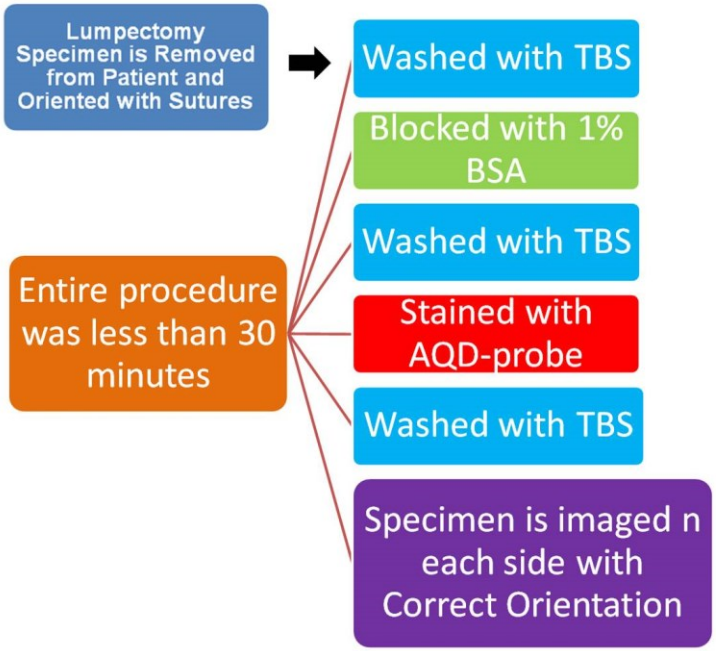

Figure 6.2. The proposedprocess of margin determination using AQD-Tn mAb probe

There are two major steps that affect the sensitivity and specificity of AQD-Tn mAb probe: blocking time and staining time. First, blocking time was investigated. To find the optimal blocking time, fresh livers were washed with TBS for 2 min twice and then immersed in 1% bovine serum albumin (BSA) for various amounts of time. After washing in TBS three times, the livers were stained with AQD-Tn mAb complex for 1 hour at room temperature. The livers were suspended in 1% BSA solution by thin wire to maximize surface exposure. The blocking solution was stirred continuously to help the diffusion of BSA onto the tissue's surface. The livers were then washed again with TBS and imaged. After the optimal blocking time was identified, staining time was evaluated to develop the optimal margin assessing procedure for the whole tumor. Different time periods were examined and it was narrowed down to 15 minutes as the sufficient blocking time. Smaller time intervals were studied to further shorten the blocking time. As shown in Figure 6.4a, no BSA blocking resulted in strong non-specific binding of the QD-mAb probe on liver's surface both dorsal and ventral sides. As the blocking time increased, non-specific binding decreased and reached the saturated point at 10 minutes. The integrated intensity was similar between 10 minute and 15 minute blocking (Figures 6.4c and 6.4d). This was also at the same level as a control liver without AQD-Tn mAb probe exposure. Therefore, 10 minutes blocking should be sufficient to prevent non-specific binding.

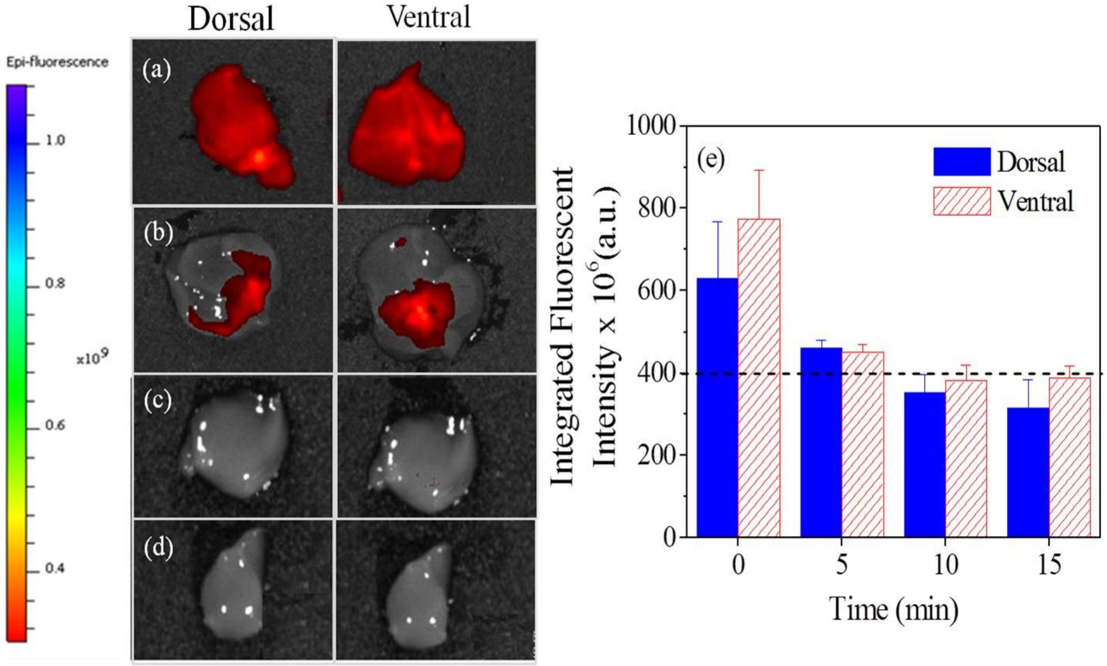

Figure 6.3. Blocking study for non-specific staining using liver. (a) no blocking – 0 min; (b) 5 min blocking; (c) 10 min blocking; (d) 15 min blocking; (e) quantification of the integrated fluorescent intensity versus time. Dash-line indicates acceptable background signal.

Total margin evaluation time is one of the most critical requirements for intraoperative margin status determination. FSA has been reported to have good sensitivity and specificity to cancer cells but has difficulties in performing frozen sections on adipose tissue results in increasing surgery time and cost due to additional pathology evaluation [26]. The most significant disadvantage of FSA is the inability to evaluate the entire surface area with sampling rate of 10-15% surface area. Using antibody-antigen binding mechanism, the AQD-Tn mAb probe was able to stain and identify cancer areas quantitatively in less than 30 minutes to prevent the prolonged anesthesia period for patients.

6.1.4 Simulation of Intraoperative Margin Assessment

As previously mentioned, although livers and kidneys showed no positive signal, they still had some background intensity around 400×10^6. Thus, this was the cut-off level to differentiate between cancer and normal mouse tissue. Optimal staining time was 15 minutes (data not shown). The excised tumors were divided into 3 different regions: a tumor region, a muscle region, and an overlap between tumor and muscle or margin region. Comparing the fluorescent image with the bright field image, we could see that bright dark to turquoise blue-region (region 1 in Figures 6.5a and 6.5b) correlated with the tumor and gray region correlated with the muscle (region 3). The tumors were clearly identified by the AQD-Tn mAb probe. AQD probe was also specific to the tumor and not the muscle as evidenced by the unstained muscle area. Region 2 was more ambiguous based on the image in Figure 6.5a and 6.5b. In the dorsal view (Figure 6.5a), the color map showed that region 2 was red corresponding to integrated fluorescent intensity of less than 400×10^6 (Figure 6.5c). This indicated the region to be free of cancer cells. Meanwhile, the ventral bright field image looked like muscle area whereas the fluorescent image indicated the presence of cancer cells with quantitative fluorescent intensity value of 503×10^6(p/s/cm^2/sr)/(µW/cm^2), indicating the method was sensitive and specific to detect small non-palpable lesions. The red color in the images could be interpreted as negative region (integrated fluorescent intensity less than 400×10^6(p/s/cm^2/sr)/(µW/cm^2).

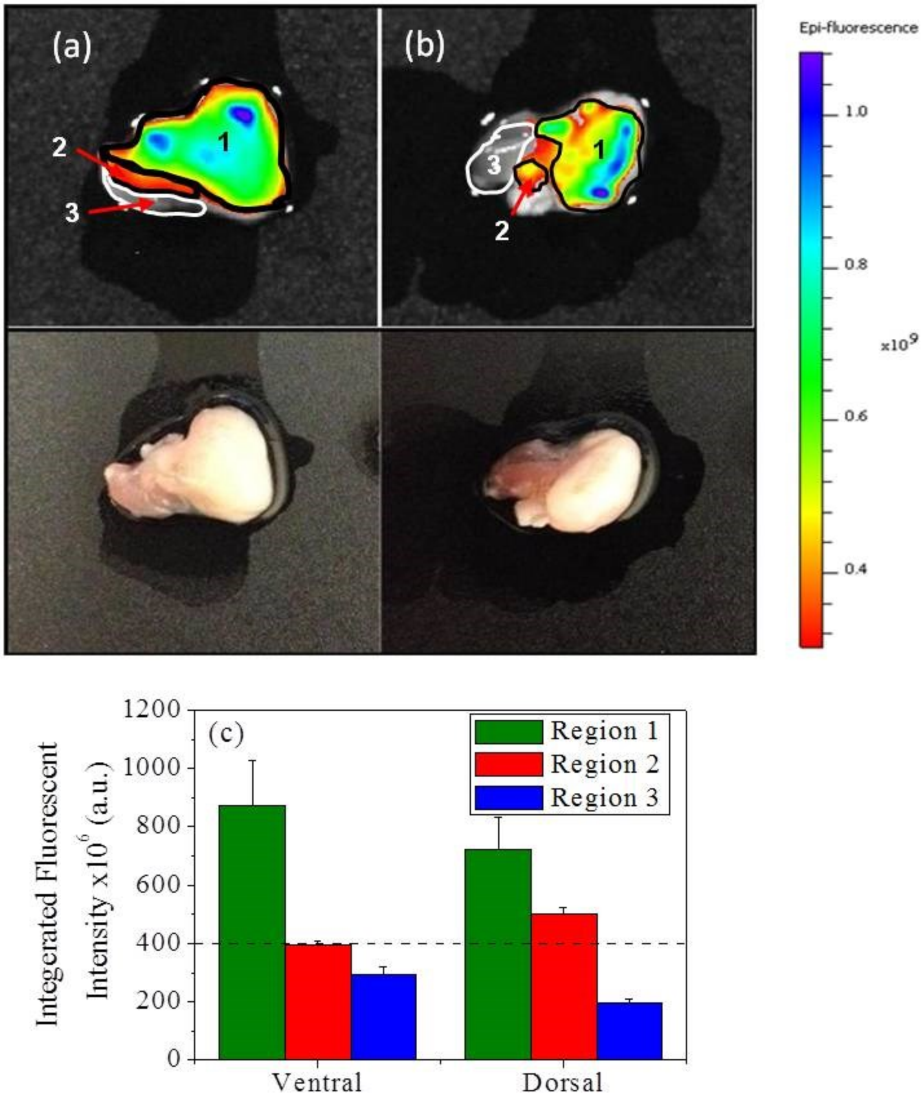

Figure 6.4. Animal tumor imaging. Top panel: fluorescent imaging using IVIS system. Bottom panel: bright field images of the same tumor. Two orientations of the tumor were imaged (a) ventral side; (b) dorsal side; (c) The integrated fluorescent intensity was quantified using IVIS software for 3 regions of the tumor. Dash-line indicates the cut-off betweennormal and cancer areas.

To further confirm the presence or absence of cancer cells in region 2 of both dorsal and ventral sides, the tumor was embedded in paraffin and examined using the H&E-stained sections of these regions. Figure 6.6 showed the areas in the square boxes of the tumor, with each region separated by the red line. For the dorsal side, the square box contained all three regions – tumor, interface and muscle.

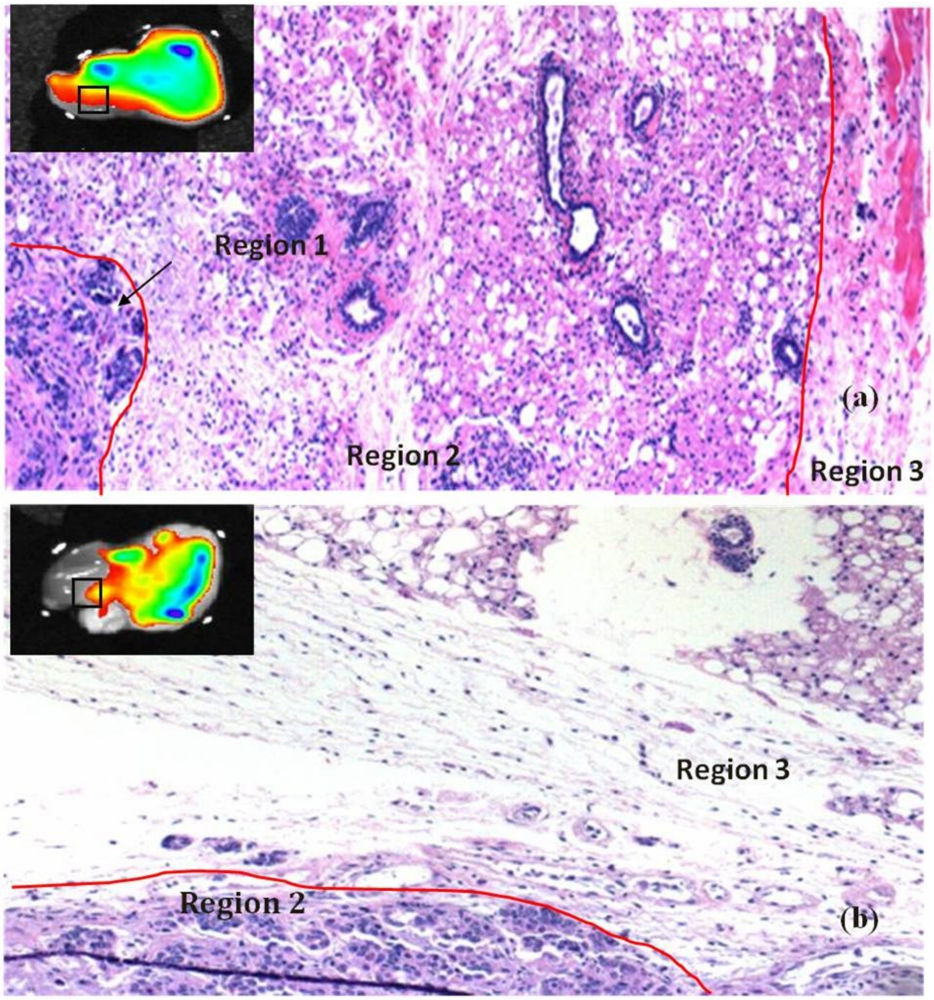

Figure 6.5. H&E stained sections correlated to the regions (square box) of the examined tumor. (a) Dorsal side; (b) Ventral side. Cancer cells presence was absent in region 2 of the dorsal side. Cancer cells were detected in dorsal side by AQD-Tn mAb probe and confirmed by H&E stained section.

Meanwhile, the square box in the ventral side consisted of only region 2 and region 3 due to larger area of region 2 to be included in the image. Clearly, dorsal region 2 (Figure 6.6a) contained only inflammatory and fibroblasts cells, which correlated to the red color in the whole tumor examination indicating negative signal. The presence of cancer cells were observed in H&E section of ventral region 2 (Figure 6.6b), which confirmed the above positive assessment. The results suggested that this method was sensitive and specific to identify cancer cells in areas that could have been missed by gross examination during tumor removal process. By applying the quantitative analysis of AQD-Tn mAb probe signal, normal and cancer regions could be distinguished in real-time.

All sides of the tumor are evaluated which give the surgeon the exact location of cancer area. Furthermore, no additional intraoperative pathological evaluation is needed to decide whether an area contains cancer cells or not. Manipulations of the surgical specimen have no impact on the microscopic examination of the operative specimen as shown in the interference study is another advantage of this method. The specimen can undergo normal histologic examinations for further margin confirmation and other necessary markers evaluations.

6.1.5 Whole Mouse Imaging

One tumor was left inside a mouse. The mouse was euthanized and the entire peritoneum was opened to expose the tumor and internal organs on the ventral side. On the dorsal side, the tumor was left underneath the skin. However, since the skin around the shoulder blade was removed and exposing the abdomen, the AQD-Tn mAb probe could get to the tumor even if it was covered with skin. Although the cancer cells were injected subcutaneously on the back of the mouse, the tumor invaded through the ventral side. There was little to no muscle on the tumor’s surface. The whole animal was immersed in blocking solution and then AQD-Tn mAb probe suspensions. All the internal organs (such as lung, liver, kidney, etc.) and the tumor were exposed to the probe. This experiment was done to demonstrate the specificity and sensitivity of the probe when the tumor was surrounded by many normal tissues. The total staining procedure was 25 minutes. The mouse was then washed with TBS and imaged with the IVIS system.

Figure 6.7 shows the dorsal and ventral pictures of the mouse. The tumor was exposed at the ventral side and underneath the skin at the dorsal side. We found that AQD-Tn mAb probe resulted in the ability to visualize areas of tumors that were not apparent with white light because the appearance of the tumor was not easily distinguished from the other tissues with good fluorescence contrast, indicating highly specific tumor targeting of AQD-Tn mAb probe. The positive signal was strong enough to identify the outline of the tumor surface (fluorescence was much greater than 400×10^6(p/s/cm^2/sr)/(μW/cm^2). All the other organs showed no positive signal confirmed the specificity and sensitivity of the AQD-Tn mAb probe.

AQD-Tn mAb probe was capable of staining the whole tumor inside the mouse body locally once the tumor surface was exposed. Although there was positive signal of tumor underneath the skin at the dorsal side, the skin was relatively thin (less than 1 mm). With the depth of 2 mm (consider negative margin), no signal could be observed due to the penetration depth of 610 nm wavelength. Therefore, it minimized the risk of fault positive margin predication. We will examine this aspect in our future studies. The tumor imaging inside the mouse further indicated that AQD-Tn mAb probe was very sensitive and specific to cancer cells only. This can potentially be developed as a tool to examine the cavity after tumor is removed for additional information about the margin.

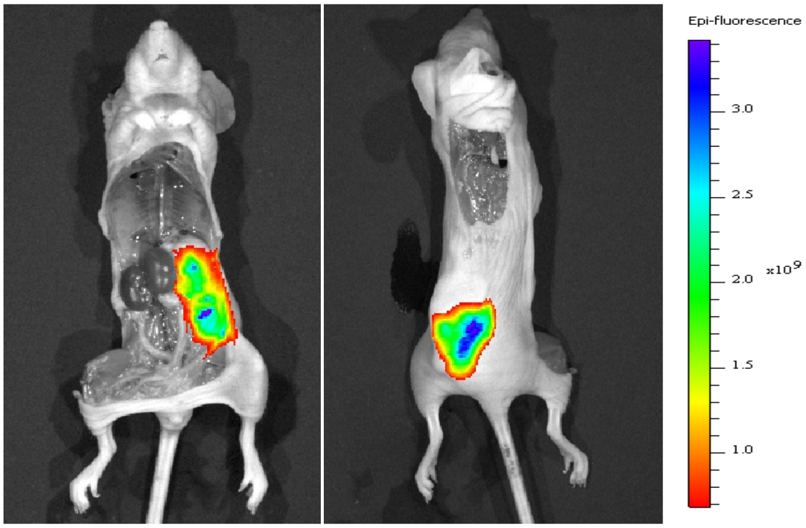

Figure 6.6. Whole mouse tumor imaging. (a) ventral site where the tumor was exposed. (b) dorsal site, tumor was underneath the skin. Other organs had negative signal, indicating AQD-Tn mAb prove was specific and sensitive to the tumor.

6.1.6 Interference of the AQD probes on Microscopic Examination of the Operative Specimen

To examine the potential interference of the method with standard pathological procedures, we studied 10 tumor bearing nude mice. Each mouse had one control tumor and an average of two AQD-treated tumors. A total of 17 AQD-treated tumors and 10 control tumors were evaluated. The AQDs-treated tumors were stained with the AQDs-probe as described in section 6.1.1. The control tumors were untreated by AQDs-probe. Both the AQDs-treated and the control tumors were submitted to the pathological department for the same regular pathological examination. Both the AQDs-treated tumors and the control tumors were fixed in 10% formaline for 12 hours and then embedded in paraffin. The blocks were cut into 5 µm sections at the surfaces of the specimens where the AQDs-treated tumors were stained by the AQDs-probe. Both sets of sections (control and treated) were stained with H&E and immunohistochemistry (IHC) stained for 8 different markers: Tn antigen, VEGF, MSH6, MLH1, PMS2, p27, p53 and ki67. Interpretation was performed using Aperio ScanScope XT IHC Image Analysis algorithms (FDA-cleared *in-vitro* Diagnostic) and light microscopy (Olympus BX50) in the carcinoma component.

Using multiple routine evaluated markers, we found that there was no difference between the H&E staining of an AQDs-stained tumor and that of a control tumor. There was also no difference between the IHC staining of the various markers: Tn antigen, VEGF, MSH6, MLH1, PMS2, p27, p53 and ki67 on an AQDs-treated tumor and that of the various markers on a control tumor. As examples, Figure 6.8 showed the H&E staining and IHC staining of ki67, p53 and Tn antigen of a control tumor (Figure 6.8a) and those of an AQD-treated tumor (Figure 6.8b). As can be seen, there was no difference between the H&E staining of the control tumor and that of an AQDs-treated tumor nor was there a difference between the IHC staining of ki67, p53, and Tn antigen of a control tumor and of an AQDs-strained tumor.

Furthermore, quantitative grades of ki67 expression were 38.2 ± 5.2% in the control tumors and 31 ± 6.4% in AQD-treated tumors. For p53 expression, the quantitative grades were 38.6 ± 3% and 41.5±3.7% in the control tumors and AQD-treated tumors respectively. This result clearly indicates that the AQDs-based assessment method would not interfere with the standard histological examinations of the surgical specimens.

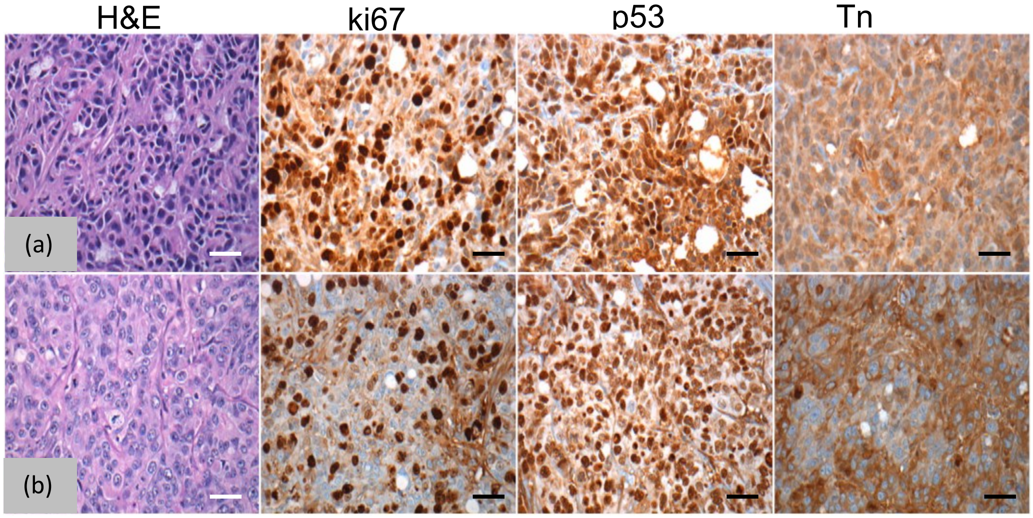

Figure 6.7. Interference examination of AQD- Tn mAb probe on standard pathological evaluations. (a) Control tumors; (b) AQD-treated tumors. Different markers were evaluated such as Tn antigen, p53, and ki67. No interference with the following pathological examination was found. Scale bar: 100 μm.

No additional intraoperative pathological evaluation is needed to decide whether an area contains cancer cells or not. Manipulations of the surgical specimen have no impact on the microscopic examination of the operative specimen as shown in the interference study is another advantage of this method. The specimen can undergo normal histologic examinations for further margin confirmation and other necessary markers evaluations.

6.1.7 Tumor Staining using OQD-Tn mAb probes

Commercial OQDs have been introduced heavily as fluorescent probes for molecular imaging the last five years due to their narrow emission spectrum and high photostability. However, the OQDs are inefficient to conjugate with other biomolecules, in which a large amount of protein or antibody is required for a successful coupling. As described in section in chapter 4, the conjugation efficiency of OQDs to protein such as streptatividin and antibody are 6% and 0.03% respectively. In this study, we tested the performance of OQD-Tn mAb probes on *ex vivo* tumor staining for margin evaluation and compared to the AQD-Tn mAb probes. Two ratios were used for this evaluation OQD/mAb = 80 and 100 according to the previous study described in chapter 4.3.3.

The tumors were xenograted subcutaneously with HT29 colon cancer cells, which express Tn antigen strongly. The tumors were harvested after 3 weeks of injection. The fresh tumors were immediately processed *ex vivo* with the staining procedure as described below, imaged and analyzed with IVIS imaging system (Lumina XR, Caliper, CA). First, the entire tumor's surface was washed with TBS then emerged in 1% bovine serum albumin solution (BSA) for non-specific blocking for 10 minutes. Next, the tumor was removed from BSA solution and washed with TBS to remove BSA residue. The tumor was then immersed in AQD-Tn mAb and OQD-Tn mAb solutions for Tn-antigen staining of cancer cells at different time periods (10 minutes, 20 minutes and 30 minutes). Finally, the tumor was washed again with TBS. The tumor was placed inside of FluorChem E (Protein Simple) for acquiring images. Each image acquisition would take about 30 seconds to complete. Figure 6.9 showed the fluorescent signal from the tumor staining with both AQD and OQD probes. Both the dorsal and ventral sides of the tumors were imaged. AQD-Tn mAb probes were used a positive control sample. Figure 6.9e summarized the integrated fluorescent intensity versus staining time for each ratio. To achieve the similar staining result as AQD-Tn mAb probe (AQD/mAb = 7/1 ratio), the ratio of OQD to mAb had to be 1/100 as showed in Figure 66c and 66d. To achieve the same intensity level, it would take up to 30 minutes for the OQD/mAb = 1/80 ratio compare. There was no difference in fluorescent staining intensity as staining time was increased from 10 minutes to 30 minutes for OQD/Ab = 1/100 indicates that the probe had saturated the tumor. It is possible to use OQDs as contrasting agents for margin assessment method. However, due to the large amount of antibody need (100 times more than AQDs), it is not practical to use OQDs as labeling agent for this molecular imaging method.

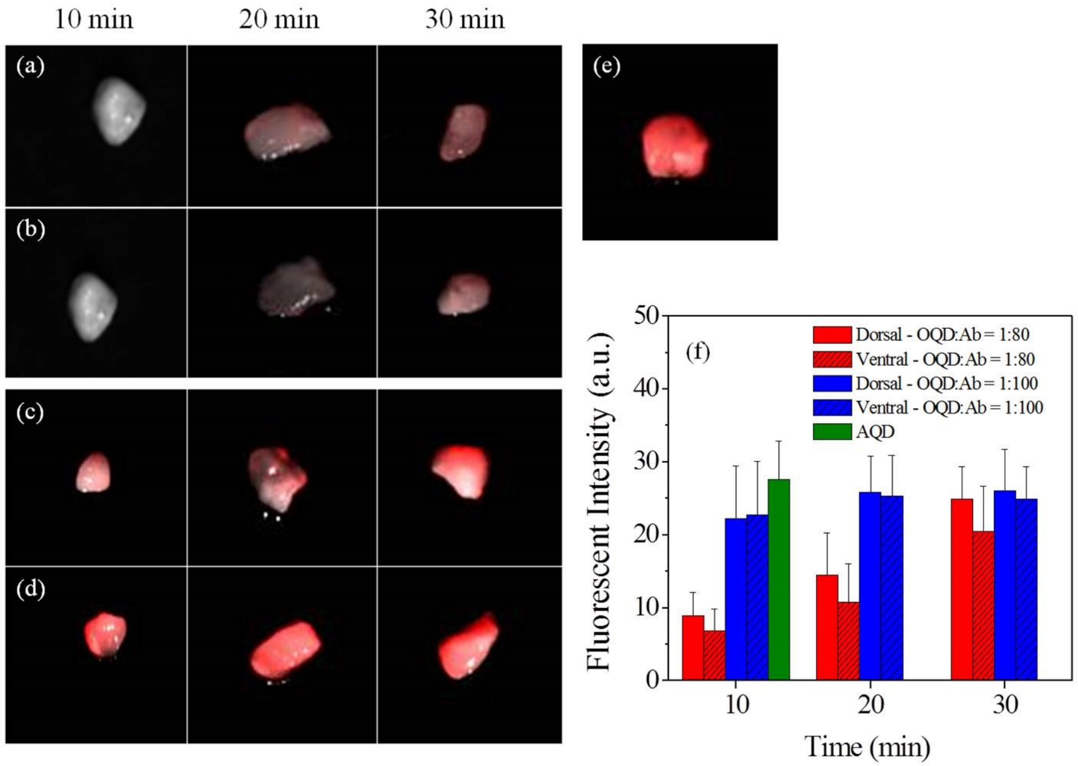

Figure 6.8: OQD-Ab probes staining of mouse tumor versus staining time. (a) Dorsal view OQD:Ab = 1:80; (b) Ventral view OQD:Ab = 1:80; (c) Dorsal view OQD:Ab = 1:100; (d) Ventral view OQD:Ab = 1:100; (e) AQD-mAb probe staining for 10 min (AQD/Ab = 7); (f) Fluorescent intensity quantification.

6.2 BREAST CANCER MARGIN EVALUATION ON HUMAN EXCISED SPECIMENS

From the data collected during the animal study, the AQD-Tn mAb probes demonstrated high sensitivity and specificity as well as a staining procedure of less than 30 minutes. The probe is ready to be tested on clinical human lumpectomy specimens.

6.2.1 Clinical Protocol

An *ex vivo* study using AQD-Tn mAb molecular probes to evaluate lumpectomy specimens in patients undergoing surgery for breast malignancies was approved by the

Institutional Review Board at Drexel University College of Medicine (Protocol #1209001546). Informed consent was obtained from eligible patients undergoing a lumpectomy. The surgeries were performed on 11 patients by Dr. Ari Brooks at Hahnemann University Hospital. The imaging study was performed post excision and did not alter the standard operating procedures. The study goal was to establish a threshold level to separate positive and negative margin.

In each lumpectomy case, the surgeon removed the specimen, then placed sutures to orient the specimen for pathological assessment. The specimens were immediately undergoing the staining procedure for margin evaluation with AQD-mAb probes. First, the entire tumor's surface was washed with TBS then emerged in 1% bovine serum albumin solution (BSA) for non-specific blocking for 10 minutes. Next, the tumor was removed from BSA solution and washed with TBS to remove BSA residue. The tumor was placed inside of IVIS for acquiring images to serve as negative control signal. The tumor was then immersed in AQD-Tn mAb solution for Tn-antigen staining of cancer cells at 37°C for 10 minutes. Finally, the tumor was washed again with TBS. The tumor was placed inside of IVIS for acquiring images of all the six orientations according to the sutures. Each image acquisition would take about 30 seconds to complete. In case of palpable tumors, a core biopsy was taken in the middle of the tumor from the sample specimen to serve as a positive control. The core biopsy was then snapped frozen in liquid nitrogen, embedded in optimal cutting temperature (OCT) medium (Tissue-Tek, Sakura, Torrance, CA), and cut into 5 μm section. The section was stained with H&E to verify the presence of cancer cells in the core biopsy.

After the evaluation, the specimens were submitted to pathology for standard pathological examination. The pathological assessment consists of the pathologic status of the entire imaged margin (close, positive or negative) within the six inked corners as well as the type of residual carcinoma found at the margin, if any, was recorded. Cancer within 2 mm of the inked margin is considered “close” margin has the same therapeutic implication as a positive margin. Re-excision of the margin is usually required. If there was no residual carcinoma within 2 mm of the inked margin, the margin was determined as “negative”. The pathology reports were used as the confirmation for the margin prediction using AQD-mAb probes.

6.2.2 Margin evaluation using AQD-Tn mAb molecular probes

There were a total of 11 patients that were that were evaluated using CdPbS AQD-mAb probes as prepared using the protocol outlined in Sec.6.1.1. Figure 6.10 shows an example of a positive margin case (case 5) that was predicted by AQD imaging and later confirmed by pathological report. Six orientations were imaged: anterior, posterior, superior, inferior, lateral and medial. Comparing the fluorescent image with the bright field image, we could see that bright turquoise blue to red-region correlated with the tumor and the gray region correlated with the normal tissue. For this particular case, the posterior and inferior margins were positive for lobular carcinomas stage III according to the pathology report. AQD image also showed that posterior and inferior margins were positive.

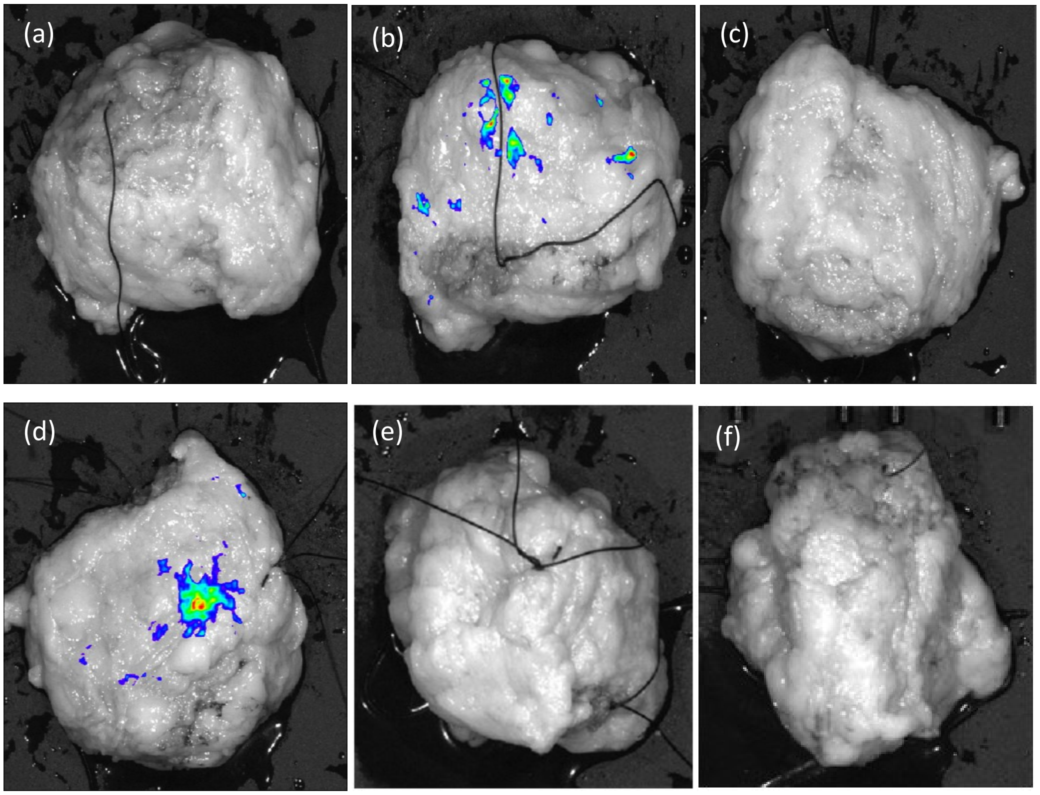

Figure 6.9. Case 5 – Positive excised lumpectomy specimen stained with CdPbS-Tn antigen probes. (a) Superior; (b) Inferior; (c) Anterior; (d) Posterior; (e) Lateral; (f) Medial margin.

The color map showed that the positive regions were $8.24 \times 10^8 \pm 3.12 \times 10^7$(p/s/cm^2/sr)/(μW/cm^2) and $9.79 \times 10^6 \pm 1.3 \times 10^7$ (p/s/cm^2/sr)/(μW/cm^2) for posterior and inferior margins respectively. The core biopsy positive control for this case was $10.5 \times 10^8 \pm 2.67 \times 10^7$(p/s/cm^2/sr)/(μW/cm^2). Clearly, the positive signal form the margins were very close to the positive control. The negative margins all have the signal around 5×10^8 (p/s/cm^2/sr)/(μW/cm^2) level which was similar to the negative control signal ($4.72 \times 10^8 \pm 7.17 \times 10^7$(p/s/cm^2/sr)/(μW/cm^2)). This level was higher than the threshold level in the animal study, which was around 4×10^8 (p/s/cm^2/sr)/(μW/cm^2), probably due to the higher content of adipose tissue and collagen in the breast tissue.

To further validate the presence of cancer cells in the positive control core biopsy, the sample was examined with H&E stained sections. Figure 6.11 showed the area in the square box of core biopsy 1 and the entire area of core biopsy 2. The presence of cancer cells were observed in the H&E sections, which confirmed the above positive assessment of the method. The result suggested that the a positive control using the core biopsy of the same tumor is reliable.

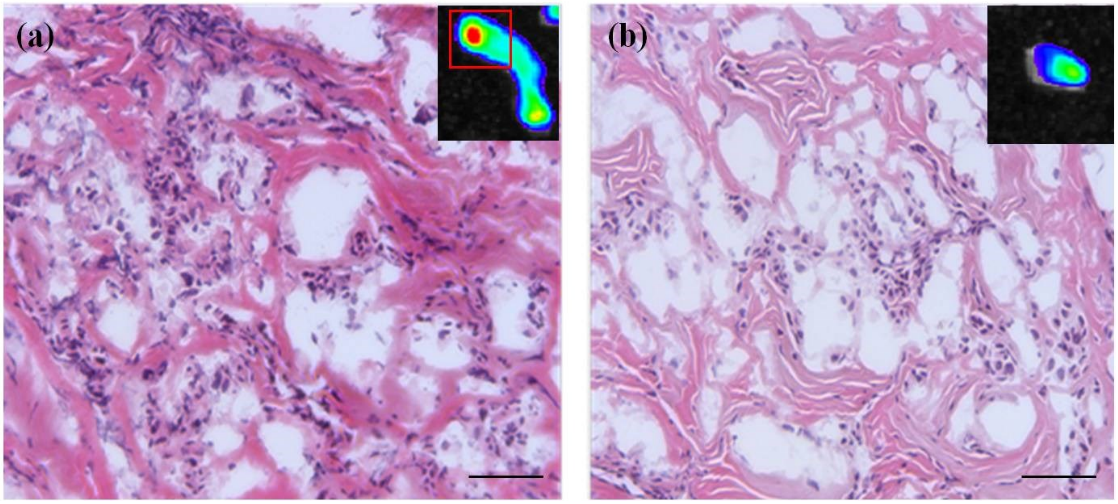

Figure 6.10: H&E stained sections correlated to the positive control core biopsy of the examined tumor (case 5). (a) core 1, the H&E image correlated to the square box region of the core biopsy; (b) core 2 of the sample tumor. Cancer cells were detected in both of the cores (purple nuclei). Scale bar: 200 µM.

Another example for positive signal was from a re-excision case (case 10), where the patient had two positive margins from previous excision: superior and inferior margins. The specimen underwent the same staining procedure as described above for AQD evaluation. Two separate specimens were obtained for this case. The superior re-excision was labeled case 10a and the inferior re-excision was labeled 10b. Figure 6.12 showed both the superior and inferior re-excisions. The left column is superior margin. The right column is inferior margin. Because these specimens are relatively small (8x4x2 cm^3), one image can capture three margins at the same time. In the future, a designed specimen holder may be needed to define the margin boundary from each orientation to ensure the accuracy of prediction and correlate it with pathology report.

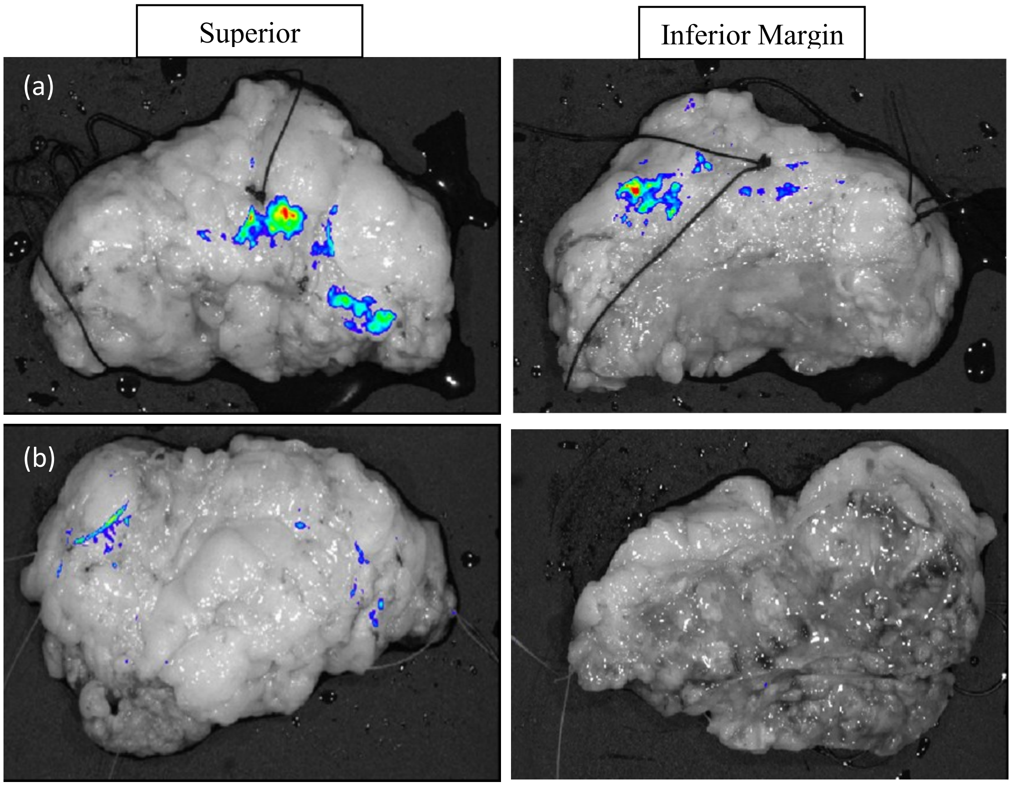

Figure 6.11: Case 10 –re-excised lumpectomy specimen stained with CdPbS-Tn mAb probes. (a) Superior re-excision (positive margin) (10a); (b) Inferior re-excision (close margin) (10b); Left column: superior margin, Right column: Inferior margin.

Since the case was a re-excision, it was expected that the old superior margin (or new inferior margin) and the old inferior margin (or new superior margin) to be positive. The results showed indeed these two margins were positive from the AQD evaluation Since the old interior margin was a close margin, the area of exposed cancer cells was smaller compared to the old superior margin, which was a positive margin. The new inferior margin for case 10b was negative, which was confirmed by pathologic examination. The new superior margin for case 10a, however, was positive in AQD evaluation, which was in conflict with the pathological assessment. According to the pathology report, the new superior margin was free from residue carcinomas but had atypical ductal hyperplasia (ADH), a benign breast condition. Multiple studies have reported that women with ADH are at increased risk of developing breast cancer in the future[216-219]. From our own study with TMAs, Tn antigen express strongly for the cases with ADH. Although the result for the case 10a contradicted with the pathology report, it is consistent with our earlier data on ADH. It would be of interest to continue monitoring this patient or any future patients with the same conditions for developing breast cancer.

Figure 6.13a summarized the average fluorescent intensity per unit area of the positive and negative regions from each margin of the 11 cases. There was still not a clear cut for a positive and negative threshold. The background signal was also varied from one case to another. However, the majority of negative signal was at the 5×10^8 $(p/s/cm^2/sr)/(\mu W/cm^2)$ level. The true positive margins had the significant stronger signal than the other negative margin.

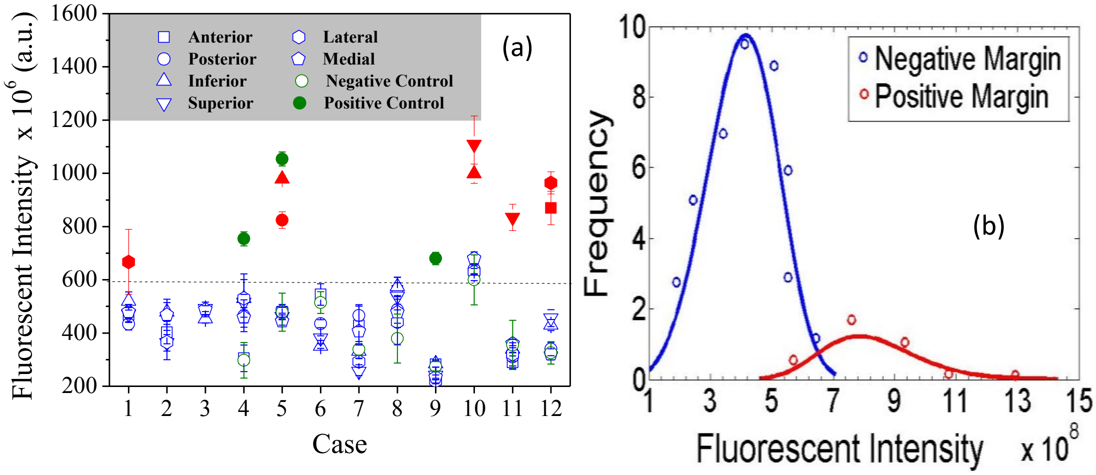

Figure 6.12: (a) Summary of fluorescent signal of 11 lumpectomy cases, solid symbols: positive margins, open symbols: negative margins ; (b) Frequency distribution of 11 cases with *p* value = 0.000391 (confident level = 95%, α = 0.05). The positive margins are statistically different than the negative values. Open symbols are histograms of the distribution and solid lines are the fitted-curves.

Based on the results shown in Figures 6.13a, we obtained histograms of the fluorescent intensity of positive and negative margins. After fitting the histograms with a lognormal distribution using MATLAB, the fitted distribution of the fluorescent intensity of the positive margins (red), and that for the negative margins (blue) based on AQD staining are shown in Figure 6.13b. As can be seen, the intensity distribution for the negative margins overlaps with those of the positive margins a intensity= $5.7\text{x}10^8(\text{p/s/cm}^2/\text{sr})/(\mu\text{W/cm}^2)$. Indeed, this threshold could separate positive and negative margins with p value of 0.000391. A prediction regarding the positive margin could be made using this threshold. However, the data set is too small right now to have a definite conclusion. More data is needed for the study.

6.2.3 Interference study on core biopsy samples

To examine the potential interference of the method with standard pathological procedures, we studied 6 cases of core biopsy samples. The core biopsy was taken from the same patient tumor. Each case had one control core and one AQD-treated core biopsy. A total of 6 AQD-treated cores and 6 control cores were evaluated. The AQDs-treated core were stained with the AQD-probe as described in section 6.2.1. The control cores were not treated by AQD-probes. Both the AQD-treated and the control cores were snapped frozen in liquid nitrogen and embedded in OCT. The blocks were cut into 5 μm sections at the surfaces of the specimens where the AQDs-treated cores were stained by the AQDs-probe. Both sets of sections (control and treated) were stained with H&E and immunohistochemistry (IHC) stained for 3 different markers: Tn antigen, VEGF, and HER2. Interpretation was performed by a pathologist

Using multiple evaluated markers, we found that there was no difference between the H&E staining of an AQDs-stained core and that of a control core. As examples, Figure 6.14 showed the H&E staining and IHC staining of VEGF, HER2 and Tn antigen of a control core (Figure 6.14b) and those of an AQD-treated core (Figure 6.14a). As can be seen, there was no difference between the H&E staining of the control tumor and that of an AQD-treated tumor nor was there a difference between the IHC staining of a control tumor and that of an AQD-stained tumor.

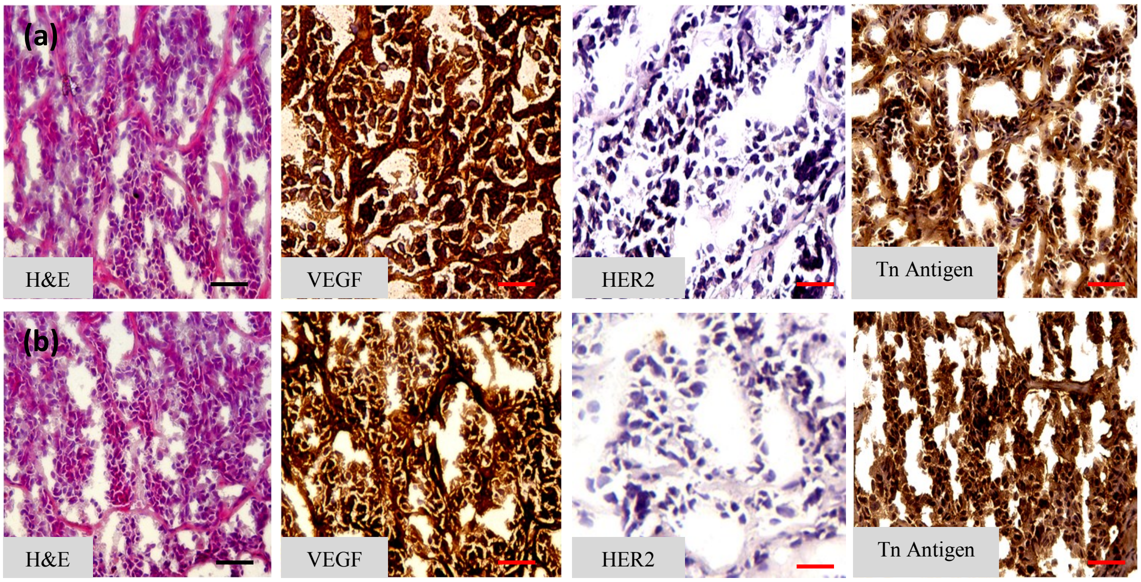

Figure 6.13: Interference examination of QD-stained tumors compared to control core biopsy. VEGF, HER2, and Tn Antigen were evaluated and no interference was found. (a) AQD-treated samples; (b) negative control samples. Scale bar: 200 µm.

A more direct test will be studied, in which 5 µm sections from the cases that were evaluated by AQD-probe will be requested after pathology processes the specimens. The markers level will be compared for before and after surgery to ensure there is no damage to the tissue by AQD method.

No additional intraoperative pathological evaluation is needed to decide whether an area contains cancer cells or not. Manipulations of the surgical specimen have no impact on the microscopic examination of the operative specimen as shown in the interference study is another advantage of this method. The specimen can undergo normal histologic examinations for further margin confirmation and other necessary markers evaluations.

The AQD-Tn mAb probes can determine the margin status within 30 minutes with high sensitivity and specificity. The current blocking protocol requires 10 minutes as described in section 6.2.1. It has been know that serum/cell ratio can affect the sensitivity of immunoassays. Increasing serum/cell ratio can improve the sensitivity of antibody-antigen binding. Due to the law of mass action, concentration effect is more pronounced for low affinity binding such as bovine serum albumin (BSA) blocking. By increasing the BSA concentration, the blocking time can be shortened. For the future study, we will investigate different BSA concentration versus time needed to achieve minimum tissue autofluorescence especially in adipose tissue should be investigated.

Another factor that affects the total procedure time is the binding between AQD-Tn mAb probe and the antigen. There are many factors that can affect the antigen-antibody reaction such as temperature, pH, ionic strength, incubation duration, etc. At low ionic strength, the reaction is faster. At ionic strength (I) 0.04, 5 minutes incubation showed similar result as 20 minutes incubation at I = 0.09. Combination of all these factors should help shorten the staining time. The kinetics of antibody binding to cancer cells will be studied by varying different parameters such as the time of soaking of tissue in AQD suspensions, ionic strength in range of 0.04 to 0.09, minimize sedimentation by shaking, incubation temperature and enzymatic treatment with fictin, papin or bromelin. The PL intensity should be used to correlate the optimal parameters to achieve the maximum binding in the shortest time.

6.3 CUSTOM-BUILT IMAGING SYSTEM FOR MARGIN EVALUATION

For clinical application, a compact and simpler imaging system is needed to evaluate the specimens. IVIS system is not appropriate for operating room since it's not portable. To set-up the system, first a LED light was guided through the arm containing a dichroic mirror to direct the light through a 460 nm excitation filter and excite the sample. Any positive signal comes from the specimen would travel through the zoom lens and a 700 nm long pass filter before it is captured by the NIR CCD camera. It's important to note that the emission filter has to be placed in front of the CCD camera and not the zoom lens to block out transmitted light from the light source which will cause autofluroescent signal. Figure 6.15a shows the schematic set-up of the imaging system and Figure 6.15b is the real picture of the system. The light source arm angle can be adjusted if needed. Additional light source arm would be helpful to improve the signal from the specimen. After the image is captured, it can be analyzed using imageJ with selected region of interest (ROI).

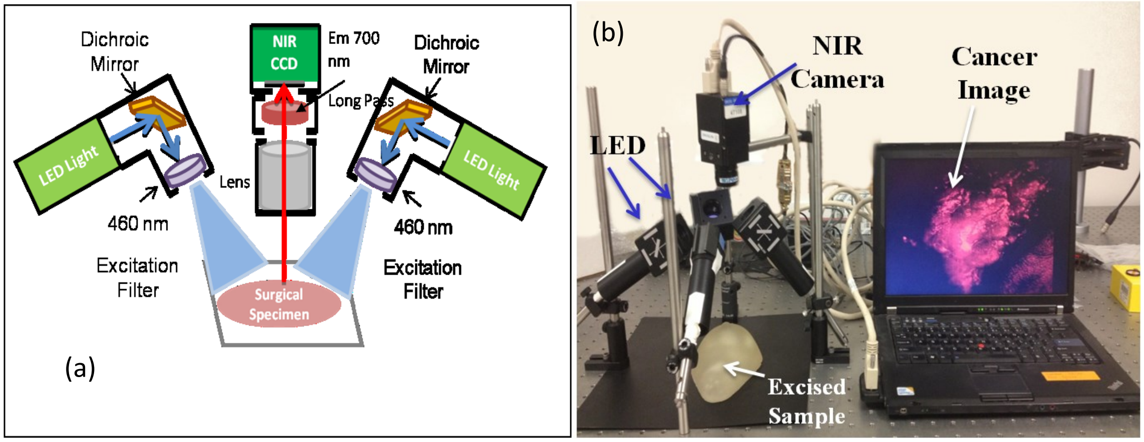

Figure 6.14: : Custom-builtAQD Imaging System. (a) Schematic representation; (b) Real system picture.

The newly built system (AQD system) was tested on human core biopsy samples and was found to be comparable to IVIS in term of signal strength. The signal processing using ImageJ was also similar to IVIS system. Using the same samples that were imaged by IVIS, AQD system was used to take similar pictures. As an example, we show the fluorescent images taken by the setup of the core biopsy sample of a patient after chemotherapy in Figs. 6.16a and 6.16b. The red color indicates residual cancer—that pieces 1 and 2 had residual cancer and pieces 3, 4, and 5 are cancer-free was later confirmed by the H&E staining of the sections from these pieces. This result indicates that the methodology can accurately detect residual cancer after chemotherapy. Note theses core biopsy samples were 1-2 mm in width.

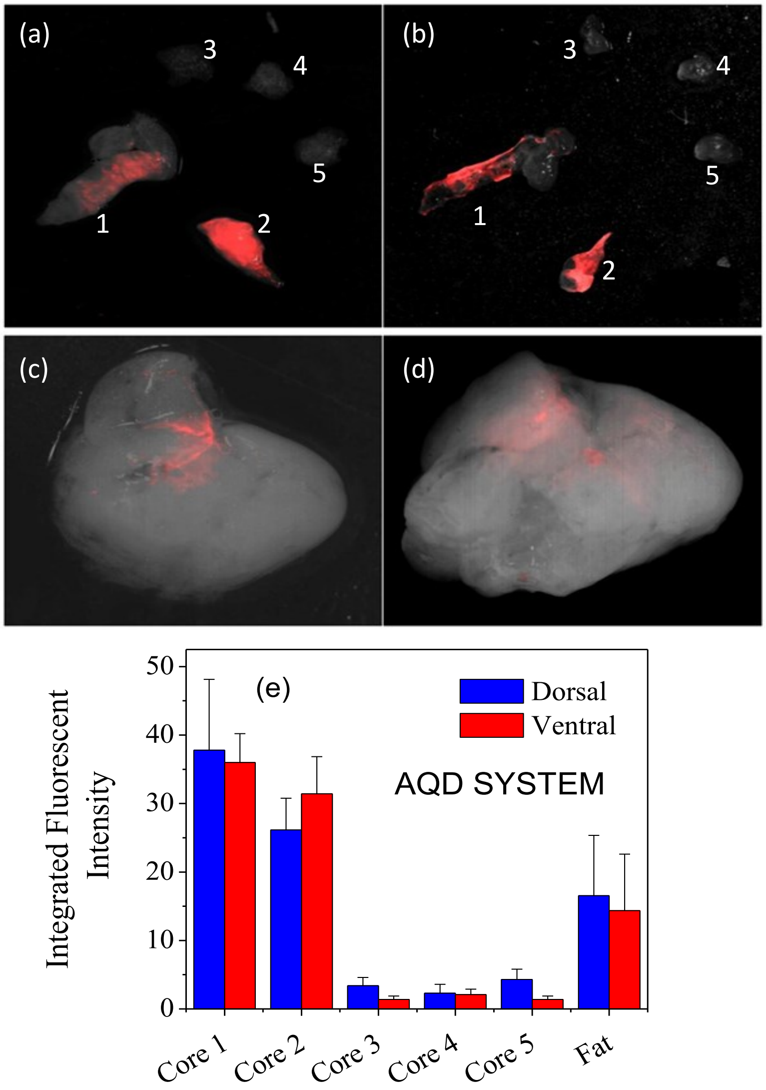

Figure 6.15: : Core Biopsy Specimens stained with CdPbS AQDs probes and imaged by newly built imaging system. (a) Ventral view of the cores; (b) Dorsal view of the cores; (c) Ventral view of the normal tissue (fat);(d) Dorsal view of the normal tissue (fat); (e) Integrated fluorescent intensity using ImageJ analysis software.

Figure 6.17a and 6.17b showed that core 1 and 2 were partially positive, which was similar to the IVIS system. Core 3,4 and 5 were negative. The normal tissue also showed some positive signal. The signal to noise ratio is > 1.5 which was a little smaller than the IVIS. This could due to the weaker light source of the AQD system since there was only one LED light. Pathology report has confirmed that the area where the core was taken contained cancer cells. Thus, the result indicates that the method is sensitive and specific with the custom-built imaging system. However, the maximum capture area of AQD system was 2x2 cm, which is not enough for lumpectomy specimens. Modification of the system was needed. Three more LED light sources were added into the system as shown in Figure 6.16b and a zoom lens was replaced with an optical lens.

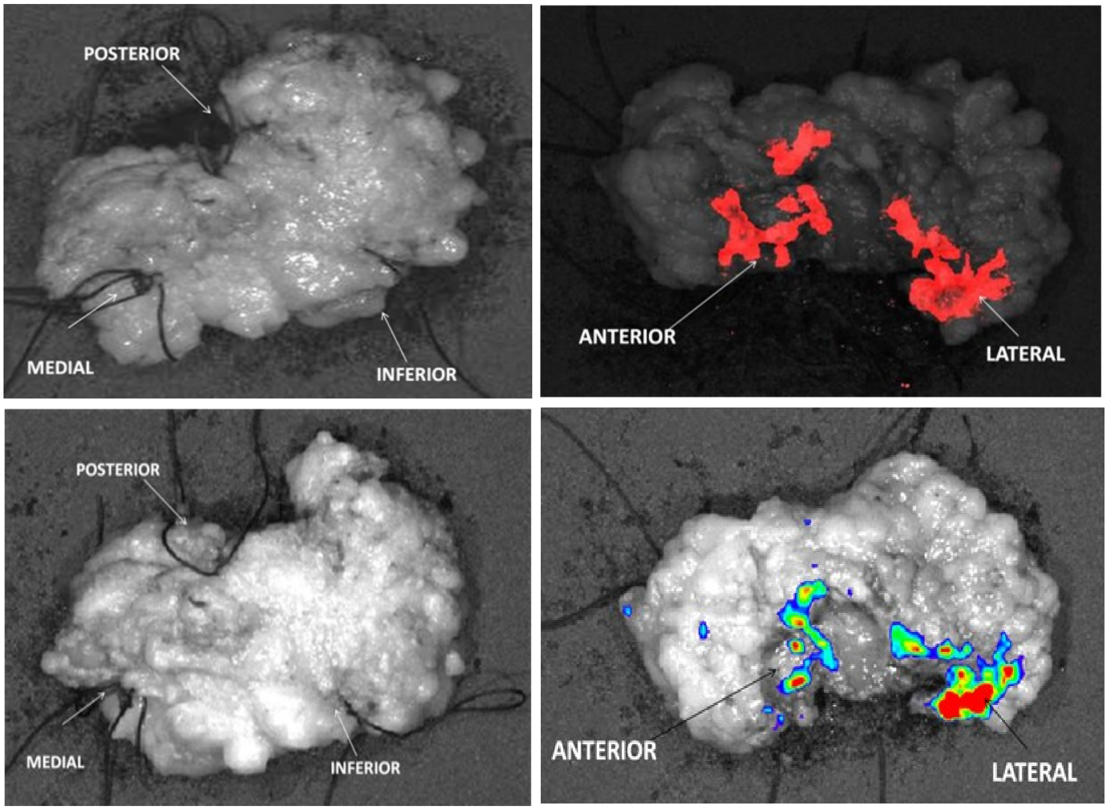

Figure 6.16: Comparison between the custom-built AQD imaging system and IVIS system. Top panel: AQD system. Bottom panel: IVIS system.

Figure 6.17 showed an example of an AQD-treated lumpectomy specimen evaluating by the custom-built imaging system and IVIS system (case 11). The case was a re-excision with positive inferior and medial margins. It was expected that the superior and lateral of the new re-excision specimens to be positive. Both imaging systems showed positive signal for these two margins. Other margins were negative. The cancerous region was slight larger on the superior margin for the home-built system compare to the IVIS system, indicating that the system was slightly more sensitive than the IVIS system due to the custom-designed to fit the spectra of CdPbS AQDs. More data is needed to evaluate this imaging system.

6.4 SUMMARY

The present AQD-Tn mAb probe does not depend on the physical-mechanical characteristic of the tissue but assessing the differences between normal and cancer at the molecular level. TACA Tn antigen has been reported to be expressed exclusively in cancer cells and not normal tissue. Using this molecular signature of cancer cells, tissue heterogeneity is not an issue; as the results presented above clearly showed that the AQD-Tn mAb probe was capable of displaying very small spots consisting of 100 to 200 cancer cells from the animal model studies. This is a key advantage compared to most of the current developing optical-based imaging technologies which rely on signal average over a large area and thus are unable to image cancer in a heterogeneous background. The advantages of the AQDs as the fluorescent tag of a cancer molecular probe include brightness, without photo-bleaching, and can be accessible to 700 nm long-pass emission filter that minimizes background tissue autofluorescence. The results showed that the AQD-Tn mAb was effective to image tumor margin in less than 30 min in both animal tumor model and clinical human lumpectomy specimens, in which the positive margins were confirmed by pathology reports. The integrity of the surgical specimen was not affected by the AQD treatment and there was no difference in the quality and intensity of standard H&E as well as IHC stains. The AQD-Tn mAb molecular probe offers the potential to quantitatively and accurately assess margin during surgery to help reduce re-excision rate. A home-built imaging system can be used to replace IVIS in a true clinical setting for evaluating margin status during surgery.

CHAPTER 7: GENE DELIVERY THERAPY AND MOLECULAR TRACKING APPLICATION OF AQDS

7.1 INTRODUCTION

Gene therapy which replaces the defective gene in the diseased cells with a correct gene is a promising approach for treating diseases involving defective genes [220]. Effective gene therapy requires the ability to deliver the correct gene to the nuclei of the diseased cells efficiently and at the same time the ability not to trigger intracellular enzymatic activities that can cause life-threatening side effects. Gene delivery using a viral vector has been investigated extensively. While viral vectors such as retroviruses, adenoviruses, and adeno-associated viruses have been known for their superior gene delivery efficiencies they can also cause potentially life-threating side effects such as immunogenicity and carcinogenicity [221]. As a result, there has been a major effort to shift to gene therapies utilizing non-viral vectors.

Various cationic lipids [222, 223], chitosan [224-226], amphipol [227], polyethyleneimine (PEI) [98, 99, 221, 228-232], polyphosphoramidate [233], dendrimers [234] and peptides [228, 235, 236] have been examined to couple with nanoparticles to form a positively charged complex as a non-viral gene delivery vector. Complexing negatively charged genes to a positively charged complex by electrostatic attractions enabled the release of the genes from the endosomes into the cytoplasm through the “proton sponge” effect and it enhanced the stability of genes against nuclease degradation [227, 237]. Quantum dots (QDs) are semiconductor nanoparticles with superior photoluminescence properties without photobleaching. Due to these advantages, using QDs for non-viral gene delivery has the additional benefit also tracking the gene delivery in real time as it happens. QD Live-cell tracking has been demonstrated in the internalization of bioconjugated QDs in living cells [238-240] and in QDs-attached plasmid DNA (pDNA) in intracellular tracking of the pDNA after the delivery by cationic liposomes [241].

Cellular uptake is one of the key steps for gene transfection. Besides that, endosomal escape, cytoplasmic mobility and nuclear entry of foreign genes are also important for nonviral gene delivery systems [242, 243]. So far, the ability of a non-viral vector involving complexing a nanoparticle, QD included, to a positively charged molecule to deliver a foreign gene directly to the cell's nucleus is limited.[243, 244]. Various techniques have been investigated to utilize QDs both as a carrier to directly carry the gene into the nucleus and as a tracking agent image the gene delivery event. The efficiency of nuclear localization signal (NLS), consisting of either one (monopartite) or two (biparitite) stretches of basic amino acids[245], mediated delivery has been shown to be around 25% [100]. Microinjection and nano-needle-based methods provided direct delivery of QDs into the nucleus without endosomal escape [244]. However, these methods often injured and damaged the cells in the process and had no potential for gene delivery *in vivo*.

A more practical approach would be to complex genes with a complex containing QDs for both gene delivery and for imaging. A major limitation of utilizing the traditional QDs synthesized in an organic solvent (OQDs thereafter) for gene transfection was that they invariably aggregated [243] which made the next step--delivery into the nuclei--difficult if not impossible. On the other hand, Li et al had shown that QDs can be directly synthesized in water completely using 3-mercaptoproponic acid (MPA) was used as the capping molecule [246]. As a result, MPA was directly chelated to the cations on the AQD surface during synthesis. In addition, the number of the MPA on an AQD surface could be further enhanced by extra MPA and cations relative to anion. As a result of such MPA optimization, CdSe AQDs, for example, with a nominal MPA:Cd:Se=4:3:1 could incorporate four times as many MPA's on an AQD surface as compared to OQDs synthesized using the traditional organic solvent route that required solvent and ligand exchanges to be soluble in water. As a result, CdSe AQDs exhibited a zeta potential of -30mV versus -22 mV of the OQDs, which could provide much better colloidal stability than the OQDs when complexed with other molecules. In earlier studies, CdS AQDs and CdPbS AQDs were demonstrated to be able to be optimally complexed with branched PEI to be delivered into cytoplasm without aggregation by means of endocytosis. More importantly, PEI-AQD complexes formed under a high PEI/AQD molar ratio were shown to be overall positively charged and had a size of less than 30 nm. It is known that for a molecule or complex to get into a cell nucleus it must possess positive charges and less than 40 nm in size such that it can bind to the chaperone protein, importin to pass through the channels in the nuclear membrane which was known to be 35 nm in size. Thus, an overall positively charged AQD-PEI complexes less than 24nm in size seem ideal as a non-viral vector for carrying genes into the nuclei.

The goal of this study is to investigate the efficacy of MPA-capped CdSe AQDs electrostatically complexed with branched PEI both as a non-viral gene delivery vector and as a fluorescent probe for tracking the delivery of genes into nuclei. The MPA-caped CdSe AQDs that were completely synthesized in water were the model AQDs. A nominal

MPA:Cd:Se=4:3:1 was chosen for optimal photoluminescence and zeta potential. The gene delivery study was carried out in vitro using a human colon cancer cell line, HT29 (ATCC). The model gene was a plasmid DNA (pDNA) that can express red fluorescent protein (RFP). Positively charged branched PEI was employed to provide a proton buffer to the AQDs to allow for endosomal escape [98, 99, 247]. Branched PEI which had lower chain flexibility than linear PEI [248] has been shown to offer better stability [248]and reduced cytotoxicity [98, 99, 133, 249] for the resulting complexes. We will show that using a PEI-AQD complex with a PEI/AQD molar ratio of 300 and a nominal pDNA/PEI-AQD ratio of 6, we were able to achieve 75±2.6% RFP expression efficiency with cell vitality remained at 78±4% of the control.

7.2 MATERIAL AND METHODS

7.2.1 Chemicals

PEI (25 kDa, branched) was purchased from Sigma Aldrich (St. Louis, MO, USA) for complex preparation. 50 based-pair double-stranded DNA fragment tagged with cyanine 3 (Cy3) was purchased from Pierce (Rockford, IL, USA) and used as a tracking DNA (tDNA) without protein expression. pDNA encoded with red fluorescent protein (RFP) (pCAG-DsRed 4.7 kbp) was obtained from Addgene (Cambridge, MA, USA).

7.2.2 PEI-AQD-pDNA and PEI-tDNA complex formation and characterization

The synthesis of MPA-capped CdSe AQDs is described in chapter 3. To prepare PEI-AQD and PEI-tDNA complexes for extracellular characterization, the PEI was first dissolved in DI water at 7.73 mM concentration. The PEI solution was added to 500 μL of the 3.2 mM MPA-capped CdSe AQDs suspension and tDNA solution so that the final PEI/AQD = 300 and PEI/tDNA = 100, respectively. The mixed solutions were incubated for 1 hour at room temperature. The final volume of these PEI-AQD and PEI-tDNA mixtures was adjusted to 1 mL. Free PEIs that did not attach to the surface of the AQDs or tDNA were removed using 30 kDa filters (Millipore Co., Beillerica, MA, USA) at a spinning speed of 10000 rpm for 5 minutes. Circular pDNA was added to the PEI-AQD suspension at different ratio ranging from 0 to 60 to form the PEI-AQD-pDNA complexes. Tracking DNA (tDNA) was 50 bp and tagged with Cy3 fluorophore for tracking the pathway of the PEI-tDNA complex. The particle size and zeta potential of complexes were measured by ZetaSizer (Malvern, CA, USA).

7.2.3 Cell Culture and Transfection Experiment

Most gene therapy studies are aimed at cancer and hereditary diseases that are linked to a genetic defect. Cancer cell lines are ideal models to develop these gene therapy techniques. HT-29 human colon cancer cells were seeded in 6-well plates with a square cover slit in each well. HT29 cells were grown in McCoy's 5A with 10% fetal bovine serum (FBS) and 1% penicillin/streptomycin. All cell cultures were incubated at 37°C and 5% CO_2 until 80% confluence before starting transfection.

After 24 h of incubation, the cells were washed with fresh medium. PEI-AQD-pDNA complexes (or PEI-tDNA) complexes with various ratios were added to each well. The total DNA amount was 40 ng/well. Cells were incubated for 24 h with each complex in cell medium. HT29 cells were then washed thrice with PBS and replaced with fresh cell culture medium. Multiple time points were evaluated for the complexes' location and transfection efficiency.

Cells were fixed with 4 % paraformaldehyde in PBS for 15 min. After washing, DAPI counter stained solution was added. Internalized of AQDs and DNA were visualized with an Olympus Fluorview 100 laser-scanning confocal microscope (Olympus, Japan). Colocalization of AQDs and nuclei were measured using ImageJ colocalization functions.

7.2.4 Cytotoxicity MTS assay

HT29 cells were seeded at a density of 2 x 10^4 cells/well on 24 well plates. After 24 hours incubation, the cells were incubated in the presence of PEI-AQD-pDNA complexes in fresh DMEM medium. The concentrations of PEI-AQD-pDNA complexes were similar to the ones that were used in the transfection assays. Non-treated cells were used as negative control. Cytotoxicity were measured using the CellTiter 96 Aqueous one solution cell proliferation assay system (Promega, Madison, WI, USA) according to manufacturer's protocol. The cells were exposed to the methoxyphenyl-tetrazolium salt (MTS) compound and incubated for 4 hours. The colorimetric formazan was quantified using a plate reader at 490 nm (Infinite M200, Tecan, USA).

7.3 RESULTS and DISCUSSIONS

7.3.1 Distribution of PEI-AQD and PEI-tDNA complexes

The delivery of AQDs into the nuclei was first evaluated using the PEI-AQD complex first. The PEI-AQD complex used in this study with a nominal PEI/AQD molar of 300 consisted of a negatively charged AQD core coated with positively charged PEI as schematically shown in Figure 1a. The positively charged PEI was attracted to the negatively charged AQD to form PEI-AQD core-shell structure with AQD being the core and the PEI's being the shell at the optimal ratio of PEI/AQD = 300 [99]. For comparison, tDNA was mixed directly with PEI with various PEI/tDNA ratio to investigate the transfection efficiency of PEI alone. The HT-29 colon cancer cells were treated with the PEI-AQD and PEI-tDNA complexes to investigate the translocation of AQDs and tDNA through the cell membrane into cytoplasm and later into the nuclei. After 24 h incubation of cells with these complexes, cells were replaced with fresh medium and analyzed by confocal fluorescent microscopy. No fluorescent signal inside the cells was observed using uncomplexed tDNA and uncomplexed AQDs (see supplemental information). Note PEI-AQD complex entered the cells through endocytosis (see supplemental information). In Figure 1b, we show the confocal fluorescent microscopy images of HT29 cells at different times after transfection with the PEI-AQD complexes. At 24 h, the image shows that the complexes had entered the cells. At 48 h, PEI-AQD complexes had moved toward the peri-nuclear region. At 72 h, the majority of PEI-AQDs had translocated inside the nuclei. At 96 hr, the PEI-AQD complex started to move out of the nucleus. In comparison, the confocal fluorescent microscopy images of HT29 cells transfected with the PEI-tDNA complexes at t = 24, 48, 72, and 96 h are shown in Figure 1c. Although the PEI-tDNA complexes could also entered the cytoplasm of the cells (see the image at t=72 h) only a small percentage of the complexes could enter the nucleus.

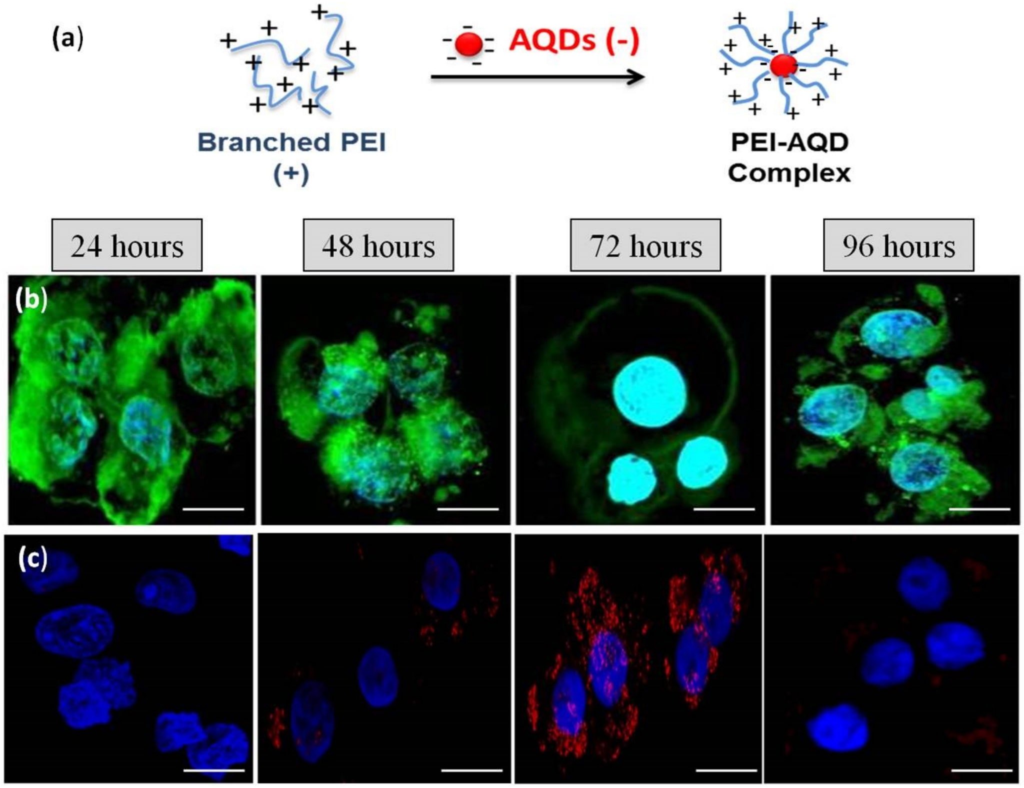

FIgure 7.1: (a) Schematic representation of the formation of the PEI-AQD complex (PEI/AQD = 300) by electrostatic interaction. (b) Z-stack confocal images of PEI-AQD complexes (green) transfected in HT29 cells compared to (c) those of PEI-tDNA (red) transfected in HT29 cells at various times. Bar: 100 µm and Blue: DAPI – nucleus, Cyan: overlay of AQD and nucleus. At 72 h post transfection, most of the PEI-CdSe QD translocated into the nuclei whereas only small amount of PEI-tDNA colocalized with the nuclei.

To examine if indeed the PEI-AQD complexes were inside the nucleus at t =72 h, we examine the confocal images at various depths which were shown in Figure 7.2a. As can be seen, the PEI-AQD complexes were indeed in the nuclei of HT29 cells. To further show that the AQDs were indeed inside the nuclei, we examined that the cross sections of the cells containing the z-axis by three dimension (3D) reconstruction. Figure 7.2b is a xy-plane confocal image of a slice within a z stack.

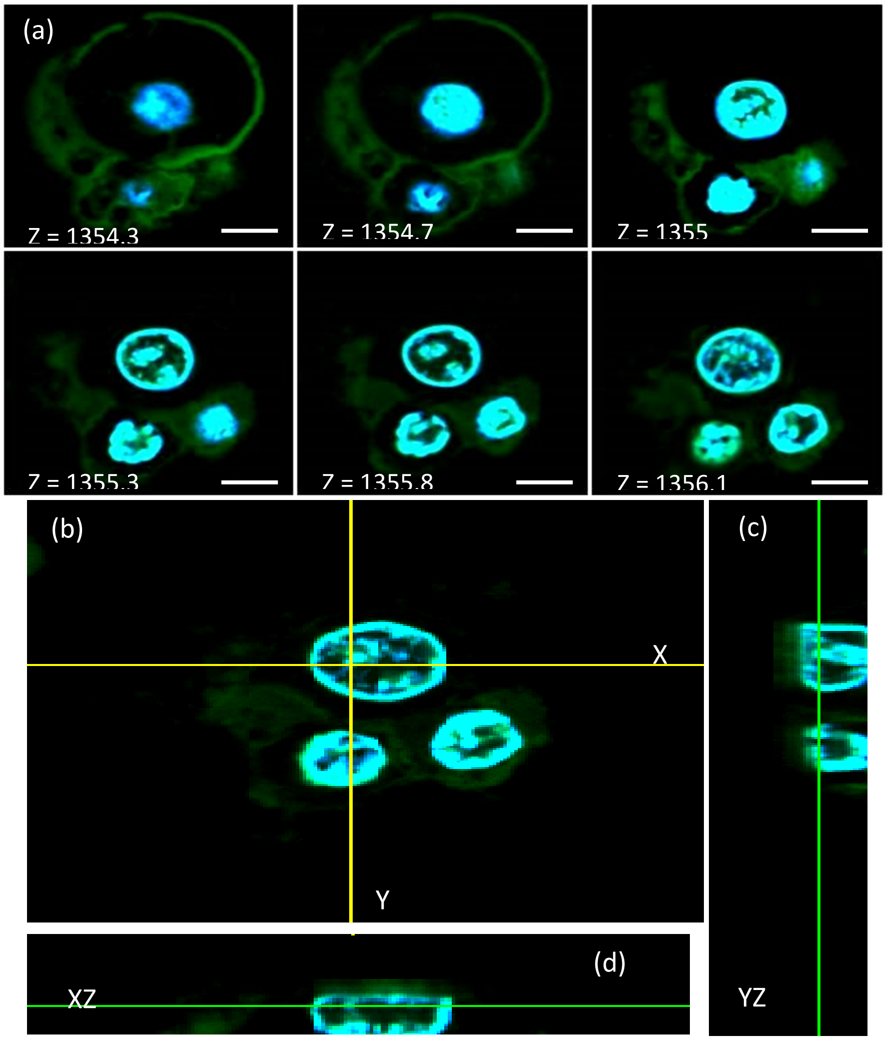

FIgure 7.2: (a) z-section confocal images at different depth and (b) the image represents a slice in the middle of the z-stack with projections in the z-axis of the same cell high-lighted in the yellow cross indicated that AQDs translocated inside the nuclei. Bottom image (xz axis) represents the front view of the cell. Left image (yz axis) represents the side view of the cell. Bar: 100 µm.

Figure 7.2c and 7.2d are the xz cross-section image along the vertical yellow line in Figure 7.2b and the yz cross-section image along the horizontal yellow line in Figure 7.2b. Clearly, in the xz and yz cross-section images the green fluorescent signals of the AQDs overlap completely with the blue signals of the DAPI (nuclei) to result in a cyan color, indicating that the PEI-AQD complexes had indeed translocated into the nucleus at this time point.

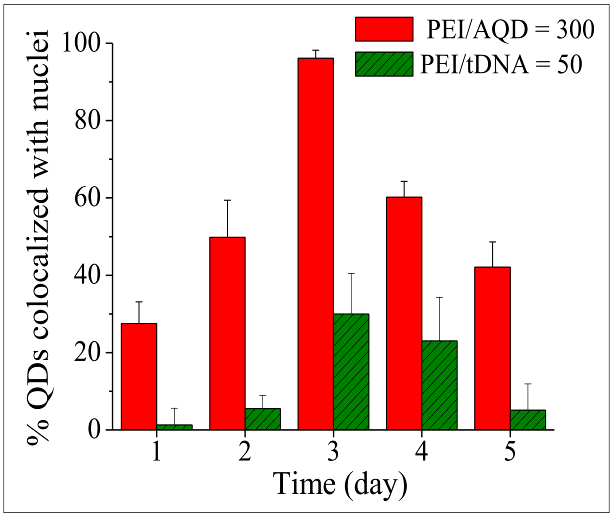

Figure 7.3: Colocalization analysis calculated by ImageJ. 96.1±2.1% of PEI/AQD = 300 complexes were translocated into the nuclei at 72 h post transfection whereas PEI-tDNA = 50 only has 30±10.5% translocated. The data was analyzed based on 400 cells in the glass slide area.

To quantify the percentage of cells whose nuclei colocalize with the PEI-AQD complexes or the PEI-tDNA complexes we analyzed the images using the ImageJ algorithm and obtained the percentage of colocalization using the Manders' method[250]. In Figure 7.3, we plot the resultant percentage of cells whose nuclei were colocalized with PEI-AQD and that of cells whose nuclei were colocalized with the PEI-tDNA versus time. As can be seen, the PEI-AQD complexes exhibited a 96±2% colocalization efficiency on day 3. Note this is the first time in which such a high degree of translocation of any nanoparticles (fluorescent or otherwise) into nuclei has been observed.

In comparison, although the PEI-DNA complexes could also entered the nuclei at 72 h post transfection only 30±11% of the PEI-DNA complexes was translocated into the nuclei. It is also worth noting that previously QDs could only enter the nuclei with the help of a viral nuclear translocation signal (NLS) peptide with 25% transfection efficiency [3]. In comparison, the current PEI-AQD complexes could enter the nuclei without the need of using a NLS peptide.

There are two major mechanisms to facilitate nuclear translocation: passive diffusion and active transportation. For passive diffusion, metabolites and macromolecules that are less than 10 nm and 40-60 kDa could potentially diffuse through the double membrane [251]. Larger molecules up to 40 nm in diameter can be actively transported through the nuclear pore complex (NPC) [252, 253].We attribute the ability of the PEI-AQD complex to enter the nuclei to the fact that it had a small size of 24 ±2 nm and the fact that it had a positive zeta potential of 30 ±3 mV. The complex was able to be transported across the nuclear membrane into the nuclei due to the active transport through the importin-α within the NPCs.. The NLS conjugated QDs relied on the binding between the peptide and Importin α, which has two binding sites in the central regions. Importin α-NLS complex then binds to importin β to be transported from the cytoplasm into the nuclear side of the NPC [254]. There are many NLS sequences exist. However, there are two common features of all the NLSs: they are usually short, generally less than twelve amino acids and contain a high portion of positively charged amino acids which make the whole sequence positive [255, 256]. This feature is also present in the PEI-AQD complex. The whole PEI-AQD complex was positive due to the PEI covered surface. Importin α, which is a highly basic amino-terminal region of roughly 40 amino-acid residues, could have bound to the complex in a similar fashion as binding to NLS through electrostatic interaction [257]. Similar mechanism was observed with PEI-tDNA complex. However, the yield for PEI-tDNA in the nuclei was much lower, only 30±10.5% compared to 96.1±2.1% of PEI-AQD. One possible reason could be that the size of the tDNA fragment is small. Only a small amount of PEI bound to the small fragment to neutralize the negative charge on the surface of the tDNA resulting in less positive complexes overall. In addition, due to the linearity of tDNA, the PEI-tDNA complex was not as compact as the PEI-AQD complex reducing the transfection efficiency. More study is needed to have a full understanding why the translocation efficiency of PEI-tDNA is lower than that of PEI-AQD complex.

7.3.2 Delivery of pDNA with 75±3% RFP expression efficiency using PEI-AQD as carrier

First, we investigated the capability of PEI-AQD complex with pDNA to express RFP. Using the optimal ratio of PEI/AQD = 300 which resulted in the average size of 24±2 nm and zeta potential of 30±2.5 mV [98, 99], pDNA was added to the suspension at different ratios and combined with PEI-AQD complex through electrostatic reaction. The schematic procedure for the PEI-AQD-pDNA complex is illustrated in Figure 7.4a. Figure 7.4b shows the particle size and Figure 7.4c shows the zeta potential of the complexes as a function of the pDNA/PEI-AQD ratio. As the pDNA/PEI-AQD ratio increased, the size of the complexes increased from 24 nm to 85 nm due to the heterogeneous aggregation since more negative charges were added into the system. The optimal size was 31.5±5.3 nm, achieved from pDNA/PEI-AQD= 5 and 6. This ratio had an average of 21 ± 2.4 mV positive net charge, which was critical for the complex to be up-taken into the cells. From previous PEI-DNA complex study [221], the optimum PEI-DNA size was 130 nm which was about 4 times larger than the PEI-AQD-pDNA complex in this study. The current complex was more compact than previous study which was one of the main reasons to deliver DNA into the cell nucleus.

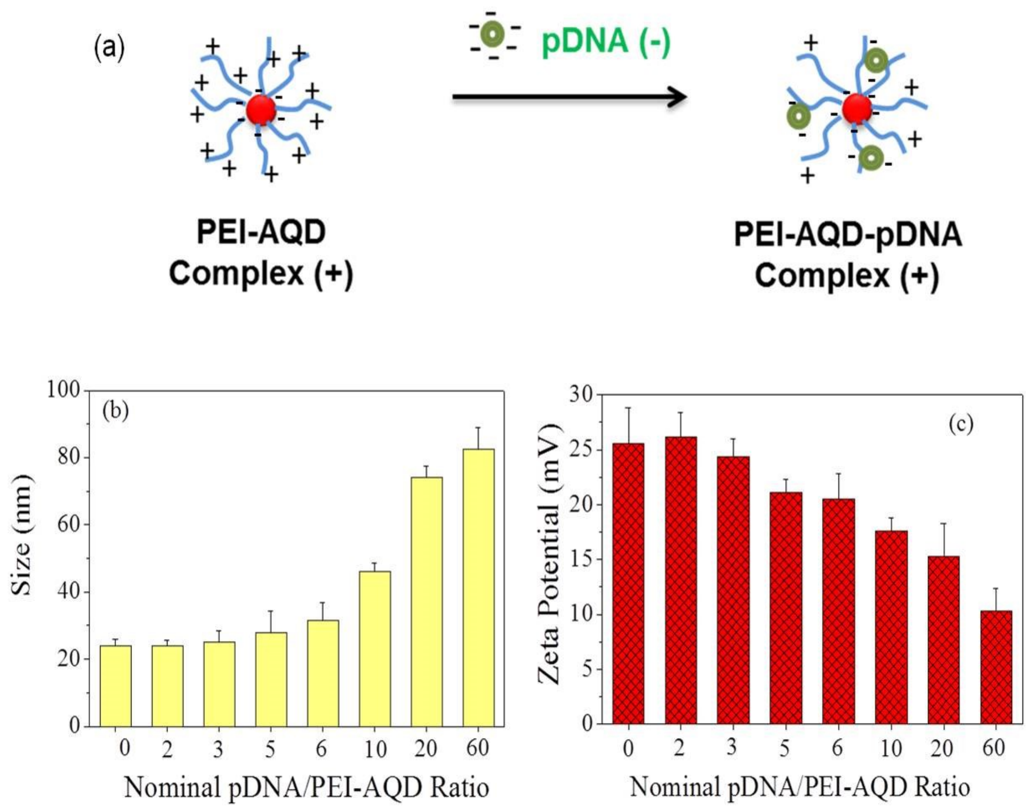

Figure 7.4: (a) A schematic of the formation of the PEI-AQD-pDNA complex, (b) size and (c) zeta potential versus the nominal pDNA/PEI-AQD ratio. The optimal size with pDNA was about 31.5±5.3 nm for pDNA/PEI-AQD = 6 with a zeta potential of 21 ± 2.4mV.

After the complexes were formed, pDNA was delivered into the cell with PEI-AQD as carrier to express red fluorescent protein (RFP). Typical RFP red fluorescent and DAPI blue staining images of HT29 colon cancer cell internalized with different pDNA/PEI-AQD complexes are shown in Figures 7.5a and 7.5b. Figure 7.5a shows cells treated with pDNA/PEI-AQD= 6 and the majority of the cells expressed RFP while AQDs were located within the nuclei. On the other hand, Figure 7.5b shows that with pDNA/PEI-AQD=60, the RFP expression was not uniform and much less than that in Figure 7.5a.

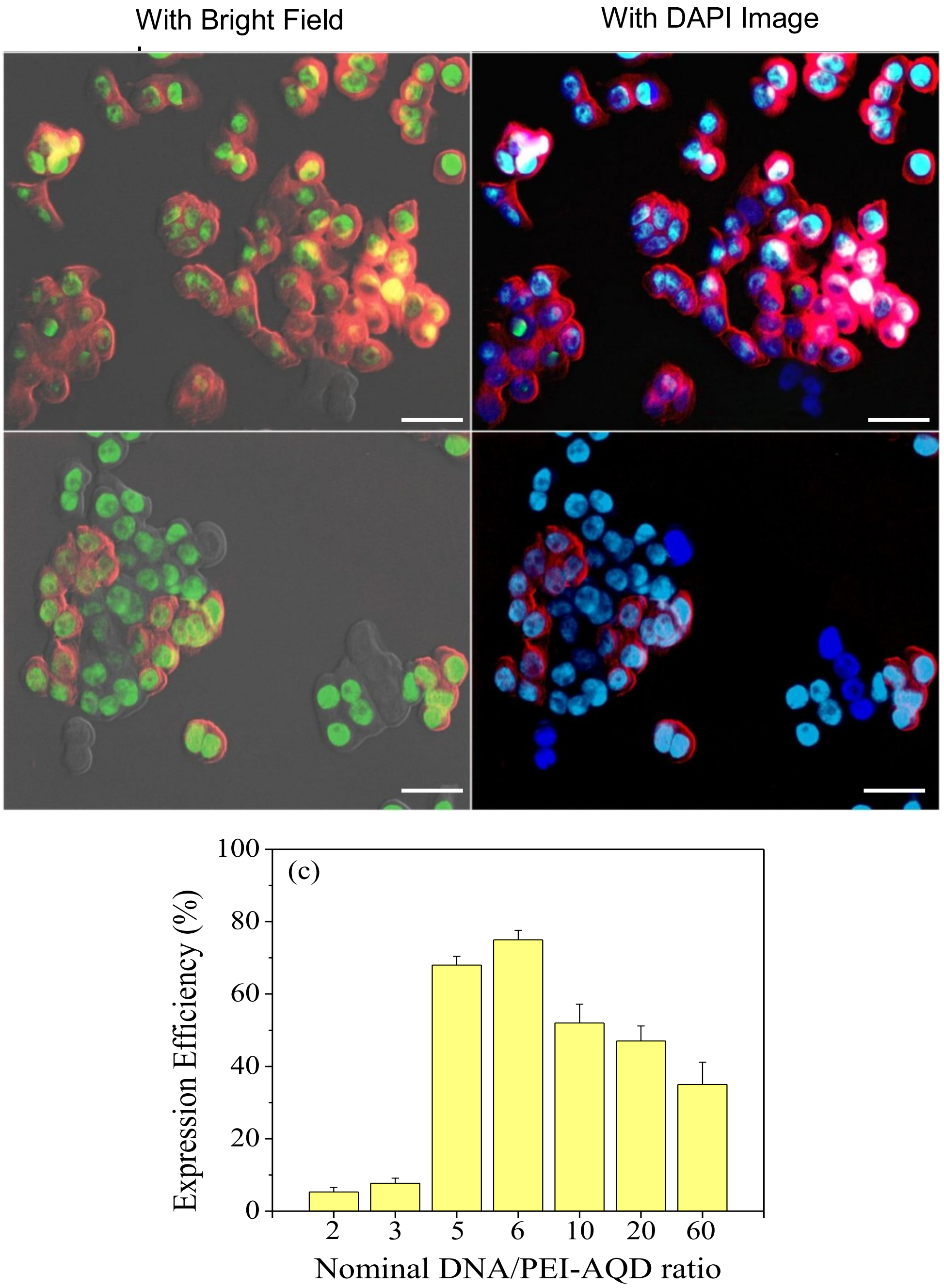

Figure 7.5: Fluorescence image of PEI-AQD-pDNA complex transfecting HT29 with a (a) pDNA/PEI-AQD = 6 and (b) pDNA/PEI-AQD = 60 overlayed with bright field image (left) and further overlayed DAPI (right), and (c) (c) red fluorescent protein expression efficiency versus pDNA/PEI-AQD ratios where the amount of the pDNA was kept at 40 ng/well for all cases. Green: AQDs, Red: RFP expression, Blue: DAPI – nuclei, Cyan: overlay of AQDs and nuclei. Scale bar = 200 μm.

Because the surface charge of PEI-AQD-pDNA complex was small, the proton sponge buffer might not be effective in causing endosomolysis to release of the PEI-AQD-pDNA into the cytoplasm. Yezhelyev et al. had found that the tertiary amines on the PEI backbone had strong proton absorbing capability which can lead to rapid osmotic swelling [258]. With insufficient PEI on the surface of complex reducing the proton sponge effect [258], the majority of PEI-AQD-pDNA system was trapped inside the endosome. In addition, most of the nanoparticles had been shown to aggregate in the plasma membrane after entering the cells [259, 260]. With sufficient PEI, such as a PEI/AQD=300, we believe the PEI/AQD complex can cause endosomal escape by proton sponge effect and be released into the cytoplasm. After endosomal escape, the PEI-AQD-pDNA system was distributed uniformly in the cytoplasm.

Upon escaping the endosome and lysosome, PEI-AQD-pDNA complex further crossed the nuclear envelops and enter into the nuclei. Until now, there is no transfection agent that could directly carry DNA across the nuclear envelop after the cells are transfected. Experimental evidence has shown that QDs coupled with NLS could be delivered into cell nuclei. These NLSs are often derived from adenoviral proteins. Kuo et al. has shown that CdSe/ZnS conjugated with NLS peptide could facilitate the transportation of QDs across the plasma membrane into the nucleus through diffusion [100]. However, at high concentration, the QDs aggregated in the cytoplasm and at very low concentration, only 25% of the NLS peptide conjugated QDs could enter the cell nucleus.

Another factor for nuclear delivery is the size of the complex. Even with the active transportation with importin α/β through NPC, a size that is larger than 40 nm would not pass through the perinuclear region to go into the nucleoplasm region [253]. The PEI-AQD-pDNA complex (31.5 ±5.3 nm) remained close to its original size of 24 nm. It could easily pass through the NPC with the importin α/β translocation mechanism. In addition, we have tested other ratios of pDNA/PEI-AQD that had larger size around 100 nm, which reduced the efficiency to 35±6.2% (pDNA/PEI-AQD= 60). These complexes were internalized by the cells and escaped lysosomes. However, none of them could enter the nuclei. This is consistent with the size effect for delivery pDNA into nuclear region [261]. At 96 hour, the complexes were exported out of the cell nucleus. CRM1/exportin is known to bind leucin-rich nuclear export sequence proteins to export them out of the nucleus[262]. Leucin is an essential amino acid and has a neutral net charge under physiological condition. This indicates that PEI started to dissociate from the AQD surface after unloading the pDNA thus reducing the complex positive net charge close to neutral to allow CRM1/exportin to transport the complex out of the nucleus. The exact mechanism, however, is still unclear at this point and will be investigated in the futureClearly the ratio of pDNA to PEI-AQD is important for the success of delivery of the complexes into nuclei. Figure 7.5c summarizes the transfection efficiency as a function of pDNA/PEI-AQD ratio. The protein expression efficiency was obtained by examining the entire plates for the percentage of cells that expressed RFP for each ratio. The highest protein expression efficiency was 75±3% at pDNA/PEI-AQD = 6 (Figure 7.5c). The transfection efficiency depends on the surface charge density, size and stability of the complex [263].

To ensure PEI-AQD actually carried DNA into the nucleus, we used tDNA with Cy3 for tracking as a model. We examined the delivery of tDNA into nuclei using the

PEI-AQD complex as carrier. First, we examined the delivery of the tDNA by the PEI-AQD complex by forming PEI-AQD-tDNA complexes of various tDNA/PEI-AQD molar ratios. Figure 6a showed that PEI-AQD-tDNA complexes were delivered into the nuclei after 72-hour treatment. Most of the AQD fluorescent signal colocalized with the nuclei location (cyan color – mixture of green and blue colors Figure 7.6b).

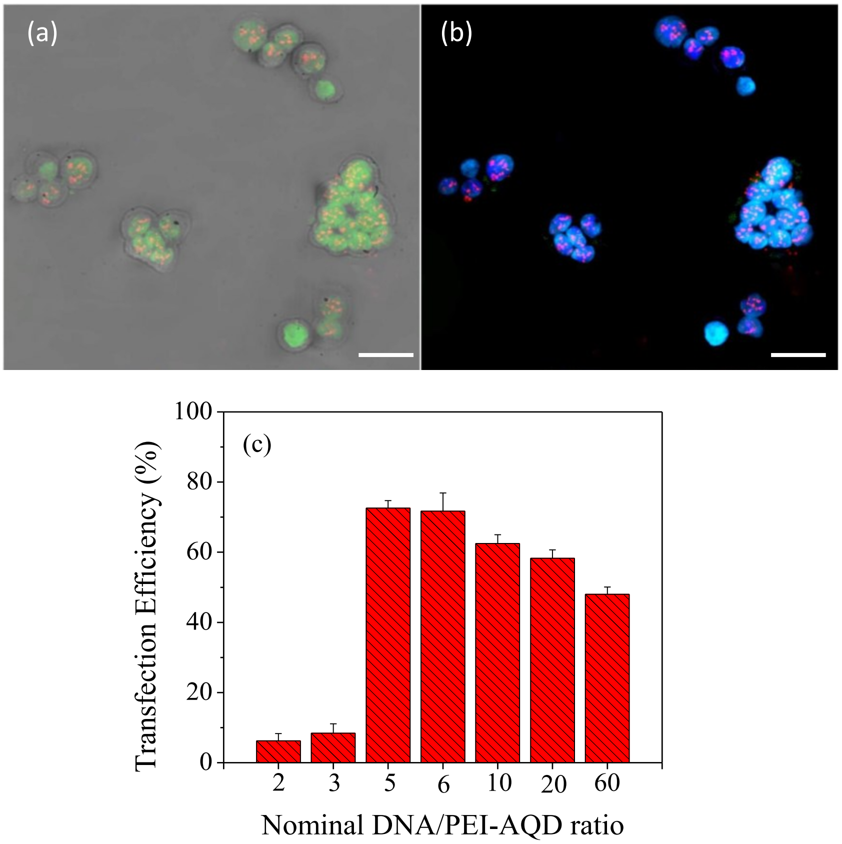

Figure 7.6. Transfection of complexes with tDNA/PEI-AQD = 6 into the HT29 cells: (a) green and red fluorescent images overlayed with the bright field image, (b) green, red and blue fluorescent images overlayed with the bright field image, and (c) transfection efficiency versus tDNA/PEI-AQD ratios where the amount of tDNA was fixed at 40 ng per well. Green: AQDs, Red: DNA tagged with Cy3, Blue: DAPI – nuclei, Cyan: overlay of AQDs and nuclei. Scale bar = 200 μm.

Furthermore, the red color of Cy3 colocalized with the nuclei indicating tDNA were delivered into the nuclei. The result indicates that PEI-AQD complex not only delivers the tDNA into the cytoplasm but also directly into the nuclei enhancing the transfection efficiency. Figure 6c summarized the transfection efficiency of tDNA into the nucleus with PEI-AQD as a carrier with tDNA/PEI-AQD = 6 having the highest transfection efficiency. This indicates that PEI-AQD can also carry plasmid DNA into the cell nucleus for expressing protein of interest.

7.3.3 Cytotoxicity

The cytotoxicity of semiconductor QDs has been one of the major concerns for the use of QDs in biomedical applications. A wide range of studies have been conducted to investigate the effects of QDs *in vitro* and *in vivo.* Generally, a well-capped QD system is believed to not exhibit cytotoxicity for short periods of time [100, 264, 265]. Since the PEI-AQD complexes were observed at longer time than the conventional transfection studies which usually stops at 24 h, it is important to investigate the potential cytotoxicity of the cytoplasmically loaded AQDs. The PEI-AQD-pDNA complexes at different ratios were tested on HT29 cells. Figure 7.7 shows PEI-AQD-pDNA complexes do not cause cell damage when mixed with cells and the cell viabilities were in range of 70-85%, which was higher than the 67% of lipofectamine, the commonly used cell transfecting agent [249]. The optimal ratio of pDNA/PEI-AQD = 6 exhibited cell viability at 78.5 ±4.3%.

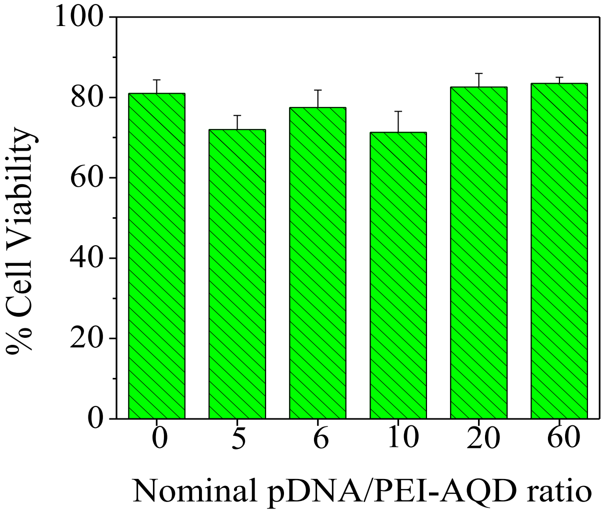

Figure 7.7: Cell viability of HT29 cells as determined by MTS assay after incubation with each complex for 72 h. The pDNA concentration of all complexes is 40 ng/well.

7.4 SUMMARY

In the study, we have developed a new delivery system that could deliver AQDs directly to the nuclei. AQDs with directly functionalized groups attached to their surface during synthesis have the advantages of ample sites for binding or linkage. PEI was able to link and cover more area on the surface of the AQDs and enabled the PEI-AQD complex to enter the nuclei with 96% efficiency, much higher than any current transfection methods including microinjections and NLS coupling. When the PEI-AQD complex is coupled with pDNA, it resulted in protein expression efficiency of 75±2.6%. The PEI-AQD-pDNA complex was stable in cellular environment without aggregation. Our results show that PEI-AQD complex can be coupled with DNA to enhance the delivery of DNA into nuclei which in turn can increase the gene therapy efficiency for nonviral vector delivery. Not only PEI-AQD can be a gene carrier but also a tracker for gene trafficking into the nuclei and present a great potential as intranuclear imaging probe for bioprocessing events.

CHAPTER 8: CONCLUSIONS

In this thesis study an intraoperative method for *ex vivo* breast cancer margin assessment using AQDs coupled with Tn antigen as marker with high sensitivity and high specificity has been developed. Below are the accomplishments of the study.

- We have successfully synthesized CdSe AQDs (4 nm) with emission wavelength peak at 610 nm and NIR CdPbS AQDs (3 nm) with emission wavelength peak at 850 nm.

- The CdSe AQDs exhibited a cubic zinc-blend structure with high quantum yield of 70±2.5%, comparable to that of commercial CdSe/ZnS core/shell OQDs (81.6±2.5%). NIR CdPbS AQDs exhibited a cubic rock-salt structure.

- MPS-replaced AQDs were able to stabilize the AQDs and provide thiol groups on the surface for different conjugation strategy.

- For biotin-streptavidin-biotin sandwich, the best imaging condition for AQDs occurred when one AQD was bound with 3±0.3 SA with a nominal SA/AQD ratio of 4 corresponding to an SA conjugation efficiency of 75±7.5%.

- Multiple AQDs can be attached to a single SA molecule or antibody, which cannot be achieved with OQDs.

- SM(PEG)12 was the optimal length linker. With 3 AQDs per antibody, minimal amount of the probe is needed for strong fluorescent signal without amplification. This is important for application in live cell tracking and *in vivo* imaging. AQDs are 20-100 times more efficient in bioconjugation than OQDs.

- Tn antigen expression was shown to have 95% sensitivity and 90% specificity in identifying the cancer cells using CdSe AQD-SA probes, which was higher than that of VEGF (sensitivity=90%, and specificity=78%).

- AQD probes were more sensitive and specific compared to the HRP-IHC method (sensitivity=90%, and specificity=80% for Tn antigen).

- Direct staining of Tn antigen expression using NIR CdPbS AQD-Tn mAb probes showed even higher sensitivity and specificity (sensitivity=95% specificity=96%) compared to the indirect staining method of CdSe AQD-SA probes

BIBIOGRAPHY

1. Heron, M. (2007) Deaths: leading causes for 2004, *Natl Vital Stat Rep 56*, 1-95.

2. Ferlay, J., Autier, P., and M., B. (2007) Estimates of the cancer incidence and mortality in Europe in 2006, *Ann Oncol 18*, 581-592.

3. (2012) Breast Cancer Overview, American Cancer Society.

4. Medina-Franco, H., Abarca-Perez, L., Garcia-Alvarez, M. N., Ulloa-Gomez, J. L., Romero-Trejo, C., and Sepulveda-Mendez, J. (2008) Radioguided occult lesion localization (ROLL) versus wire-guided lumpectomy for non-palpable breast lesions: a randomized prospective evaluation, *J Surg Oncol 97*, 108-111.

5. Veronesi, U., Cascinelli, N., and Mariani, L. (2002) Twenty year follow-up of a randomized study comparing breast-conserving surgery with radical mastectomy for early breast cancer, *Am J Surg 347*, 1227-1232.

6. Fisher, B., Anderson, S., and Bryant, J. (2002) Twenty-year follow-up for a randomized trial comparing total mastetomy, lumpectomy and lumpectomy plus radiation for the treatment of breast cancer, *N Engl J Med 347*, 1233-1241.

7. Balch, G. C., Mithani, S. K., Simpson, J. F., and Kelley, M. C. (2005) Accuracy of intraoperative gross examination of surgical margin status in women undergoing partial mastectomy for breast malignancy, *Am J Surg 71*, 22-28.

8. Cabioglu, N., Hunt, K. K., Sahin, A. A., Kuerer, H. M., Babiera, G. V., Singletary, S. E., Whitman, G. J., Ross, M. I., Ames, F. C., Feig, B. W., Buchholz, T. A., and Meric-Bernstam, F. (2007) Role for intraoperative margin assessment in patients undergoing breast-conserving surgery, *Ann Surg Oncol 14*, 1458-1471.

9. Jacob, L. (2008) Positive margins: the challenge continues for breast surgeons, *Ann Surg Oncol 15*, 1271-1272.

10. Chagpar, A., T., Y., A., S., Hunt, K. K., Whitman, G. J., Ames, F. C., Ross, M. I., Meric-Bernstam, F., Babiera, G. V., Singletary, S. E., and Kuerer, H. M. (2003) Intraoperative margin assessment reduces reexcision rates in patients with ductal carcinoma in situ treated with breast-conserving surgery, *Am J Surg 186*, 371-377.

11. Kreike, B., Hart, A. A., and van de Velde, T. (2008) Continuing risk of ipsilateral breast relapse after breast-conserving therapy at long term follow-up, *Int J Radiat Oncol Biol Phys 71*, 1014-1021.

12. Fisher, E. R., Anderson, S., Redmond, C., and Fisher, B. (1992) Ipsilateral breast tumor recurrence and survival following lumpectomy and irradiation: pathological findings from NSABP protocol B-06, *Semin Surg Oncol 8*, 161-166.

13. Haffty, B. G., Reiss, M., Beinfield, M., Fisher, D., Ward, B., and McKhann, C. (1996) Ipsilateral breast tumor recurrence as a predictor of distant disease: implications for systemic therapy at the time of local relapse, *J Clin Oncol 14*, 52-57.

14. Rouzier, R., Extra, J. M., Carton, M., Falcou, M. C. V.-S., A., Fourquet, A., Pouillart, P., and Bourstyn, E. (2001) Primary chemotherapy for operable breast cancer: incidence and prognostic significance of ipsilateral breast tumor recurrence after breast-conserving surgery, *J Clin Oncol 19*, 3828-3835.

15. Clarke, M., Collins, R., Darby, S., Davies, C., Elphinstone, P., Evans, E., Godwin, J., Gray, R., Hicks, C., James, S., MacKinnon, E., McGale, P., Peto, R., Taylor, C., Wang, Y., and (EBCTCG), E. B. C. T. C. G. (2005) Effects of radiotherapy and of differences in the extent of surgery for early breast cancer on local recurrence and 15 year survival: an overview of the randomized trials, *The Lancet 366*, 2087-2106.

16. Méndez, J. E., Lamorte, W. W., de Las Morenas, A., Cerda, S., Pistey, R., King, T., Kavanah, M., Hirsch, E., and Stone, M. D. (2006) Influence of breast cancer margin assessment method on the rates of positive margins and residual carcinom, *Am J Surg 192*, 538-540.

17. Olson, T. P., Harter, J., Munoz, A., Mahvi, D. M., and Breslin, T. (2007) Frozen Section Analysis for Intraoperative Margin Assessment During Breast-Conserving Surgery Result in Low Rates of Re-excision and Local Recurrence, *Ann Surg Oncol 14*, 2983-2960.

18. Poggi, M. M., Danforth, D. N., Sciuto, L. C., Smith, S. L., Steinberg, S. M., Liewehr, D. J., Menard, C., Lippman, M. E., Lichter, A. S., and Altemus, R. M. (2003) Eighteen-year results in the treatment of early breast carcinoma with mastectomy versus breast conservation therapy: the National Cancer Institute Randomized Trial, *Cancer 98*, 697-702.

19. Singletary, S. E. (2002) Surgical margins in patients with early stage breast cancer treated with breast conservation therapy, *Am J Surg 184*, 383-393.

20. Miller, A. R., Brandao, G., Prihoda, T. J., Hill, C., Cruz, A. B. J., and Yeh, I. T. (2004) Positive margins following surgical resection of breast carcinoma: analysis of pathologic correlates, *J Surg Oncol 86*, 134-140.

21. Cao, D., Lin, C., Woo, S. H., Vang, R., Tsangaris, T. N., and Argani, P. (2005) Separate cavity margin sampling at the time of initial breast lumpectomy significantly reduces the need for reexcisions, *Am J Surg Pathol 29*, 1625-1632.

22. Dunne, C., Burke, J. P., Morrow, M., and Kell, M. R. (2009) Effect of Margin Status on Local Recurrence after Breast Conservation and Radiation Therapy for Ductal Carcinoma In Situ, *J Clin Oncol 27*, 1615-1620.

23. Pleijhuis, R. G., Graafland, M., Vries, J., Bart, J., Jong, J. S., and Dam , G. M. (2009) Obtaining adequate surgical margins in breast-conserving therapy for patients with early-stage breast cancer: current modalties and future directions, *Ann Surg Oncol 16*, 2717-2730.

24. Veronesi U., C. N., Mariani L. (2002) Twenty year follow-up of a randomized study comparing breast-conserving surgery with radical mastectomy for early breast cancer, *Eng J Med 347*, 1227-1232.

25. Valdes, E. K., Boolbol, S. K., Cohen, J. M., and Feldman, S. M. (2007) Intra-operative touch preparation cytology; does it have a role in re-excision lumpectomy, *Ann Surg Oncol 14*, 1045-1050.

26. Olson, T. P., Harter, J., Munoz, A., Mahvi, D. M., and Breslin, T. M. (2007) Frozen Section Analysis for Intraoperative Margin Assessment During Breast-Conserving Surgery Result in Low Rates of Re-excision and Local Recurrence, *Ann Surg Oncol 14*.

27. Dener, C., Inan, A., Sen, M., and Demirci, S. (2009) Intraoperative frozen section for margin assessment in breast concerving surgery, *Scand J Surg 98*, 34-40.

28. Pappo, I., Spector, R., Schindel, A., Morgenstern, S., Sandbank, J., Leider, L. T., Schneebaum, S., Lelcuk, S., and Karni, T. (2010) Diagnostic performance of a novel device for real-time margin assessment in lumpectomy specimens, *J Surg Res 160*, 277-281.

29. Nguyen F.T., Z. A. M., Chaney E.J., Kotynek J.G., Oliphant U.J., Bellafiore F.J., Rowland K.M., Johnson P.A., Boppart S.A. (2009) Intraoperative evaluation of breast tumor margins with optical coherence tomography, *Cancer Res 69*, 8790-8797.

30. Izuishi, K., Tajiri, H., Fujii, T., Boku, N., Ohtsu, A., Ohnishi, T., Ryi, M., Kinoshita, T., and Yoshida, S. (1999) The histological basis of detection of adenoma and cancer in the colon by autofluorescence endoscopic imaging, *Endoscopy 31*, 511-516.

31. De Veld, D. C., Witjes, M. J., Sterenborg, H. J., and Roodenburg, J. L. (2005) The status of *in vivo* autofluorescence sprectroscopy and imaging for orfal oncology, *Oral Oncol 41*, 117-131.

32. Burkholder, H. C., Witherspoon, L. E., and R.P., B. (2007) Breast surgery techniques: preoperative bracketing wire localization by surgeon. Am J Surg, *Am J Surg 73*, 574-578.

33. Wallace, A. M., Daniel, B. L., Jefferey, S. S., Birdwell, R. L., Nowels, K. W., Dirbas, F. M., Schraedley-Desmond, P., and Ikeda, D. M. (2005) Rates of reexcision for breast cancer after magnetic resonance imaging-guided bracket wire localization, *J Am Coll Surg 200*, 527-537.

34. Law, T. T., and Kwong, A. (2009) Surgical Margins in Breast Conservation Therapy: How Much Should We Excise?, *Southern Med J 102*, 1234-1238.

35. Nguyen, Q. T., Olson, E. S., Aguilara, T. A., Jiang, T., Scadeng, M., Ellies, L. G., and Tsien, R. Y. (2010) Surgery with molecular fluorescence imaging using activatable cell-penetrating peptides decreases residual cancer and improves survival, *PNAS 107*, 4317-4322.

36. van Dam, G. M., Themelis, G., Crane, L. M. A., Harlaar, N. J., Pleijhuis, R. G., Kelder, W., Sarantopoulos, A., de Jong, J. S., Arts, H. J. G., van der Zee, A. G. J., Bart, J., Low, P. S., and Ntziarchristos, V. (2011) Intraoperative tumor-specific fluorescence imaging in overaian cancer by folate receptor-a targeting: first in-human results, *Nat Med 17*, 1315-1320.

37. Deliolanis, N. C., Schultz, C. P., and Ntziachristos, V. (2012) Fluorescence Imaging, In *Biomedical Imaging: Principles and Applications* (Salzer, R., Ed.), p 248, Wiley, Hoboken, NJ, USA.

38. Zhou, M., and Ghosh, I. (2007) Quantum dots and peptides: A bright future together, *Biopolymers 88*, 325-339.

39. Watanabe, M., Fujioka, K., Akiyama, N., Takeyama, H., Manabe, N., Yamamoto, K., and Manome, Y. (2011) Conjugation of Quantum Dots and JT95 IgM Monoclonal Antibody for Thyroid Carcinoma without abolishing the specificity and activity of the antibody, *IEEE Trans Nanobioscience 10*, 30-36.

40. Xia, Z., Xing, Y., So, M. K., Koh, A. L., SInclair, R., and Rao, J. (2008) Multiplex detecion of protease activity with quantum dor nano sensors preapred by interinmediated specific bioconjugation, *Anal Chem 80*, 8649-8655.

41. Wu, X., Liu, H., Liu, J., Haley, K. N., Treadway, J. A., Larson, J. P., Ge, N., Peale, F., and Bruchez, M. P. (2003) Immunofluorescent labeling of cancer

marker Her2 and other cellular targets with semiconductor quantum dots, *Nat. Biotechnol. 21*, 41-46.

42. Jaiswal, J. K., Goldman, E. R., Mattoussi, H., and Simon, S. M. (2004) Use of quantum dots for live cell imaging, *Nat Methods 1*, 73-78.
43. Wu, C. S., Oo, M. K. K., Cupps, J. M., and Fan, X. (2011) *Biosen Bioelectron 26*, 3870.

44. Kim, S., Lim, Y. T., Soltesz, E. G., De Grand, A. M., Lee, J., Nakayama, A., Parker, J. A., Mihaljevic, T., Laurence, R. G., Dor, D. M., Cohn, L. H., Bawendi, M. G., and Frangioni, J. V. (2004) Near-infrared fluorescence type II quantum dots for entinel lymph node mapping, *Nat Biotechnol 22*, 93-97.

45. Wang, J., Yong, W. H., Sun, Y., Vemier, P. T., Koeffler, H. P., Gundersen, M. A., and Marcu, L. (2007) Receptor-targeted quantum dots: fluorescenct probes for brain tumor diagnosis, *J Biomed Opt 12*.

46. Zhang, C. Y., and Hu, J. (2010) Single Quantum Dot - Based Nanosensor for Multiple DNA Detection, *Analytical Chemistry 82*, 1921-1927.

47. Cady, N. C. (2009) Quantum Dot Molecular Beacons for DNA Detection, *Mehods Mol Biol 544*, 367-379.

48. Kim, J. H., Chaudhary, S., and Ozkan, M. (2007) Multicolor Hyrid nanoprobes of molecular beacon conjugated quantum dots: FRET and gel electrophoresis assisted target DNA detection, *Nanotechnology 18*, 195105.

49. Papagiannaros, A., Upponi, J., Hartner, W., Mongayt, D., Levchenko, T., and Torchilin, V. (2010) Quantum dot loaded immunomicelles for tumor imaging, *BMC Medical Imaging 10*, 22-31.

50. Jiang, W., Papa, E., Fischer, H., Mardyani, S., and Chan, W. C. (2004) Semiconductor quantum dots as contract agents for whole animal imaging, *Trends Biotechnol 22*, 607-609.

51. Arriagada, R., Le, M. G., Rochard, F., and Contesso, G. (1996) Conservative treatment versus mastectomy in early breast cancer: patterns of failure with 15 years of follow-up data. Institut Gustave-Roussy Breast Cancer Group, *J Clin Oncol 14*, 1558-1564.

52. Kurniawan, E. D., Wong, M. H., Windle, I., Rose, A., Mou, A., Buchanan, M., Collins, J. P., Miller, J. A., Gruen, R. L., and Mann, G. B. (2008) Predictors of surgical margin status in breast-conserving surgery within a breast-screening program, *Ann Surg Oncol 15*, 2542-2549.

53. Thind, C. R., Desmond, S., Harris, O., Nadeem, R., Chagla, L. S., and Audisio, R. A. (2005) Radio-guided localization of clinically occult breast lesions (ROLL): a DGH experience, *Clin Radiol 60*, 681-686.

54. Schimidt-Ullrich, R., Wazer, D. E., Tercilla, O., Safaii, H., Marchant, D. J., Smith, T. J., Homer, M. A., and Robert, N. J. (1989) Tumor margin assessment as a guide to optimal conservation surgery and irradiation in early stage breast carcinoma, *Int J Radiat Oncol Biol Phys 17*, 733-738.

55. Haid, A., Knauer, M., Dunzinger, S., Jasarevic, Z., Koberle-Wuher, R., Schuster, A., Toeppker, M., Haid, B., Wenzl, E., and Offner, F. (2007) Intra-operative sonography: a valuable aid during breast-conserving surgery for occult breast cancer, *Ann Surg Oncol 14*, 3090-3101.

56. Klimberg, V. S. (2003) Advances in the diagnosis and excision of breast cancer, *Am Surg 69*, 11-14.

57. Smith, L. F., Rubio, I. T., Henry-Tillman, R., Korourian, S., and Klimberg, V. S. (2000) Intraoperative ultrasound-guided breast biopsy, *Am J Surg 180*, 419-423.

58. Cendan, J. C., Coco, D., and Copeland, E. M. (2005) Accuracy of intraoperative frozen-section analysis of breast cancer lumpectomy-bed margins, *J Am Coll Surg 201*, 194-198.

59. Riedl, O., Fitzal, F., and Mader, N. (2009) Intraoperative frozen section analysis for breast-conserving therapy in 1016 patients with breast cancer, *Eur J Surg Oncol 35*, 264-270.

60. Pleijhuis, R. G., Graafland, M., Vries, J., Bart, J., Jong, J. S., and Dam, G. M. (2009) Obtaining adequate surgical margins in breast-conserving therapy for patients with early-stage breast cancer: current modalities and future directions, *Ann Surg Oncol 16*, 2717-2730.

61. Bakhshandeh, M., Tutucuoglu, O. S., Fischer, G., and Masood, S. (2007) Use of imprint cytology for assessment of surgical margins in lumpectomy specimens of breast cancer patients, *Diagnostic Cytopathology 35*, 656-659.

62. Weinberg, E., Cox, C., Dupon, E., White, L., Ebert, M., Greenberg, H., Diaz, N., Vercel, V., Centeno, B., Cantor, A., and Nicosia, S. (2004) Local recurrence in lumpectomy patients after imprint cytology margin evaluation, *Am J Surg 188*, 349-354.

63. Jacobs, L. (2008) Positive margins: the challenge continues for breast surgeons, *Ann Surg Oncol 15*, 1271-1272.

64. Thill, M., Roder, K., Diedrich, K., and Dittmer, C. (2011) Intraoperative assessment of surgical margins during breast conserving surgery of ductal carcinoma in situ by use of radiofrequency spectroscopy, *The Breast 20*, 579-580.

65. Alweis, T. M., Kaufman, Z., Lelcuk, S., Pappo, I., Kami, T., Schneebaum, S., Spector, R., Schindel, A., Hershko, D., Zilberman, M., Sayfan, J., Berlin, Y., Hadary, A., Olsha, O., Paran, H., Gutman, M., and Carmon, M. (2008) A prospective, randomized, controlled, multicenter study of a real-time, intraoperative probe for positive margin detection in breast-conserving surgery, *Am J Surg 196*, 483-489.

66. Kami, T., Pappo, I., Sandbank, J., Lavon, O., Kent, V., Spector, R., Morgenstern, S., and Lelcuk, S. (2007) A device for real-time, intraoperative margin assessment in breast-conservation surgery, *Am J Surg 194*, 467-473.

67. Backer, M. V., Levashova, Z., Patel, V., Jehning, B. T., Claffey, K., Blankenberg, F. G., and Backer, J. M. (2007) Molecular imaging of VEGF receptors in angiogenic vasculature with single-chain VEGF-based probes, *Nat Med 13*, 504-509.

68. Sampath, L., Kwon, S., Ke, S., Wang, W., Schiff, R., Mawad, M. E., and Servick-Muraca, E. M. (2007) Dual-labeled trastuzumab-based imaging agent for the detection of human epidermal growth factor receptor 2 overexpression in breast cancer, *J Nucl Med 48*, 1501-1510.

69. Lee, S. B., Hassan, M., Fisher, R., Chertov, O., Chernomordik, V., Kramer-Marek, G., Gandjbakhche, A., and Capala, J. (2008) Affibody molecules for in vivo characterization of HER2-positive tumors by near-infrared imaging, *Clin Cancer Res 14*, 3840-3849.

70. Terwisscha van Scheltinga, A. G. T., van Dam, G. M., Nagengast, W. B., Ntziachristos, V., Hollema, H., Herek, J. L., Schroder, C. P., Kosterink, J. G. W., Lub-de Hoog, M. N., and de Vries, E. G. E. (2011) Intraoperative Near-Infrared Fluorescence Tumor Imagingvwith Vascular Endothelial Growth Factor and Human Epidermal Growth Factor Receptor 2 Targeting Antibodies, *J Nucl Med 52*, 1778-1785.

71. Ntziachristos, V. (2006) Fluorescence Molecular Imaging, *Annial Review of Biomedical Engineering 8*, 1-33.

72. Bremer, C., Ntziachristos, V., Weitkamp, B., Theilmeier, G., Heindel, W., and Weissleder, R. (2005) Optical imaging of spontaneous breast tumors using protease sensing 'smart' optical probes, *Invest Radiol 40*, 321-327.

73. Tung, C. H., Mahmood, U., Bredow, S., and Weissleder, R. (2000) In vivo imaging of proteolytic enzyme activity using a novel molecular reporter, *Cancer Res 60*, 4953-4958.

74. Stanciute, D., Didziapetriene, J., and Kadziauskas, J. (2004) Expression of matrix metalloproteinases in patients with malignant tumors, *Medicina 40*, 1143-1150.

75. Madajewski, B., Judy, B. F., Mouchli, A., Kapoor, B., Holt, D., Wang, M. D., Nie, S., and Singhal, S. (2012) Intraoperative Near-Infrared Imaging of Surgical Wounds after Tumor Resections Can Detect Residual Disease, *Clin Cancer Res 18*, 5741-4751.

76. Mohs, A. M., Mancini, M. C., Singhal, S., Provenzale, J. M., Leyland-Jones, B., Wang, M. D., and Nie, S. (2010) A Handheld Spectroscopic Device for In Vivo and Intraoperative Tumor Detection: Contrast Enhancement, Detection Sensitivity, and Tissue Penetration, *Anal Chem 82*, 9058-9065.

77. Murray, C. B., Norris, D. J., and Bawendi, M. G. (1993) Synthesis and Characterization of Nearly Monodisperse CdE (E = S, Se, Te) Semiconductor Nanocrystallites, *J Am Ceram Soc 115*, 8706-8715.

78. Mazumder, S., Dey, R., Mitra, M. K., Mukherjee, D., and Das, G. C. (2009) Review: Biofunctionalized Quantum Dots in Biology and Medicine, *Journal of Nanomaterials 2009*.

79. Kim, S., and Bawendi, M. G. (2003) Oligomeric ligands for luminescent and stable nanocrystal quantum dots, *J. Am. Chem. Soc. 125*, 14652-14653.

80. Kim, S. W., Kim, S., Tracy, J. B., Jasanoff, A., and Bawendi, M. G. (2005) Phosphine oxide polymer for water-soluble nanoparticles, *J Am Ceram Soc 125*, 4556-4557.

81. Yu, W. W., Chang, E., Drezek, R., and Colvin, V. L. (2006) Water-Soluble quantum dots for biomedical applications, *Biochemical and Biophyscical Research Communication 348*, 781-786.

82. Lesnyak, V., Gaponik, N., and Eychmuller, A. (2013) Colloidal semiconductor nanocrystals: the aqueous approach, *Chem Soc Rev 42*, 2905-2929.

83. Schumacher, W., Nagy, A., Waldman, W. J., and Dutta, P. K. (2009) Direct synthesis of aqueous CdSe/ZnS-Based Quantum Dots using Microwave Irradiation, *J Phys Chem C 113*, 12132-12139.

84. Vossmeyer, T., Katsikas, L., Giersig, M., Popovic, I. G., Diesner, K., Chemseddine, A., Eychmuller, A., and Weller, H. (1994) CdS nanocluster - synthesis, characterization, size-dependent oscillator strength, temperature shift of

the excitonic transition energy, and reversible absorbency shift, *J Phys Chem 98*, 7665-7673.

85. Chen, H. M., Huang, X. F., Xu, L., Xu, J., Chen, K. J., and Feng, D. (2000) Self-assembly and photoluminescence of CdS-mercaptoacetic clusters with interenal structures, *Supperlattices Microstruct 27*, 1-5.

86. Rogach, A. L., Eychmuller, A., Kornowski, A., and Weller, H. (1998) Thiol-stabilized CdSe and CdTe Nanocrystals in the size Quantization Regime: Synthesis, Optical and Structural Properties, *Macromol. Symp 136*, 87-89.

87. Gao, M. Y., Kristein, S., Mohwald, H., Rogach, A. L., Kornowski, A., Eychmuller, A., and Weller, H. (1998) Strongly photoluminescent CdTe nanpcrystals by proper surface modification, *J Phys Chem B 102*, 8360-8363.

88. Zhou, D., Han, J., Liu, Y., Liu, M., Zhang, X., Zhang, H., and Yang, B. (2010) Nucleation of aquepus semiconductor nanocrystals: a neglected factor for determining the photoluminescence, *J Phys Chem C 114*, 22487-22492.

89. Li, H., Shih, W. Y., and W.-H., S. (2010) Highly photoluminescent and stable aqueous ZnS quantum dots, *Ind. & Eng. Chem. Res. 49*, 578-582.

90. Li, H., Shih, W. Y., and W.-H., S. (2007) Non-heavy metal ZnS quantum dots with bright blue photoluminescence by a one-step aqueous synthesis, *Nanotechnology 18*, 5604.

91. Li, H., Shih, W. Y., and Shih, W. H. (2007) Synthesis and characterization of aquoues carboxyl-capped CdS quantum dots for bioapplications, *Ind. & Eng. Chem. Res. 46*, 2013-2019.

92. Jin, S., Hu, Y., Gu, Z., Liu, L., and Wu, H.-C. (2011) Application of Quantum Dots in Biological Imaging, *Journal of Nanomaterials 2011*, 1-13.

93. Cao, Y. A., Kang, K., Li, Z. G., Zhao, C., Shi, C. M., and Yang, J. (2010) Near-infrared quantum-dot-based non-invasive in vivo imaging of squamous cell carcinoma U14, *Nanotechnology 21*, 475104.

94. Jiang, W., Shinghal, J. N., Wang, C., and Chan, W. C. W. (2006) Optimizing the synthesis of red- to near-IR-emitting CdS-capped $CdTe_xSe_{1-x}$ alloyed quantum dots for biomedical imaging, *Chemistry of Materials 18*, 4845-4854.

95. Jaiswal, J. K., Mattoussi, H., Mauro, J. M., and Simon, S. M. (2003) Long-term multiple color imaging of live cells using quantum dot bioconjugates, *Nat. Biotechnol. 21*, 47-51.

96. Gac, S. L., Vermes, I., and Berg, A. V. D. (2006) Quantum dots based probe conjugated to annexin V for photostable apoptosis detection and imaging, *Nano Lett 6*, 1863-1869.

97. Bagalkot, V., Zhang, L., Levy-Nissenbaum, E., Jon, S., Kantoff, P. W., Langer, R., and Farokhzad, O. C. (2007) Quantum dot-aptamer conjugates for synchronous cancer imaging, therapy, and sensing of drug delivery based on bi-fluorescence resonance enegery transfer, *Nano Lett 7*, 3065-3070.

98. Li, H., Shih, W. H., Shih, W. Y., Chen, L., Tseng, S. J., and Tang, S. C. (2008) Transfection of aqueous CdS quantum dots using polyethylenimine, *Nanotechnology 19*, 1-8.

99. Au, G. H. T., Shih, W. Y., Tseng, S. J., and Shih, W. H. (2012) Aqueoues CdPbS quantum dots for near-infrared imaging, *Nanotechnology 23*, 275601.

100. Kuo, C. W., Chueh, D. Y., Singh, N., Chien, F. C., and Chen, P. (2011) Targeted Nuclear Delivery using Peptide-Coated Quantum Dots, *Bioconjugate Chemistry*.

101. Biju, V., Muraleedharan, D., and Nakayama, K. I. (2007) Quantum dot-insect neuropeptide conjugates for fluorescence imaging, transfection and nucleus targeting of living cells, *Langmuir 23*, 10254-10261.

102. Rizvi, S. B., Ghaderi, S., Keshtgar, M., and Seifalian, A. M. (2010) Semiconductor quantum dots as fluorescent probes for in vitro and in vivo bio-molecular and cellular imaging, *Nano Review 1*.

103. Gao, X., Cui, Y., Levenson, R. M., Chung, L. W. K., and Nie, S. (2004) In vivo cancer targeting and imaging with semiconductor quantum dots, *Nat. Biotechnol. 22*, 969-976.

104. Chen, L.-D., Liu, J., Yu, X.-F., He, M., Pei, X.-P., Tang, Z.-Y., Wang, Q.-Q., Pang, D. W., and Li, Y. (2008) The biocompatibility of quantum dot probes used for the targeted imaging of hepatocelluar carcinomas metastasis, *Biomaterials 29*, 4170-4176.

105. Richards-Kortum, R., and Sevick-Muraca, E. (1996) Quantitative optical spectroscopy for tissue diagnosis, *Ann Rev Phys Chem 47*, 555-666.

106. Ramanujam, N. (2000) Fluorescence Spectroscopy of Neoplastic and Non-Neoplastic Tissues, *Neoplasia 2*, 89-117.

107. Koenig, F., McGovern, F. J., Enquist, H., Larne, R., Deutsch, T. F., and Schomacker, K. T. (1998) Autofluorescence guided biopsy for the early diagnosis of bladder carcinoma, *J Urol 159*, 1871-1875.

108. Alfano, R. R., Tang, G. C., Pradhan, A., Lam, W., Choy, D. S. J., and Opher, E. (1987) Fluorescence spectra from cancerous and normal breast and lung tissue, *IEEE J Quatum Electron 23*, 1806-1811.

109. Lohmann, W., and Kunzel, S. (1990) Fluorescence tomographical studies on breast tissue with cancer, *Naturwissenschaften 77*, 476-478.

110. Rogach, A. L., and Ogris, M. (2010) Near-infrared-emitting semiconductor quantum dots for tumor imaging and targeting, *Curr. Opin. Mol. Ther. 12*, 331-339.

111. Allen, P. M., Lin, W., Chauhan, V. P., Lee, J., Ting, A. Y., Fukumura, D., Jain, R. K., and Bawendi, M. G. (2010) InAs(ZnCdS) Quantum Dots Optimized for Biological Imaging in the Near-Infrared, *J. Am. Chem. Soc. 132*, 470-471.

112. Ntziachristos, V., Ripoll, J., and Weissleder, R. (2002) Would near-infrared fluorescence signals propagate through large human organs for clinical studies?, *Opt. Lett. 27*, 572-592.

113. Obonvo, O., Fisher, E., Edwards, M., and Douroumis, D. (2010) Quantum dots synthesis and biological applications as imaging and drug delivery systems, *Crit. Rev. Biotechnol. 30*, 283-301.

114. Sargent, E. H. (2005) Infrared Quantum Dots, *Advanced Mat. 15*, 515-522.

115. Yang, M., Baranov, E., and Jiang, P. (2000) Whole-body optical imaging of green fluorescent protein-expressing tumors and metastases, *Proc. Natl. Acad. Sci. USA 97*, 1206-1211.

116. He, X., Gao, J., Gambhir, S. S., and Cheng, Z. (2010) Near-infrared fluorescent nanoprobes for cancer molecular imaging: status and challenges, *Trends in Molecular Medicine 16*, 574-583.

117. Xie, R., Chen, K., Chen, X., and Peng, X. (2010) InAs/InP/ZnSe core/shell/shell quantum dots as near-infrared emitters: Bright, narrow-band, non-cadmium containing, and biocompatible, *Nano. Res. 1*, 457-464.

118. Park, J., Dvoracek, C., Lee, K. H., Galloway, J. F., Bhang, H. C., Pomper, M. G., and Searson, P. C. (2011) CuInSe/ZnS Core/Shell NIR Quantum Dots for Biomedical Imaging, *Small 27*, 3148-3152.

119. Rogach, A. L., Kornowski, A., Gao, M., Eychmuller, A., and Weller, H. (1999) Synthesis and Characterization of a size series of extremely small thiol-stabilized CdSe nanocrystals, *J Phys Chem B 103*, 3065-3069.

120. Williams, A. T. R., Winfield, S. A., and Miller, J. N. (1983) Relative Fluorescence Quantum Yield Using a Computer Controlled Luminescence Spectrometer, *Analyst 108*, 1067-1071.

121. Karstens, T. K., K. (1980) Rhodamine-B and Rhodamine-101 as reference substances for fluorescence quantum yield measurement, *J. Phys. Chem. 84*, 1871-1872.

122. Gupta, P., and Ramrakhiani, M. (2009) Influence of the Particle Size on the Optical Properties of CdSe Nanoparticles, *The Open Nanoscience Journal 3*, 15-19.

123. Yang, X. Q., Chen, C., Peng, C. W., Hou, J. X., Gong, Y. P., Zhu, X. B., Pang, D. W., and Li, Y. (2011) Quantum dot-based quantitative immunofluorescence detection and spectrum analysis of epidermal growth factor receptor in breast cancer tissue arrays, *International Journal of Nanomedicine 6*, 2265-2273.

124. Rogach, A. L., Harrison, M. T., Kershaw, S. V., Kornowski, A., Burt, M. G., Eychmuller, A., and Weller, H. (2001) Colloidally Prepared CdHgTe and HgTe Quantum Dots with Strong Near-Infrared Luminescence, *Phys Status Solidi B 224*, 153-158.

125. Hartnett, P., O'Malley, R., Shih, W. Y., and Shih, W.-H. (2009) REU poster, Drexel University, PA, Philadelphia.

126. Fernee, M., Watt, A., Warner, J., Riches, J., Heckenberg, N., and Rubinsztein-Dunlop, H. (2004) Investigation of the role of cadmium sulfide in the surface passivation of lead sulfie quantum dots, *Journal of Crystal Growth 270*, 380-383.

127. Denton, A. R., and Ashcroft, N. W. (1991) Vegard's law, *Phys Rev A 43*, 3161.

128. Shih, W. Y., Shih, W. H., and Aksay, I. A. (1996) Heteroflocculation in binary colloidal suspensions: monte carlo simulations, *J Am Ceram Soc 79*, 2587-2591.

129. Liu, J., Sarikaya, M., Shih, W. Y., and Aksay, I. A. (1990) Fractal colloidal aggregates with finite interparticle interactions: energy dependence of the fractal dimension, *Phys Rev A 41*, 3206.

130. Li, H., Shih, W. Y., and W.-H., S. (2007) Stable aqueous ZnS quantum dots obtained using (3-mercaptopropyl)trimethoxysilane as a capping molecule, *Nanotechnology 18*, 5605.

131. Li, Z., and Du, Y. M. (2003) Biomimic synthesis of CdS nanoparticles with enhance luminescence *Mater Lett 57*, 2480-2484.

132. Aldana, J., Wang, Y. A., and Peng, X. G. (2001) Photochemical instability of CdSe nantocrystals coated by hydrophilic thiols, *J Am Ceram Soc 123*, 8844-8850.

133. Grabarek, Z., and Gergely, J. (1990) Zero-length crosslinking procedure with the use of active esters, *Anal Biochem 185*, 131-135.

134. Staros, J. V., Wright, R. W., and Swingle, D. M. (1986) Enhancement by n-hydroxysulfosuccinimide of water-soluble carbodimide-mediated coupling reactions, *Anal Biochem 156*, 220-222.

135. EDC - A water soluble carbodiimide crosslinker for zero-length, carboxyl-to-amine conjugation, Thermo Scientific.

136. Konska, G., Guerry, M., Caldefie-Chezet, F., De Latour, M., and Guillot, J. (2006) Study of the expression of Tn antigen in different types of human breast cancer cells using VVA-B4 lectin *Oncol Rep 15*, 305-310.

137. Nakagoe, T., Sawai, T., Tsuji, T., Jibiki, M., Nanashima, A., Yamagushi, H., Yasutake, T., and Ayabe, H. (2001) Pre-operative serum level of sialyl Tn antigen predict liver metastasis and poor prognosis in patients with gastric cancer, *Eur J Surg 27*, 731-739.

138. Davidson, B., Berner, A., Nesland, J. M., Risberg, B., Kristensen, G. B., Trope, C. G., and Bryne, M. (2000) Carbohydrate antigen expression in primary tumors, mestastic lesions, and serous effusions from patients diagosed with eptithelial ovarian carcinoma: evidence of up regulated Tn and Sialyl Tn antigen expression in effusions, *Hum Pathol 31*, 1081-1087.

139. Konno, A., Hoshino, Y., Terashima, S., Motoki, R., and Kawaguchi, T. (2002) Carbohydrate expression profile of colorectal cancer cells is relevant to metastitic pattern and prognosis, *Clinical & Experimental Metastasis 19*, 61-70.

140. Springer, G. (1997) Immunoreactive T and Tn epitopes in cancer disgnosis, prognosis and immunotherapy, *J of Mol Med 75*, 594-602.

141. Probes, M. (2007) Qdot ITK Carboxyl Quantum Dots, Invitrogen.

142. Liu, H. Y., and Gao, X. (2011) Engineering Monovalent Quantum Dot-Antibody Conjugates with a Hybrid Gel System, *Bioconjugate Chemistry 22*, 510-517.

143. Clarke, S., Pinaud, F., Beutel, O., You, C., Piehler, J., and Dahan, M. (2010) Covalent Monofunctionalization of peptide-coated quantum dots for single-molecule assays, *Nano Lett 10*, 2147-2154.

144. Pathak, S., Davidson, M. C., and Silva, G. A. (2007) Characterization of the Functinal Binding Properites of Antibody Conjugated Quantum Dots, *Nano Lett 7*, 1839-1848.

145. Zhang, J. L., Han, B. X., Liu, D. X., Chen, J., Liu, Z. M., Mu, T. C., Zhang, R., and Yang, G. Y. (2004) Effects of ultrasound on the microenvironment in reverse micelles and synthesis of nanorods and nanofibers, *Phys Chem Chem Phys 6*, 2391-2395.

146. Kirchner, C., Liedl, T., Kudera, S., Pellegrino, T., Munoz Javier, A., Gaub, H. E., Stolzle, S., Fertig, N., and Parak, W. J. (2005) Cytotoxicity of collodial CdSe and CdSe/ZnS nanoparticles, *Nano Lett 5*, 331-337.

147. Jovin, T. M. (2003) Quantum dots finally come of age, *Nature Biotechnology 21*, 32-33.

148. Choi, Y., Kim, K., Hong, S., Kim, H., Kwon, Y. J., and Song, R. (2011) Intracellular protein target detection by quantum dots optimized for live cell imaging, *Bioconjugate Chemistry 22*, 1576-1586.

149. Swift, J. L., and Cramb, D. T. (2008) Nanoparticles as fluorescence lables: is size all the matters?, *Biophys J 95*, 865-876.

150. Groc, L., Lafourcade, M., Heine, M., Renner, M., Racine, V., Sibarita, J. B., Lounis, B., Choquet, D., and Cognet, L. (2007) Surface trafficking of neurotransmitter receptor: comparison between single molecule/quantum dot strategies, *J Neurosci 27*, 12433-12437.

151. Howarth, M., Liu, H., Puthenveetil, S., Zheng, Y., Marshall, L. F., Schmidt, M. M., Wittrup, K. D., Bawendi, M. G., and Ting, A. Y. (2008) Monovalent reduced-size quantum dots for imaging receptors on living cells, *Nat Methods 5*, 397-399.

152. Wang, K., Ruan, J., Qian, Q., Song, H., Bao, C., Zhang, X., Kong, Y., Zhang, C., Hu, G., Ni, J., and Cui, D. (2011) BRCAA1 monoclonal antibody conjugated fluorescent magnetic nanoparticles for in vivo targeted magnetofluorescent imaging of gastric cancer, *Journal of Nanobiotechnology 9*, 9-23.

153. Yang, P., Quan, Z., Lu, L., Huang, S., and Lin, J. (2008) Luminescence functionalization of mesoporous silica with different morphologies and applications as drug delivery systems, *Biomaterials 29*, 692-702.

154. Li, L., Chen, D., Zhang, Y., Deng, Z., Ren, X., Meng, X., Tang, F., Ren, J., and Zhang, L. (2007) Magnetic and fluorescent multifunctional chitosan nanoparticles as a smart drug delivery system *Nanotechnology 18*, 405102.

155. Hsu, A. R., Hou, L. C., Veeravagu, A., Greve, J. M., Vogel, H., Tse, V., and Chen, X. (2006) In vivo near-infrared fluorescence imaging of integrin alphavbeta3 in an orthotopic glioblastoma model, *Mol Imaging Biol 8*, 315-323.

156. Sato, A., Klaunberg, B., and Tolwani, R. (2002) In vivo bioluminescence imaging, *Comparative medicine 2*, 266-276.

157. Gu, F. X., Karnik, R., Wang, A. Z., Alexis, F., Levy-Nissenbaum, E., Hong, S., Langer, R. S., and Farokhzad, O. C. (2007) Targeted nanoparticles for cancer therapy, *Nano Today 2*, 14-21.

158. Tsai, C.-P., Chen, C.-Y., Hung, Y., Chang, F.-H., and Mou, C.-Y. (2009) Monoclonal antibody-functionalized mesoporous silica nanoparticles (MSN) for selective targeting breast cancer cells, *J Mater Chem 19*, 5767-5743.

159. Goldman, E. R., Balighian, E. D., Mattoussi, H., Kuno, M. K., J.M., M., Tran, P. T., and Anderson, G. P. (2002) Avidin: a natural bridge for quantum dot-antibody conjugates, *J. Am. Chem. Soc. 124*, 6378-6382.

160. Levy, R., Wang, Z., Duchesne, L., Doty, R. C., Cooper, A. I., Brust, M., and Fernig, D. G. (2006) A generic approach to monofunctionalized protein-like gold nanoparticles based on immobilized metal ion affinity chromatography, *Chembiochem 7*, 592-594.

161. Fu, A., Micheel, C. M., Cha, J., Chang, H., Yang, H., and Alvisatos, A. P. (2004) Discrete Nanostructures of Quantum Dots/Au with DNA, *J Am Ceram Soc 126*, 10832-10833.

162. Xing, Y., Chaudry, Q., Shen, C., Kong, K. Y., Zhau, H. E., Chung, L. W., Petros, J. A., O'Regan, R. M., Yezhelyev, M. V., Simons, J. W., Wang, M. D., and Nie, S. (2007) Bioconjugated quantum dots for multiplexed and quantitative immunohistochemistry, *Nat Protoc 2*, 1152-1165.

163. Zdobnova, T. A., Drofeev, S. G., Tananaev, P. T., Vasiliev, R. B., Balandin, T. G., Edelweiss, E. F., Stremovskiy, O. A., Balavaeva, I. V., Turchin, I. V., Lebedenko, E. N., Zlomanov, V. P., and Deyev, S. M. (2009) Fluorescent immunolabeling of cancer cells by quantum dots and antibody scFv fragment, *J Biomed Opt 14*.

164. Tiwari, D. K., Tanaka, S. I., Inouye, Y., Yoshizawa, K., Watanabe, T. M., and Jin, T. (2009) Synthesis and Characterization of anti-HER2 antibody conjugated CdSe/CdZnS Quantum Dots for Fluorescence Imaging of Breast Cancer Cells, *Sensor 9*, 9332-9354.

165. Acchione, M., Kwon, H., Jochheim, C. M., and Atkins, W. M. (2012) Impact of linker and conjugation chemistry on antigen binding, Fc receptor binding and

thermal stability of model antibody-drug conjugates, *Landes Bioscience 4*, 362-372.

166. Mattson, G., Conklin, E., Desai, S., Nielander, G., Savage, M. D., and Morgensen, S. (1993) A practical approach to cross-linking, *Mol Bio Rep 17*, 167-183.

167. Sulfo-SMCC, Thermo Scientific.

168. Dausset, J., Moullee, J., and Bernard, J. (1959) Acquired hemolytic anemia with polyaggutinability of red blood cells due to a new factor present in normal human serum (anti-Tn), *Blood 14*, 1079-1073.

169. Dahr, W., Uhlenbruck, G., Gunson, H. H., and van der Hart, M. (1975) Studies on Glycoproteins and Glycopeptides from Tn-Polyagglutinable Erythrocytes, *VoxSanguinis 28*, 249-252.

170. Springer, G. F., Desai, P. R., Ghazizadeh, M., and Tegtmeyer, H. (1995) T/Tn pancarcinoma autoantigens: fundamental diagnostic and prognostic aspects., *Cancer Detect Prev 19*, 173-182.

171. Danussi C., C., A., Campa C., Mucignat M.T., Spessotto P., Uggeri F., Paoletti S., Colombatti A. (2009) A newly generated functional antibody identifies Tn antigen as a novel determinant in the cancer cell-lympactic endothelium interaction, *Glycobiology 19*, 1056-1067.

172. Zuang, D., S., Y., and Dennis, J. W. (1991) Tn antigen and UDP-Gal: GalNAc-Rß1-3-galactosyltranferase expression in human breast carcinoma, *Cancer Biochem Biophys 12*.

173. Kumar S.R., S. E. R., Quinn T.P., Deutscher S.L. (2005) Thomsen-Friedenreich and Tn antigens in nipple fluid: carbohydrate biomarkers for breast cancer detection, *Clinical Cancer Research 11*, 6868-6871.

174. Konska, G., Vissac, C., Zagla, K., Chezet, F., Vasson, M. P., Bernard-Gallon, D., and Guillot, J. (2002) Ultrastructural localization of binding sites for PNA and VVA-B4 lectins in human breast cancer cell lines detected by confocal fluorescent miscroscopy, *Int J Oncol 21*, 1009-1014.

175. Demichelis, S., Alberdi, C. G., Servi, W. J., Isla-Larrain, M. T., Segal-Eiras, A., and Croce, M. V. (2010) Comparative Immunohistochemiscal study of MUC1 and carbohydrate antigens in breast benign disease and normal mammary gland, *Appl Immunohistochem Mol Morphol 18*, 41-50.

176. Springer, G. F. (1997) Immunoreactive T and Tn epitopres in cancer diagnosis, prognosis, and immunotherapy, *J Mol Med 75*, 594-602.

177. Desai, P. (2000) Immunoreactive T and Tn antigen in maligancy: role in carcinoma diagnosis, prognosis, and immunotherapy, *Transfus Med Rev 14*, 312-325.

178. Konska, G., Guillot, J., De Lamour, M., and Fonck, Y. (1998) Expression of Tn antigen and N-acetyllactosamine residues in malignant and benign human breast tumors detected by lectins and momoclonal antibody 84D4, *Int J Oncol 12*, 361-367.

179. Ju, T., Otto, V. I., and Cummings, R. D. (2011) The Tn Antigen - Structural Simplicity and Biological Complexity, *Angewandte Chemie 50*, 1770-1791.

180. Etzler, M. E., Gupta, S., and Borrebaeck, C. (1981) Carbohydrate binding properties of th Dolichos biflorus lectin and its subunits, *J Biol Chem 256*, 2367-2370.

181. Bird, G. W., and Wingham, J. (1981) Anti-Tn from Marrubium candidissimum, *Rev Fr Transfus Immunohematol 24*, 347-348.

182. Wu, A. M., Wu, J. H., Liu, J. H., and Singh, T. (2004) Recognition profile of Bauhinia purpurea agglutinin (BPA), *Life Sci 74*, 1763-1779.

183. Moore, B. P. L., and Marsh, S. (1975) Identification of Strong Sd(a+) and Sd(a++) Red Cells by Hemagglutinins from Salvia horminum, *Transfusion 15*, 132-134.

184. Newman, R. A., and Uhlenbruck, G. G. (1977) Investigation into the Occurrence and Structure of Lectin Receptors on Human and Bovine Erythrocyte, Milk-Fat Globule and Lymphocyte Plasma-Membrane Glycoproteins, *Eur J Biochem 76*, 149-155.

185. Vega, N., and Perez, G. (2006) Isolation and characterisation of a Salvia bogotensis seed lectin specific for the Tn antigen, *Phytochemistry 67*, 347-355.

186. Wu, A. M. (2008) Polyvalent GalNAcα1→Ser/Thr (Tn) and Galβ1→3GalNAcα1→Ser/Thr (T α) as the most potent recognition factors involved in Maclura pomifera agglutinin–glycan interactions, *Journal of Biomedical Science 12*, 135-152.

187. Tollefsen, S. E., and Kornfeld, R. (1983) The B4 lectin from Vicia villosa seeds interacts with N-acetylgalactosamine residues alpha-linked to serine or threonine residues in cell surface glycoproteins, *J Biol Chem 258*, 5172-5176.

188. Ju, T., Lanneau, G. S., Gautam, T., Wang, Y., Xia, B., Stowell, S. R., Willard, M. T., Wang, W., Xia, J. Y., Zuna, R. E., Laszik, Z., Benbrook, D. M., Hanigan, M.

H., and Cummings, R. D. (2008) Human Tumor Antigens Tn and Sialyl Tn Arise from Mutations in Cosmc, *Cancer Res 68*, 1636-1646.

189. Conzelmann, A., and Lefrancois, L. (1988) Monoclonal antibodies specific for T cell-associated carbohydrate determinants react with human blood group antigens CAD and SDA, *J Exp Med 167*, 119-131.

190. Ferrara. (2004) Vascular endothelial growth factor: basic science and clinical progress, *2004 25*, 581-611.

191. Ferrara, N., Houck, K., Jakeman, L., and Leung, D. W. (1992) Molecular and biological properties of the vascular endothelial growth family of proteins, *Endocr Rev 13*, 18-32.

192. Liu Y., C. S. R., Morita T., Kourembanas S. (1995) Hypoxia regulates vascular endothelial growth factor gene expression in endothelial cells, *Circ Res 77*, 638-643.

193. Xu W.G., W. G., Zou Y.H, Song J.N., Yang X.Q., Wang W.Y. (2007) Vascular endothelial growth factor expression in invasive carcinoma of breast, *Chinese Journal of Cancer Research 19*.

194. Vogl G., D. O., Hauser-Kronberger C. (2005) Angiogenic potential of ductal carcinomas *in situ* (DCIS) of human breast, *Histopathology 47*, 617-324.

195. Krishman C., L. T. A. (2006) Ductal carcinoma in situ of the breast with osteroblast-like giant cells, *Human pathology*, 369-372.

196. Santra, S., Dutta, D., Walter, G. A., and Moudgil, B. M. (2005) Fluorescent nanoparticle probes for cancer imaging, *Technol Cancer Res Treat 4*, 593-602.

197. Oliveira, V. C., Carrara, R. C. V., Simoes, D. L. C., Saggioro, F. P., Carlotti Jr, C. G., Covas, D. T., and Neder, L. (2010) Sudan Black B treatement reduces autofluorescence and improve resolution of in situ hydridazation specific fluroescent signals of brain sections, *Histol Histopathol 25*, 1017-1024.

198. Dahan, M. (2006) From analog to digial: exploring cell dynamics with single quantum dots, *Histochem Cell Biol 125*, 451-456.

199. Au, G. H. T., Shih, W. Y., and Shih, W. H. (2013) High conjugation efficiency aquoues quantum dots for bioimaging,*Analyst,* In press

200. Altman, D. G., and Bland, J. M. (1994) Diagnostic tests 3: receiver operating characteristic plots, *BMJ 309*, 188.

201. Springer, G. F. (1995) T and Tn pancarcinoma markers: autoantigenic adhesion molecules in pathogenesis, prebiopsy carcinoma-detection, and long-term breast cancinoma immunotherapy, *Crit Rev Oncog 6*, 57-85.

202. Konska, G., Guerry, M., Caldefie-Chezet, F., De Latour, M., and Guillot, J. (2006) Study of the expression of Tn antigen in different types of human breast cancer cells using VVA-B4 lectin, *Oncology Report 15*, 305-310.

203. Iorns, E., Drews-Elger, K., Ward, T. M., Sonja, D., Clarke, J., Berry, D., Ashry, D. E., and Lippman, M. (2012) A New Mouse Model for the Study of Human Breast Cancer Metastasis, *PLoD ONE 7*, 47995.

204. Jenkins, D. E., Hornig, Y. S., Oei, Y., Dusich, J., and Purchio, T. (2005) Bioluminescent human breast cancer cell lines that permit rapid and sensitive in vivo detection of mammary tumors and multiple metastases in immune deficient mice, *Breast Cancer Research 7*, R444.

205. Walker, R. A. (2006) Quantification of immunohistochemistry - issues concerning methods, utility and semiquantitative assessment I, *Histopathology 49*, 406-410.

206. Cregger, M., Berger, A. J., and Rimm, D. L. (2006) Immunohistochemistry and Quantitative Analysis of Protein Expression, *Arch Pathol Lab Med 130*, 1026-1030.

207. Fritz, P., Wu, X., Tuczek, H., Multhaupt, H., and Schwarzmann, P. (1995) Quantitation in immunohistrochemistry. A research method or a diagnostic tool in surgical pathology? , *Pathologica 87*, 300-309.

208. McCabe, A., Dolled-Filhart, M., Camp, R. L., and Rimm, D. L. (2005) Automated quantitative analysis (AQA) of in situ protein expression, antibody concentration adn prognosis, *J Natl Cancer Inst 97*, 1808-1815.

209. Szeszel, M. K., Crisman, C. L., Crow, L., McMullen, S., Major, J. M., Natarajan, L., Saquib, A., Feramisco, J. R., and Wasserman, L. M. (2005) Quantifying estrogen and pregesterone receptor expression in breast cancer by digital imaging *J Histochem Cytochem 53*, 753-762.

210. Baschong, W., Suetterlin, R., and R.H., L. (2001) Control autofluorescence of archival formaldehyde-fixed, paraffin-embedded tissue in confocal laser scanning microscopy (CLSM), *J Histochem Cytochem 49*, 1565-1572.

211. Chen, H., Xue, J., Zhang, Y., Zhu, X., Gao, J., and Yu, B. (2009) Comparison of quantum dots immunofluorescence histochemistry and conventional immunohistochemistry for detection of caveolin-1 and PCNA in the lung cancer tissue microarray, *J Mol Hist 40*, 261-268.

212. Harvey, J. M., Clark, G. M., Osborne, C. K., and Allred, D. C. (1999) Estrogen receptor status by immunohistrochemistry is surperior to the ligand-binding assay for predicting respond to adjuvant endocrine therapy in breast cancer, *J. Clin. Oncol. 17*, 1477-1481.

213. Rudiger, T., Hofler, H., Kreipe, H. H., Nizze, H., Pfeifer, U., Stein, H., Dallenbach, F. E., Fischer, H. P., Mengel, M., vo Wasielewski, R., and Muller-Hermelink, H. K. (2002) Quality assurance in immunohistochemistry: results of an interlaboratory trail involving 172 pathologists, *Am J Surg Pathol 26*, 873-882.

214. Zhao, Q., Jiang, H., Cao, Z., Yang, L., Mao, H., and Lipowska, M. (2011) A handhold fluorescene molecular tomography system for interoperative optical imaging of tumor margins, *Med Phys 38*, 5873-5879.

215. Cohen, E., Ophir, I., and Shaul, Y. B. (1999) Induced differentiation in HT29, a human colon adenocarcinoma cell line, *J Cell Sci 112*, 2657-2666.

216. Marshall, L. M., Hunter, D. J., Connolly, J. L., Schnitt, S. J., Byrne, C., London, S. J., and Colditz, G. A. (1997) Risk of Breast Cancer Associated with Atypical Hyperplasia Lobular and Ductal Types, *Cancer Epidemology, Biomarkers and Prevention 6*, 297-301.

217. Palli, D., del Turco, R., Simoncini, R., and Bianchi, S. (1991) Benign breast disease nad brease cancer: a case-control study in a cohort in Italy, *Int J Cancer 47*, 703-706.

218. Dupont, W. D., and Page, D. L. (1985) Risk factors for breast cancer in women with proliferative breast disease, *N Engl J Med 312*, 146-151.

219. Cohen, M. (2004) Cancer Upgrades at Excisional Biopsy after Diagnosis of Atypical Lobular Hyperplasia or Lobular Carcinoma in Situ at Core-Needle Biopsy: Some Reasons Why, *Radiology 213*, 617-621.

220. Haider, M., Haterfi, A., and Ghandehari, H. (2005) Recombinant polymers for cancer gene therary: a minireview, *J Control Release 109*, 108-119.

221. Ahn, H. H., Lee, J. H., Kim, K. S., Lee, J. Y., Kim, M. S., Khang, G., Lee, I. W., and Lee, H. B. (2008) Polyethyleneimine-mediated gene delivery into human adipose derived stem cells, *Biomaterials 29*, 2415-2422.

222. Li, P. C., Li, D., Zhang, L. X., Li, G. P., and Wang, E. K. (2008) Cationic lipid bilayer coated gold nanoparticles-mediated transfection of mammalian cells, *Biomaterials 29*, 3617-3624.

223. Liu, J. W., Stace-Naughton, A., and Brinker, C. J. (2009) Silica nanopartical supported lipid bilayers for gene delivery, *Chem Commun 34*, 5100-5102.

224. Tan, W. B., Jiang, S., and Zhang, Y. (2007) Quantum-dot based nanoparticles for targeted silencing of HER2/neu gene via RNA interference, *Biomaterials 28*, 1565-1571.

225. Tan, W. B., and Zhang, Y. (2005) Surface modification of gold and quantum dots nanoparticles with chitosan for bioapplications, *J Biomed Mater Res A 75*, 56-62.

226. ZHou, X. F., Zhang, X. H., Zha, X., Fu, Q., and Liu, B. (2008) The effect of conjugation to gold nanoparticles on the ability of low molecular weight chitosan to transfer DNA vaccine, *Biomaterials 29*, 111-117.

227. Qi, L., and Gao, X. (2008) Quantum-dot-amphipol nanocomplex for intracellular delivery and real-time imaging of siRNA, *ACS Nano 2*, 1403-1410.

228. Lee, H., Kim, I. K., and Park, T. G. (2010) Intracellular trafficking and unpacking of siRNA/quantum dot-PEI complexes modified with and without cell penetrating peptide: confocal and flow cytometric FRET analysis, *Bioconjugation Chem 21*, 289-295.

229. Song, W. J., Du, J. Z., Sun, T. M., Zhang, P. Z., and Wang, J. (2010) Gold nanoparticles capped with polyethyeneimine for enhance siRNA delivery, *Small 6*, 239-246.

230. Xia, T. A., Kovochich, M., Liong, M., Meng, H., Kabehie, S., George, S., Zink, J. O., and Nel, A. E. (2009) Polyethyleneimine coating enhances the celluar uptake of mesoporous silica nanoparticles and allows safe delivery of siDNA and DNA constructs, *ACS Nano 3*, 3273-3286.

231. Jia, N. Q., Lian, Q., Shen, H. B., Wang, C., Li, X. Y., and Yang, Z. N. (2007) Intracellular delivery of quantum dots tagged antisense oligodeoxynucleotides by functionalized multiwalled carbon nanotubes, *Nano Lett 7*, 2976-2980.

232. Arsianti, M., Lim, M., Marquis, C. P., and Amal, R. (2010) Assembly of polyethyenimine-based magnetic iron oxide vectors: insights into gene delivery, *Langmuir 26*, 7314-7326.

233. Ho, Y. P., Chen, H. H., Leong, K. W., and Wang, T. H. (2006) Evaluating the intracellular stability and unpacking of DNA nanocomplexes by quantum dots-FRET, *J Control Release 29*, 3617-3624.

234. Gonzalez, B., Colilla, M., de Laorden, C. L., and Vallet-Regi, M. (2009) A novel synthetic strategy for covalently bonding dendrimers to ordered mesoporous silica: potential drug delivery applications, *J Mater Chem 19*, 9012-9024.

235. Jung, J. J., Solanki, A., Memoli, K. A., Kamei, K., Kim, H., and Drahl, M. A. (2010) Selective inhibition of human brain tumor cells through multifunctional quantum dots-based siRNA delivery, *Angew. Chem. Int. Ed. 49*, 103-107.

236. Vazquez, E., Cubarsi, R., Unzueta, U., Roldan, M., Domingo-Espin, J., Ferrer-Miralles, N., and Villaverde, A. (2010) Internalization and kinetics of nuclear migration of protein-only, arginine-rich nanoparticles, *Biomaterials 31*, 9333-9339.

237. Rosi, N. L., Giljohann, D. A., Thaxton, C. S., Lytoon-Jean Abigail, K. R., Han, M. S., and Mirkin, C. A. (2006) Oligonucleotide-modified gold nanoparticles for intracellular gene regulation, *Science 312*, 1027-1030.

238. Medintz, I. L., Pons, T., Delehanty, J. B., Susumu, K., Brunel, F. M., Dawson, P. E., and Mattoussi, H. (2008) Intracellular delivery of quantum dot-protein cargos mediated by cell penetrating peptides, *Bioconjugate Chemistry 19*, 1785-1795.

239. Delehanty, J. B., Medintz, I. L., Pons, T., Brunel, F. M., Dawson, P. E., and Mattoussi, H. (2006) Self-assembled quantum dot-peptide bioconjugates for selective intracellular delivery, *Bioconjugate Chemistry 17*, 920-927.

240. Pinaud, F., Clarke, S., Sittner, A., and Dahan, M. (2010) Probing cellular events, one dot at a time, *Nat Methods 7*, 275-285.

241. Srinivasan, C., Lee, J., Papadimitrakopoukos, F., Silbart, L. K., Zhao, M. H., and Burgess, D. J. (2006) Labelling an interacellular tracking of functionally active plasmid DNA with semiconductor quantum dots, *Mol Ther 14*, 190-201.

242. Mintzer, M. A., and Simanek, E. E. (2009) Nonviral vectors for gene delivery, *Chem Rev 109*, 259-302.

243. Li, Y., Duan, X., Jing, L., Yang, C., Qiao, R., and Gao, M. (2011) Quantum dot-antisense oligonucleotide conjugates for multifunctional gene transfection, mRNA regulation, and tracking biological processes, *Biomaterials 32*, 1923-1931.

244. Yum, K., Wang, N., and Yu, M. F. (2010) Electrochemically controlled deconjugation and delivery of single quantum dots into the nucleus of living cells, *Small 6*, 2109-2113.

245. Lange, A., Mills, R. E., Lange, C. J., Stewart, M., Devine, S. E., and Corbett, A. H. (2007) Classical Nuclear Localization Signals: Definition, Function, and Interaction with Importin α, *Journal of Biological Chemistry 282*, 5101-5105.

246. Li, H., Shih, W. Y., and Shih, W. H. (2007) Non-heavy metal ZnS quantum dots with bright blue photoluminescence by a one-step aqueous synthesis *Nanotechnology 18*, 205604.

247. Duan, H., and Nei, S. (2007) Cell-penetrating quantum dots based on multivalent and endosome-disrupting surface coatings, *J Am Chem Soc 129*, 3333-3338.

248. Lee, Y., Miyata, K., Oba, M., Ishii, T., Fukushima, S., Han, M., Koyama, H., Nishiyama, N., and Kataoka, K. (2008) Charge-conversional terary polyplex with endosome distruption moeity: a new paradaigm for the efficient and safe gene delivery, *Angew. Chem. Int. Ed. 47*, 5163-5166.

249. Leung, K. C.-F., Chak, C.-P., Lee, S.-F., Lai, J. M. Y., Zhu, X.-M., Wang, Y.-X. J., Sham, K. W. Y., and Cheng, C. H. K. (2013) Enhanced cellular uptake and gene delivery of glioblastoma with deferoxamine-coated nanoparticle/plasmid DNA/branched polyethylenimine composites, *Chem. Comm. 49*, 549-553.

250. Zinchuk, V., Zinchuk, O., and Okada, T. (2007) Quantitative Colocalization analysis of multicolor confocal immunofluorescence microscopy images: pushing pixels to explore biological phenomena, *Acta Histochem Cytochem 40*, 101-111.

251. Weis, K. (1998) Importins and exportins: how to get in and out of the nucleus, *Trends Biochem Sci 23*, 185-189.

252. Nigg, E. A. (1997) Nucleocytoplasmic transport: signals, mechanisms and regulation, *Nature 386*, 779-787.

253. Lowe, A. R., Siegel, J. J., Kalab, P., Siu, M., Weis, K., and Liohardt, J. T. (2010) Selectivity mechanism of the nuclear pore complex characterized by single cargo tracking *Nature 467*, 600-604.

254. Kumata, M., Nitahara-Kasahara, Y., Miyamoto, Y., Yoneda, Y., and Aida, Y. (2005) Importin-α Promotes Passage through the Nuclear Pore Complex of Human Immunodeficiency Virus Type 1 Vpr, *J Virol 76*, 3557-3564.

255. Dingwall, C., and Laskey, R. A. (1991) Nuclear targeting sequences-a consensus?, *Trends Biochem Sci 1991*, 478-481.

256. Chen, Q. Q., Chen, X. Y., Jiang, Y. Y., and Liu, J. (2005) Identification of novel nuclear localization signal within the ErbB-2 protein *Cell Research 15*, 504-510.

257. Cingolani, G., Petosa, C., Weis, K., and Muller, C. W. (1999) Structure of importin-α bound to the IBB domain of importin-β *Nature 399*, 221-229.

258. Yezhelyev, M. V., Qi, L., O'Regan, R. M., Nie, S., and Gao, X. (2008) Proton-spong coated quantum dots for siRNA delivery and intracellular imaging, *J Am Chem Soc 130*, 9006-9012.

259. Nativo, P., Prior, I. A., and Brust, M. (2008) Uptake and intracellular fate of surface-modified gold nanoparticles, *ACS Nano 2*, 1639-1644.

260. de la Fuente, J. M., and Berry, C. C. (2005) Tat Peptide as an efficienct molecule to translocate gold nanoparticles into the cell nucleus, *Bioconjugate Chemistry 16*, 1176-1180.

261. Chithrani, B. D., Ghazani, A. A., and Chan, W. C. W. (2006) Determining the size and shape dependence of gold nanoparticle uptake into mammlian cells, *Nano Lett 6*, 662-668.

262. Nguyen, K. T., Holloway, M. P., and Altura, R. A. (2012) The CRM1 nuclear export protein in normal development and disease, *Int. J. Biochem Mol Biol 3*, 137-151.

263. Vachutinsky, Y., Oba, M., Miyata, K., Hiki, S., Kano, M. R., Nishiyama, N., Koyama, H., Miyazono, K., and Kataoka, K. (2011) Antiangiogenic gene therapy of experimental pancreatic tumor by sFlt-1 plasmid DNA carried by RGD-modified creosslinked polyplex micelles, *J. Controlled Release 149*, 51-57.

264. Guo, G., Liu, W., Liang, J., He, Z., Xu, H., and Yang, X. (2007) Probing the cytotoxicity of CdSe quantum dots with surface modification, *Materials Letters 61*, 1641-1644.

265. Li, Y., Zhou, Y., Wang, H. Y., Perrett, S., Zhao, Y., Tang, Z., and Nie, G. (2011) Chirality of Glutathione Surface Coating Affects the Cytotoxicity of Quantum Dots, *Angewandte Chemie International Edition 50*, n/a.

VITA

GIANG HOANG THUY AU

EDUCATION

•	2009-2013	Ph.D. in Biomedical Engineering Drexel University, Philadelphia, PA, USA
•	2006-2009	M.S./B.S. in Biomedical Engineering Drexel University, Philadelphia, PA, USA

PUBLICATIONS

1. Au G.H.T., Shih W.Y., Shih W.-H.. (2013) "High-conjugaton-efficiency Aquoues CdSe Quantum Dos for Bioimaging". *Analyst,* (in Press)
2. Au G.H.T., Shih W.Y., Shih W.-H., Mejias L., Swami W.K., Wasko K., Brooks A.B.(2012) "Assessing Breast Cancer Margin ex vivo using Aqueous Quantum-Dot-Molecular Probes". *International Journal of Surgical Oncology*, **2012,** 862157.
3. Giang H.T. Au, Wan Y. Shih, Wei-Heng Shih. (2012) "Aqueous CdPbS Quantum Dots for Near-Infrared Imaging." *Nanotechnology*, **23**, 275601.
4. Mejias L., Au G.H.T., Morales D., Brooks A.B., Shih W.-H., Shih W.Y., Swami V.K.(2012) "Methods Comparing Quantum Dots Immunofluorescence and Immunohistochemistry for Real Time Breast Cancer Margin Detection". *Arch. Pathol. Lab. Med.* **136**: 1135.
5. Au G.H.T., Shih W.Y., Mejias L., Swami V.K., Brooks A.B., Shih W.-H. "Quantitative Assessment of Tn antigen in Breast Tissue Micro-arrays using CdSe Aqueous Quantum Dots" *Biomaterials* , (in Review)
6. Shih W.-H., Au G.H.T., Shih W.Y., Brooks A.B., Swami V.K.. "Near-Infrared Quantum Dots for Clear Margin Determination during Breast Cancer Surgery" *Poster Presentation at the 6th Ear of Hope Conference – The Department of Defense (DoD) Breast Cancer Research Program* – August 2011.

PATENTS

1. Wei-Heng Shih, Giang H.T. Au, and Wan Shih, Ari B. Brooks "Methods for Making Water Soluble Quantum Dots," International Patent Pending #PCT/US2011/057083, October 2011 .
2. Wan Shih, Giang H.T. Au, Wei-Heng Shih, Ari B. Brooks, Vanlila K. Swami "Clear Margin Determination during Surgery," International Patent Application PCT/US2012/039532, May 2013.

HONORS and AWARDS

- Calhoun Fellowship, School of Biomedical Engineering, Drexel University
- First Place for Drexel Research Day Graduate Student Poster Competition, 2011-2012
- Best Biomedical Engineering Senior Design Project, Drexel University, 2009
- Dean Scholarship, Drexel University, 2006-2009
- Member of Tau Beta Pi – Engnieering Honors Society, Phi Theta Kappa-Honors Society